

# Synthesis and Characterisation of Defect Perovskite Materials ( $A_2BX_6$ and $A_3Bi_2X_9$ )

Lina Zhang

Supervisor: Professor Robert Palgrave

Date: 03/10/2023

# **Declaration**

I, Lina Zhang confirmed that the work presented in this thesis is my own. Where information has been derived from other sources, I confirm that has been indicated in the thesis.

#### **Abstract**

Lead-free halides with perovskite-related structures such as defect-ordered perovskites in the form of Cs<sub>3</sub>Bi<sub>2</sub>X<sub>9</sub> and A<sub>2</sub>BX<sub>6</sub> are of interest for photovoltaic applications. The main content is about the characterisations of mixed halide A<sub>2</sub>BX<sub>6</sub> vacancy double perovskites and the characterisations of doping mixed valences Sn<sup>2+</sup> and Sn<sup>4+</sup> into defect-ordered triple perovskite Cs<sub>3</sub>Bi<sub>2</sub>X<sub>9</sub>(X=Cl<sup>-</sup> or Br). Substitutional doping was used to produce mixed halides in A<sub>2</sub>BX<sub>6</sub> vacancy double perovskites via solution-phased synthesis and high temperature solid-state synthesis. The products of solution synthesis are series Cs<sub>2</sub>SnBr<sub>6-6x</sub>Cl<sub>6x</sub> and Cs<sub>2</sub>Snl<sub>6-6x</sub>Br<sub>6x</sub> (where x= 0 to 1 in increments of 0.1, and x= 0 represents nominal Br%=0). A distortion of pure cubic Cs<sub>2</sub>SnX<sub>6</sub>(X=Cl, Br or I) structures was caused by changing the spacing of the BX<sub>6</sub> octahedra related to the size of A-site to maintain the overall symmetry. Optical band gap was varied by the ratio of mixed halides in composition from 4.53 eV in Cs<sub>2</sub>SnCl<sub>6</sub> to 1.38 eV in Cs<sub>2</sub>Snl<sub>6</sub> and showed a highly non-linear correlation with changes of mixed halide ratio in the composition. The high temperature solid-state approach to mix halides in the compounds was unsuccessful.

Moreover, addition of SnX<sub>2</sub> into Cs<sub>3</sub>Bi<sub>2</sub>X<sub>9</sub>(X=Cl or Br) resulted mixed valences (Sn<sup>2+</sup> and Sn<sup>4+</sup>) in the Cs<sub>3</sub>Bi<sub>2</sub>X<sub>9</sub> with no change of the general phase structures, using solution-phased synthesis (SpS) and solid-state grinding (SsG). The mixed-valence compounds showed intense absorption in the visible and near infrared region due to the intervalence charge transfer. The double substitution complex enhanced the stability of Sn<sup>2+</sup> in the compounds. The similar approaches doping Sn into Cs<sub>3</sub>Sb<sub>2</sub>Cl<sub>9</sub> or Rb<sub>3</sub>Bi<sub>2</sub>Br<sub>9</sub> are unsuccessful.

## **Impact Statement**

Due to the massive demand for energy and the relatively limited energy resources on the planet, seeking renewable energy sources to satisfy the demand without causing damage or burden to earth is important for the sustainability of the planet. The supply and use of non-renewable resources are both limited and damaging to the environment. Therefore, research into alternative ways of generating energy is urgent. The sun is the most powerful energy source for life on earth. To harvest the useful energy from the sun, a good light absorber of solar energy is needed.

To pursue a better material for a new-generation perovskite solar cells, a light absorber with high solar light absorption and an efficient technique to deposit on the thin film with high uniformity are required. The research is focused on finding a good light absorber. Perovskites have good light absorption properties and is made of common and low-cost materials. However, the disadvantage of perovskites is that is susceptible to degradation in air and moisture. The most efficient perovskite compound, CH<sub>3</sub>NH<sub>3</sub>Pbl<sub>3</sub>, contains a toxic element (lead, Pb). For these reasons, the research is focusing on stable and lead-free perovskite-like materials such as double perovskites in the A<sub>2</sub>BX<sub>6</sub> (where A site can be Cs<sup>+</sup>, CH<sub>3</sub>NH<sub>3</sub><sup>+</sup>, or CH<sub>3</sub>CH<sub>2</sub>NH<sub>3</sub><sup>+</sup>, and B-site can be Te<sup>4+</sup> or Sn<sup>4+</sup>, and X site can be Cl<sup>-</sup>, Br or l<sup>-</sup>) and defect-ordered triple perovskites in the A<sub>3</sub>B<sub>2</sub>X<sub>9</sub> (where A-site can be Cs<sup>+</sup> or Rb<sup>+</sup>, and B-site can be Sb<sup>3+</sup> or Bi <sup>3+</sup>, and X-site can be Cl<sup>-</sup>, Br or l<sup>-</sup>).

This research is to study the characterisations of these perovskite-like materials and to analyse the change of optical properties, crystal growths and analytic compositions of these compounds, using different synthesis methods (Solution-phased synthesis or

High temperature Solid-state grinding method). This offers insights for better performance of light absorbers in the field by modulating crystal structure, electronic properties, optical properties of perovskite-like materials.

# Acknowledgements

First, I would like to thank both of my supervisors Prof. Robert Palgrave and Dr. Bob Schroeder for their continuous support and guidance throughout my journey. Initially, my project started off being fully experimental, and I am very grateful for the freedom and flexibility given by my supervisors in pursuing my project. As such, I continued my research after my master project on perovskite-like materials. Prof. Robert G. Palgrave supported me with my decision, and he has been incredibly helpful and supportive on giving me advice in different kinds of synthesis as well as science in general. I could not thank you enough for also being such a good mentor to support me through my master project and PhD thesis. I am extremely lucky to have you as my supervisors.

Second, I am grateful for all the help and advice received from the following individuals such as Mr Martin Vickers from PXRD lab, Mr Martyn Towner from Turner lab, and Dr Steve Firth from Raman lab and XRF lab. Thank you all for your kind assistance and the training sessions through my PhD.

Third, to all my colleagues, Prajna, Yuhan, Roxanna, Tim, Gogulan and others in Robert Palgrave Research Group, I am so glad to have you all though my PhD journey. Thank you for all the help and advice on my research project. You have made my time here at UCL incredibly enjoyable. Thank you for being supportive throughout my PhD journey.

Additionally, I want to thank Dr Sanjay Sathasiviam for all the help and guidance for both my thesis and viva. Thank you for being there for me. I could not have done it without you. You are incredible!

Lastly, I would like to thank my husband and my parents for their unconditional love and support through my PhD journey. I could not have completed it without them. At last, I want to thank myself for being consistent and determined though the highs and lows of my PhD.

THANK YOU ALL.

#### Contents

1	lr	Introduction				
	1.1	9	Semiconductors and Band Gap	12		
	1.2	F	Photovoltaic Cells	18		
	1	.2.1	First generation solar cells: Silicon	19		
	1	.2.2	Second generation solar cells: Thin-film solar cells	20		
	1	.2.3	Third generation solar cells: Emerging solar absorber materials	22		
	1.3	F	Perovskite materials	24		
	1.4	H	How a Perovskite Solar Cell Works	27		
	1.5	[	Doping	28		
	1.6	(	Organic/ Inorganic Halide Perovskite Compounds (ABX <sub>3</sub> )	32		
	1.7	١	Vacancy-ordered Double Perovskite Compounds (A <sub>2</sub> BX <sub>6</sub> )	39		
	1.8	١	Vacancy-ordered triple perovskites(A <sub>3</sub> B <sub>2</sub> X <sub>9</sub> )	44		
	1.9	A	Aims and Motivations	51		
2 Characterisation Methodology		acterisation Methodology	53			
	2.1	F	Powder X-ray Diffraction	53		
	2	.1.1	Characterisation	55		
	2	.1.2	Rietveld Refinement	57		
	2.2	>	X-ray Photoelectron Spectroscopy	59		
	2	.2.1	Characterisation	62		
	2.3	F	Raman Spectroscopy	64		
	2	.3.1	Characterisation	66		
	2.4	ι	Ultraviolet-Visible Spectroscopy	67		
	2	.4.1	Characterisation	68		
	2	.4.2	Tauc Method	68		
	2	.4.3	Eliot Model	69		
	2.5	٦	Thermogravimetry Analysis (TGA)	71		
	2.6	>	X-ray Fluorescence	73		
	2.7	٦	Fitration to calculate percentage of Sn <sup>2+</sup>	74		

3		Defe	ct-ordered double perovskites(A <sub>2</sub> BX <sub>6</sub> )	77
	3.	1 N	/lixed halide materials Cs₂SnX <sub>6</sub> (X=Cl⁻, Br⁻, or l⁻)	78
		3.1.1	Experimental Methodology	79
3.1.2		3.1.2	Results and Discussion.	83
		3.1.3	Conclusion	133
	3.	2 <i>A</i>	$A_2SnCl_{6-6x}Br_{6x}$ series with different A-site ions (A=Cs <sup>+</sup> , CH <sub>3</sub> NH <sub>3</sub> <sup>+</sup> , CH <sub>3</sub> CH <sub>2</sub> NH <sub>3</sub> <sup>+</sup> ) .	136
		3.2.1	Experimental methodology	136
		3.2.2	Results and Discussion	138
		3.2.3	Conclusion	144
	3.	3 E	3-site ions Mixing	146
		3.3.1	Experimental Methodology	146
		3.3.2	Results and Discussion	149
		3.3.3	Conclusion	156
4		Bism	uth halide materials(A <sub>3</sub> Bi <sub>2</sub> X <sub>9</sub> ) doping Sn <sup>2+</sup>	159
	4.	1 (	S <sub>3</sub> Bi <sub>2</sub> Br <sub>9</sub> Materials doping Sn <sup>2+</sup>	159
		4.1.1	Experimental Methodology	160
		4.1.2	Results and Discussion	162
		4.1.3	Conclusion	175
	4.	2 (	Cs <sub>3</sub> Bi <sub>2</sub> Cl <sub>9</sub> Materials doping Sn <sup>2+</sup>	176
		4.2.1	Experimental Methodology	177
		4.2.2	Results and Discussion	179
		4.2.3	Conclusion	196
	4.	3 8	Sn doping attempts on Other A <sub>3</sub> B <sub>2</sub> X <sub>9</sub>	196
		4.3.1	Results and Discussion (Cs <sub>3</sub> Sb <sub>2</sub> Cl <sub>9</sub> )	197
		4.3.2	Results and Discussion (Rb <sub>3</sub> Bi <sub>2</sub> Br <sub>9</sub> )	200
		4.3.3	Conclusion	206
5		Conc	lusion and Future Direction	207
6		Appe	ndix	212
	6.	1 [	Detailed information about Reagents and Solvents	212

6	5.2	Compositional Calculation Data	214
6	6.3	Analytic atomic ratio and unit cell parameters of Cs <sub>2</sub> SnX <sub>6</sub>	218
6	6.4	XPS Analysis of Sn doped Cs <sub>3</sub> Bi <sub>2</sub> Br <sub>9</sub>	220
7	Pub	olications	222
8	List	of Figures	223
9	List	of Tables	228
10	List	of Equations	228
11	Bib	liography	229

# 1 Introduction

As the world population grows, and as new technologies are developed energy demands will increase. As computers and technologies become more powerful there will be an increase in consumption to power them. World energy sources are mainly from fossil fuels. Consumption of fossil fuels emit greenhouse gasses such as Carbon dioxide (CO<sub>2</sub>). An increase in the concentration of greenhouse gases causes global warming. CO<sub>2</sub> is seen as the main contributor of global warming and doubling the concentration can cause the average global surface temperature to increase by 3.8 °C.

Greenhouse gases are the gases that can trap heat within the atmosphere. They are Carbon dioxide (CO<sub>2</sub>), Methane (CH<sub>4</sub>), Nitrous oxide (N<sub>2</sub>O), Fluorinated gases and water vapour. The sun shines on earth and warms up the earth's surface on the daytime, and the surface releases heat into the atmosphere when it cools down at night. The greenhouse gases in the atmosphere can trap some heat. Hence, the earth's temperature is at about 14 °C. Without it, the earth is too cold for any life to exist. However, that is the natural greenhouse effect without the consequences of human activities.

Human activities have caused a dramatic increase in the release of greenhouse gases into the atmosphere. Burning fossil fuels releases CO<sub>2</sub> into the atmosphere.

CH<sub>4</sub> is emitted during the production and transport of fossil fuels apart from methane emission from livestock and other agricultural practices and the decay of organic waste from waste landfills. N<sub>2</sub>O also is emitted from agricultural and industrial uses. Water vapour is the most abundant greenhouse gases which increases the atmosphere temperature but only persists for a few days. CO<sub>2</sub> can remain in the earth's atmosphere for a very long time. That is why the concentration of CO<sub>2</sub> is accumulated continuously. The group of gases above are natural greenhouse gases which human activities have cause a huge increase in concentration. Humans have also emitted fluorinated gases such as hydrofluorocarbons, perfluorocarbons and sulphur hexafluoride which are released from industrial production and do not naturally exist in the atmosphere.

Global warming can be devastating to the environment and can cause extreme weather conditions leading to widespread damage, failed crop yields and the endangerment of wildlife. Due to this it is vital to limit the emission of greenhouse gasses and to ensure global warming does not get out of control.<sup>2</sup> The Paris Agreement was formed, which is a legally binding international treaty on climate change. The goal is to limit global warming to 1.5 °C above pre-industrial levels.<sup>3</sup> As a result, countries signed up to the Paris Agreement have introduced policies to reduce the reliance on fossil fuels and to increase the production of energy via renewable sources.

Due to the massive demand for energy and the relatively limited energy resources on the planet, seeking renewable energy sources to satisfy the demand without causing damage or burdens to earth is important for the sustainability of the planet. The demand of energy is forever increasing due to the increasing global population, and it is impossible to rely on non-renewable energy such as coal and gas. The supply and use of non-renewable resources are both limited and damaging to the environment. Therefore, research into alternative ways of generating energy is urgent.

The sun is the most powerful energy source for life on earth. Nuclear reactions within the body of the sun release the energy. It is called solar energy.<sup>4</sup> The average solar energy received from the sun to Earth's surface is about 1000 Wm<sup>-2</sup> on a clear day (about 510.1 trillion terawatt (TW) per year).<sup>5</sup> The world consumption in 2021 was around 25,300 terawatt-hours, this means the power received from the sun is far greater than the energy consumption on earth. To harvest the useful energy from the sun a good converter of solar energy is needed.

There are three ways to harvest solar energy. These are solar fuel, solar thermal and solar electricity. Solar fuel is a non-fossilised organic biomass material formed because of photosynthesis such as wood. Energy can be extracted through combustion of the fuels. Solar thermal harvests energy through collecting and concentrating heat from the sun into substances such as water, oil or a gas and using the high heat to generate electricity through different engines and because of this initial cost is high and unsuitable to use in a domestic setting. Solar electricity is provided by photovoltaic (PV) cells converting solar energy into electricity directly.<sup>6</sup>

However, the usage of solar power has a few challenges nowadays. It requests a large amount of initial cost for the installation. The current production of solar panels may not be fully sustainable as some serious drawbacks of different solar products cannot be ignored such as toxic emission during the production. Another serious issue is the disposal problem of the solar panels and batteries. So far these waste products cannot be recycled and has been landfilled. This might cause further problems in the future. That is why solar power is a promising solution to the energy crisis, and it can help reduce the carbon emissions although it alone cannot solve all the energy problems. Other sustainable energy sources such as wind power, geothermal power and biofuel, are needed. Alternate energy sources can be applied based on the local environment and weather, an example would be Iceland harnessing their geothermal resources to generate electricity and heat.

# 1.1 Semiconductors and Band Gap

In context of one atom as a system, it is composed of a positively charged nucleus containing protons and neutrons, surrounded by negatively charged electrons. According to Pauli exclusion principle, each electron is unique with the exclusive set of quantum numbers consisting of its energy, orbital angular momentum, and spin. This leads to the electron distribution of one atom which means that electrons must follow certain principles such as the Aufbau principle, Hund's rule,

and the maximum occupancy of each orbital being two electrons with opposite spins to fill in the atomic orbitals.

When two atoms are bonding, their atomic orbitals overlap. When atomic orbitals overlap, the electrons from the participating atoms redistribute themselves, resulting in the formation of new molecular orbitals. When sufficient atoms bond and form a solid, the atomic orbitals of neighbouring atoms within the solid overlaps and merges, leading to the formation of molecular orbitals that covers over multiple atoms. These molecular orbitals resulted from hybridisation of atomic orbitals from different atoms.

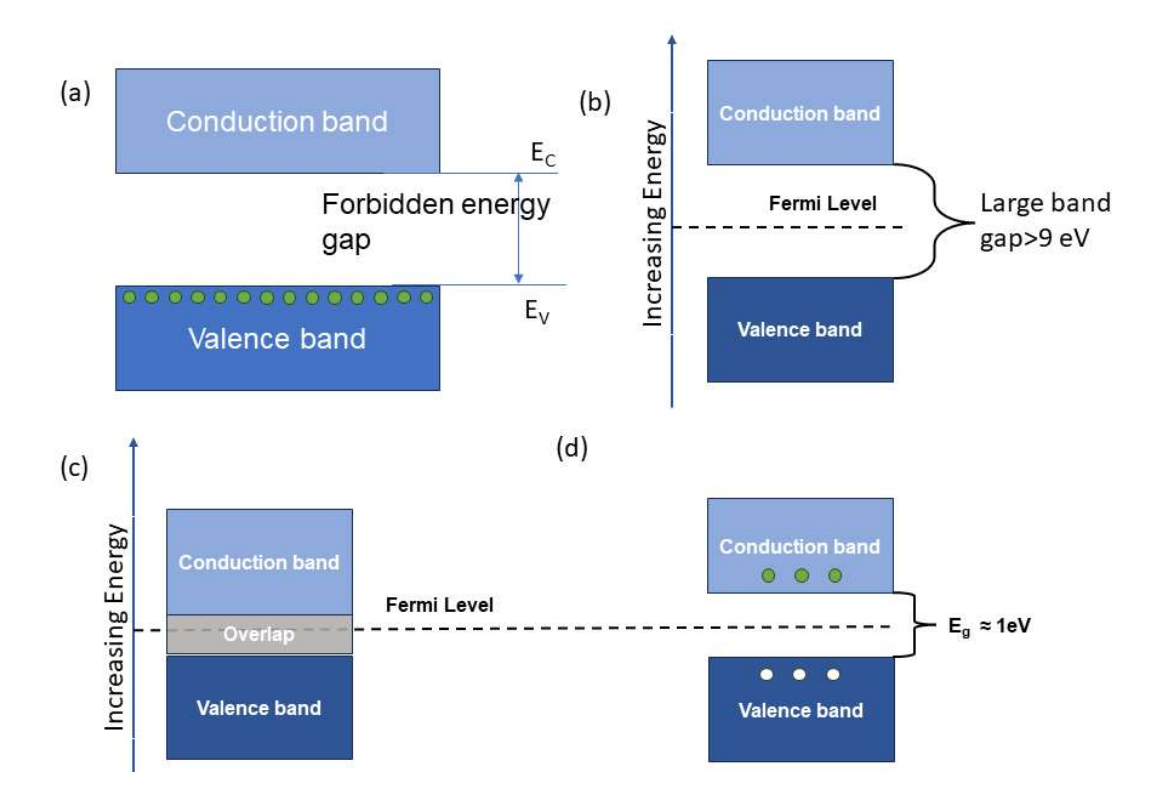


Figure 1.1 The schematic diagram representing (a)conduction band, valence band and forbidden energy gap. The schematic diagram of the energy band structures of (b) Insulator (such as ceramic), (c)Conductor (such as metal), and (d) Semiconductor (such as silicon).

The hybridisation of atomic orbitals from different atoms results in the discrete energy levels of individual atoms to broaden and become continuous energy ranges known as energy bands. These energy bands are separated into two main areas: the valence band and the conduction band in Figure 1.1(a). The valence band is composed of the occupied molecular orbitals that comes from the atomic orbitals of the constituent atoms. These orbitals are filled with electrons and contribute to the bonding and stability of the solid. Electrons in the valence band are not free to move throughout the material. The conduction band, on the other hand, comprises of empty or partially filled molecular orbitals. Electrons in the conduction band have higher energy levels and are relatively free to move throughout the solid, enabling electrical conductivity. The band gap is the gap between the valence band and the conduction band. It is the difference in energy between the lowest point of the conduction band (conduction band edge) and the highest point of the valence band (valence band edge). It represents the minimum energy that is needed to excite an electron from the valence band to the conduction band.

Materials can be classified as conductors such as metals, insulators such as ceramics, or semiconductors such as silicon based on the size of their band gap shown in Figure 1.1. In conductors, the valence band and conduction band overlap or have minimal energy barriers, allowing electrons to move easily from the valence band to the conduction band, resulting in good electrical conductivity in Figure 1.1(c). In contrast, insulators in Figure 1.1(b) have a large band gap, where the energy required to promote electrons from the valence band to the conduction band is significant. Hence, insulators have very limited electron flow

and exhibit poor electrical conductivity. Semiconductors in Figure 1.1(d) have a moderate band gap, allowing electrons to be excited from the valence band to the conduction band under certain conditions, such as applying an external electric field or increasing the temperature. This property makes semiconductors intermediate in their conductivity between insulators and conductors.

Semiconductors are divided as the intrinsic and extrinsic semiconductors. The intrinsic semiconductors have a natural and moderate bandgap. A small fraction of electrons can be excited into the conduction band easily by increasing the temperature. They form a small electric current. The hole left in the valence band can be filled by other electrons in the valence band. The small current is too little to quantify. Take silicon as an example, silicon (Si) theoretically should not have any empty state in the valence band and no electron in the conduction band at absolute zero (0 K). However, there is thermal energy at room temperature. The thermal energy provides the electrons from the valence band enough energy to excite into the conduction band as the bandgap of silicon is about 1.1 eV at room temperature. An empty state called a hole (a positive charged carrier) is left in the valence band; an electron moves into the conduction band which is a negative charged carrier.

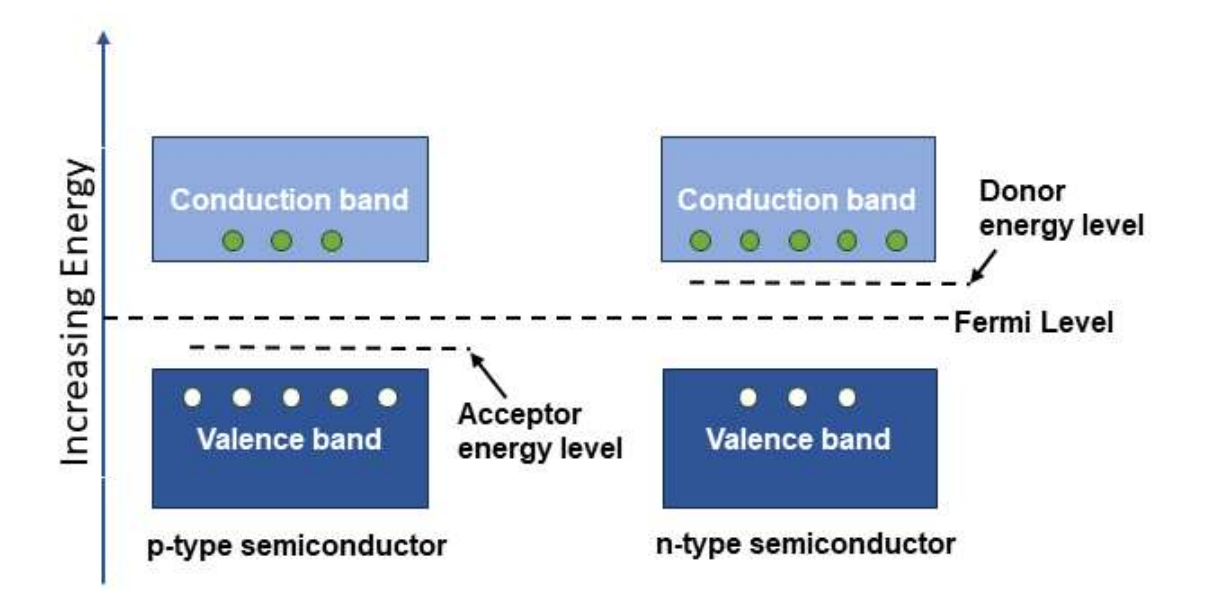


Figure 1.2 The schematic band diagram of a p-type semiconductor and a n-type semiconductor.

The extrinsic semiconductors have impurities (dopants) to increase the electric current like applying an external electric field. The extrinsic semiconductors are divided into two types, n-type semiconductors and p-type semiconductors shown in Figure 1.2. An n-type semiconductor is doped to have more electrons. For example, if an impurity such as Phosphorus (P) was intentionally introduced in a semiconductor, Si. P has 5 electrons in the outermost orbit (valence shell). Si has 4 electrons in the valence shell. There is one electron left attached to a P atom with a weak bond. The weak bond to the P atom can be broken easily at room temperature. Hence, every phosphorus atom that was introduced would provide an extra electron freely moving around the conduction band of the semiconductor when the weak bonds to P atoms is broken. The number of electrons is equal to the number of phosphorus atoms added to silicon. The majority of current carrier here is electron.

A p-type semiconductor is doped to have more holes.<sup>7</sup> For example, Boron (B) was introduced to Si as an impurity. B has three valence electrons. Every silicon atom wanted to be surrounded by four nearest neighbour atoms, so it got four electrons to pair up in the outermost shell. Boron will satisfy its bonding to its four nearest neighbours by pulling an electron out of the valence band to form the bond to Si. Then a hole was introduced in the valence band of the semiconductor. Every boron atom was put in, one hole was introduced to the valence band. The number of holes is equal to the number of boron atoms putting into silicon. The majority of current carrier here is hole.

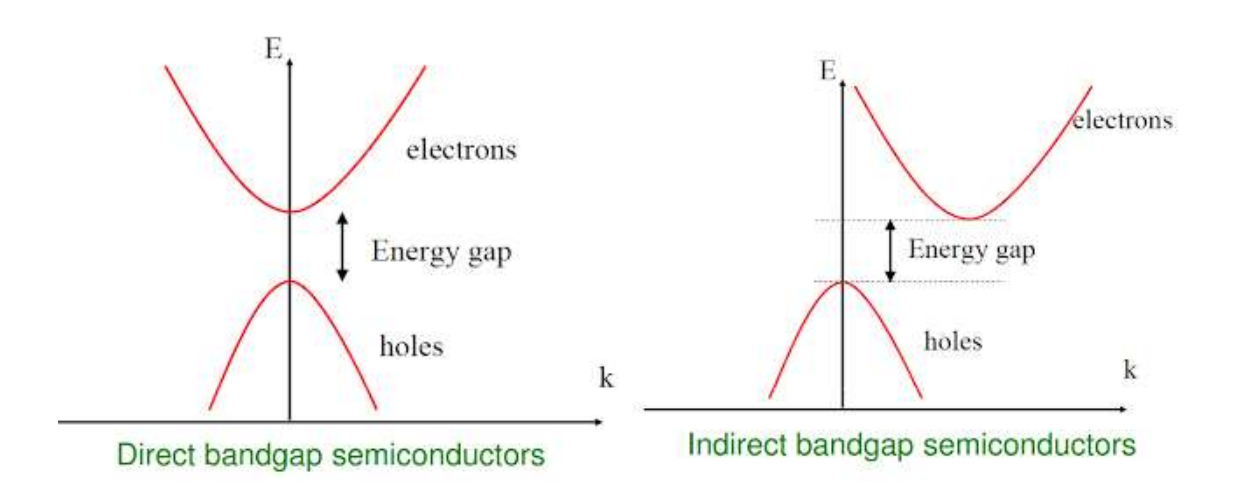


Figure 1.3 The Schematic diagram of direct bandgap and indirect bandgap semiconductors.

In terms of bandgap, semiconductors also can be divided into direct and indirect bandgap semiconductors shown in Figure 1.3. In quantum mechanics, electrons within an atom can be described as waves. The energy of an electron is given by

#### $E=p^2/2m=h^2k^2/2m$

where p is momentum, m is mass of an electron, h is Planck's constant, and k is propagation constant. Thus, E is proportional to  $k^2$  which is an equation of parabola. Thus, the graph of E vs k is a parabola.

The upper parabola in the conduction band represents the free electrons, and the lower parabola in the valence band represents holes. If maximum of valence band and minimum of conduction occur at the same momentum value, then such semiconductor is a direct bandgap semiconductor. Electrons make an energy transition,  $E_g$ , from valence band to conduction band without any change in its momentum. If maximum of valence band and minimum of conduction occur at two different momentum values of k, such semiconductor is with an indirect bandgap. To make a transition from maximum point in valence band to minimum point in conduction band, the electron requires additional energy for the change in momentum before the energy gap,  $E_g$ .

### 1.2 Photovoltaic Cells

The improvements in solar cell materials and manufacturing methods pushed forward the solar cell industry and increase the contribution to the global energy demands in the past decade. With further research and more advanced technologies, photovoltaic can produce cleaner energy at low cost.<sup>8</sup> Nowadays

PV cells can be divided into four major generation solar cells. There are silicon solar cells, thin-film solar cells, emerging solar cell technologies and hybrid solar cells.

#### 1.2.1 First generation solar cells: Silicon

This type of solar cells based on monocrystalline silicon, polycrystalline silicon, or gallium arsenide (GaAs). Thick crystalline silicon layers were the main component of the first-generation solar cells. Over 80% of the global installed solar cells are based on silicon. It dominates the PV cells market with over 90% of the market share.<sup>9</sup>

Although silicon well established in the PV cell industry, there are pros and cons of the first-generation solar cells. For example, monocrystalline silicon(m-si) solar cells are stable with the life span of 25 years. They showed high performance with power conversion efficiency (PCE) of 15-24% but they are sensitive to high temperature. They also suffer from light absorption problem and material loss. More importantly, the manufacturing cost of m-si solar cells is high. Comparing to that, polycrystalline silicon based solar cells have less wastes of silicon and higher light absorption with a simple and profitable manufacturing production. However, P-si solar cells are also affected by high temperature. More importantly the PCE of them is low. Although GaAs based solar cells can overcome technical disadvantages above with high stability (such as life span of 18 years), better light absorption and high PCE (28-30%) but the cost is still extremely high. 10,11

Hence, although crystalline silicon solar cells have many advantages such as raw materials abundancy, non-toxicity and good cell performance, the processing cost of m-si is too high due to a large amount of refined silicon required in the production. Most commercial m-si solar cells have used boron-doped single crystal wafers around 400um thick grown by Czochralski process. Although it is free from lattice defects, it contains impurities such as oxygen, carbon and transition-metal ions which can be beneficial or detrimental. Some annealing conditions form oxygen which causes gettering. Gettering is the effect of trapping unwanted transition-metal ions to improve the purity of surrounding silicon. Oxygen also enhances the mechanical strength of silicon wafers by immobilising any dislocations caused by device processing. However, oxygen impurities can react with boron to form active boron-oxygen complex under light which affect solar cell performance. 12 Defects in polycrystalline silicon solar cells reduced cell efficiency. 13 Refined silicon also requires high temperature in the silicon manufacturing process. Heat waste would be another issue in the large-scale production.<sup>14</sup>

#### 1.2.2 Second generation solar cells: Thin-film solar cells

The market for thin film solar cells is much lower compared with silicon even though much less material is required for thin-film solar cells (less than 1% of material required compared with crystalline silicon cells). <sup>15</sup> A lower cost replacement for the crystalline silicon cells has been designed using thin film

photovoltaic cells based on cadmium telluride (CdTe) /cadmium sulphide (CdS), gallium selenide and copper (CIGS). Thin film has improved and desired mechanical properties that are ideal for flexible application, they are highly heat resistant and manufacturing cost is lower due to less material required. For example, CdTe/ CdS has an indirect band gap of around 1.45 eV, and CIGS has an indirect band gap of about 1.7 eV, which is related to optimally high light absorption rate of about 10<sup>5</sup> cm<sup>-1</sup>. Theoretically PCE of CdTe based solar cells can reach 28-30% with a band gap of 1.5 eV. Laboratory-based CdTe solar cells have been reached a PCE record of about 22% by First Solar. As a result, thin film has great potential to be a replacement for crystalline silicon cells. However, CdTe/ CdS is highly toxic. It can cause acute health problems such as pneumonitis, pulmonary oedema, and death.

To produce an efficient thin-film solar cell, a light absorber with high solar light absorption and an efficient technique to deposit on the thin film with high uniformity is required. The current research is focused on finding a good light absorber. For this reason, the research aim is searching stable, toxicity-free, earth-abundant, and affordable solar absorber materials with low-cost manufacturing productions.

# 1.2.3 Third generation solar cells: Emerging solar absorber materials

Third generation solar cells are sometimes referred to as "emerging technologies" due to the poor market share in solar cells even though some of these have been studied for more than 25 years.<sup>22</sup> Third generation solar cells represent a variety of different approaches from low-cost but low efficiency systems to high-cost high efficiency systems to be used in a vast array of applications such as solar cells for buildings to space applications.<sup>23,24</sup>

The latest approach in the advancement of silicon photovoltaic cells focus on generating additional energy levels in the semiconductor band structure. Currently the most advanced research of manufacturing technology and improvement of efficiency is focused on third generation solar cells. The introduction of extra energy levels in the semiconductor's band gap (IBSC and IPV cells) and the increasing application of ion utilisation in the manufacturing process such as the ion-implantation technology is a current method used to increase the efficiency of PV cells. The ion-implantation technology is to improve the conductivity by reducing the recombination rate of electron-hole pairs to improve the light-harvesting ability.

Other examples of emerging technologies include organic materials (OSC) photovoltaic cells, perovskites (PSC) photovoltaic cells, dye-sensitized (DSSC) photovoltaic cells, quantum dots (QD) photovoltaic cells and multi-junction

photovoltaic cells.<sup>25</sup> Record efficiencies achieved (over time) for different third-generation technologies can be seen in Figure 1.5 in Chapter 1.3, with most being considerably lower than c-Si or second-generation technologies. The main advantages of these materials are their tunability and abundant components. As research progresses, record efficiencies of several technologies are likely to continue growing. Perovskite PV is growing fast in cell efficiency with less time frame comparing with OSC, DSSC and QD photovoltaic cells shown in Figure 1.5. However, the environmental impact of emerging PVs is hard to measure in detail as they are yet to be manufactured on a large scale.

In summary, OSCs have lower cell efficiency compared to second generation solar cells and have clear advantages in terms of environmental impact and material abundance, the comparisons are not so clear-cut for other third-generation cells. The record-certified efficiency of DSSC from NREL have not been exceeded since 2012 and 2014 respectively, which suggests a low potential for further improvements. QD solar cells often involves metal chalcogenide nanocrystals such as PbS or PbSe which consist of toxic or rare elements.

Perovskite solar cells share the same low cost, abundant material advantages of OSCs but have comparable efficiencies to second generation technologies. Therefore, in recent years there has been a significant increase in research in perovskite solar cells. Hence, research of lead-free halide perovskites is important.

This research focuses on the synthesis and characterisation of perovskites and perovskite-like materials as light absorbers. Hopefully the synthesis methods of tuning and optimising the structural, electronic, and optical properties mentioned in this report can improve the performance of future potential solar cells and provide guidance in search for new light absorber materials.

#### 1.3 Perovskite materials

Perovskite is any material with a crystal structure that has the same structure as a mineral called Perovskite. It consists of CaTiO<sub>3</sub> (Calcium titanate). It was named after a Russian minerologist Lev Perovski. Perovskite applies to materials that have the same crystal structure as CaTiO<sub>3</sub>. This is known as the perovskite structure (ABX<sub>3</sub>) in Figure 1.4.<sup>26</sup> Perovskite structure is a cubic structure with corner-sharing BX<sub>6</sub> octahedra where X can be oxides or halides.<sup>27,28</sup> The general chemical for perovskite material is ABX<sub>3</sub>, where A and B are two cations in very different sizes, and X is an anion that bonds to both cations. A-site cations are normally much larger than B-site cations. The ideal cubic structure has the B-site cations in 6-fold coordination surrounded by an octahedron of anions and A-site cations in 12-fold cub octahedral coordination. In the idealized cubic unit cell of ABX3, A-site atoms sit at cube corner coordination (0, 0, 0); B-site atoms sit at the body-centred coordination (½, ½, ½); X-site atoms sit face-centred coordination positions (½, ½, 0), (½, 0, ½) and (0, ½, ½).

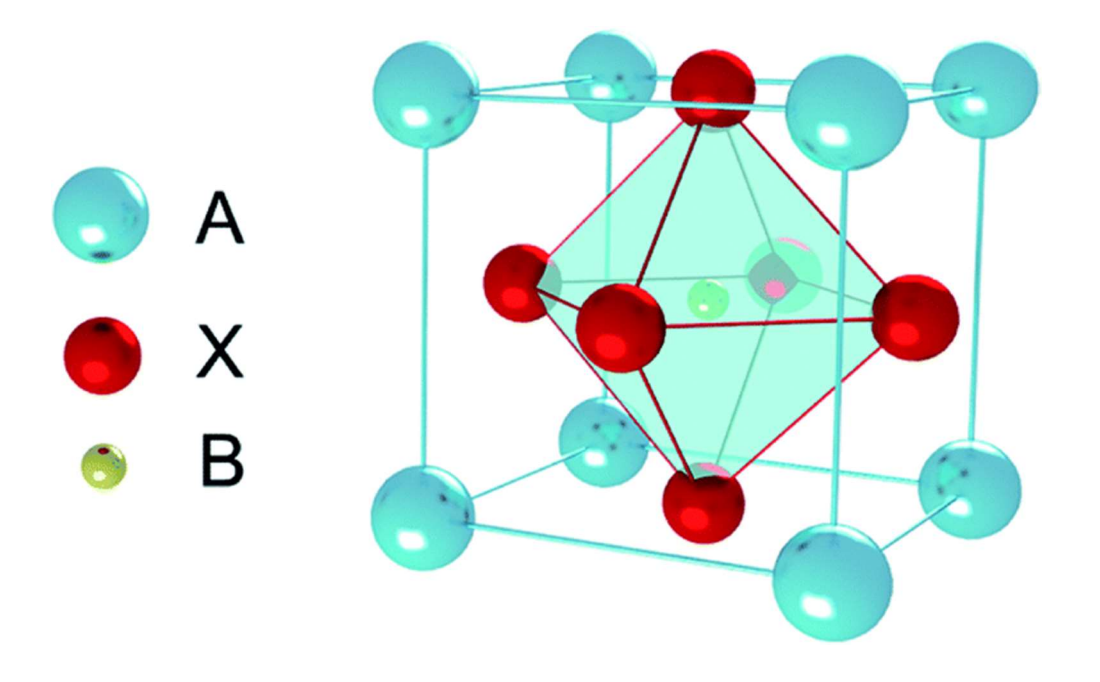


Figure 1.4 The schematic diagram of perovskite structure ABX3.29

For example, CH<sub>3</sub>NH<sub>3</sub>Pbl<sub>3</sub> is in the category of the perovskite structure which an organic A-site ion group with a formal oxidation state of +1, a B site cation with a formal oxidation state of +2 and an X-site ion with a formal oxidation state of -1.<sup>30</sup> X-site ion decides whether it is an inorganic oxide perovskite ABO<sub>3</sub> or a halide perovskite where X anions are halogen ions. A site ion decides whether it is an alkali perovskite or an organic-inorganic perovskite.<sup>31</sup> CH<sub>3</sub>NH<sub>3</sub>Pbl<sub>3</sub> is in the undistorted cubic structure which is highly symmetrical. The symmetry can be lowered to orthorhombic, tetragonal, or trigonal in many perovskites when the composition is changed.

Miyasaka discovered that perovskites have a light absorption function. He and his colleagues reported that CH<sub>3</sub>NH<sub>3</sub>PbBr<sub>3</sub> cells have a light energy conversion efficiency of 2.2%. <sup>32</sup> The efficiency can reach 3.8% when CH<sub>3</sub>NH<sub>3</sub>Pbl<sub>3</sub>

compounds are used as light absorbers in the solar cells.<sup>33</sup> Since then there is an increasing trend in the scientific research of halide perovskite compounds (CH<sub>3</sub>NH<sub>3</sub>BX<sub>3</sub>, B=Pb or Sn, X=Cl, Br, or l).

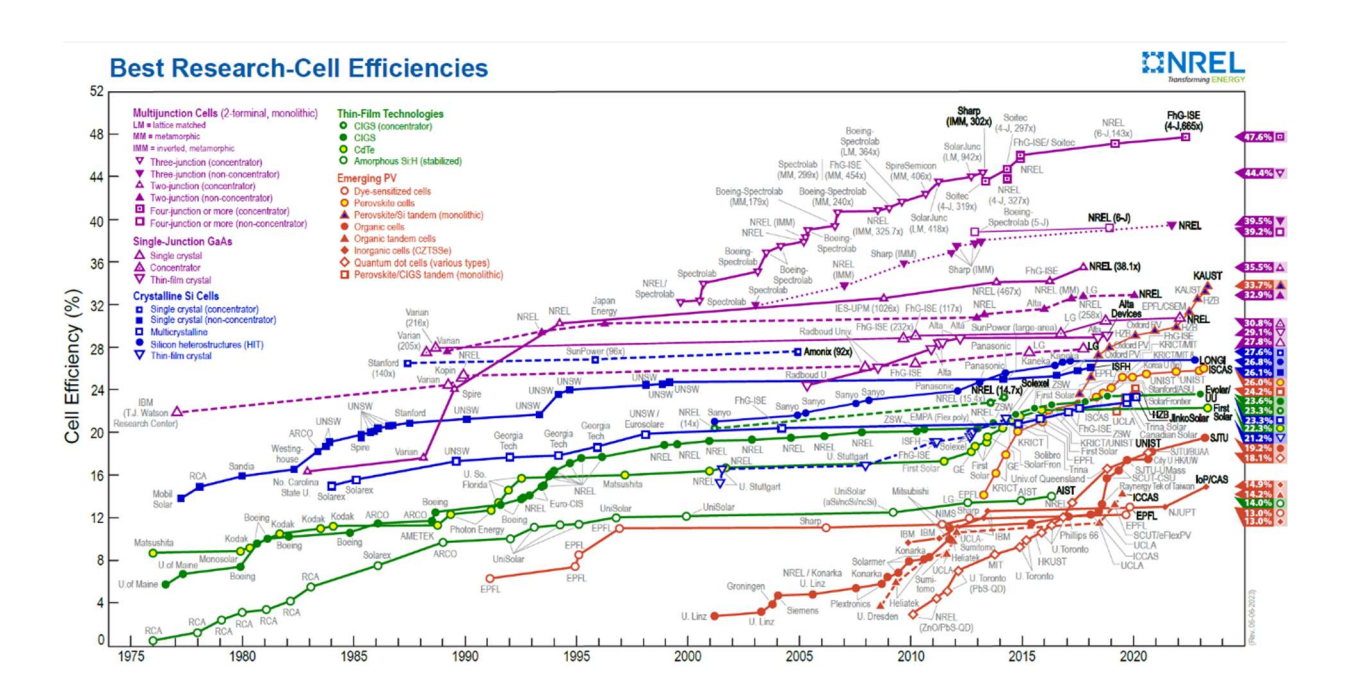


Figure 1.5 A chart of the highest confirmed conversion efficiencies for various research solar cells from 1976 to 2023.39

There is an increasing curve of power conversion efficiency (PCE) of using halide perovskites as light absorbers in the solar cells made by different research groups with respect to the timeline in Figure 1.5. Professor Park and his group from Sungkyunkwan University (SKKU) made many contributions.<sup>34</sup> Park and his coworkers improved the efficiency of CH<sub>3</sub>NH<sub>3</sub>Pbl<sub>3</sub> perovskite solar cells continuously and dramatically from 6.5%<sup>35</sup> to 17%<sup>36,37</sup> and finally reached to average 20.1% over 50 cells in 2016.<sup>38</sup> So far, the best research-cell efficiencies can reach 26% in the lab, which is recorded by National Renewable Energy

Laboratory (NREL). <sup>39</sup> Hence, what his group contributed to the industry of perovskite solar cells is promising.

#### 1.4 How a Perovskite Solar Cell Works

The mechanism of perovskite solar cells is based on the theory of the photovoltaic effect. 40 The photovoltaic effect is converting light into electricity when a material is exposed to light. A solar cell uses a semiconductor and perovskite crystals to generate electricity. Perovskite compounds are used as light absorbers because it has relatively high light absorption efficiencies, long-range charge transport, low excitation-binding energy, and high dielectric constant. 41,42

When a non-extrinsically perovskite crystal is sandwiched by a N-type semiconductor and a P-type semiconductor shown in Figure 1.6, it is called p-i-n junction. The perovskite crystals absorb light energy in the form of photons which excites electrons (-ve) from the valence band to the conduction band. Once the energy surpasses the bandgap of the perovskite, the electrons are excited to the conduction band from the valence band. It leaves behind a hole (+ve) in the valence band in the perovskite crystal. As there is a difference in charge in the perovskite crystal, the positive and negative charges can be collected at opposite electrodes in the solar cell. Negative charges are collected by an anode made by the combination of an N-type semiconductor (as the electron transporting material) and FTO (Fluorine doped Tin Oxide). Positive charges are collected by

a cathode made by the combination of a P-type semiconductor (as the hole transporting material) and a metal electrode. An electric current is produced by the electric potential caused by moving electrons in the same direction. The energy difference caused by the diffusion of positive and negative charges at the electrodes results in a voltage. The voltage allows the solar cell to create a current via the external circuit generating electricity.<sup>43</sup>,44

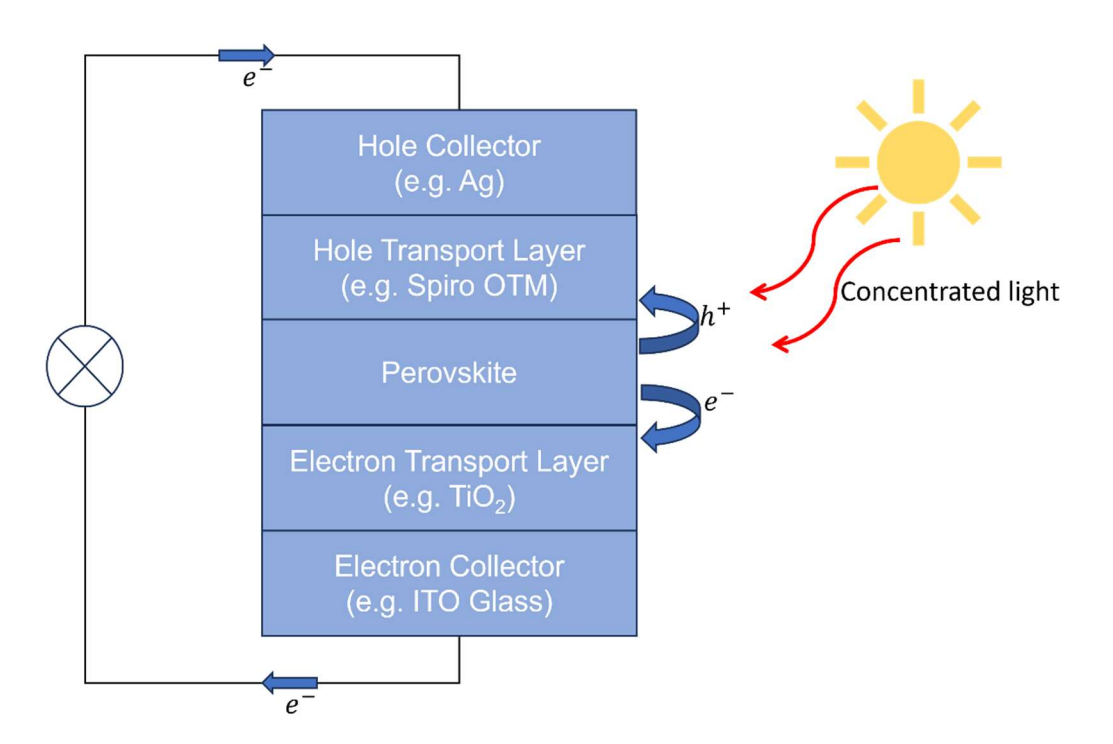


Figure 1.6 The diagram of the mechanism of a perovskite solar cell.

# 1.5 Doping

There are two types of doping techniques which are substitutional doping and interstitial doping shown in Figure 1.7. Interstitial doping is to fix ions into the

interspace of the unit cell structure which is normally much smaller than the elements from the compound.<sup>49</sup> It introduces an additional atom into the lattice gap to improve film quality, reduce band gap, and enhance light absorption in order to enhance the performance and stability of perovskite solar cells. However, high concentration of dopants can also cause lattice distortion. Hence, to overcome the challenge, the selection of cations with suitable sizes to occupy the interstitial sites and with a higher valence state is important. For example, different cations, such as Nd<sup>3+</sup>, Ca<sup>2+</sup> and Na<sup>+</sup>, were doped into the nearby iodine vacancy in the perovskite crystal structures of α-FAPbl<sub>3</sub> respectively. The interstitial doping of those cations affects the iodide migration. A trivalent cation (Nd<sup>3+</sup>) can slow down ion migration more effectively than Na<sup>+</sup>. <sup>45</sup> Substitutional doping is to replace ions in the compound with the same chemical or electronic stoichiometry .46 It is to replace an atom in a lattice site with another atom with the same oxidation state or another two atoms with mixed valencies. For example, doping of the mixed valent antimony (Sb<sup>3+</sup> and Sb<sup>5+</sup>)<sup>47</sup> to replace Sn<sup>4+</sup>, or the substitution of Ti<sup>4+</sup> with Co<sup>3+</sup> or Ge<sup>4+</sup> are cases of substitutional doping mixed valencies.48

#### a. Substitutional

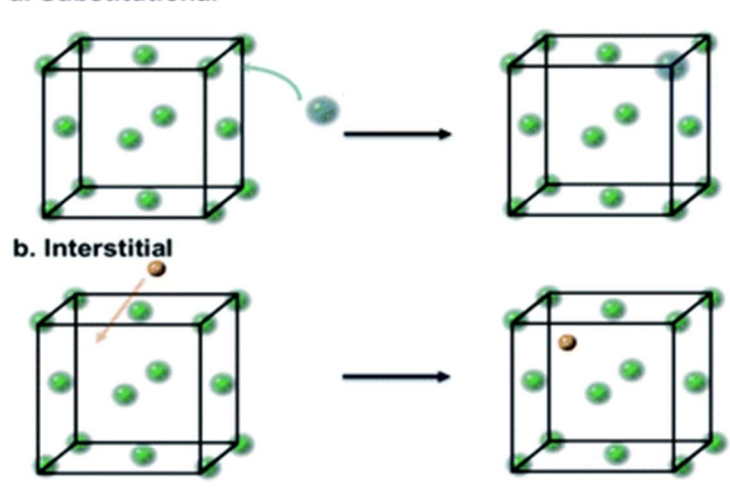


Figure 1.7 A schematic of substitutional and interstitial atomic modification by light elements to face-centred-cubic (FCC) a host metal lattice (green). (a) Substitutional atomic displacement by foreign light atoms (blue). (b) Interstitial atomic modification by foreign light atoms (brown).<sup>49</sup>

Both interstitial doping and substitutional doping can alter electronic and transport properties, lattice parameters, phase transitions, and consequently various physicochemical properties. For example, different proportions of organic cation doping can modulate the band gap and improve the stability of hybrid perovskite. Films of two-dimensional hybrid perovskites (PEA)<sub>2</sub>(MA)<sub>2</sub>[Pb<sub>3</sub>I<sub>10</sub>] are more moisture resistant than films of 3D perovskite MAPbI<sub>3</sub>. Partially substitution of X-site ions with other halogen ions influences the perovskite material's band structure. It caused a significant change in light absorption ability and an enhancement of carrier transport.<sup>50,51</sup>

Take the formation of interstitial alloys as another example. The size of dopants of interstitial alloys is small enough to diffuse into the sites. Elements from the

first period of p-block have small atomic radii and dominant s-p orbitals and often occupy the relatively large interstitial sites which are the octahedral hole in face-centre-cubic (FCC) and hexagonal-close-packed (HCP) structures, and the trigonal prismatic hole in hexagonal structures. Geometric and electronic conditions affect the crystal structure. The geometric properties are based on Hagg's rule which interstitial formation depends on the ratio of the atomic radius of dopants to the atomic radius of the host metal. The electronic properties of the interstitial alloys are different to the pristine metal due to the hybrid orbitals which affect the nature of metallic bonding in the crystal structure. Doping impurities into the interstitial system can also cause lattice expansion which transform the crystal structure due to repulsive electrostatic interaction.<sup>49</sup>

Substitutional doping in perovskite materials has been researched by replacing the A, B, and X sites.<sup>52</sup> For example, the variants of ABX<sub>3</sub> formed by substitutional doping such as APbI<sub>3</sub> by replacing A-site cations with alkaline metal ions or inorganic groups such as MA<sup>+</sup>, CH<sub>3</sub>NH<sub>3</sub><sup>+</sup>, or FA<sup>+</sup>, CH<sub>3</sub>CH<sub>2</sub>NH<sub>3</sub><sup>+</sup>. Studying the changes of properties of the variants is not only to better understand the theories/ trends of moderation of perovskites by doping but also to improve the current performance of solar cell techniques.

Here, substitutional doping techniques were only used in this thesis. One case is substitutional doping of the same oxidation state which is mixing halides from the halogen group in the periodic table in Chapter 3.1 or which is substitution of Asite ions in Chapter 3.2. The other case is substitutional doping of mixed valencies of Sn<sup>2+</sup> and Sn<sup>4+</sup> mentioned in Chapter 4.

# 1.6 Organic/ Inorganic Halide Perovskite

# Compounds (ABX<sub>3</sub>)

In the section of the literature review, the unit cell structure, the composition, and the light absorption property of ABX<sub>3</sub> perovskite can be discussed first. As it is mentioned, lead halide perovskites such as pure CH<sub>3</sub>NH<sub>3</sub>Pbl<sub>3</sub> thin films deposited utilizing a Lewis acid-base adduct approach can reach an average PCE (Power conversion efficiency) of 20.1% over 50 solar cells, which is reported by Park and his co-workers in 2016.<sup>38</sup> To study the unit cell structure of CH<sub>3</sub>NH<sub>3</sub>Pbl<sub>3</sub>, the general structure of a perovskite needs to be understood.

Perovskite is a mineral composed of CaTiO<sub>3</sub> (Calcium titanate), perovskite also applies to compounds that share the same type of crystal structure as CaTiO<sub>3</sub>, this is known as the perovskite structure. Perovskite structure consists of a cubic structure with corner-shared BX<sub>6</sub> octahedra (X = halides or oxides). <sup>53</sup> CH<sub>3</sub>NH<sub>3</sub>PbI<sub>3</sub> is in the category of the perovskite structure (ABX<sub>3</sub>) which an A-site ion with a formal oxidation state of +1, a B site cation with a formal oxidation state of +2 and an X-site ion with a formal oxidation state of -1.<sup>54</sup>

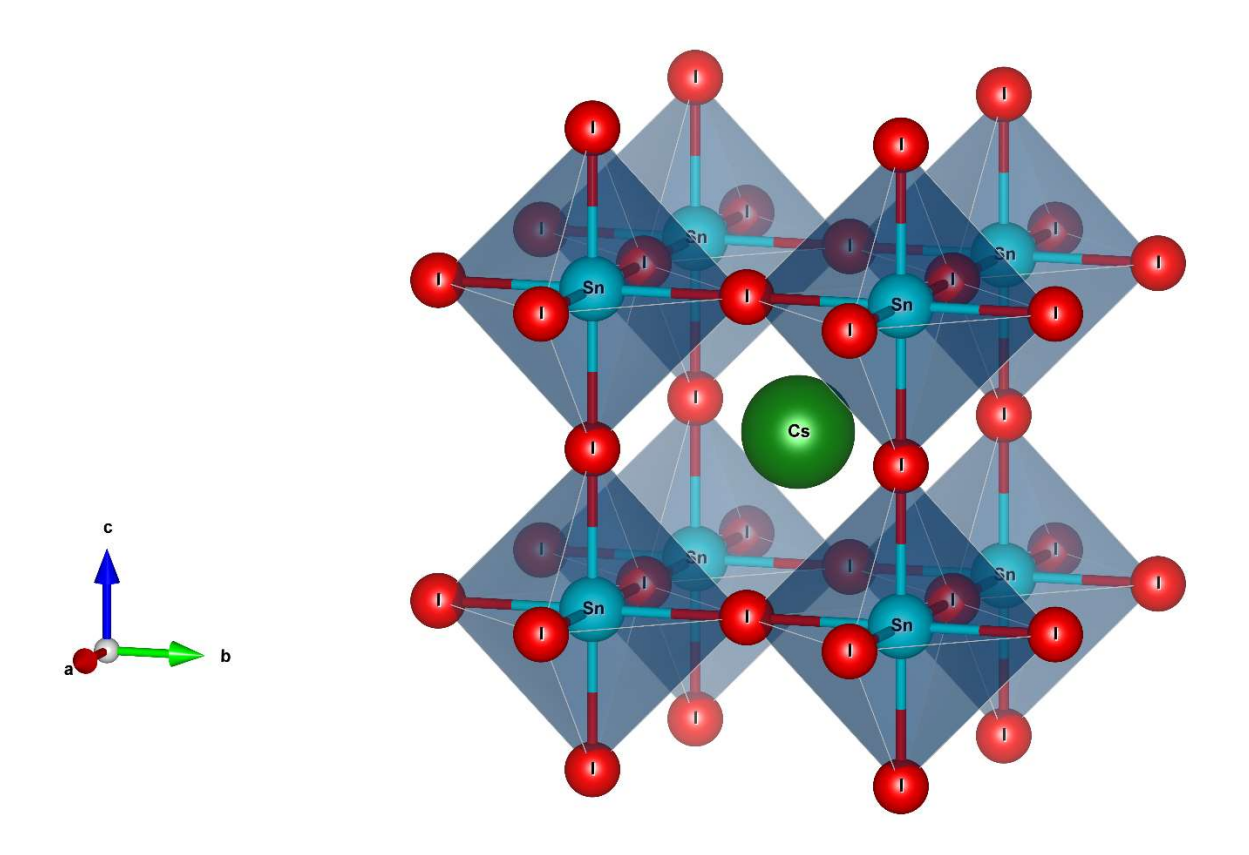


Figure 1.8 The unit cell structure of CsSnl<sub>3</sub>.

X site ion decides whether it is an inorganic oxide perovskite ABO<sub>3</sub> or a halide perovskite where X anions are halogen ions. A site ion decides whether it is an alkali perovskite or an organic-inorganic perovskite. Hence, CH<sub>3</sub>NH<sub>3</sub>Pbl<sub>3</sub> is an organic-inorganic halide perovskite compound. Lead ions (Pb<sup>2+</sup>) are relatively stable in the cubic structure of the compound, but lead is poisonous,<sup>55</sup> and it is restricted in industrial applications.<sup>56</sup> To replace it, Sn<sup>2+</sup> ions can be considerable at the beginning since they share the same oxidation level of 2+. CsSnl<sub>3</sub> compounds are also in the category of ABX<sub>3</sub>, which can be used in the study of replacing lead. It is also a Pm-3m cubic structure consisting of two different types of cations and one type of anion. A molecule of CsSnl<sub>3</sub> have one Cs<sup>+</sup> ion as the A-site cation, one Sn<sup>2+</sup> ion as the B-site cation and three I<sup>-</sup> ions as the X-site anions in the face-centred cubic unit cell structure. The general unit cell structure

of CsSnl<sub>3</sub> is shown in Figure 1.8, each B-site cation is surrounded by 6 X-site anions. 6 halide ions are shared by Cs<sup>+</sup> ions. A-site cations such as Cs<sup>+</sup> are located at the corners of the cube. A-site cations are normally small, so the unit cell structure can remain cubic. Each A-site cation is surrounded by 12 ions. X sites always are occupied by halogen anions.<sup>57</sup> This is the same structure as the one in Figure 1.4, but it is shown in different perspective angles by seeing Cs atom as the centre of the cell. In this way, the corner-sharing octahedra can be seen visually.

Although lead halide perovskite compounds and tin halide perovskite compounds have the same cubic structures, Pb<sup>2+</sup> ions are much more stable than Sn<sup>2+</sup> ions. Sn<sup>2+</sup> ions are oxidised easily and become Sn<sup>4+</sup> ions. <sup>58,59</sup> This is because the stability of Group 14 elements goes down as the atomic number goes down when they are in the oxidation state of +2. Hence, it limits the possible replacements. The solar cell using CH<sub>3</sub>NH<sub>3</sub>Snl<sub>3</sub> as the light absorber can reach an efficiency of 6% in the inert atmosphere, but Sn<sup>2+</sup> ions are decomposed into Sn<sup>4+</sup> ions when the tin-based solar cells are exposed in moisture and air. In the research of stable lead-free perovskite compounds, tin (IV) halide double perovskite compound becomes an interesting research direction later as it is a derivative of tin (II) halide perovskite. It is non-toxic and stable in moisture and air.

The light absorption of ABX<sub>3</sub> compounds is related to the composition of halide ions consisting of the compounds. Light absorption can be observed by Ultraviolet-Visible (UV-vis) Spectroscopy. Data of perovskite compounds

collected via UV-vis spectroscopy can be used to calculate the band gaps of halide perovskite compounds. The band gaps are tunable by mixing halide ions. CsSnI<sub>3</sub> has a smaller bandgap around 1.2 to 1.3 eV<sup>60</sup> which is smaller than the bandgap of CH<sub>3</sub>NH<sub>3</sub>PbI<sub>3</sub> (around1.55 eV).<sup>61</sup> CsSnI<sub>3</sub> has the smallest bandgap amongst CsSnI<sub>3</sub>, CsSnBr<sub>3</sub> and CsSnCl<sub>3</sub>. The bandgap of CsSnBr<sub>3</sub> is around 1.8 eV. CsSnCl<sub>3</sub> has the biggest bandgap which is 2.4 eV reported by Hayatullah et al.<sup>62</sup>

To reach an ideal bandgap 1.34 eV, according to W. Shockley's statement<sup>63</sup>, the bandgap of CsSnl<sub>3</sub> needs to be increased. William Shockley and Hans J. Queisser suggested that a single p-n junction can reach maximum theoretical efficiency of 33% with an ideal bandgap of 1.34 eV due to a maximum electrical power created by the semiconductor in a single p-n junction solar cell. This is called Shockley- Queisser Limit shown in Figure 1.9(b). This is because solar cell voltage depends on potential differences of perovskites which is the band gap. The correlation between the band gap and the voltage is proportionally increasing. When the band gap is huge, it requests more energy to excite electrons from the valence band to the conduction band. The correlation between the band gap and the current is proportionally decreasing. Equation 1.3 and Figure 1.9(a) shows details of I-V characteristic curve and how to reach theoretical optimal power.

Equation 1.2

$$Fill Factor = \frac{I_{mp} \times V_{mp}}{I_{sc} \times V_{oc}}$$

$$P_{max} = FF \times V_{oc} \times I_{sc}$$

Where  $P_{max}$ = Maximum Electrical power,  $V_{oc}$ = open-circuit voltage,  $I_{sc}$ = short-circuit current, FF= Fill Factor which is the relationship between the maximum power and the product of the open circuit voltage multiplied by the short-circuit current,  $I_{mp}$ = electrical current at the maximum power,  $V_{mp}$ = electrical voltage at the maximum power when the solar cell is connected to the external circuit. When the band gap decreases, the current will get bigger, and the voltage will get smaller. Hence, the ultimate light absorption efficiency depends on the band gap of the semiconductor shown in Figure 1.9(b) It will be mentioned in the Project Aims later for us to design the better perovskite materials.

The ideal diode equation for solar cells assumes that the solar cell is an ideal diode with zero series resistance and shunt resistance, and no recombination losses. In practice, solar cells exhibit non-ideal behaviour, which can result in a discrepancy between the measured and expected values of the open circuit voltage. The Shockley diode equation was used to model Current-voltage relationships of semiconductors in moderate constant current forward bias or reverse bias:

Equation 1.4

$$J=J_L-J_o(e^{qV/nkT}-1)$$

k=Boltzmann constant, T=absolute temperature (k) of the p-n junction, q= an electron's charge about  $1.602 \times 10^{-19} \, \text{C}$ , and kT/q is the thermal voltage(V<sub>T</sub>) where is about 0.0259 V at room temperature(T=300k). The term of qV/nkT can be rearranged as V/nV<sub>T</sub>. J= the net current density flowing through the diode, Jo= dark saturation current density which is the diode leakage current density in the absent of light, n= the ideality factor which is a number between 1 and 2 increasing as the current decreases, J<sub>L</sub> is the light generated current density, V= the voltage of the diode. Equation 1.4 captures both the light-generated current and the diode's intrinsic characteristics such as dark saturation current density which both can be used to calculate net current of solar cell to analyse the performance of the device.

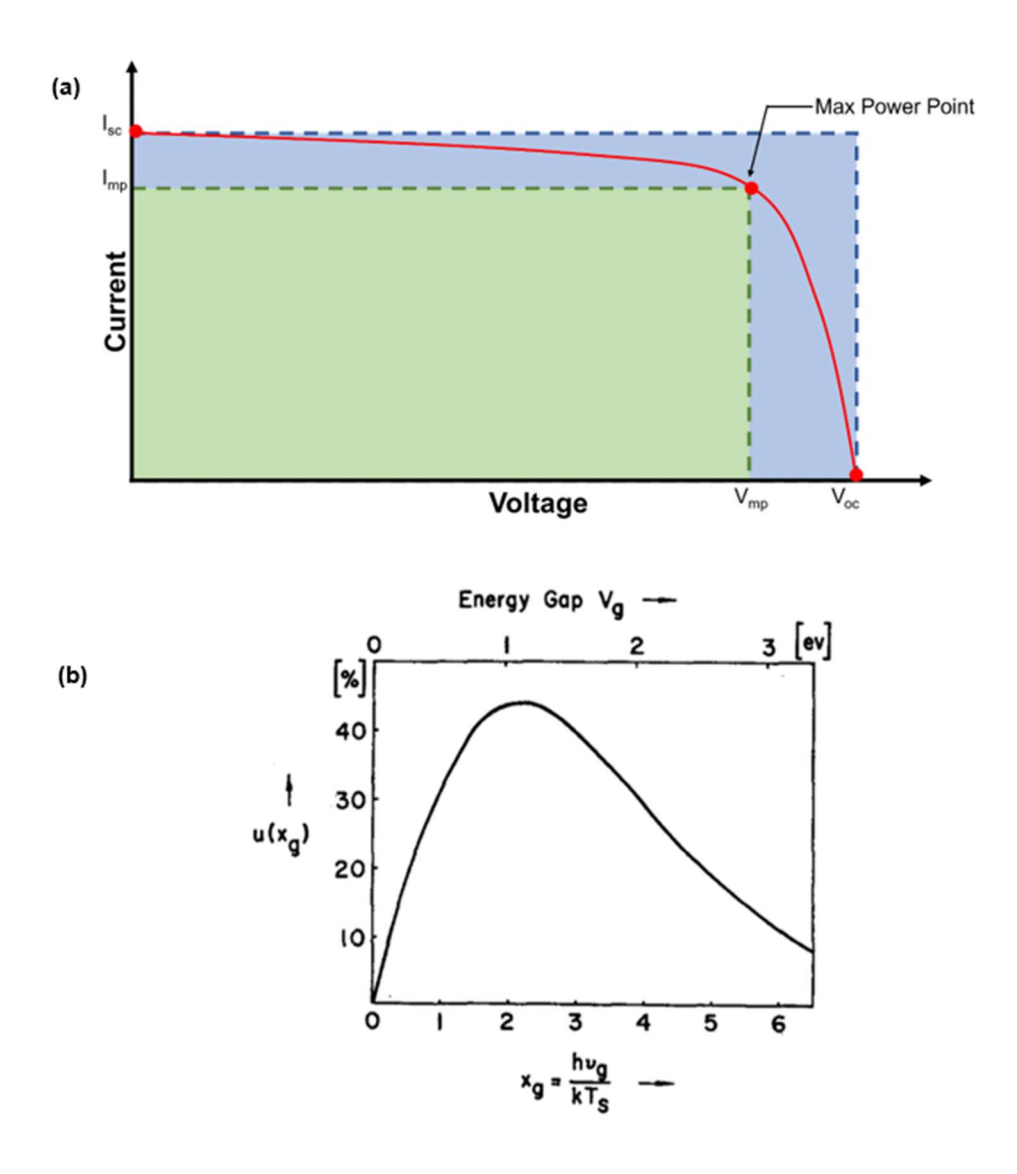


Figure 1.9 (a) Solar cell I-V characteristic curve (b) The diagram of the change of the band gaps,  $V_g$ , affecting the ultimate efficiency,  $u(x_g)$ , of a single p-n junction solar cell.<sup>63</sup>

A small amount of bromine (Br) added into CsSnI<sub>3</sub> can change the band gap of the compounds. Band gap variations depend on the composition of mixed halide perovskite compounds due to the modified Vegard's law with asymmetry weighed function.<sup>64</sup> The ratio of halide (I, Br) ions in the CsSnI<sub>x</sub>Br<sub>3-x</sub> play a key role for high

light absorption. Mixing halide ions in the vacancy-ordered double perovskite compounds A<sub>2</sub>BX<sub>6</sub> (Perovskite-like compounds) can also tune the band gaps.<sup>65</sup>

Although organometal halide perovskite compounds performed excellently in the cells, the degradation and instability<sup>66</sup> of lead halide perovskite (APbX<sub>3</sub>) affect the cell performance when it is exposed to air and moisture.<sup>67</sup> Also, lead is toxic.<sup>68</sup> To solve those problems, there is an intense search for materials with similar composition and structure. The defect ordered perovskite compounds in the structure form of A<sub>2</sub>BX<sub>6</sub> are the derivative of inorganic/organic halide perovskite compounds (ABX<sub>3</sub>). They are also in the cubic structure. Studying A<sub>2</sub>BX<sub>6</sub> might overcome the problems whilst maintaining the excellent properties.

### 1.7 Vacancy-ordered Double Perovskite

# Compounds (A<sub>2</sub>BX<sub>6</sub>)

Vacancy-ordered double halide perovskites (A<sub>2</sub>BX<sub>6</sub>) are lead-free compounds. It can avoid the problem of toxicity, which is environmentally friendly. It can be easily made via solution synthesis at a low cost. It is a stable compound compared to CsSnX<sub>3</sub> compounds. A<sub>2</sub>BX<sub>6</sub> is a derivative of perovskite compounds (ABX<sub>3</sub>). The structure of A<sub>2</sub>BX<sub>6</sub> halide perovskite is like the structure of K<sub>2</sub>PtCl<sub>6</sub>.<sup>69</sup> The structure of A<sub>2</sub>BX<sub>6</sub> can be the cubic structure as Cs<sub>2</sub>Snl<sub>6</sub> in Figure 1.10 when half of the octahedral B-site atoms (Sn) in the unit cell of ABX<sub>3</sub> are missing. It creates a new structure of isolated [Snl<sub>6</sub>]<sup>2-</sup> Octahedra, in contrast to the corner-

sharing octahedra found in ABX<sub>3</sub> compounds such as Cs<sub>3</sub>Snl<sub>3</sub> in Figure 1.8. There are no sharing iodine atoms like the ones in Figure 1.8. The structure of A<sub>2</sub>BX<sub>6</sub> also can be a hexagonal or orthorhombic structure, which can be checked out from the tolerance factor of the perovskite compounds. Hence, lead-free defect halide perovskites are potential replacements that prevent lead poisoning and the degradation of the devices.

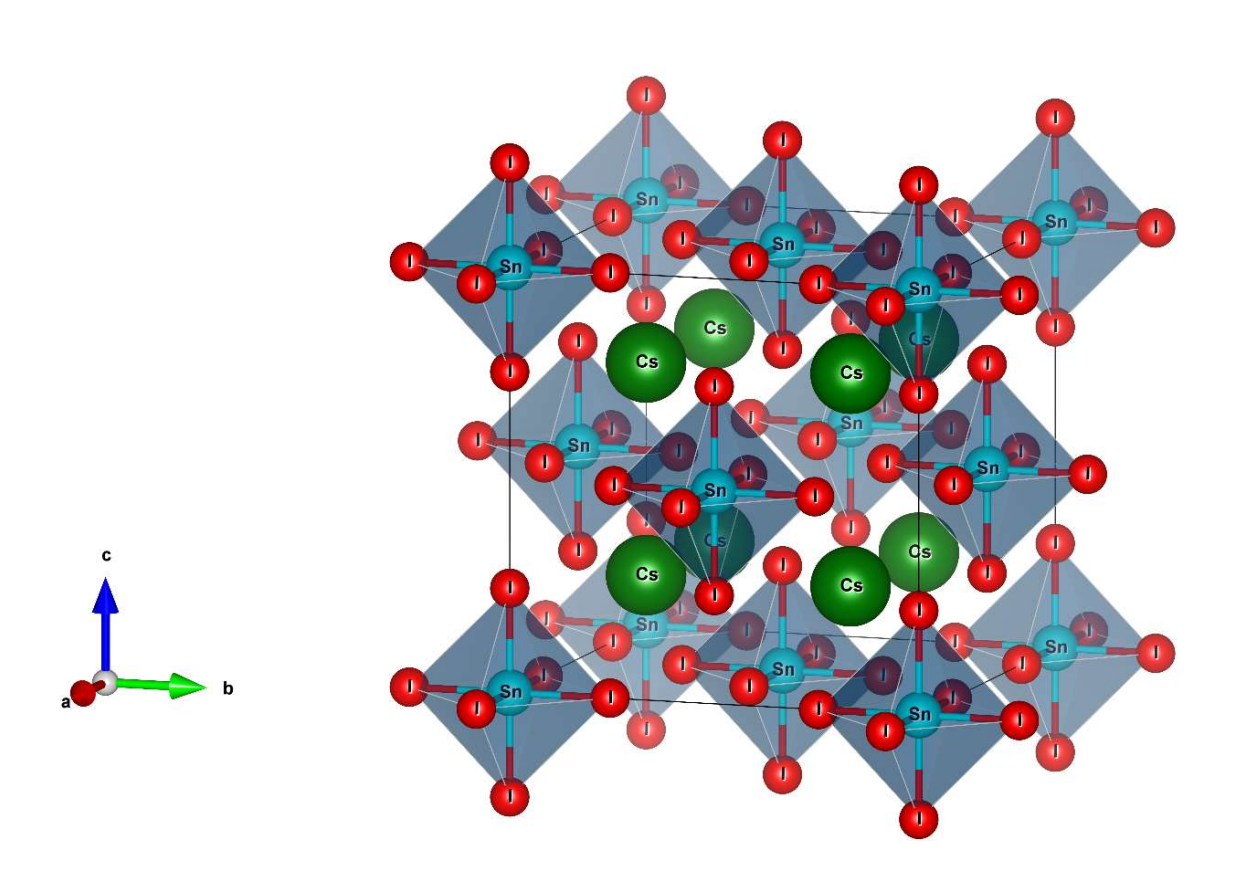


Figure 1.10 The unit cell structure of  $Cs_2SnI_6$ . Six iodine anions are normally around one  $Sn^{4+}$  cation, forming  $[SnI_6]^{2-}$  Octahedral structure.

A halide perovskite A<sub>2</sub>BX<sub>6</sub> is in the Fm-3m cubic structure generally consisting of two different types of cations and one type of anions. A molecule of Cs<sub>2</sub>SnI<sub>6</sub> have

two Cs<sup>+</sup> ion as the A-site cations, one Sn<sup>2+</sup> Ion as the B-site cation and six I<sup>-</sup> Ions as the X-site anions in the cubic unit cell structure. The general unit cell structure of Cs<sub>2</sub>SnI<sub>6</sub> is shown in Figure 1.10, A-site cations such as Cs<sup>+</sup> ions are at the corners of the cube. Each B-site cation, Sn<sup>2+</sup>, is surrounded by 6 X-site anions, I<sup>-</sup> ions. The surrounding 6 halide ions are also sharing with Cs<sup>+</sup> ions, which is like Figure 1.8 but forms the isolated [SnI<sub>6</sub>]<sup>2</sup>- octahedra structure. The positions of halides in the unit cell structure shifted little and stayed roughly in the same locations. For example, mixed halide defect ordered tin perovskite compounds A<sub>2</sub>BX<sub>6</sub> can not only inherit the properties such as high light absorption and comparable electron mobility from ABX3 compounds, but also can solve the problems of degradation and instability by adopting the stable cubic unit cell structure with only half of the octahedral B-site atoms from ABX3 cubic structure. It creates vacancies and formed isolated octahedral structures of [BX<sub>6</sub>]<sup>2-,70</sup> In the [SnX<sub>6</sub>]<sup>2-</sup> octahedron, the length of the four horizontal Sn–X bonds is slightly shorter than the length of the two longitudinal Sn-X bonds, revealing that the [SnCl<sub>6</sub>]<sup>2-</sup> octahedron is distorted. For example, the length of the four horizontal Sn–Cl bonds is 2.4154 Å when the length of the two longitudinal Sn–Cl bonds is 2.4479 Å for  $(C_4H_7N_2)_2SnCl_6$ .  $Sn^{4+}$  with  $4d^{10}$   $5s^0$  outer electron configuration can lead to a rigid crystal structure and a stereochemical inactive environment. The binding energy peaks at 487.4 eV and 495.7 eV were corresponded to the  $3d_{5/2}$  and  $3d_{3/2}$  orbitals of  $Sn^{4+}$ .71

The band gaps of halide perovskite compounds  $A_2BX_6$  can be tuned by changing the composition of X-site anions. The change in bandgap is not linear in correlation with the composition of X-site but instead bow-shaped, which is called

the bowing band gap effect. This is because the nature of halogen purely affects the energy level in the valence band but influences the energy level in the conduction band. <sup>72</sup> Plus, Cs<sub>2</sub>Snl<sub>6</sub> has a direct optical band gap of 1.3 eV, which is close to an ideal band gap 1.34 eV due to the theory of Shockley-Queisser Limit. <sup>73</sup> Mixed halide compounds showed a lower optical band gap than pure halide compounds. For example, Cs<sub>2</sub>Snl<sub>6x</sub>Br<sub>6-6x</sub> compounds with a small percentage of iodine has a lower bandgap than pure Cs<sub>2</sub>SnBr<sub>6</sub> compounds. <sup>74</sup> Characterization and Synthesis of different A<sub>2</sub>BX<sub>6</sub> made by changing A site ions, B site ions or X site ions individually can be used to define the relationship between composition and the unit cell structure.

In addition to the tunable properties of both ABX<sub>3</sub> and A<sub>2</sub>BX<sub>6</sub> compounds, temperature changes might cause the change of the structures during crystallisations in the research of mixed halide compounds.<sup>75,76</sup> To increase the stability of mixed halide perovskite compounds in the solar cell applications, the analysis of the change of unit cell structures and local structures of A<sub>2</sub>BX<sub>6</sub> compounds due to different temperatures is necessary. This is because the changes in temperature can cause the movements and the vibrations of local structure which can be used to control the growth orientation of the perovskite nanoparticles.<sup>77</sup>

Mixed halide compounds have a certain combination of the two halide anions in the octahedra structure which cannot be measured by XRD instrument because XRD technology detect the general phase changes and the size changes of the unit cell structures of samples. However, Raman spectroscopy can be used to observe the distribution of local structures of mixed halide compounds such as different stretching modes of mixed halide octahedra shown in the subchapter of Symmetry analysis of series Cs<sub>2</sub>SnCl<sub>6-6x</sub>Br<sub>6x</sub> and Cs<sub>2</sub>Snl<sub>6-6x</sub>Br<sub>6x</sub> in Chapter 3. XRD patterns can be used to observe the unit cell structures and to calculate the unit cell parameters. Raman spectra can be used to observe the local halide distribution. The aim is to see if it is possible to produce different local distributions of halides within the same overall composition and the unit cell structure by heating mixed halide compounds. To pursue a better material for new-generation perovskite solar cells, the search for new lead-free halide perovskite materials to preserve the good properties and overcome the drawbacks of lead halide perovskite compounds is ongoing.

It is interesting that structural phase transitions of methylamine, MA=[CH<sub>3</sub>NH<sub>3</sub>]<sup>+</sup>, halide perovskite compounds can be triggered by temperature. The speed and angle of the rotation of [CH<sub>3</sub>NH<sub>3</sub>]<sup>+</sup> ions are affected by temperature. When MAPbX<sub>3</sub> compounds are heated up to high temperature, the rotation of MA<sup>+</sup> cations become faster. This is more stable at a low temperature. Hence, the stability of MAPbX<sub>3</sub> compounds depends on temperature.

The specific amount of thermal energy applied to the compounds can help the crystallization of compounds toward the specific direction. <sup>78,79</sup> Also, Raman spectra of perovskite compounds can be shifted due to the expansion of the lattice structure, which is affected by the temperature difference. <sup>80,81</sup> Will the

temperature affect compounds in the formula of  $A_2BX_6$  in the same way since  $A_2BX_6$  is the derivation of compound in the formula of  $ABX_3$ ?

### 1.8 Vacancy-ordered triple perovskites(A<sub>3</sub>B<sub>2</sub>X<sub>9</sub>)

Bi<sup>3+</sup> cations have higher valency, which cannot form the universal ABX<sub>3</sub> perovskite structure with the corner-sharing  $[BX_6]^{3-}$  octahedra. However, Bi<sup>3+</sup> cations can form distorted  $[BX_6]^{3-}$  octahedra, resulting in halide perovskite derivatives, A<sub>3</sub>B<sub>2</sub>X<sub>9</sub> with low symmetry lattices. There are three main phase structures of A<sub>3</sub>B<sub>2</sub>X<sub>9</sub> reported, one-dimensional(1D) orthorhombic structure with space group (Pmcn) or (Pmna) such as Cs<sub>3</sub>Bi<sub>2</sub>Cl<sub>9</sub>, two-dimensional(2D)trigonal structure with space group (P3m1) such as Cs<sub>3</sub>Bi<sub>2</sub>Br<sub>9</sub>, and zero-dimensional(0D) hexagonal structure with space group (P6<sub>3</sub>/mmc) such as Cs<sub>3</sub>Bi<sub>2</sub>l<sub>9</sub> shown in Figure 1.11. The orthorhombic structure exhibits infinite 1D double chains based on corner-connected  $[BX_6]^{3-}$  octahedra, and the 2D layered trigonal structure exhibits 2D corrugated layers featuring corner-sharing  $[BX_6]^{3-}$  octahedra. A large amount of A<sub>3</sub>B<sub>2</sub>X<sub>9</sub> reported in the 0D hexagonal structure with isolated  $[B_2X_9]^{3-}$  clusters due to the close packed A<sub>3</sub>X<sub>9</sub> with B cations fitted in octahedral interstitial sites.

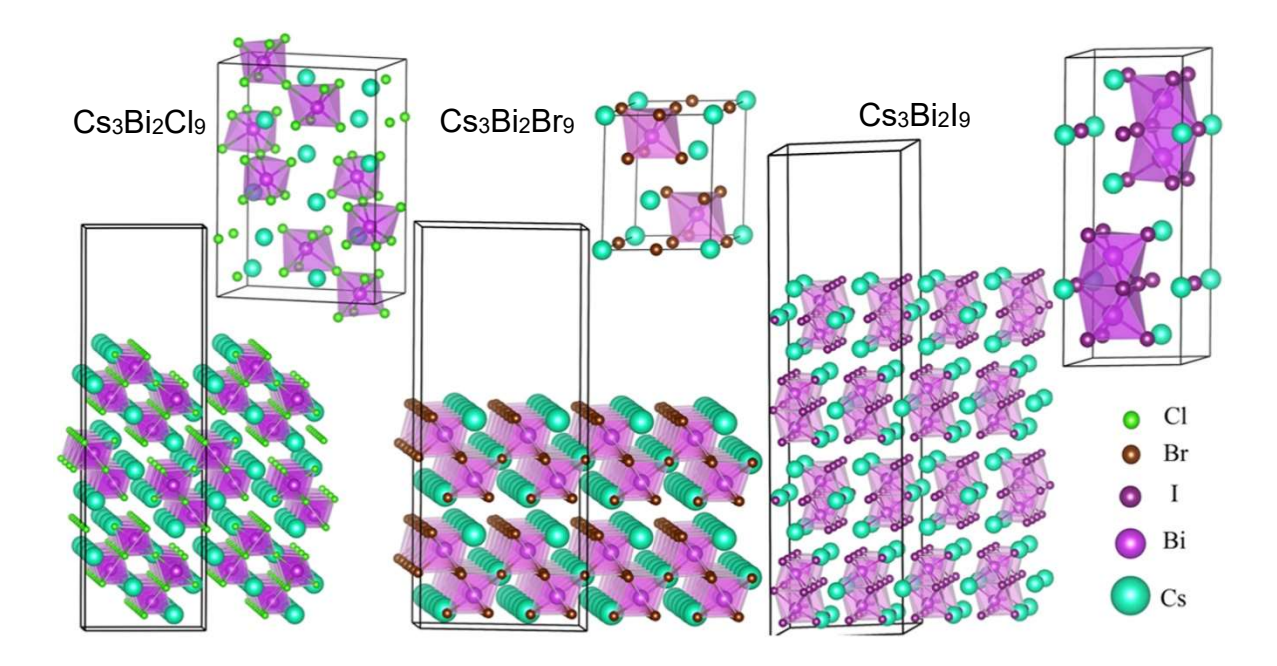


Figure 1.11 The crystal structure of Cs<sub>3</sub>Bi<sub>2</sub>Cl<sub>9</sub> in Pmcn space group, Cs<sub>3</sub>Bi<sub>2</sub>Br<sub>9</sub> in P-3m1 space group and Cs<sub>3</sub>Bi<sub>2</sub>I<sub>9</sub> in P6<sub>3</sub>/mmc space group. <sup>82</sup>

Any A<sub>3</sub>B<sub>2</sub>X<sub>9</sub> in the two-layered trigonal structures can be called vacancy-ordered triple perovskites because their structures are mostly like the cubic perovskite structure of ABX<sub>3</sub> without every third B-site cation. The residue of local B-site cations formed an irregular coordination environment like a distorted trigonal structure with three short B-X bonds and three long B-X bonds. The short B-X bonds would be shared by neighbouring octahedra in each layer.

Due to their large specific surface area, perovskite materials are more susceptible to surface defects than bulk single crystals and polycrystalline thin films. Consequently, it is essential to comprehend and manage their defect population to unlock the potential of perovskite materials. This perspective paper provides an overview of recent research on the defect chemistry of perovskite materials

and outlines various approaches to reduce their defect density in the context of their use in light-emitting devices. The article explores a range of methods to decrease the defect density, including advanced synthesis techniques, new surface-capping strategies, doping with metal ions and rare earths, engineering elemental compensation, and the adaptation of core-shell heterostructures to perovskite materials.

Currently, there exist three main methods to minimize the usage of lead in metal halide perovskite. The first approach involves substituting the Pb<sup>2+</sup> ion with divalent Sn<sup>2+</sup> or Ge<sup>2+</sup>. The second method involves substituting two divalent Pb<sup>2+</sup> ions with one monovalent M<sup>+</sup> cation and one trivalent M<sup>3+</sup> cation. The third technique involves substituting two divalent Pb<sup>2+</sup> ions with one tetravalent Pd<sup>4+</sup> or Sn<sup>4+</sup> cation, or three Pb<sup>2+</sup> ions with two trivalent ions such as Sb<sup>3+</sup> or Bi<sup>3+</sup>.

By using equivalent substitution,  $Sn^{2+}$  or  $Ge^{2+}$  based halide perovskite nanocrystals (NCs) maintain the three-dimensional (3D) perovskite structure. However, the oxidation of  $Sn^{2+}$  or  $Ge^{2+}$  ion to the tetravalent state in air reduces their stability.<sup>83</sup> The 3D double-perovskite AMM'X6 (A = Cs or CH<sub>3</sub>NH<sub>3</sub>; M = Ag or Au; M' = Bi, Sb, or In; X = Cl, Br, or I) retains the 3D perovskite crystal structure and charge neutrality via hetero-valent substitution. The double-perovskite  $Cs_2AgBiBr_6$  and  $Cs_2AgInCl_6$  NCs exhibit tuneable band gaps using substituting or doping strategies.<sup>84,85</sup> However, the use of noble-metal Ag in these 3D double-perovskite NCs increases the cost of optoelectronic devices.

Cs<sub>2</sub>PdBr<sub>6</sub> and Cs<sub>2</sub>SnI<sub>6</sub> halide materials possess remarkable stability toward light, humidity, and heat. However, the tetravalent state Pd<sup>4+</sup> or Sn<sup>4+</sup> produces a zero-dimensional (0D) form of vacancy-ordered perovskite. Based on the fourth strategy, high-quality two-dimensional (2D) perovskite such as Cs<sub>3</sub>Bi<sub>2</sub>Br<sub>9</sub>, MA<sub>3</sub>Bi<sub>2</sub>Br<sub>9</sub> and Cs<sub>3</sub>Sb<sub>2</sub>Br<sub>9</sub> can be synthesized. Nevertheless, the low colloidal stability and resulting poor dispersibility may restrict their use in optoelectronic device fabrication.<sup>86</sup>

Recent research by Yan et al. (2019) incorporated Au nanoparticles with CaTiO<sub>3</sub> nanocrystals and investigated the visible-light photocatalytic performance of CaTiO<sub>3</sub> nanocrystals assembled with Au nanoparticles on the surface. It was found that the Au nanoparticles acted as electron traps resulting in an improvement of the separation and transfer of photoexcited charge characters. Another observation is an increase in the visible-light absorption of CaTiO<sub>3</sub> due to Au nanoparticles induced surface states. This is further confirmed by the deepening of the apparent colour for the 4.3% Au doped CaTiO<sub>3</sub> composite (dark grey), and pure CaTiO<sub>3</sub> is in cream white. This is a promising finding as this suggests that using surface engineering can be used effectively to manipulate the bandgap and enhance photocatalytic performance of materials.<sup>87</sup>

The research by Chantalle et al. (2021) used doping technique to manifest light absorption of trigonal perovskite material such as Cs<sub>3</sub>Bi<sub>2</sub>Br<sub>9</sub>. Pure Cs<sub>3</sub>Bi<sub>2</sub>Br<sub>9</sub> is in pale yellow. By incorporating Sn dopants, the appearance of the samples underwent significant changes, resulting in darkening of the powder, even with

low concentrations. At an analytical Sn concentration of approximately 8% or higher, the powders became jet-black. The Sn-doped Cs<sub>3</sub>Bi<sub>2</sub>Br<sub>9</sub> demonstrated remarkable optical properties, with a strong and broad absorption spanning both the visible and near-infrared regions. As the Sn concentration increased, the absorption peak maximum gradually decreased in energy from 2.08 eV (at 7.9% Sn concentration) to 1.90 eV (at 23.5% Sn concentration). This significant shift in the optical spectra indicated the potential for a mixed-valence compound, which is recognized for its strong visible light absorption.<sup>88</sup>

The target is to substitute the lattice site of  $Bi^{3+}$  with both  $Sn^{2+}$  and  $Sn^{4+}$ . The process is using  $SnBr_2$  as the doping precursor. Some  $Sn^{2+}$  were oxidised into  $Sn^{4+}$  in air. The co-existence of  $Sn^{2+}$  and  $Sn^{4+}$  occupied the lattice sites of  $Bi^{3+}$ . This is called a double-substitutional complex. The reason why this kind of defect-defect interactions are preferable in the compounds is that the Sn-Bi bond needs less formation energy than that of Sn-Br or Sn-Cs. For example, a small second separation energy minimum appears at about 8.1 Å relating to the next-nearest neighbouring substitution site within the same octahedral layer, the Sn-Bi substitution located in the neighbouring  $BX_6$  layer requested about 7.9Å for separation.

In view of the findings obtained so far, the Robin–Day classification is briefly discussed here for mixed valency compounds. This classification is based on the level of electron delocalization in the compound. There are three classes of mixed valency compounds. The first class, Class I, includes materials where valencies

are trapped on a single site, resulting in no electrical conductivity and a simple absorption spectrum that is the sum of constituent ions. Pb<sub>3</sub>O<sub>4</sub> is an example of a Class I compound.

The second class, Class II, is characterised by sites occupied by ions differing in valence, yet still distinguishable. There is some localisation of distinct valences, albeit with a low activation energy for their interconversion. Class II compounds require some thermal activation to induce electron transfer between sites, and they are semiconductors. Class II materials exhibit an intense intervalence charge transfer band, resulting in a broad and intense absorption in the infrared or visible part of the spectrum, as well as magnetic exchange coupling at low temperatures. Vanadium oxides and the Fe(II)/ Fe(III) cyanide complex, Prussian blue, are well-known examples of Class II compounds.

The third class, Class III, has mixed valence that is completely delocalised, and the valence is not distinguishable by spectroscopic methods. This class is possible when the ligand environment is similar or identical for each of the two metal sites in the complex. The resulting materials do not behave as metals or semiconductors, nor do they exhibit "single ion" properties, such as electronic, vibrational, or Mössbauer spectra characterising the metal in either of its oxidation states. They do usually exhibit strong optical absorption caused by electron hopping between sites. The Creutz-Taupe complex and sodium tungsten bronzes are typical examples of Class III compounds.

Sn-doped Cs<sub>3</sub>Bi<sub>2</sub>Br<sub>9</sub> displays unique properties that distinguish it from classical Robin-Day compounds. It has been suggested that it may be classified as a Class II compound, although a transition to a Class III phase is also possible. Previous research has examined Cs<sub>2</sub>Sn<sub>x</sub>Sb<sub>1-x</sub>Cl<sub>6</sub>, which contains Sb(iii) and Sb(v) ions and observed that the energy of the IVCT absorption maximum increases as Sb concentration increases. This trend is common in many mixed valence systems, but Sn: Cs<sub>3</sub>Bi<sub>2</sub>Br<sub>9</sub> exhibits the opposite trend in its optical properties, which is highly unusual. However, can this doping technique apply to other trigonal A<sub>3</sub>B<sub>2</sub>X<sub>9</sub> materials such as Cs<sub>3</sub>Sb<sub>2</sub>Cl<sub>9</sub>? Or is this doping technique workable for A<sub>3</sub>B<sub>2</sub>X<sub>9</sub> in other phase structures such as the 1D orthorhombic structure and the 0D dimmer?

Luo et al. (2020) investigated the impact of crystal structure on the electronic and optical properties of Cs<sub>3</sub>Bi<sub>2</sub>Cl<sub>9</sub> using first-principles simulations. They found that the bandgap of Cs<sub>3</sub>Bi<sub>2</sub>Cl<sub>9</sub> decreased with increasing lattice parameter, which was attributed to the change in the Bi-Cl bond length and the degree of Bi-Cl hybridization. The band gaps of Cs<sub>3</sub>Bi<sub>2</sub>X<sub>9</sub> (X=Cl, Br, or I) changed with the different halogen atoms, and the indirect bandgap leads to the lower photoluminescence quantum efficient (PLQE). The optical absorption of the Cs<sub>3</sub>Bi<sub>2</sub>X<sub>9</sub> is affected by the electronic transition between the 6p orbital of Bi atom and X atom. The researchers also found that the bandgap of Cs<sub>3</sub>Bi<sub>2</sub>Cl<sub>9</sub> was more sensitive to lattice parameter changes along the c-axis than the a-axis. The surface structure of Cs<sub>3</sub>Bi<sub>2</sub>Cl<sub>9</sub> have distinct effect on the improving of infrared region but inhabiting in visible regions. Cs<sub>3</sub>Bi<sub>2</sub>Cl<sub>9</sub> has the most evident absorption peak and behaves an obvious anisotropic optical absorption in visible regions. These findings provide valuable insights into the crystal structure-property

relationship of Cs<sub>3</sub>Bi<sub>2</sub>Cl<sub>9</sub> and highlight the importance of controlling the crystal structure to manipulate the bandgap for various applications.

The bandgap of Cs<sub>3</sub>B<sub>i2</sub>Cl<sub>9</sub> has also been studied in the context of its optical properties. Ali et al. (2019) investigated the photoluminescence properties of Cs<sub>3</sub>Bi<sub>2</sub>Cl<sub>9</sub> nanocrystals and found that the emission spectra exhibited a broad peak at around 460 nm, which was attributed to exciton emission. <sup>89</sup> The researchers also observed a red shift in the peak position with increasing temperature, which was attributed to the thermal expansion of the crystal lattice. These findings suggest that the exciton peak can be used to probe the bandgap and thermal properties of Cs<sub>3</sub>Bi<sub>2</sub>Cl<sub>9</sub>.<sup>90</sup>

### 1.9 Aims and Motivations

The world needs to transition to meet climate change goals and reduce air pollution. The research into the technologies of harvesting different kinds of potential sustainable energy such as wind power, geothermal power, solar power, etc... requires more focus and investments. Harvesting solar power is a way to help to reduce CO<sub>2</sub> emission and slow down global warming. This motivated me to study how to improve solar cells.

A good starting point can be to find an efficient, stable light absorber which is easy to manufacture at a low cost. The properties of a good hybrid solar absorber include carrier mobility, high absorption coefficient, correct band gap of materials for a certain light source and stability. These affect the performance of solar cells as summarised in the review above. Perovskite solar cells are a class of technologies that have these properties and are an increasingly popular field of research due to fast developments within the last decade, comparable to the improvements in silicon solar cell architectures, over a century. The review covered why the current major type of perovskites solar cell is based on CH<sub>3</sub>NH<sub>3</sub>PbI<sub>3</sub>. It can reach good efficiency and good electron mobility due to the corner-sharing octahedral structure of [PbI<sub>6</sub>]<sup>4-</sup>, but drawbacks of solar cells based on CH<sub>3</sub>NH<sub>3</sub>PbI<sub>3</sub> are lead's toxicity and instability, they degrade easily when they are expose to air and moisture.

To overcome these drawbacks, this thesis explores lead-free perovskite-like compounds, that share similar octahedral structures. These include compounds such as the defect-ordered perovskites in term of A<sub>2</sub>BX<sub>6</sub> and A<sub>3</sub>B<sub>2</sub>X<sub>9</sub> made with different synthesis and doping methods. Doping techniques can improve optoelectronic properties, to improve visible light absorption. This thesis aims to expand the understanding of these perovskite-like compounds, compared to the ABX<sub>3</sub> compound, and compare properties such as band gap bowing due to optical absorption, stability, structural and compositional transitions across different halide series, and different types of dopants. The motivations of this thesis hope to expand the knowledge and help to improve the field of solar cell absorber materials for devices in the future.

# 2 Characterisation Methodology

# 2.1 Powder X-ray Diffraction

X-rays are generated by a cathode ray tube. It produces monochromatic radiation (with a single wavelength,  $\lambda$ ). Crystal powders are composed of atoms in an arranged order repeatedly in the lattice planes (Miller planes), and the distance between planes are well defined as d, which is called the d spacing. When an incoming beam of X-rays illuminate on a powder sample, its energy is absorbed by electrons around atoms, but this is less energy than the minimum of the occupied energy states of electrons. Electrons cannot be released from the atoms, then this energy must be remitted in a new form of radiation but with the same energy. This is called elastic scattering.

Remitted radiation interacts with each other causing interference. If the remitted waves are in alignment and the signal is amplified, constructive interference occurs. (If the waves are not in alignment and signal cancel out each other, destructive interference occurs.)

In this case here, when the atomic lattice planes are irradiated, X-rays are scattered from the uniformly packed atoms. This forms strong amplification of the reemitted signal at the angle  $\theta$  to the surface as the same as incoming radiation when the scattered waves constructively interfere. This effect is called diffraction.

When the remitted waves are in alignment, the second wave  $\lambda 2$  in Figure 2.1 must travel a whole number of wavelengths. In this case, one half of a wavelength is travelled on the incident side, and the other half on the remitted side to produce one additional wavelength. The third wave would travel two wavelengths, one on the incident side and one on the remitted side. The same series occurs through the crystal. The angle of diffraction can be determined by the right-angle triangle formed by the half of a wavelength on the remitted side and the d- spacing between lattice planes. The angle opposed to the half of a wavelength on the remitted side is  $\theta$ , half the angle between incoming radiation and diffracted radiation. The relationship between the diffraction angle and d-spacing between the atoms is  $\sin \theta = \frac{\lambda}{d}$ . Rearranging it, Bragg's Law equation yields below.

#### Equation 2.1

#### nλ=2dsinθ

Where n is the diffraction order, for first order, n=1;  $\lambda$  is the X-ray wavelength, for example, Cu K $\alpha$ =1.5406 nm, and Mo K $\alpha$ = 0.7093 nm; d is the interplanar spacing in Å;  $\theta$  is the angle of incoming radiation and called the Bragg's angle.

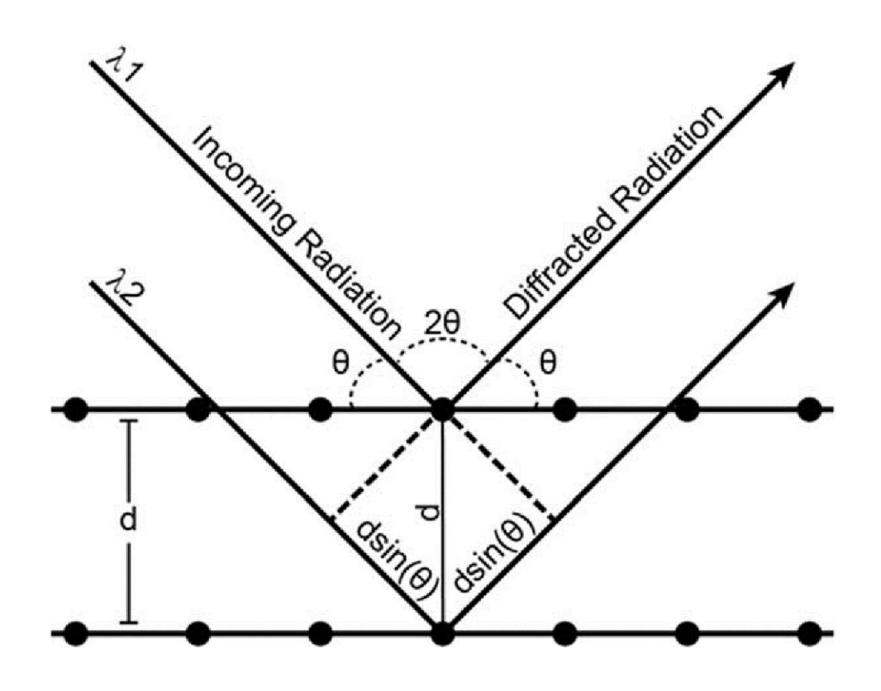


Figure 2.1 The schematic diagram of Bragg's law.91

Powder X-ray diffractions (XRD) is very useful in the phase identification and quantification. It is helpful to analyse crystal structure by measuring the unit cell parameters. Here in the study of samples of defect-ordered double perovskite materials (in terms of A<sub>2</sub>BX<sub>6</sub>), it was used to observe the change of size and shape of the unit cell and to predict the growth direction of mixed halide materials. In as-synthesised powder material, it can be used to distinguish different phases. In the study of bismuth halide materials (in terms of A<sub>3</sub>B<sub>2</sub>X<sub>9</sub>), It was used to determine whether secondary phases are formed and what they are.

### 2.1.1 Characterisation

Samples of defect-ordered double perovskite materials (in terms of  $A_2BX_6$ ) were grounded into fine powders before they were tested in the sample foils by the

Powder X-ray Diffraction (XRD) instrument (Stoe STADI-P). By using the Stoe STADI-P diffractometer along with the STOE Dectris Mythen 1k detector, the powder XRD data was recorded in transmission geometry with the detector using Mo K $\alpha$ 1 radiation with  $\lambda$ = 0.70930nm. The powder XRD data was recorded in 0.495° over a default angular range from 2.000° to 40.115° providing 77 data points for analysis. Depending on the resolution required the time of each step can be adjusted where the longer the step time the better the resolution hence improved accuracy. Hence, for samples of defect-ordered double perovskite materials, all powder XRD data was collected on the STOE diffractometer in transmission geometry using monochromatic Mo K $\alpha$  radiation over an angular range of  $2.000^{\circ} \le 20 \le 40.115^{\circ}$  with a step size of  $0.495^{\circ}$  at 15 seconds per step.

However, bismuth halide materials are not suitable for the STOE diffractometer using monochromatic Mo K $\alpha$  radiation due to too much fluorescence/ noises in the PXRD spectra caused by bismuth. Samples of bismuth halide materials (in terms of  $A_3B_2X_9$ ) were grounded into fine powders and tested in the sample type of thin foils by the STOE diffractometer using Cu K $\alpha$ 1 radiation with  $\lambda$ = 1.5106nm. Hence, for samples of bismuth halide materials, all powder XRD data was collected on the STOE diffractometer in transmission geometry using monochromatic Cu K $\alpha$  radiation over an angular range from 2.000° to 60.410° with a step size of 0.495° at 5 seconds per step.

### 2.1.2 Rietveld Refinement

Before 1967 single peak was fitted to powder XRD patterns to obtain individual integrated intensities of Bragg peaks and structure factors. In 1967 Hugo Rietveld discovered and implemented whole powder XRD pattern fitting to a diffraction data from a neutron source.<sup>92</sup> Then the whole pattern fitting method was explored to profile shape limited by unit cell.

Rietveld refinement here used to calculate unit cell parameters of samples and to confirm if unwanted secondary phases exist in the sample. Rietveld refinement can be conducted to refine a crystal structure in GSAS II software. To model a crystal structure with Rietveld, crystallographic parameters where the parameters are influenced by the sample and experimental parameters where the parameters is influenced by the scattering experiment must be fitted. Controls determine how the program will operate which indicates high number of refinement cycles.

Rietveld refinement was used for phase identification and measurements of unit cell parameters and bond lengths. The unit cell structure defines the repeating unit of the atomic distribution in the crystal structure of a material. Rietveld refinement is to generate a best fit of diffraction pattern to the X-ray pattern of the input sample according to the input reference phase file of a crystal structure. Different instrument parameters and experimental parameters need to be refined step by step to improve the calculated diffraction pattern. Peak shape is limited by instrumental parameters which can be improved by refining the Gaussian and

Lorentz parameters in many refinement cycles. Weighed profile R factor, Rw, is used to determine how good the fit is (between the calculated and the experimental patterns). The chi² value also can determine how good the fit is, which is related to GOF value(the Goodness of Fit), where it decreases with a model with the better fit. There are also constraints, it is common that there is not enough data to fit all the parameters required to refine a sample therefore, a level of knowledge of the system and expertise is required to add constraints that simplifies the refinement to the minimum by lowering the degrees of freedom.

Rietveld refinement is an analysis technique to analyse powder X-ray diffraction patterns and to determine the crystal structure of a material by refining a possible model to fit the diffraction patterns of samples. First, powder data was imported by click 'GSAS powder data file', and the data file needs to be '.raw' format. Second, phase information was added by importing a model or models of general structure analysis of something like the experimental data in a 'cif.' File which can be found in ICSD database. Third, the background parameters were set by selecting the background function as chebyschev-1 and selecting number of background coefficients by 10 to refine the background. Fourth, the instrument parameters were set by selecting the source type, MoKα or CuKα (which depends on the PXRD instruments used for the samples.) and selecting I(L2)/I(L1)=0. Fifth, Debye- Scherrer was chose as diffractometer type. They are basic types that need to refine step by step. After that, unit cell parameters can be refined by clicking 'Refine unit cell' on the pages of phases. 'U, V, W' from Instrument Parameters on GSAS 2 are the Gaussian peak shape functions while 'X,Y, Z' are the Lorentz peak shape functions, and 'SH/L' is the parameter relating the

asymmetry of the peak shape. To achieve the ultimate fit for the peak shape of the experimental data, the parameters mentioned above were refined step by step. The unit cell parameters were refined after that. To confirm the reliability of the refinement, the value of R-factor (Rw) needs to be close to 1 as possible. (Rw is acceptable/good if it is below 10.) The difference of the XRD data of the sample and the computed XRD data generated from the refined parameters taking ICSD cif file as the starting structure also showed how good the peak fitting is.

### 2.2 X-ray Photoelectron Spectroscopy

X-ray Photoelectron Spectroscopy (XPS) is a surface technique to determine the chemical composition distribution, chemical and electron properties of the surface of a material. The surface depth of material can be 1 nm to 5 nm which can be detected by the XPS spectrometer. The reason why the XPS spectrometer cannot be detected over 5 nm is the occurrence of photoemission is limited by the increasing possibility of inelastic collisions of electron with the increased depth of the testing sample.<sup>93</sup>

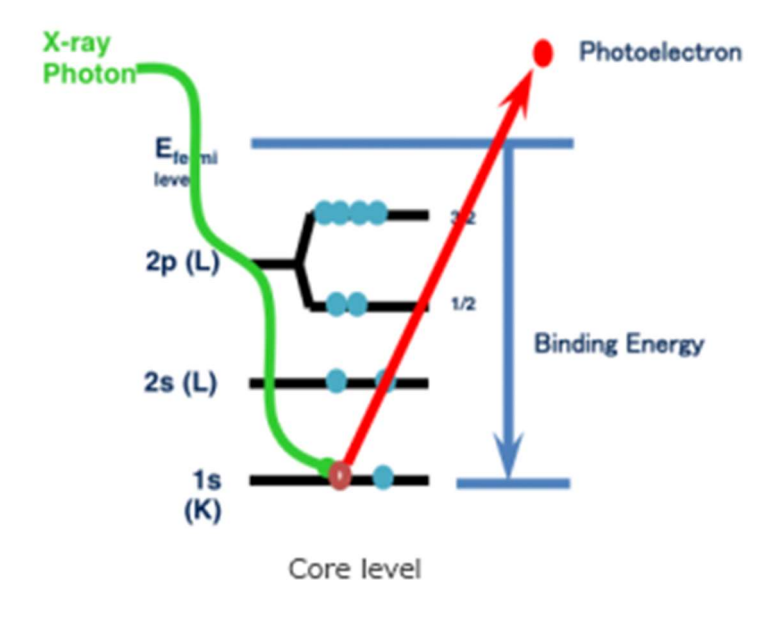


Figure 2.2 The schematic mechanism of the XPS spectrometer.

XPS surface analysis is conducted by irradiating the surface of a sample with monoenergetic soft X-rays and measuring the energy of the detected electrons In Figure 2.2. Al K $\alpha$  (1486.6 eV) was used here. The photons have limited power to penetrate a sample on the order of 1-10  $\mu$ m. These photon energies interacted with atoms on the surface transferring energy to electrons and causing electrons to be emitted by photoelectric effect. The kinetic energies of the emitted electrons were measured by

Equation 2.2

$$KE = hv - BE - \Phi_{sample} - (\Phi_{spectrometer} - \Phi_{sample}) = hv - BE - \Phi_{spectrometer}$$

Where hv is the energy of the photon; BE is the binding energy of the atomic orbital where the electron comes from;  $\Phi$ s is the work function of the spectrometer which is a constant value. The work function of the sample was also considered

which is the energy required for an electron to escape from fermi lever to the vacuum, but it was cancelled out during the adjustable instrumental correction.

The binding energy is regarded as the energy difference between the initial and final states after a photoelectron has left an atom. There are corresponding various energies of the emitted electrons due to a variety of possible final states of the ions of each element. Hence, the binding energy peaks in a XPS spectrum indicates information of an element's oxidation state and chemical environment. The XPS spectrometer measures the kinetic energies of emitted electrons to determine binding energies of different elements because electrons in different atomic orbitals required different energy to escape.

#### Equation 2.3

$$BE = hv - KE - \Phi_{spectrometer}$$

The Fermi level is zero binding energy, and the depth beneath the Fermi level indicates the relative energy of the ion remaining after electron emission, or the binding energy of the electron. The binding energy is proportional to the distance below the line indicating the Fermi level, and the ionization cross-section is proportional to the length of the line. The line lengths indicate the likelihoods of the various ionization processes. The p, d and f levels become split upon ionization, leading to vacancies in the  $p_{1/2}$ ,  $p_{3/2}$ ,  $d_{3/2}$ ,  $d_{5/2}$ ,  $f_{5/2}$  and  $f_{7/2}$ . The spin-orbit splitting ratio is 1:2 for p levels; the spin-orbit splitting ratio is 2:3 for d levels; the spin-orbit splitting ratio 3:4 for f levels.

### 2.2.1 Characterisation

To collect X-ray Photoelectron Spectroscopy (XPS) spectra, a Thermo Scientific K-alpha spectrometer was used. This spectrometer uses a 72W monochromatic Al Kα x-ray source to detect the sample surface with the energy being equal to 1486.6 eV. It can concentrate on a 400 micron in diameter surface. Charge compensation is required to neutralize the charge on the surface by replacing the electrons, this was done using a dual-beam flood gun. High resolution scans with a binding energy step size of 0.1 eV was applied. In situ Ar ion etching was performed using 2 keV Ar ion beam in a background with a pressure of 2x10<sup>-7</sup> mbar.

Using Thermo Advantage software or Casa XPS software the spectra obtained can be analysed. The XPS technique is used to identify the composition of samples. It can show what elements the sample consists of and the percentages of elements. It also can show the position and energy of the valence band peaks and which orbitals they correspond to. This is a good technique to find out the actual ratio of halogen atoms in the sample compounds. Spectra were analysed via Casa XPS software. Charging correction was performed by manually setting up adventitious 1s carbon (C1s) peak energies at 284.8 eV.

Peak fitting was to separate overlapping peaks in the same region of the spectrum to extract useful information which was conducted on CASA XPS software. It is conducted by clicking the icon of library to open the periodic table

and selecting elements of the sample. Peak fitting was conducted by creating regions and doing components in the tab of Quantification Parameters, and then adjusting the borders to lower background signals. Casa XPS software calculates atomic percentages of a sample by diving the peak area above the background by the relative sensitivity factor and then by comparing with all other elements. It is often to apply constraints to the peak widths, or area ratio or the relative position of the components to contain a good fit to the XPS data and to retrieve correct results.

XPS data was used to report atomic fractions after peak fitting which is called an atomic percent(at. %). There is always an under lying assumption that the sample was homogeneous and single phase within the XPS sampling depth. The calculation is based on Equation 2.4 below which assumed the atomic fraction is homogeneous.

Equation 2.4

$$X = \frac{I_p/S_p}{\sum_j I_j/S_j}$$

Where I is the area of the peaks of the selected element, S is the sensitivity factor, and X is homogeneous atomic fraction. For example, for each element, a normalized peak area,  $I_j/S_j$  was obtained by selecting a peak and dividing the area of that peak ( $I_j$ ) by the sensitivity factor( $S_j$ ). The equivalent homogeneous atomic fraction( $X_j$ ) of each element is that elements normalized peak area divided by the sum of all normalized peak areas. To get atomic percent (at. %), simply multiply  $X_j$  by 100%.

### 2.3 Raman Spectroscopy

In Raman Spectroscopy the light scattered by a sample was observed. Generally, the scattering of a solid was observed when the sample was pressed into a thin glass film and is irradiated directly. The scattered light can be observed in any direction with respect to the incident light. The incident light must be a single frequency, monochromatic light for a Raman experiment. The frequency of the incident radiation can be defined as  $v_0 \, \text{cm}^{-1}$ . When this light is directed at a sample light is reflected with the same frequency  $v_0 \, \text{cm}^{-1}$ , this is called Rayleigh scattering in Figure 2.3. However, a small fraction of scattered light with a frequency  $v_i$  is different from  $v_0$ , which can be defined as Raman Scattering. This is because a small amount of energy is absorbed by the sample when the incident light is reflected off the sample with a frequency other than  $v_0.94$ 

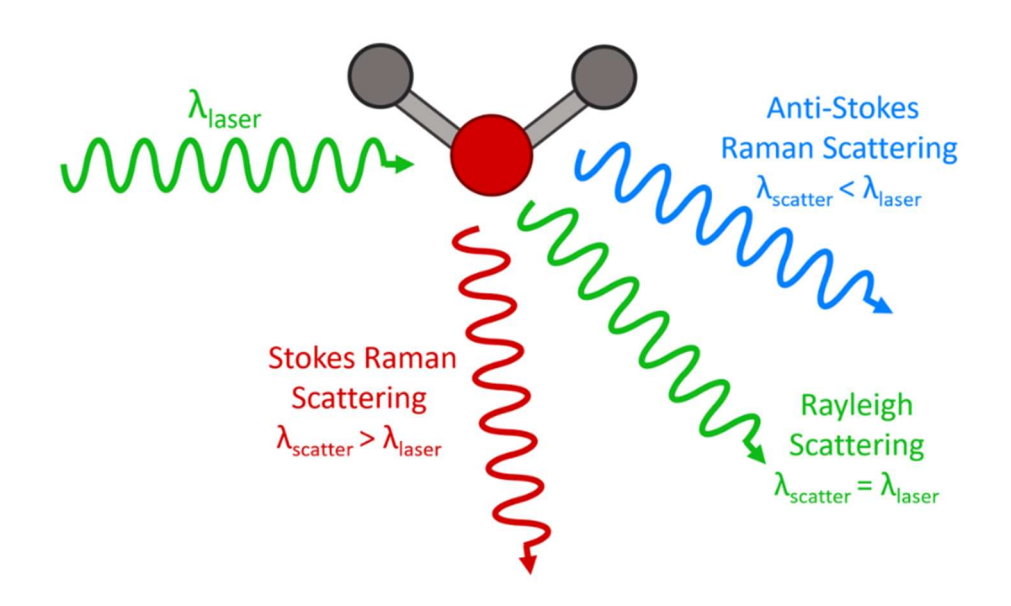


Figure 2.3 Three different kinds of scattering happened when light irradiates with a molecule.

The vibrations of molecular and extended structure can be measured by using Raman spectroscopy. The change of local structures can be observed via the Raman testing when the samples are heated up. Each Sample was incident on the microscopy thin films. For example, the Raman spectra was recorded for certain members of the Cs<sub>2</sub>SnX<sub>6</sub> mixed halide series that represented the complete compositional range. The vibrational spectroscopy of A<sub>2</sub>BX<sub>6</sub> compounds is well studied as these are useful isolated compounds [BX<sub>6</sub>]<sup>2</sup>-Octahedra. The Raman spectrums of Cs<sub>2</sub>SnX<sub>6</sub> (x=Cl, Br, I) consist of 3 peaks with Raman shift above 50 cm<sup>-1</sup> and can be explained by considering only Sn-X vibrations in octahedral symmetry. Vibrational spectra of mixed halide A<sub>2</sub>BX<sub>6</sub> compounds have been much less reported.

### 2.3.1 Characterisation

Raman spectra was required using a Renishaw inVia the Raman microscope with a 633 nm He-Ne laser (9.3 mW). The laser was focus onto samples via a 50× objective lens (N.A.= 0.75) and the grating used was 1800 lines mm<sup>-1</sup>. It resulted a spectral resolution of 1 cm<sup>-1</sup>. All spectra were calibrated using the silicon Raman band at 520.5 cm<sup>-1</sup>. The excitation wavelength was 633 nm and the acquisition time was 20 seconds. The laser spot size was around 1 um<sup>2</sup>. All spectra were calibrated with respect to Si and measured at room temperature.

Raman spectra were obtained from a Raman spectrometer with 633nm laser when samples were tested. For example, a tiny amount of a sample was deposited on a microscope glass slide which was placed on the microscope X-Y translation mechanical stage. The crystal structure of the sample could be observed by adjusting the position of the stage and the resolution of objective lenses, the focus, and the intensity of laser power. The laser beam was incident on a sample particle, Raman spectra were retrieved from the software.

To have Raman-active vibrations, there must be a change in the molecule's polarizability. This means that the position of the electron cloud changes during vibrations. If a vibration is infrared (IR) active, there must be a change in the molecule's dipole moment during vibrations. The reason why Raman analysis was used to analyse the perovskite-like compounds here is that Raman spectroscopy is especially sensitive to lattice vibrations in the crystals which is

important for the discussion of symmetry analysis of series  $Cs_2SnCl_{6-6x}Br_{6x}$  or  $Cs_2Snl_{6-6x}Br_{6x}$  in Chapter 3.1.2.

## 2.4 Ultraviolet-Visible Spectroscopy

An absorption spectrophotometer is a device used to measure absorbed light intensity as a function of wavelength. In UV-visible spectrophotometers, a beam of light from a suitable UV and/or visible light source is passed through a prism or diffraction grating monochromator. The light then passes through the sample to be analysed before reaching the detector. UV-visible spectrophotometers have five main components: the light source, monochromator, sample holder, detector, and interpreter. The standard light source consists of a deuterium arc (190–330 nm) and a tungsten filament lamp (330–800 nm), which together generates a light beam across the 190–800 nm spectral range. The monochromator produces a compact optical path and reduces optical aberrations. Modern instruments use grating monochromators in reflection mode as the dispersing element. Here a single beam spectrophotometer was in use (a Shimadzu UV-2600 spectrometer). The UV-2600i is a single monochromator system, whose wavelength range can easily be expanded to the near-infrared region of 1400 nm using the optional integrating sphere.

Ultraviolet-visible (UV-vis) Spectroscopy was used in combination with Optical Diffuse-Reflectance spectroscopy to measure and calculate the optical band gaps of all powder samples. In Diffuse-Reflectance spectroscopy, measurements were carried out with the use of integrating sphere inside the UV spectrometer.

The integrating spheres allow part of the incident light beam to reflect in all directions where some of them were refracted and scattered inside the sample. The intensity of the scattered light collected is independent of the angle of incidence.

#### 2.4.1 Characterisation

UV-vis reflectance spectra were recorded in diffuse reflectance mode (diffuse-reflectance) by a Shimadzu UV-2600 spectrometer with an integrating sphere (Shimadzu ISR-2600) to measure the reflectance of the samples in the range of 200 nm -1000 nm. The reference reflectance spectrum is measured with barium sulphate pellets.

### 2.4.2 Tauc Method

The spectra from the UV-Vis spectrometer showed a pseudo absorption profile from the reflectance. The output data from the instrument is in %Reflectance. The reflectivity(R) is converted from %Reflectance by dividing 100. The Kubleka-Munk function, F(R), is used to transform collected optical spectra into spectra that are proportional to absorption. When measuring the optical properties of powders samples, it is usually not possible to record an absorption spectrum. Hence, this is a problem for the measurement of the optical band gap since an absorption spectrum is required for Tauc method to determine band gap.

The Kubelka Munk function can be used to estimate the absorption spectrum from a diffuse reflectance spectrum. If the reflectivity, R, is converted, the Kubelka Munk function is

Equation 2.5

$$F(R) = \frac{(1-R)^2}{2R}$$

Where R is the reflectance from the collected data. Given assumption the scattering is ignored for powders, F(R) is proportional to adsorption.

A Tauc plot is a graph of  $[F(R)^*E]^2$  versus energy (E). E is the photon energy, which can be calculated from the wavelength,  $\lambda$ , in nm, as  $E(eV) = 1240/\lambda$ . The Tauc method is used to calculate the optical band gap from an absorption spectrum or from a reflectance spectrum that has been treated with the Kubelka Munk function. To use the Tauc method, plot  $(A.E)^2$  against E, where A is the absorption (or you can substitute F(R)), and E is the photon energy in electron volts. This plot should have a straight-line segment. By extrapolating the straight-line portion to the x-axis, you can determine the band gap. The bandgap is given by the x-axis intercept of the first linear region of the graph.

#### 2.4.3 Eliot Model

The optical measurements of inter-band transitions analysed by Tauc method was based on three assumptions. First, contributions from heavy and light holes

were neglected; second, the matrix element is momentum independent; third, no bounded electron-hole pair (exciton) or electron-impurity interactions are included, where the formation of executions increased the optical transition rate.<sup>95</sup>

Excitons are quasi-particles made up of bound electron and hole pairs. When an electron is excited into conduction band from valence band through either absorption of a photon or electroluminescence, this creates a hole in the valence band. This electron-hole pair can be restricted in a bound state by Coulombic interactions, which is called exciton. The energy required to separate an exciton into its constituent electron and hole charge carriers is called exciton binding energy. There are two types of excitons, Frenkel excitons and Wannier-Mott excitons. Frenkel excitons are tightly bounded electron-hole pairs within crystal unit cell or atomic radii, which is often found in insulators. Wannier-Mott excitons have a larger radius that exceeds the unit cell size which can move more freely through the crystal structure with a certain range. Wannier-Mott excitons exist in inorganic or hybrid semiconductor such as perovskites. The exciton is like a hydrogen-atom-like structure without considering centre-of-mass kinetic energy which can be expressed as

Equation 2.6

$$E_n=E_g-R_x/n^2$$

Where  $E_g$  is the gap energy, n is the quantum number of the n<sup>th</sup> energy level of excitons and  $R_x$  is effective Rydberg of exciton. At photon energy equal to  $E_n$ , excitons can be formed and the energy gap of the glass at room temperature can be expressed. Hence, R.J.Elliott invented the Elliott model for optical absorption analysis in terms of effective exciton Rydberg, involving parabolic bands

representing the contributions from heavy and light holes and constant transition momentum matrix elements between single-particle states throughout the Brillouin zone.<sup>96</sup>

The absorption coefficient data is analysed using a semi-empirical relation suggested by Manoogian and Woolley. In such model the absorption coefficient spectra are compared with an expression that includes terms for both discrete and continuous excitons. The proceeding is obtained from Elliot's model after convoluting the total absorption coefficient with a Lorentzian function (i.e., weak exciton-phonon interaction) in the form of  $\Gamma \pi^{-1}[(hv)^2 + \Gamma^2]$ . The expression which is used to analyse the optical properties is given by

 $\alpha(hv)=\alpha_0'\sum(1/n^3)(\Gamma_n/2)^2/[(\Gamma_n/2)^2+(hv-E_g+R_x/n)^2]+\alpha_1(\pi/2+\arctan[(hv-E_g)/\Gamma_c/2]))$  Where  $\alpha_0'$  represents the absorption peak at ground state exciton energy and  $\alpha_1$  is the absorption at band gap. Also,  $\Gamma_n$  and  $\Gamma_c$  are the full-width at half maximum of Lorentzian and full-width of continuum excitons, and  $R_x$  the exciton binding energy. The higher values of the exciton quantum number n can be neglected due to  $n^{-3}$  dependence of the line intensity of excitons peak and thus n=1 term is used in the summation of  $E_g$  above.

## 2.5 Thermogravimetry Analysis (TGA)

Thermogravimetric analysis (TGA) was completed using a Netzsch Jupiter TGA / DSC instrument, with data recorded in the air with a range between 20°C and 450°C with a heating rate of 10°C/min. A Thermogravimetric Analysis (TGA)

instrument consists of a furnace and a highly sensitive balance. TGA measures the mass percentage of a sample as it is heated, cooled, or held at a constant temperature in a defined atmosphere. To analyse a typical loss curve, if the percentage mass increases at the beginning with low temperatures, it is caused by the Buoyancy Effect. Once the percentage mass starts to decrease at a small rate, it can be explained by the loss of volatile components such as moisture, solvents, and monomers. The decomposition of the sample can be observed by a dramatic drop in percentage mass.

The Buoyancy Phenomenon may happen when a sample is heated in a gaseous environment i.e., Air. A sample in a gaseous environment has a buoyancy effect on it, as the gas is heated the density of the gas falls thus the sample looks like it has increased in mass even though there has been no physical or chemical change on the sample itself. The Buoyancy Phenomenon can be eliminated from the results by performing a TGA data analysis with no samples and taking away the results with no samples from the data with samples. Assuming the mass percentage of the sample remained at 100% when temperature was increasing at the early stage.

However, it may also be caused by the sensitivity of the balance of the TGA machine. When the sample is loaded, the balance fluctuates in the unit of milligrams. It caused the start point of the weight percentage over 100 Mass%. Since the difference of the weight percentage was used to predict the suspected

composition products. This can be ignored. Also, the TGA derivative graphs can imply the locations of decomposition at different stages.

## 2.6 X-ray Fluorescence

X-ray Fluorescence (XRF) describes the emission of characteristic X-rays from the sample. Short wavelength X-ray sources are utilised to excite an electron in an inner shell of an atom within the sample, causing the electron to be ejected from its shell while creating an electron hole. An electron from a higher energy shell will fill the hole, and release energy in form of a photon that is also equivalent to the difference in energy between the higher energy shell and lower energy shell. This process yields a fluorescent photon with a characteristic energy and the energy released is measured by the detector in XRF spectrometer. The wavelength or energy can be calculated via the Planck-Einstein relation, which is shown below.

Equation 2.7

#### λ=hc/E

XRF is a non-invasive technique to determine the elemental bulk composition of a material, and it is particularly useful for powder samples, specifically novel materials. As XRF is carried out in air at ambient temperature, it provides a quick and reliable way to obtain material composition information.

Samples were measured using Malvern Panalytical Epsilon 1 XRF analyser equipped with a 50 kV Ag anode X-ray tube. Samples, in form of powder, were placed in the sample holder and transferred to the detection chamber for analysis. All measurements were run in ambient air environment.

# 2.7 Titration to calculate percentage of Sn<sup>2+</sup>

The aim of an iodometric titration conducted on 1:Sn was to measure the concentration of  $Sn^{2+}$  in the solid tin(II) halides such as  $SnCl_2$  or  $SnBr_2$ . The titration involved the excessive production of  $I_2$ , then the reaction of  $I_2$  and  $Sn^{2+}$ , and finally the back titration of the remaining  $I_2$  with  $Na_2S_2O_3$ . The ionic equations were shown below.<sup>97</sup>

$$KIO_3$$
 (aq) + 5 KI (s) + 6HBr (aq)  $\rightarrow$ 3 I<sub>2</sub> (aq) +3 H<sub>2</sub>O (l) + 6KBr(aq)

In situ: 
$$I_2$$
 (aq) +  $Sn^{2+}(s) \rightarrow 2 I^-$  (aq) +  $Sn^{4+}$ (aq)

In situ: 
$$Na_2S_2O_3$$
 (aq) +  $I_2$  (aq)  $\rightarrow Na_2S_4O_6$  (aq) + 2  $I^-$  (aq)

Prior to sample preparation, all glassware was cleaned by ethanol solution(98+ wt%) and then rinsed by deionised water. For the solutions preparation, 0.535 g of potassium iodate (KIO<sub>3</sub>) solid was dissolved by deionised water to 250 ml in a beaker to obtain KIO<sub>3</sub> solution(10 mM); 0.142 g of sodium thiosulfate (Na<sub>2</sub>S<sub>2</sub>O<sub>3</sub>) solid was dissolved by ionised water to 500 ml in a beaker to obtain Na<sub>2</sub>S<sub>2</sub>O<sub>3</sub> solution (1.8 mM); 1.264 g of concentrated HBr solution (48 wt%) was dissolved by ionised water to 250 ml to obtain a diluted HBr solution (30 mM). 1% Starch

indicator was prepared by dissolving 1 g starch in 100 mL boiled water by stirring to form a gel solution.

Titration was standardised against KIO<sub>3</sub> solution in triplicate before titration of SnCl<sub>2</sub> and SnBr<sub>2</sub>. For standardisation, 1 ml of KIO<sub>3</sub> solution (10 mM) was added first, then 0.1 g of KI solid. 30 ml deionised water was used to dissolve the mixture with a good stirring. 2 ml HBr solution (30 mM) was added last to form a clear yellow solution. The resulting solution was stirred while it was titrated with Na<sub>2</sub>S<sub>2</sub>O<sub>3</sub> solution (1.8 mM). 1 ml of 1% starch indicator was added into the solution being titrated when the yellow resulting solution become faint during the titration. The tiny amount of starch gel solution would turn blue/purple. The titration continued with a long-last stirring till the blue solution turned transparent and clear which is the end point of the titration. The average amount of Na<sub>2</sub>S<sub>2</sub>O<sub>3</sub> solution (1.8 mM) used during standardisations is 28.2 ml (0.051 mmol) without any tin (II) halides. The corresponding amount of I<sub>2</sub> was 0.025 mmol. This was used as a reference for the titration against tin halides.

This experiment was used to measure the concentration of Sn<sup>2+</sup> of the bottle of tin(II) halides. Tin (II) halides are easily oxidised to tin (IV) halides in air once the commercially procured samples which come in a sealed bottle has been opened. For example, this experiment was conducted repeatedly with a bottle of SnBr<sub>2</sub> that has been opened for months. Before adding SnBr<sub>2</sub>, 1 ml of KlO<sub>3</sub> solution (10 mM) was added first, then 0.1 g of Kl solid. 30 ml deionised water was used to dissolve the mixture with a good stirring. 2 ml HBr solution (30 mM) was added

last to form a clear yellow solution. Then 0.008g SnBr<sub>2</sub> was added into the yellow solution with I<sub>2</sub> generated *in situ*, which involved the oxidation of Sn<sup>2+</sup> into Sn<sup>4+</sup>. 1ml of a starch indicator solution was added to the solution being titrated which turns the yellow solution into blue. The titration was ended when the blue colour disappeared. This experiment was conducted three times. The average amount of Na<sub>2</sub>S<sub>2</sub>O<sub>3</sub>, 5.86 mL, was used to titrate the residue of I<sub>2</sub> after the oxidation of Sn<sup>2+</sup> into Sn<sup>4+</sup>. Note that the sealed sample bottle from the commercial supplier indicated there is 98%+ SnBr<sub>2</sub>; however, the analysis performed here suggests that 32.55% of SnBr<sub>2</sub> is oxidised to SnBr<sub>4</sub> upon leaving the sample bottle exposed to air.

However, this experiment wasn't conducted on samples of Sn<sup>2+</sup> doped Cs<sub>3</sub>Bi<sub>2</sub>Cl<sub>9</sub> or Sn<sup>2+</sup> doped Cs<sub>3</sub>Bi<sub>2</sub>Br<sub>9</sub> due to the lack of the appropriate solvents to dissolve tin doped compounds. The original idea was to find out the concentrations of Sn<sup>2+</sup> in the precursors of tin (II) halides and the concentrations of Sn2+ in the products of Sn doped Cs<sub>3</sub>Bi<sub>2</sub>Cl<sub>9</sub> or Sn doped Cs<sub>3</sub>Bi<sub>2</sub>Br<sub>9</sub>. Those data can be used to calculate the ratio of Sn<sup>2+</sup> and Sn<sup>4+</sup> in the Sn doped compounds. Further studies can be explored in this direction if any good solvents are available to dissolve Sn doped compounds.

# 3 Defect-ordered double

# perovskites(A<sub>2</sub>BX<sub>6</sub>)

The main theme of this chapter is to determine whether Solution-phased Synthesis (SpS) and High Temperature Solid-state Synthesis (HTSsS) make any difference to the properties of tin halide materials. This can be done by attempting to answer the below four questions.

- Which synthesis method is better at achieving mixed halide samples without forming secondary phases or decomposing at high temperature?
- By mixing anions on the X site and cations on the B site or substituting Asite cations, is there a trend or a preference in the change of properties of tin halide perovskites in the A<sub>2</sub>BX<sub>6</sub> structure?
- Is it possible to alter the bandgap or size or shape of unit cells to achieve better performance as light absorbers by adjusting different arrangements of ions in mixed perovskites?
- Does mixed halides double perovskites have the same properties such as phase structure types of octahedra structures if they are made by different synthesis(e.g. SpS or HTSsS)?

The products of the two synthesis methods would be compared, and any structural differences were determined by a range of techniques. These techniques allowed the kinetic or thermodynamic distributions of the ions to be assessed. For example, the local halide and cation distribution were measured

using Raman spectroscopy, and the long-range structure was analysed by X-ray diffraction. To detect any changes in unit cell structures, compositions and bandgaps of samples made in different circumstances, samples were synthesized via either a solution-phased synthesis method (SpS) or a high-temperature solid-state grinding method (HTSsG). Samples were tested and valued by several techniques such XPS spectrometer, PXRD spectrometer and UV- vis spectrometer.

Also, different site-mixing technique was used to detect and modify changes on symmetry-driven structural and electronic properties of perovskite-like compounds in the formula of Cs<sub>2</sub>BX<sub>6</sub>. The study of thermal stability was to find out if Cs<sub>2</sub>SnCl<sub>6</sub>, Cs<sub>2</sub>SnBr<sub>6</sub> and Cs<sub>2</sub>Snl<sub>6</sub> compounds can react together to form a new structure by high temperature via solid-state synthesis method. The research is to expand the understanding of materials in the form of A<sub>2</sub>BX<sub>6</sub> in the field and to help modulate the properties by different doping techniques in the industry.

## 3.1 Mixed halide materials Cs<sub>2</sub>SnX<sub>6</sub> (X=Cl<sup>-</sup>, Br<sup>-</sup>, or l<sup>-</sup>)

X-site mixing is to partially substitute of lighter halide with heavier halide in the perovskite-like compounds such as Cs<sub>2</sub>SnX<sub>6</sub>. For example, by partially substituting CI with Br in the octahedral structure such as [SnCl<sub>6</sub>]<sup>2-</sup> of Cs<sub>2</sub>SnCl<sub>6</sub>, it formed [SnCl<sub>6-x</sub>Br<sub>x</sub>]<sup>2-</sup> octahedral structure in Cs<sub>2</sub>SnCl<sub>6-6x</sub>Br<sub>6x</sub> series. This is to detect and control the ongoing changes in structural properties, electrical

properties and light absorption properties by doping Br in Cs<sub>2</sub>SnCl<sub>6</sub> at an assumed increasing rate of 10% in Cs<sub>2</sub>SnCl<sub>6-6x</sub>Br<sub>6x</sub> series. The same method was used to observe the changes by doping I into Cs<sub>2</sub>SnBr<sub>6</sub> at an assumed increasing rate of 10%. The variants of Cs<sub>2</sub>SnBr<sub>6</sub> formed by partially substitutional doping half Br site anions with Iodine such as Cs<sub>2</sub>SnBr<sub>3</sub>I<sub>3</sub>. Different characterisation techniques mentioned in Chapter 2 was used to analyse samples and to study the changes in the properties of samples. This way is to expand the understanding of this type of material in the field and to help to modulate the properties by partially substituted doping halide in the perovskite-like compounds in the industry.

## 3.1.1 Experimental Methodology

The hypothesis was tested by conducting experiments of making the mixed halide perovskites and the mixed B-site ions perovskites by solution synthesis and solid-state synthesis in lab. Samples went through the steps of Preparation of Reagents and Solvents, Experimental Procedures of Synthesis and Characterizations of the chemical structure and optoelectronic properties of samples in different syntheses and thermal environments.

Chemical reagents are Caesium carbonate (Cs<sub>2</sub>CO<sub>3</sub>, 99.0%), Tin (IV) iodide (SnI<sub>4</sub>), Tin (IV) bromide (SnBr<sub>4</sub>, 99%), Tin (IV) Chloride Pentahydrate (SnCl<sub>4</sub>.5H<sub>2</sub>O), Hydriodic acid (HI, 57 wt. % in H<sub>2</sub>O, distilled), Hydrobromic acid (HBr, 48 wt. % in H<sub>2</sub>O) and Hydrochloride acid (HCl, 37% Wt. % in H<sub>2</sub>O). Solvents

are absolute ethanol solutions ( $\geq$ 98%). Detailed information of reagents and solvents are recorded in Appendix 8.1. The reactants were weighed and used straight away to make samples without purification, except the hydroiodic acid solution. 57% HI solution in storage made by Sigma-Aldrich contains  $I_3^-$  ions causing a red or black colour. This is because  $I^-$  ions are easily oxidised into  $I_3^-$  ions in the air. Hydroiodic acid solution only containing  $I^-$  ions was required for the reactions.

57 wt.% HI solution made by Sigma-Aldrich was washed by chloroform (98%) solution with tributyl phosphate (97%) to remove  $I_3^-$  ions. The proportion of the chloroform and the tributyl phosphate solutions used to wash the HI solution was 10:1. Hydriodic acid solution (57 wt.%) was poured slowly into the solution of tributyl phosphate in chloroform. The mixture separated into two layers, which were shaken together. The bottom aqueous layer was removed and repeatedly washed with fresh tributyl phosphate and chloroform solution until the washings were colourless. One is the chloroform solution with  $I_3^-$  ions on the top, the other is the aqueous HI solution with  $I_3^-$  ions. The aqueous HI solution was pale yellow with  $I_3^-$  ions, which was needed for the experiments.

#### Solution-phased synthesis (SpS) of pure Cs<sub>2</sub>SnX<sub>6</sub> (X=Cl, Br, or l)

To produce  $Cs_2SnX_6$  (X = Cl, Br, I) with a single halide anion, first caesium carbonate ( $Cs_2CO_3$ ) powder was dissolved in the corresponding hydrohalic acid solution. Secondly, the corresponding  $SnX_4$  powder was dissolved in the over 98%

absolute ethanol solution. The third step is mixing the two separate solutions evenly at room temperature using a magnetic stirrer resulting in a precipitation of a solid compound. The final step is to filter the solid compound from the mixture solution and to dry it in air overnight. Cs<sub>2</sub>SnCl<sub>6</sub>, Cs<sub>2</sub>SnBr<sub>6</sub>, Cs<sub>2</sub>Snl<sub>6</sub>, Cs<sub>2</sub>TeCl<sub>6</sub>, Cs<sub>2</sub>TeBr<sub>6</sub> and Cs<sub>2</sub>Tel<sub>6</sub> were produced using the same method (see Appendix 6.2 for detailed composition calculation of samples). For example, in a typical wet synthesis of Cs<sub>2</sub>SnBr<sub>6</sub> (~4.63 mmol, 4 g), Cs<sub>2</sub>CO<sub>3</sub>(~9.26 mmol, 1.72 g) was weighed and added slowly into a glass beaker containing an excess of HBr solution (~10 g, 48 wt.%). Heat release and white fumes were observed in the fume hood from the reaction below of Cs<sub>2</sub>CO<sub>3</sub> and HBr and left behind a colourless CsBr solution.

$$Cs_2CO_3 + 2 HBr \rightarrow 2CsBr + H_2O + CO_2 \uparrow$$

SnBr<sub>4</sub> solid (4.63 mmol, ~2.2945 g) was dissolved in absolute ethanol solution (~20 g) as a solvent. After it was dissolved completely, SnBr<sub>4</sub> solution was poured into the colourless CsBr solution. The mixture solution was stirred by the magnetic stirrer with RPM=300 and T=25° C for 10 minutes. The suspension became muddy and was filtered via a filtration setup by a few drops of absolute ethanol. The filtration setup included a Büchner funnel, a filter paper (70 mm), a rubber filter adapter, a Büchner flask and a rubber pipe connected to vacuum system. It was left in air over nights to dry out. Yellow solid sample remained on the filter paper and was ground into a fine powder by pestle and mortar. The final yellow powder finally was collected and put into a sample capsule for storage before further characterisations of the sample.

$$2CsBr + SnBr_4 \rightarrow Cs_2SnBr_6$$

#### Solution-phased synthesis(SpS) of Cs<sub>2</sub>SnX<sub>6</sub> with the mixed halides

To synthesise the mixed halide compounds such as the series Cs<sub>2</sub>SnCl<sub>6-6x</sub>Br<sub>6x</sub> or Cs<sub>2</sub>SnBr<sub>6x</sub>I<sub>6-6x</sub> (x=0 to 1 in increments of 0.1), it is like the production line of Cs<sub>2</sub>BX<sub>6</sub> (B=Sn, X = Cl, Br, or I) with a single halide anion but the mixed precursor solutions of BX<sub>4</sub> with two halides was prepared in the desired halide mole ratio, as were the mixed corresponding hydrohalic acids. For example, to synthesise 4 grams of Cs<sub>2</sub>SnCl<sub>6-6x</sub>Br<sub>6x</sub> with a nominal atom percentage of bromine in the mixed halides, x, of 0.1, Cs<sub>2</sub>CO<sub>3</sub> (4.28 mmol, 1.92 g, powder) was added into the mixed acids of HCl (~8.40 g, 37 wt.%) and 48% HBr (~1.60 g) to form the mixed solution of CsCl and CsBr. HCl (7.70 mmol, 0.76 g, 37 wt.%) and HBr (0.86 mmol, 0.30 g, 48 wt.%) are needed for the reaction. An excess of acids was used to make sure Cs<sub>2</sub>CO<sub>3</sub> reacted with acid completely. White fume and heat were released during the reaction.

$$Cs_2CO_3 + (2-2x) HCI + 2x HBr \rightarrow 2-2x CsCI + 2x CsBr + H_2O + CO_2 \uparrow (x=0.1)$$

SnCl<sub>4</sub>·5H<sub>2</sub>O (1.84 g) was first dissolved in the absolute ethanol (20 g) as a solvent with a slow whirling. SnBr<sub>4</sub> (0.26 g) was added into the same solution after SnCl<sub>4</sub>·5H<sub>2</sub>O crystals were dissolved completely with a clear solution. The mixed solution of CsCl and CsBr was poured into the mixed solution of SnCl<sub>4</sub> and SnBr<sub>4</sub> to form a muddy yellow suspension immediately in the glass beaker on the magnetic stirrer (RMP=300, T=25 °C) for 10 minutes.

$$(2-2x)$$
 CsCl + 2x CsBr +  $(1-x)$  SnCl<sub>4</sub>·5H<sub>2</sub>O + x SnBr<sub>4</sub>  $\rightarrow$  Cs<sub>2</sub>SnCl<sub>6-6x</sub>Br<sub>6x</sub> + 5H<sub>2</sub>O

The suspension was filtered via a filter funnel with a filter paper with some absolute ethanol solution under the vacuum system to wash out excessive acids, and then it was left in air to crystalise overnight.

#### High Temperature Solid-state Synthesis(HTSsS)

The solid-state approach is making samples by simply grinding two pure halide defect-ordered perovskite compounds such as Cs<sub>2</sub>SnCl<sub>6</sub>(0.5 g, 0.84 mmol) and Cs<sub>2</sub>SnBr<sub>6</sub> (0.5 g, 0.58 mmol) together evenly, and then samples were heated up to 200-400°C under dynamic vacuum in a quartz tube for 12 hours. The same procedures were also used for Cs<sub>2</sub>SnBr<sub>6</sub> and Cs<sub>2</sub>SnI<sub>6</sub>. The aim is to understand whether the temperature changes cause any changes in lattice structures or phase transitions of two pure defect-ordered halide perovskite compounds. It was also applied to the mixture of Cs<sub>2</sub>SnCl<sub>6</sub> and Cs<sub>2</sub>TeCl<sub>6</sub> to try to produce Cs<sub>2</sub>Sn<sub>x</sub>Te<sub>1-x</sub>Cl<sub>6</sub>.

#### 3.1.2 Results and Discussion

In the discussion, XPS technique was used to calculate the analytic chemical composition by measuring analytic Br% out of the total halides in the samples. The electronic structure of samples was measured by XPS. PXRD technique was used to confirm whether extra phases existed and to study the unit cell parameters in the mixed halides samples with analytic compositions. UV-vis technique was used to observe the trend of changes in light absorption in terms

of band gaps of different mixed halide samples. Raman technique was used to study if different octahedra existed in the mixed halide samples.

#### XPS photoelectron spectroscopy

The analytical composition of compounds was determined from XPS data, and it was used to confirm the actual chemical composition of samples by measuring the atomic ratio of elements. The analytic atomic compositions of samples in both series Cs<sub>2</sub>SnCl<sub>6-6x</sub>Br<sub>6x</sub> and Cs<sub>2</sub>SnBr<sub>6x</sub>l<sub>6-6x</sub> (x= 0 to 1 in increments of 0.1), x=0 represents nominal Br%=0 is shown in the Appendix 6.3. Most of the samples in both series matched the atomic ratio of Cs to Sn to X as 2:1:6, which was matched to the XRD data in Figure 3.2 later to confirm the correct compounds made via SpS method.

In the product samples, each sample has 9 atoms in the empirical formula. The nominal atomic percent of Cs to Cs<sub>2</sub>SnX<sub>6</sub> is 2/9 (~22.22%), and the nominal atomic percent of Sn is 1/9 (~11.11%). The nominal percent of the X-site atoms to Cs<sub>2</sub>SnX<sub>6</sub> is 6/9 (~66.67%). The analytic atomic percent of Cs, Sn, Cl, Br, and I, which was analysed from the XPS results of samples shown below. The nominal atomic ratios were compared to the analytic data to confirm the samples were made in an approximately correct atomic ratio. Take compound Cs<sub>2</sub>SnBr<sub>5.19</sub>I<sub>0.81</sub> as an example, the analytic Cs% was 23.33, and the analytic Sn% was 16.41 of the sample.

As the atomic ratio of mixed halides are the major focus of research here, and the difference between nominal data and analytic data of Cs% and Sn% were ignorable and acceptable if the phase ID of the sample was confirmed as the mixed halide defect-ordered double perovskite material (Cs<sub>2</sub>SnX<sub>6</sub>). The data of analytic Cs% and analytic Sn% were recorded in Appendix 6.3. Sample with nominal composition Cs<sub>2</sub>SnBr<sub>4.8</sub>I<sub>1.2</sub> is supposed to have 20% I and 80% Br in the mixed halide mixing as the compositional calculation mentioned in the Appendix 6.2. However, the analytic Br% in the sample was 86.56 which was higher than predicted; on the contrary, the analytic I% (13.45%) was less, the analytic composition of the sample was measured as Cs<sub>2</sub>SnBr<sub>5.19</sub>I<sub>0.81</sub>. This was how the analytic chemical composition for all the samples was calculated by Casa XPS software.

XPS spectra was calibrated by setting C 1s as 284.8 eV as a reference line. This is because most samples exposed to the environment will have a detectable quantity of adventitious carbon contamination. Adventitious carbon maybe be removed by argon sputtering using lowest energy beam such as 200 eV, 500 eV or argon clusters to prevent or minimize chemical damage to the underlying material. Hence, adventitious carbon contamination commonly used as a charge reference for XPS spectra. Here it can be used as a reference but not in polymers.

The XPS data of Cs<sub>2</sub>SnCl<sub>6</sub> was analysed by Casa XPS software. The Sn 3d<sub>5/2</sub> binding energy peak of Cs<sub>2</sub>SnCl<sub>6</sub> was fitted and measured as 488.1 eV, and Cs 3d<sub>5/2</sub> peak of Cs<sub>2</sub>SnCl<sub>6</sub> was 724.9 eV after the charging correction. Charging

correction is to calibrate C 1s core line as 284.8 eV. The standard elemental Sn 3d<sub>5/2</sub> peak is set as 485 eV in the Casa XPS software's library, and the standard elemental Cs 3d<sub>5/2</sub> peak as 726 eV. The differences observed in the double perovskite samples is due to the Sn and Cs being in positive oxidation states. The Sn 3d<sub>5/2</sub> binding energy peak and Cs 3d<sub>5/2</sub> peak of Cs<sub>2</sub>SnCl<sub>6</sub> was used as the reference values to calculate absolute binding energy change of core lines Sn 3d<sub>5/2</sub> and Cs 3d<sub>5/2</sub> in Figure 3.1. There is no correlation between Cs 3d<sub>5/2</sub> binding energy peaks and the different halide percentage as no trend was seen in Figure 3.1. This indicated that the Cs 3d<sub>5/2</sub> binding energy was barely affected by the different concentration of halides in the samples.<sup>98</sup> The difference of the Cs 3d<sub>5/2</sub> binding energies between mixed halide samples in series Cs<sub>2</sub>Sn Cl<sub>6-6x</sub>Br<sub>6x</sub> and Cs<sub>2</sub>SnCl<sub>6</sub> fluctuated between 0 and -1 eV. The Cs 3d<sub>5/2</sub> binding energy of Cs<sub>2</sub>SnCl<sub>6</sub> was used as a reference.

The Sn 3d<sub>5/2</sub> binding energy peaks were decreasing with heavier halides doped into samples showed in Figure 3.1. It means that the polarity of the Sn-X bonds was decreasing with heavier halides doped into mixed halide compounds.<sup>99</sup> For example, The shifts of Cs<sub>2</sub>SnBr<sub>6</sub> and Cs<sub>2</sub>SnI<sub>6</sub> was calculated relative to the binding energies observed in Cs<sub>2</sub>SnCl<sub>6</sub>. The Sn 3d<sub>5/2</sub> binding energy of Cs<sub>2</sub>SnBr<sub>6</sub> is 0.57 less than that of Cs<sub>2</sub>SnCl<sub>6</sub>, and the Sn 3d<sub>5/2</sub> binding energy of Cs<sub>2</sub>SnI<sub>6</sub> 1.27 less than that of Cs<sub>2</sub>SnCl<sub>6</sub>. The Cs 3d<sub>5/2</sub> binding energy of Cs<sub>2</sub>SnBr<sub>6</sub> and Cs<sub>2</sub>SnI<sub>6</sub> are the same, which both were 0.35 less than that of Cs<sub>2</sub>SnCl<sub>6</sub>. This was related to the decreasing trend of the electronegativity going down the halogen group in the periodic table. The polarity of a bond is determined by the difference in electronegativity between the atoms involved in the bond. The Sn-I bond has

smaller differences between the electronegativity of the bonded atoms than that of the Sn-Br bond. The decreasing trend of the Sn 3d<sub>5/2</sub> binding energy in Figure 3.1(b) is clearer than that of Figure 3.1(a) due to the uncovered range of the analytic Br% in the range between 10-30. The nominal Br% of 10, 20 and 30 resulted with the lower analytic Br% of 2.09, 10.39 and 42.18 individually. The binding energy change of Sn 3d<sub>5/2</sub> decreased with increasing I% in the Cs<sub>2</sub>SnI<sub>6-6x</sub>B<sub>6x</sub> series where x=0 to 1 in increments of 0.1, x=0 represents 0 Br% in Figure 3.1(b). They are two pairs of points deviated from the expected values which are circled in Figure 3.1 (a) and (b). Each pair represented a mixed halide sample. The deviation may be caused by the unreacted precursors in which the PXRD patterns of both samples exists the extra hkl peaks. The extra hkl peaks matches the PXRD data of SnI<sub>4</sub> and CsCl mentioned in Figure 3.2.

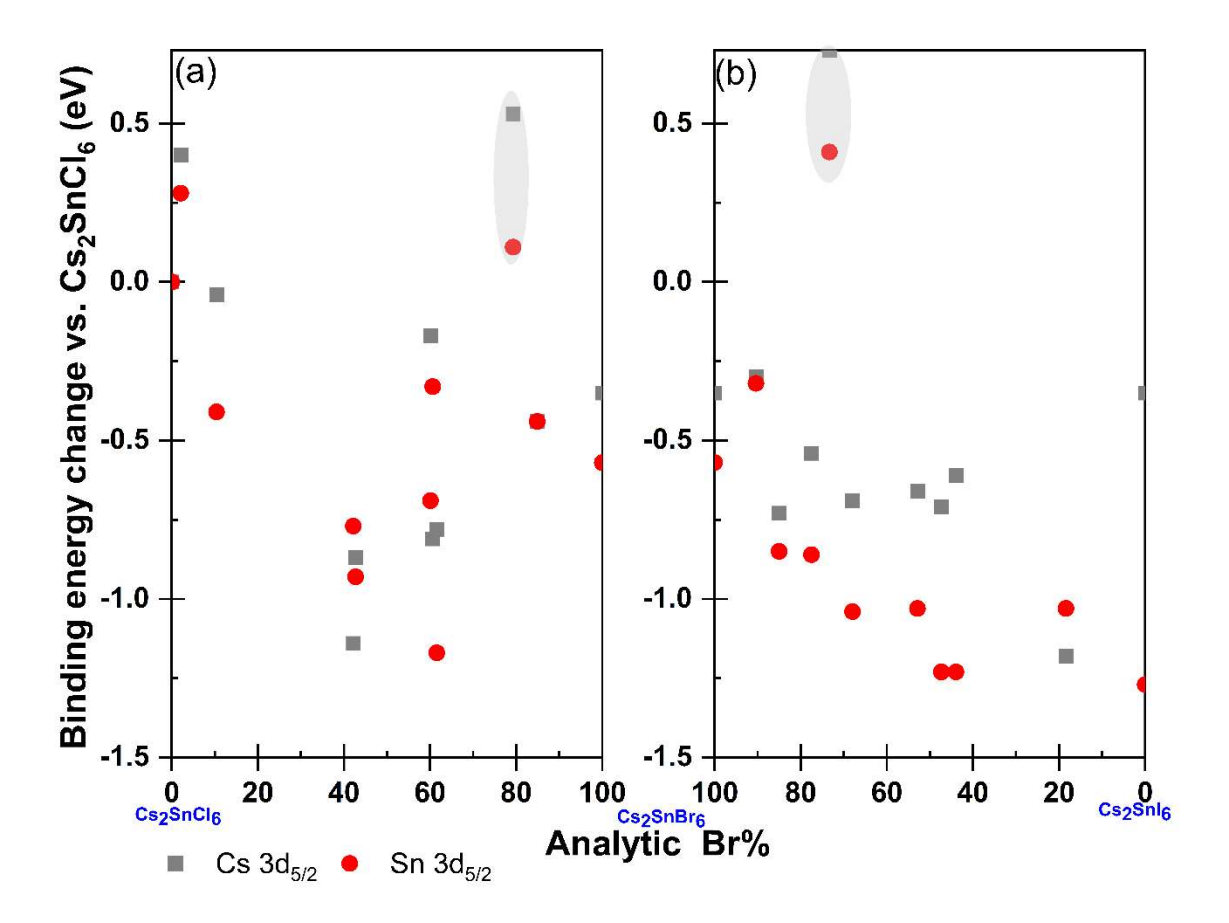


Figure 3.1 The binding energy shifts of Cs  $3d_{5/2}$  and Sn  $3d_{5/2}$  core lines with the analytic Br% in samples across  $Cs_2SnBr_{6-6x}Cl_{6x}$  series (left) and  $Cs_2Snl_{6-6x}Br_{6x}$  series (right), and two shaded data points are outliners which can be ignored.

#### Compositions and Structural characterisations

Although they all shared the cubic structure with a single-phase Fm-3m space group, the parameters of the cubic unit cell structure of samples were adjustable by altering the ratio of Br to I or the ratio of Br to CI. The lattice parameter changed with changing halide composition. In the XRD patterns of  $Cs_2SnX_6$  series with analytic chemical compositions via a solution-phased synthesis (SpS) at room temperature shown in Figure 3.2 below, listing from the bottom to the top  $(Cs_2SnCl_6 \rightarrow mixed halides series Cs_2SnBr_{6-6x}Cl_{6x} \rightarrow Cs_2SnBr_6 \rightarrow mixed halides series Cs_2Snl_{6-6x}Br_{6x} \rightarrow Cs_2Snl_6)$  shifted to smaller 20 angles. This corresponds to an increase in lattice parameter according to Bragg's law.

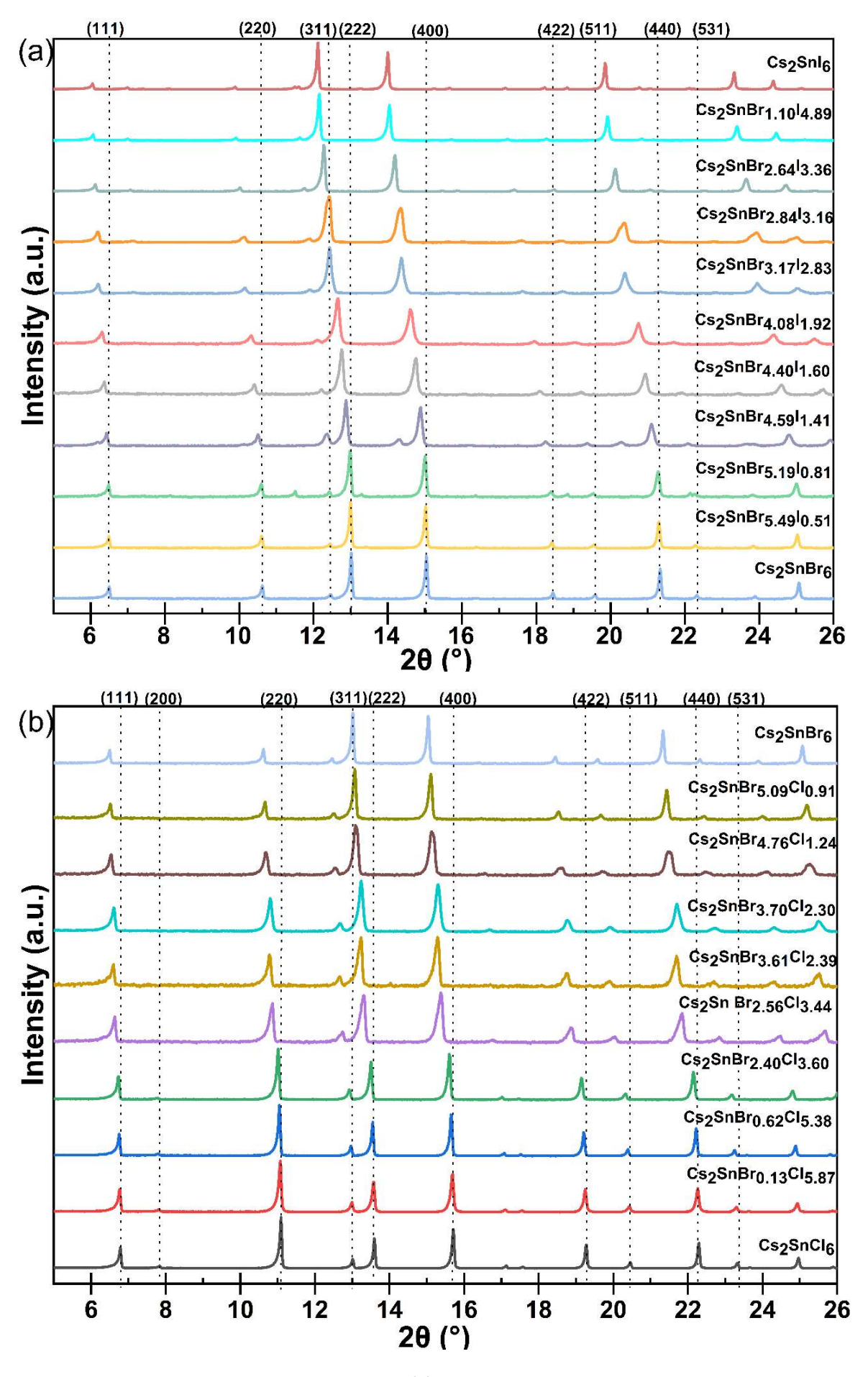
Relative peak intensity changed due to the electron density distribution of the unit cell structure factor. For example, iodine has more electrons than chloride, so the electron density of iodine is higher, which means planes containing iodide ions will diffract X-rays more than planes containing chloride. <sup>100</sup> For example, the intensities of peaks from XRD pattern of Cs<sub>2</sub>SnCl<sub>6</sub> is smaller than that of Cs<sub>2</sub>SnBr<sub>3.7</sub>Cl<sub>2.3</sub>. A small amount of Br doped in Cs<sub>2</sub>SnCl<sub>6</sub> increased the peak intensities which showed around 2θ=15.7° as the peak areas got larger.

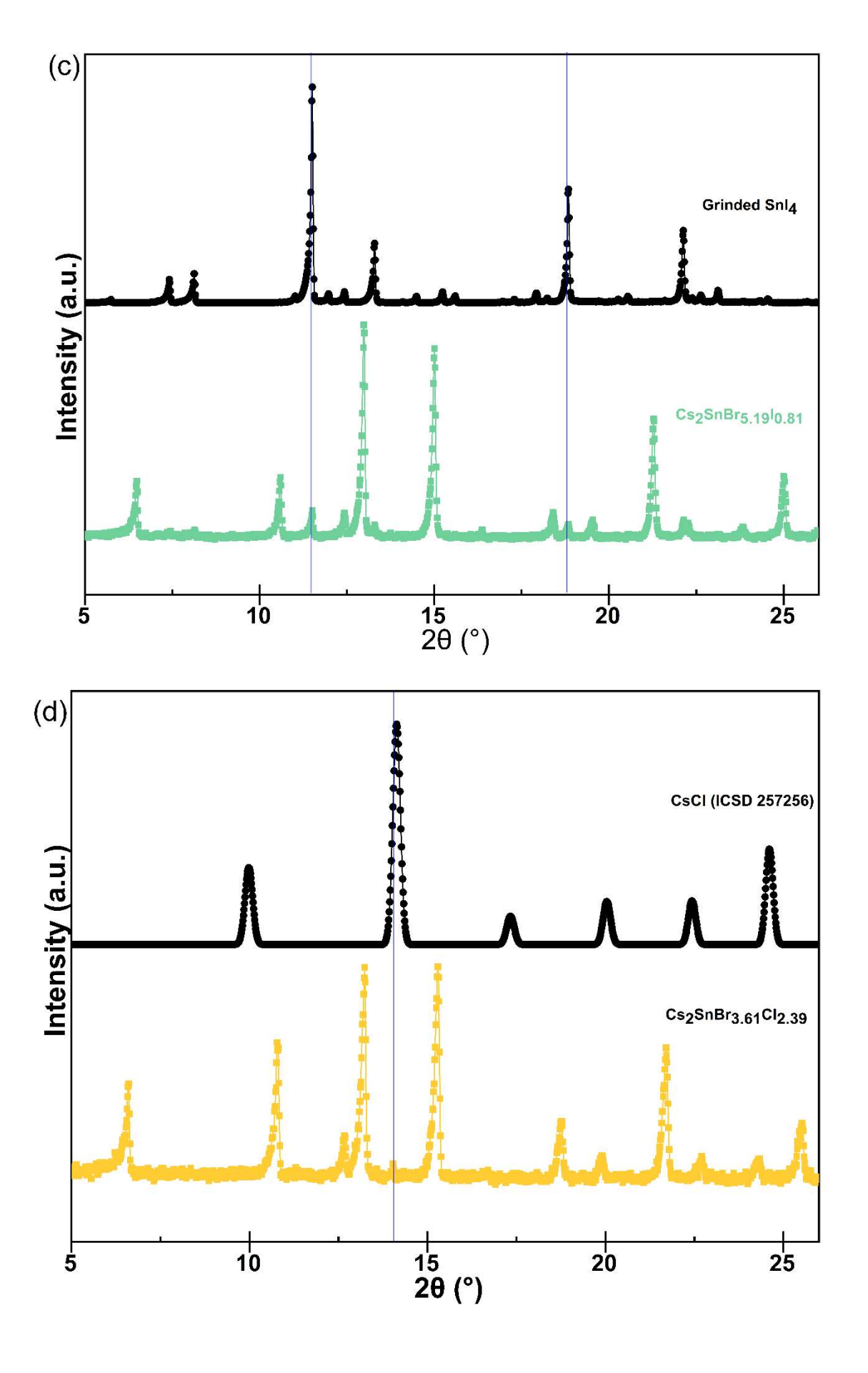
All PXRD patterns shared located Braggs peaks called Miller Indices such as (111), (220), (311), (222), (400), (422), (511), (440) and (531) apart from the extra phase resulted by SnI<sub>4</sub> on the PXRD pattern of sample  $Cs_2Sn_{5.19}l_{0.81}$ . Overall, the Braggs peaks in the PXRD pattern of  $Cs_2SnCl_6$  are all shifted to left (the low 20 value). The Braggs peaks at lower 20 range shifted less to left such as Braggs peak with Miller Indices(111) from 6.79° in sample  $Cs_2SnCl_6$  to 6.50° in sample  $Cs_2SnBr_6$ , and the Braggs peaks at higher 20 range shifted more to left such as Miller Indices (531) from  $2\theta = 22.30$ ° in sample  $Cs_2SnCl_6$  to  $2\theta = 21.32$ ° in sample  $Cs_2SnBr_6$ . The same trend also worked for series  $Cs_2Snl_{6-6x}Br_{6x}$ .

STOE Stadi-P machine produced monochromatic X-rays K alpha 1 that produce no additional peaks arising from other excitation radiations. The extra peak at 20= 14.3° for compound Cs<sub>2</sub>SnBr<sub>4.59</sub>I<sub>1.41</sub>, the extra peaks at 20= 11.5° and 18.5° for compound Cs<sub>2</sub>SnBr<sub>5.19</sub>I<sub>0.81</sub>, and the extra peak at 20= 14.0° for compound Cs<sub>2</sub>SnBr<sub>3.61</sub>CI<sub>2.39</sub> may come from unreacted precursors.

To confirm the impurity peaks coming from unreacted precursors, the PXRD patterns of the samples were compared to the XRD data of caesium halides and tin halides(IV) from ICSD database. The extra peaks of compound Cs<sub>2</sub>SnBr<sub>5.19</sub>I<sub>0.81</sub> were matched to peaks of the XRD pattern of grinded SnI<sub>4</sub> from lab shown in Figure 3.2(c). This can be the residue of SnI<sub>4</sub> left over from the filtration. The intensity of the peaks is very low so the amount of SnI<sub>4</sub> is very little which can be ignored. Peaks from side phases are cubic structures for caesium salts, whose patterns started at 2θ values above 10° and so don't obscure the

first hkl values at about 6.5°. The tiny extra peak at 20= 14.0° for compound Cs<sub>2</sub>SnBr<sub>3.61</sub>Cl<sub>2.39</sub> was matched to the peak with highest intensity of CsCl. The extra peak at 20= 14.3° for compound Cs<sub>2</sub>SnBr<sub>4.59</sub>l<sub>1.41</sub> wasn't matched to any XRD patterns of the possible residues from precursors. This may cause by the contamination from the lab. The peaks from XRD patterns of compound Cs<sub>2</sub>SnBr<sub>2.84</sub>l<sub>3.16</sub> are slightly wider than other samples' hkl peaks in Figure 3.2(a). This may cause by the two compounds with very similar chemical compositions, so peaks are overlayed at very close locations which is like the case in Figure 3.3(a). It requests further study to have any solid evidence.





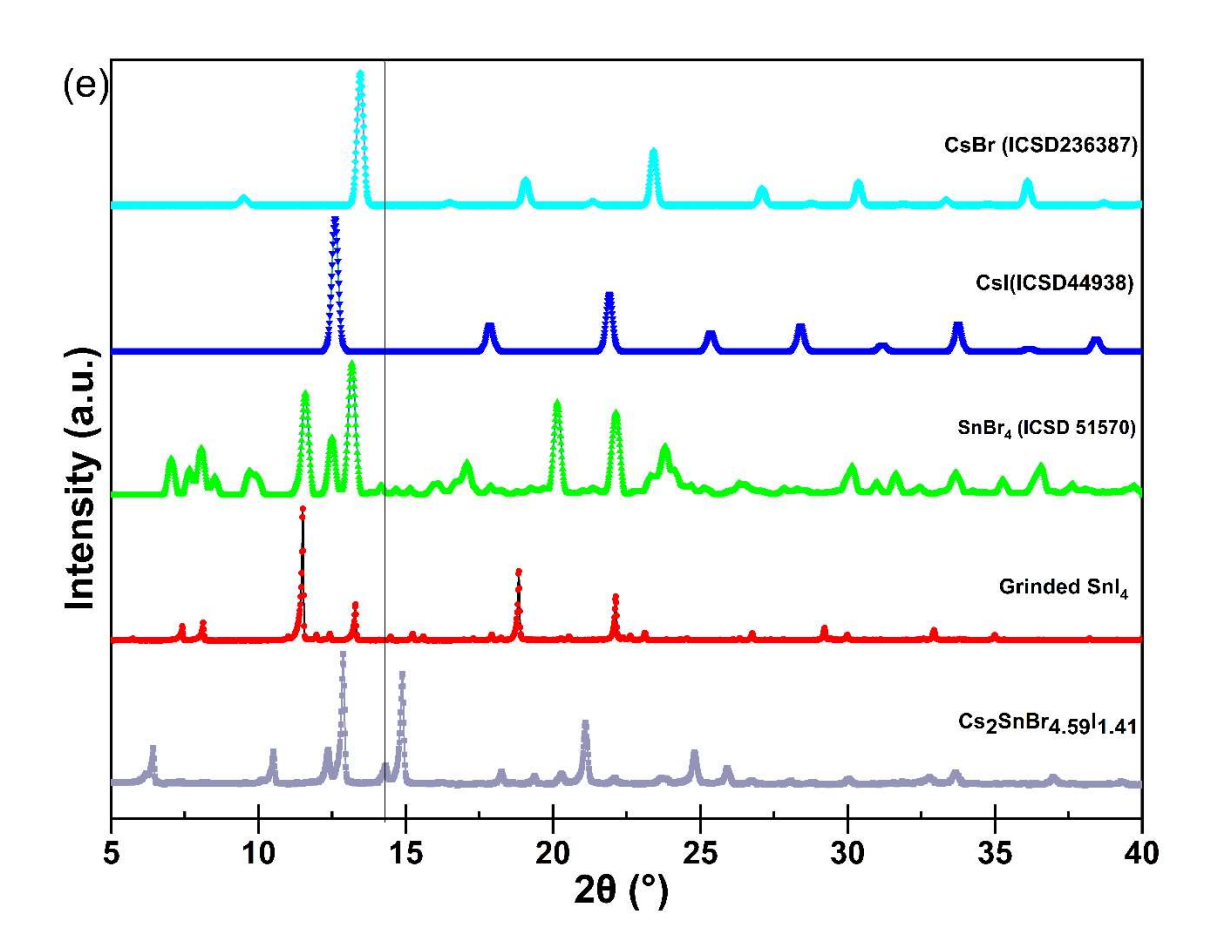


Figure 3.2 The XRD patterns of samples in series  $Cs_2SnCl_{6-6x}Br_{6x}$  (b) and  $Cs_2Sn\ Br_{6x}l_{6-6x}$  (a) ((x= 0 to 1 in increments of 0.1, x=0 represents Br%=0), (c) The comparation between the PXRD patterns of compound  $Cs_2SnBr_{5.19}l_{0.81}$  and the grinded  $Snl_4$ , (d) The comparation between the PXRD patterns of compound  $Cs_2SnBr_{3.61}Cl_{2.39}$  and CsCl from ICSD database(257256)<sup>101</sup>.

The Miller Indices such as (111), (220), (311), (222), (400), (422), (511), (440) and (531) in Figure 3.2 was used to calculate unit cell parameters of samples. Unit cell parameters can be calculated by the equation of inter-planar spacing, miller indices and lattice constants and the equation of Bragg's Law. For cubic crystals system, where the interplanar spacings (d spacings) are calculated according to

$$1/d^2=a(h^2+k^2+l^2)$$

Where d= Interplanar Spacing, h ,k ,I =Miller Indices, a=Lattice Constants.

Bragg's Law:  $2d\sin\theta=n\lambda$  was mentioned in Chapter 2.1, where n=constant,  $\lambda$ =the wavelength of the X-rays. Rearranging the equation of Bragg's Law to get  $d=n\lambda/(2\sin\theta)$ . The combination equation of the equation of d spacings in the cubic crystal systems and the equation of Bragg's Law is

$$((2 \sin \theta)/n\lambda)^2 = a(h^2+k^2+l^2)$$

To calculate unit cell parameters, the equation above is used to find out the dimensional length of unit cell as the lattice constants a, and the lattice a was used to calculate the volume of unit cells. Each unit cell has 4 of formula units of Cs<sub>2</sub>SnX<sub>6</sub>.

Due to Bragg's law, the heavier halide ions doped in the compound, the larger the lattice parameter. For example, a small percent of I doped in Cs<sub>2</sub>SnBr<sub>6</sub> caused the unit cell parameters of the compound to increase. This matches the trend of change in size of unit cell in Figure 3.3. They are 4 formula units per unit cell. The unit cell volume of Cs<sub>2</sub>SnI<sub>6</sub> is 1576.5 Å<sup>3</sup> with lattice a=11.6 Å, and the volume per formula unit of Cs<sub>2</sub>SnI<sub>6</sub> is 394.1 Å<sup>3</sup>. The unit cell volume of Cs<sub>2</sub>SnBr<sub>6</sub> is 1272.8 Å<sup>3</sup> with lattice a=10.8 Å, and the volume per formula of Cs<sub>2</sub>SnBr<sub>6</sub> is 318.2 Å<sup>3</sup>. The volume per formula of mixed halides defect-ordered perovskite materials increases when the amount of I% was doped into Cs<sub>2</sub>SnBr<sub>6</sub> increases. Also, the unit cell volume of Cs<sub>2</sub>SnCl<sub>6</sub> is 1117.9 Å<sup>3</sup> with lattice a= 10.4 Å, and the volume per formula unit of Cs<sub>2</sub>SnCl<sub>6</sub> is 279.5 Å<sup>3</sup>.

The trend is true to all samples in  $Cs_2SnCl_{6-6x}Br_{6x}$  series and  $Cs_2SnBr_{6-6x}l_{6x}$  series shown in Figure 3.3. Doping a heavier halide element into  $Cs_2SnX_6$  would increase the size of the unit cell. The samples in  $Cs_2SnCl_{6-6x}Br_{6x}$  series and  $Cs_2SnBr_{6-6x}l_{6x}$  series only grew in the dimension of lattice a since they are all in the cubic structure. Also, Cs is much smaller than organic cation group so the structure can maintain the cubic shape.

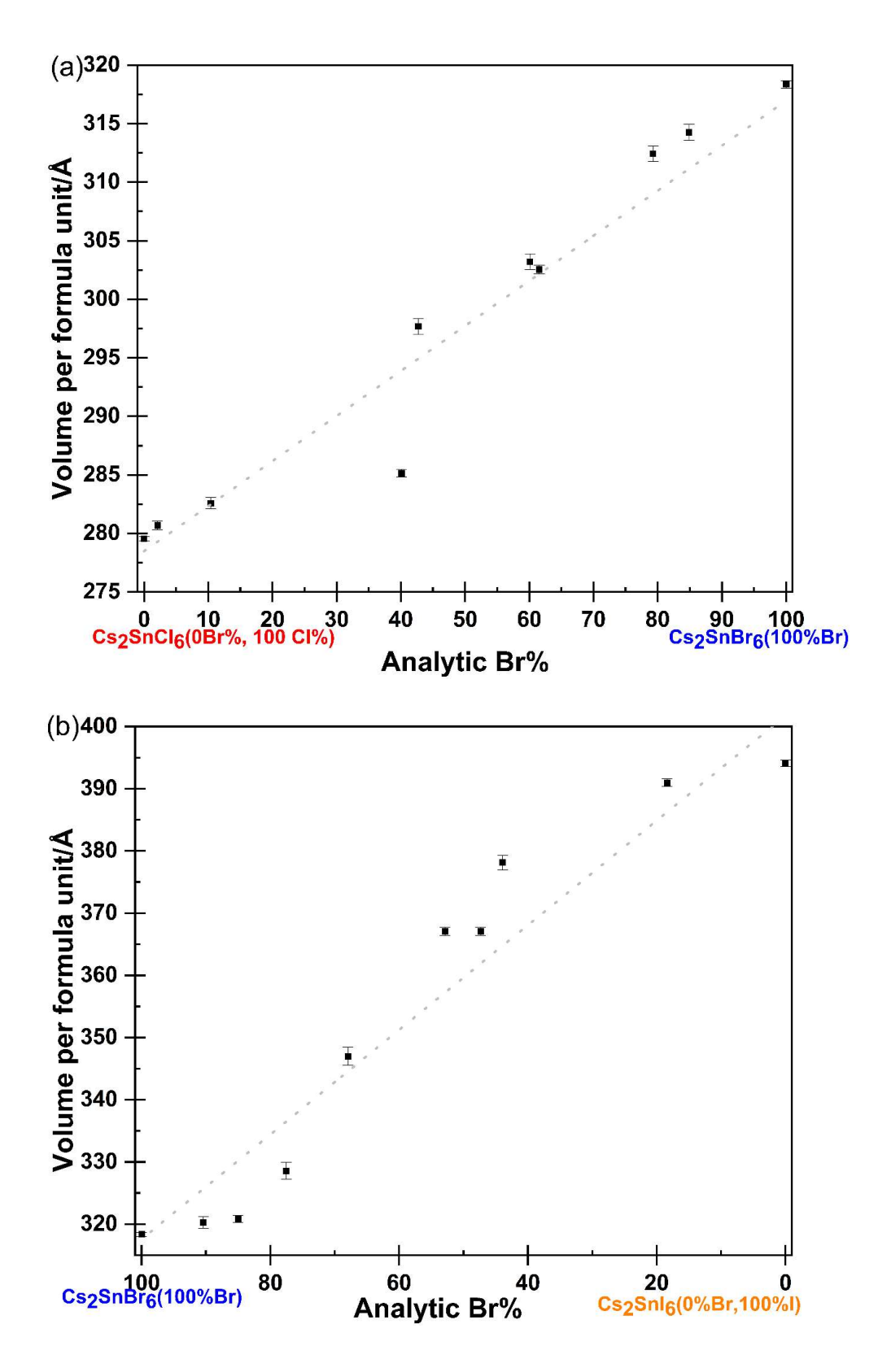


Figure 3.3 (a) The correlation between the analytic Br% and the volume per cell unit of samples in  $Cs_2SnCl_{6-6x}Br_{6x}$  series. (b) The correlation between the analytic Br% and the volume per cell unit of samples in  $Cs_2SnBr_{6-6x}I_{6x}$  series.

#### Raman Spectroscopy

The mechanism of Raman spectroscopy was shown in the section 2.3 above. A Raman spectrum features a few peaks, showing the intensity and the wavelength position of the Raman scattered light. When isolated  $[SnX_6]^{2-}$  octahedra in  $Cs_2SnX_6$  (x= CI, Br, or I) scattered incident laser light and vibrated, the different Raman scattered light can be interpreted as the different vibration levels and wavelengths of isolated  $[SnX_6]^{2-}$  octahedra.

The Raman spectra of Cs<sub>2</sub>SnCl<sub>6</sub>, Cs<sub>2</sub>SnBr<sub>6</sub> and Cs<sub>2</sub>Snl<sub>6</sub> made via the solution synthesis consist of three peaks in Figure 3.4. The peaks are shifting to lower frequencies when the compounds are made with heavier halide ions. This is expected as vibrational frequency decreases with increasing mass. For example, the three peaks in the Raman spectrum of Cs<sub>2</sub>SnCl<sub>6</sub> are represented as three different vibrations of [SnCl<sub>6</sub>]<sup>2-</sup>, which are the A<sub>1g</sub> (at ~309.6 cm<sup>-1</sup>), E<sub>g</sub> (at ~231.6 cm<sup>-1</sup>) and T<sub>2g</sub> (at ~167.7 cm<sup>-1</sup>) vibrations of the O<sub>h</sub> point group shown in Figure 3.4(c). When laser light with the wavelength, 633nm, was pointed at compound Cs<sub>2</sub>SnCl<sub>6</sub> scattering the light into three wavelengths which can be translated into different vibrations of [SnCl<sub>6</sub>]<sup>2-</sup>. <sup>102</sup> Comparing to three different vibrations of [SnCl<sub>6</sub>]<sup>2-</sup>, three different vibrations, A<sub>1g</sub>, E<sub>g</sub> and T<sub>2g</sub> shifted to lower wavenumbers ar~185.6 cm<sup>-1</sup>, ~136.8 cm<sup>-1</sup> and ~106.8 cm<sup>-1</sup> for Cs<sub>2</sub>SnBr<sub>6</sub> due to heavier halide ions, Br. The wave numbers of three vibrations of Cs<sub>2</sub>Snl<sub>6</sub> shifted to much lower wavelength then that of Cs<sub>2</sub>SnBr<sub>6</sub>.

Any BX<sub>6</sub> molecule such as [SnCl<sub>6</sub>]<sup>2-</sup>, [SnBr<sub>6</sub>]<sup>2-</sup> and [Snl<sub>6</sub>]<sup>2-</sup> octahedra belonging to the O<sub>h</sub> point group which has (3 x 7)-6 =15 degrees of vibrational freedom. From O<sub>h</sub> character table, A<sub>1g</sub>, E<sub>g</sub> and T<sub>2g</sub> modes are Raman active. Hence the Raman spectra from Cs<sub>2</sub>SnCl<sub>6</sub>, Cs<sub>2</sub>SnBr<sub>6</sub> and Cs<sub>2</sub>Snl<sub>6</sub> comprise of mainly three peaks corresponding to Sn-X vibrations in A<sub>1g</sub>, E<sub>g</sub> and T<sub>2g</sub> vibrational modes in octahedral symmetry.

Theoretically the normal vibrational modes were predicted following the  $O_h$  character table of Group theory, and they were  $A_{1g}$ ,  $E_g$ ,  $T_{1g}$ ,  $2T_{2g}$ ,  $4T_{1u}$  and  $T_{2u}$  modes. From these modes,  $T_{1g}$  and  $T_{2u}$  are silent, one  $T_{1u}$  is acoustic, and three  $T_{1u}$  are IR active. The rest  $A_{1g}$ ,  $E_g$  and two  $T_{2g}$  are Raman active. Among Raman active modes,  $A_{1g}$  is related to Sn-X symmetric stretching, and  $E_g$  mode is related to the asymmetric Sn-X stretching (which is also called doubly degenerate). One  $T_{2g}$  mode is related to the asymmetric bending X-Sn-X deformation(which is also called triply degenerate). These three modes are vibrations inside the  $[SnX_6]^{2-}$  octahedra. There is another one  $T_{2g}$  mode which is vibrations of Cs atoms in the rigid  $[SnX_6]^{2-}$  lattice.  $^{103}$ 

The spectrum of  $Cs_2SnCl_6$  reported by Kaltzoglou et al. exhibits four peaks at  $309cm^{-1}$ ,  $232~cm^{-1}$ ,  $168cm^{-1}$  and  $51cm^{-1}$  which represent  $A_{1g}$  (the symmetric stretching between Sn-X bond),  $E_g$  (the asymmetric stretching between Sn-X bond), one  $T_{2g}$  (the asymmetric bending of X-Sn-X bond deformation), and the other  $T_{2g}$  (the rattling translation motions of heavy Cs atoms in the rigid  $[SnCl_6]^{2-1}$ 

lattice structure) individually. The T<sub>2g</sub> vibrational mode at 51 cm<sup>-1</sup> has been seen in trigonal Cs<sub>2</sub>TiF<sub>6</sub> which was about 57.0 cm<sup>-1</sup>.<sup>104,105,106</sup> However, this vibrational T<sub>2g</sub> mode at 51cm<sup>-1</sup> was not seen on the Raman spectra of Cs<sub>2</sub>SnBr<sub>6</sub> and Cs<sub>2</sub>snl<sub>6</sub> due to the increase of the oscillator mass for Cs<sub>2</sub>SnBr<sub>6</sub> and Cs<sub>2</sub>snl<sub>6</sub> compounds and the low bonding strength of the Cs vibrations to the [SnBr<sub>6</sub>]<sup>2-</sup> and [Snl<sub>6</sub>]<sup>2-</sup> lattices explained by Kaltzoglou et al..<sup>107</sup> E<sub>g</sub> and A<sub>1g</sub> are stretching modes shown in Table 3.1. T<sub>1u</sub> is also a stretching mode of Sn-X bond but it is IR active only. T<sub>2g</sub> is related to a stretching mode of Cs reported by Kaltzoglou et al.,which mode is excluded from Table 3.1; this table was only used for the theoretical symmetry analysis based on stretching modes of Sn-X bonds. Hence, the number of absorptions observed in the Raman spectrum based on the symmetry analysis of Sn-X bonds is 2 for [SnX<sub>6</sub>]<sup>2-</sup> octahedra. Further studies of symmetry analysis of mixed halides octahedra combining the theoretical stretching modes, deformations and other factors of Sn-X bonds can be useful.

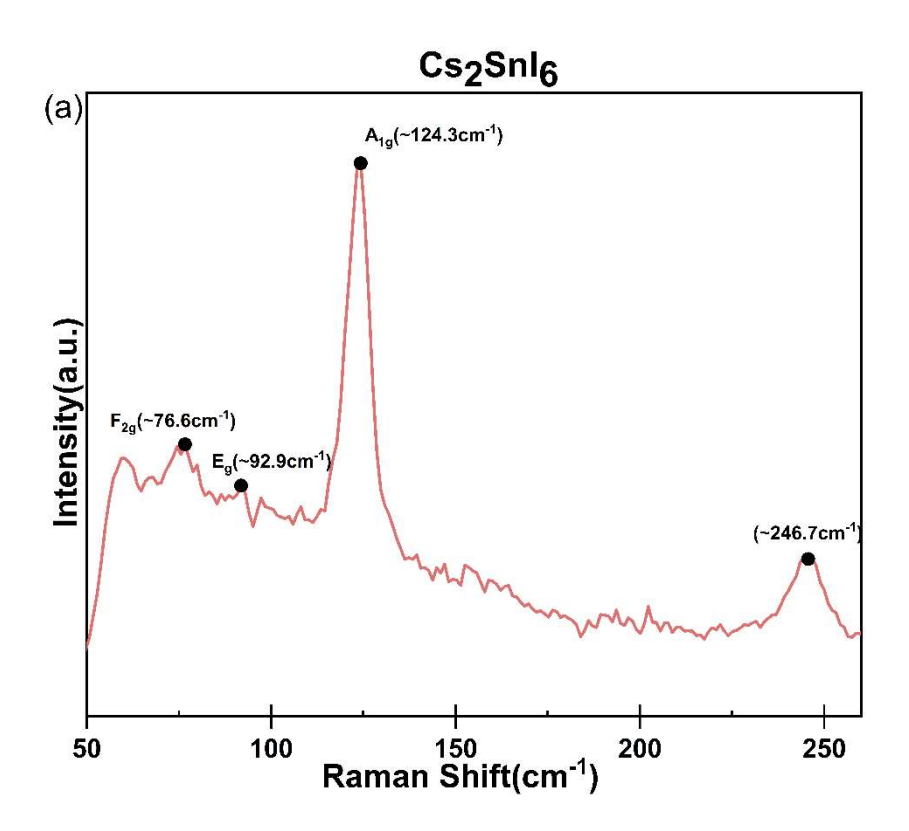
Also, there were three peaks on the Raman spectra of Cs<sub>2</sub>SnBr<sub>6</sub> reported by Kaltzoglou et al. indicating at 186cm<sup>-1</sup> (A<sub>1g</sub>), 137cm<sup>-1</sup>(E<sub>g</sub>), 106cm<sup>-1</sup>(T<sub>2g</sub>). Cs<sub>2</sub>SnI<sub>6</sub> compounds are sensitive to laser-induced damage. Although the high intense peak was seen at 126 cm<sup>-1</sup>(A<sub>1g</sub>) clearly, the two weak peaks at 92cm<sup>-1</sup>(E<sub>g</sub>) and 78 cm<sup>-1</sup>(T<sub>2g</sub>) was not seen so clearly due to the possibility of laser induced damage. Kaltzoglou et al. also showed that the different Raman instruments with different wavelengths present slightly different results. Although the Raman data points are not precise, the same compounds indicated the same pattern and the locations of Raman peaks are roughly the same locations, which are shown in Figure 3.4 as well.

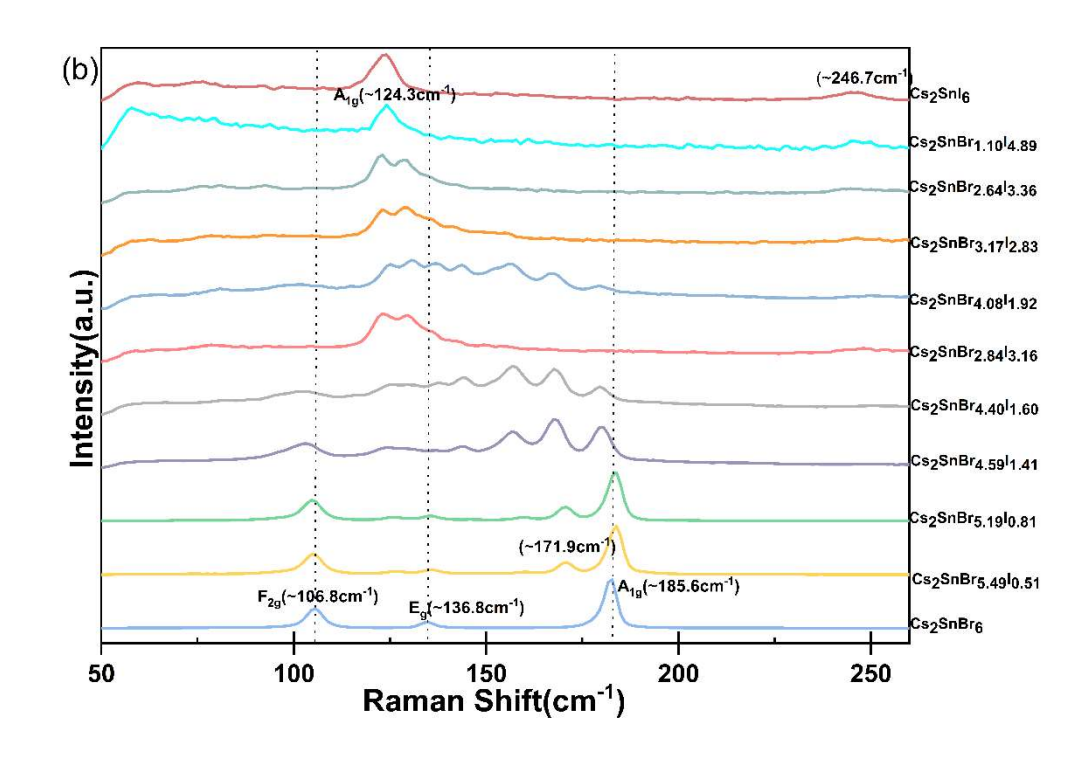
The second order mode was seen on the spectrum of Cs<sub>2</sub>Snl<sub>6</sub> at 245.9 cm<sup>-1</sup> due to the strong Raman conditions shown in Figure 3.4(a). The same situations can be observed in some cases due to the high intensity of the laser gun which can be improved by using weak laser guns with larger wavenumber. <sup>108</sup> Hence, according to the locations of the main A<sub>1g</sub> peaks in Cs<sub>2</sub>SnX<sub>6</sub>(X=Cl, Br or I), the compounds with the reduced atomic mass such as lighter halide elements have stronger Sn-X bond harmonic oscillations with Raman peaks locating at high wavenumbers.

On the other hand, the Raman spectra of Cs<sub>2</sub>SnBr<sub>4.25</sub>Cl<sub>1.75</sub> and Cs<sub>2</sub>Snl<sub>3.18</sub>Br<sub>2.82</sub> are much more complicated as the existence of several octahedron types is possible when halide ions are mixed in the isolated [SnX<sub>6</sub>]<sup>2-</sup> Octahedra when laser was pointed at the samples. For example, Cs<sub>2</sub>SnBr<sub>4.25</sub>Cl<sub>1.75</sub> not only included vibrations of pure halide octahedra, [SnCl<sub>6</sub>]<sup>2-</sup> and [SnBr<sub>6</sub>]<sup>2-</sup> but also included some of the mixed halide octahedra types such as [SnCl<sub>5</sub>Br]<sup>2-</sup>, cis-[Cl<sub>4</sub>Br<sub>2</sub>]<sup>2-</sup>, trans-[Cl<sub>4</sub>Br<sub>2</sub>]<sup>2-</sup>, fac-[Cl<sub>3</sub>Br<sub>3</sub>]<sup>2-</sup>, mer-[Cl<sub>3</sub>Br<sub>3</sub>]<sup>2-</sup>, cis-[Cl<sub>2</sub>Br<sub>4</sub>]<sup>2-</sup>, trans-[Cl<sub>2</sub>Br<sub>4</sub>]<sup>2-</sup> and [ClBr<sub>5</sub>]<sup>2-</sup>. The reason why the Raman spectra changes when you go through pure halide octahedra to mixed halide octahedra is the symmetry of the octahedra/ the symmetry of the environment decreases.

For example, pure tin halide material such as Cs<sub>2</sub>Snl<sub>6</sub>, Cs<sub>2</sub>SnBr<sub>6</sub> or Cs<sub>2</sub>SnCl<sub>6</sub> only have one type of octahedra such as [Snl<sub>6</sub>]<sup>2-</sup>, [SnBr<sub>6</sub>]<sup>2-</sup> and [SnCl<sub>6</sub>]<sup>2-</sup> individually. However, the mixed halide compounds would have higher possibility of different

types of mixed halides octahedra. For example, mixed halide materials Cs<sub>2</sub>SnCl<sub>6-6x</sub>Br<sub>6x</sub> can have [SnCl<sub>5</sub>Br]<sup>2-</sup>, cis-[Cl<sub>4</sub>Br<sub>2</sub>]<sup>2-</sup>, trans-[Cl<sub>4</sub>Br<sub>2</sub>]<sup>2-</sup>, fac-[Cl<sub>3</sub>Br<sub>3</sub>]<sup>2-</sup>, mer-[Cl<sub>3</sub>Br<sub>3</sub>]<sup>2-</sup>, cis-[Cl<sub>2</sub>Br<sub>4</sub>]<sup>2-</sup>, trans-[Cl<sub>2</sub>Br<sub>4</sub>]<sup>2-</sup> and [ClBr<sub>5</sub>]<sup>2-</sup>. To correspond the peaks to the specific mixed halide octahedra, the point group of each different mixed halide octahedra can be worked out. Symmetry analysis of each mixed halide octahedra showed that the specific point group of each mixed halide octahedra was assigned by the point group assignment scheme and demonstrated all possible Raman vibrational modes based on that point group for a given octahedra.





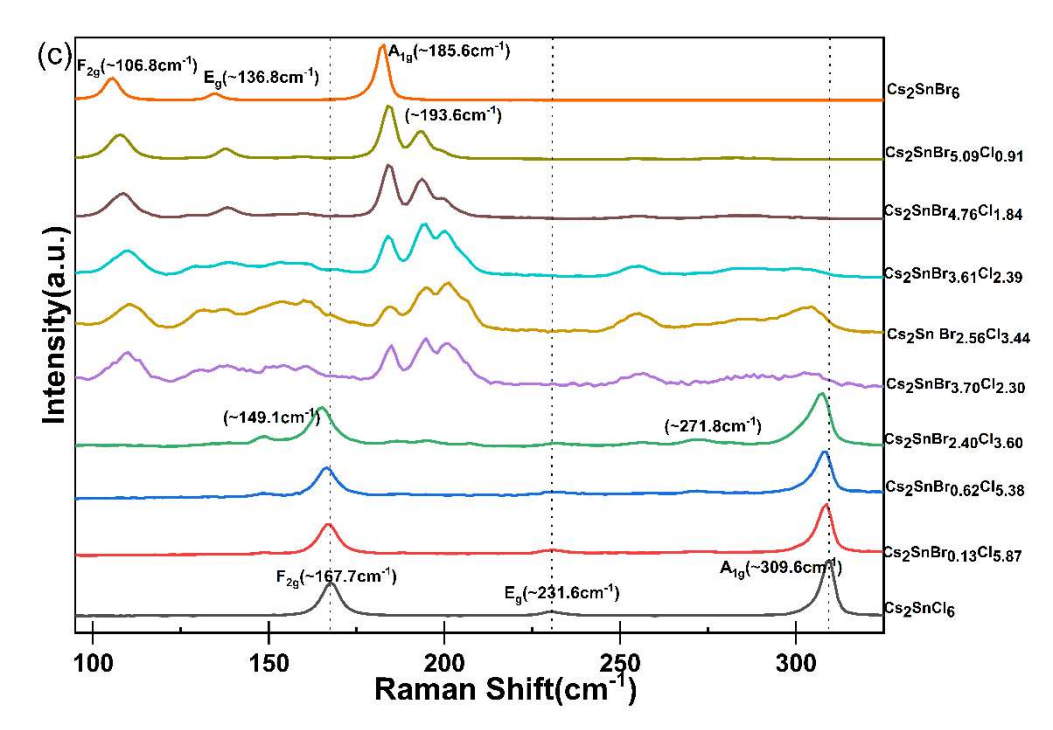


Figure 3.4 (a)The Raman spectrum of pure  $Cs_2SnI_6$  with point group locations; (b) The Raman spectra of samples in series  $Cs_2SnCI_{6-6x}Br_{6x}$ ; (c) The Raman spectra of samples in series  $Cs_2SnBr_{6x}I_{6-6x}$  ((x=0 to 1 in increments of 0.1, x=0 represents analytic Br%=0).

#### Symmetry analysis of series Cs<sub>2</sub>SnCl<sub>6-6x</sub>Br<sub>6x</sub> or Cs<sub>2</sub>Snl<sub>6-6x</sub>Br<sub>6x</sub>

Here character tables of different point groups were used to determine whether the modes of vibrations involve stretching or bending, to define the symmetry labels of the vibrational modes and to decide if the vibrational modes are Raman/IR active. In a molecule, or molecular ion, stretching and bending modes were used to describe the changes made to the bond vectors or bond angles. If the symmetry label such as  $A_1$ ,  $B_1$  and E of a normal model of vibration is associated with x, y or z in the right side of the character table, then the certain mode was IR active. If the symmetry label such as  $A_1$ ,  $B_1$  and E of a normal mode is associated with a product term such as  $x^2$  or xy in the right side of character table, then the certain mode was Raman active.

Here for a mode of vibration to be Raman active, it must give rise to a change in the polarizability of the molecule. Polarizability is the ease with which electron cloud could associate with the distorted molecule. Take samples from mixed halide series Cs<sub>2</sub>SnCl<sub>6-6x</sub>Br<sub>6x</sub> as examples to study the possibility of different types of octahedra existed in the mixed halide samples shown in Table 3.1. The similar octahedra types existed in mixed halide series Cs<sub>2</sub>Snl<sub>6-6x</sub>Br<sub>6x</sub>.

Complex	Point group	Symmetries of Sn-Cl stretching modes	Symmetries of Sn-Br stretching modes	Raman active modes	Number of absorptions observed in the Raman spectrum (based on Sn-X)
SnCl <sub>6</sub>	Oh	$A_{1g}+E_g+T_{1u}$	-	A <sub>1g</sub> +E <sub>g</sub>	2
SnCl₅Br	C <sub>4v</sub>	2A <sub>1</sub> +B <sub>1</sub> +E	A <sub>1</sub>	2A <sub>1</sub> +B <sub>1</sub> +E+A <sub>1</sub>	5

trans- SnCl <sub>4</sub> Br <sub>2</sub>	D <sub>4h</sub>	A <sub>1g</sub> +B <sub>1g</sub> +E <sub>u</sub>	A <sub>1g</sub> +A <sub>2u</sub>	A <sub>1g</sub> +B <sub>1g</sub> +A <sub>1g</sub>	3
cis- SnCl <sub>4</sub> Br <sub>2</sub>	C <sub>2v</sub>	2A <sub>1</sub> +B <sub>1</sub> +B <sub>2</sub>	A <sub>1</sub> +B <sub>2</sub>	2A <sub>1</sub> +B <sub>1</sub> +B <sub>2</sub> + A <sub>1</sub> +B <sub>2</sub>	6
fac- SnCl <sub>3</sub> Br <sub>3</sub>	Сзу	A <sub>1</sub> +E	A <sub>1</sub> +E	A <sub>1</sub> +E+A <sub>1</sub> +E	4
mer- SnCl <sub>3</sub> Br <sub>3</sub>	C <sub>2v</sub>	2A <sub>1</sub> +B1	2A <sub>1</sub> +B1	2A <sub>1</sub> +B <sub>1</sub> +2A <sub>1</sub> +B <sub>1</sub>	6

Table 3.1 The theoretical stretching modes of mixed halide octahedra based on Character Tables for commonly encountered point groups.

### Cis-[SnCl<sub>4</sub>Br<sub>2</sub>]<sup>2-</sup> octahedra

Only one rotational axis by  $180^{\circ}$  is  $C_2$  with two  $\sigma_V$  vertical reflectional mirror planes but no  $\sigma_h$  horizonal mirror planes at right angle to the  $C_2$  axis exists which means this point group is  $C_{2V}$ . The cis-SnCl<sub>4</sub>Br<sub>2</sub> octahedra belongs to the  $C_{2V}$  point group, and in this point group 6 modes of vibrations of SnCl<sub>4</sub>Br<sub>2</sub> octahedra were supposed to be detected theoretically which were  $A_1$  and  $B_2$  vibrational modes from Sn-Br bonds stretching and two  $A_1$ ,  $B_1$  and  $B_2$  vibrational modes from Sn-Cl bonds stretching.

The bonds left unchanged were found out from each symmetry operation (E, C<sub>2</sub>,  $\sigma_{V}(xz)$  and  $\sigma_{V}(yz)$ ) of the C<sub>2V</sub> character table for Sn-Br bonds in the cis-SnCl<sub>4</sub>Br<sub>2</sub> octahedra. In Sn-Br bonds the E operator leaves two Sn-Br bonds unchanged as so does reflection through the  $\sigma_{V}(yz)$  plane. However, rotation about the C<sub>2</sub> axis affects both bonds, and so does reflection though the  $\sigma_{V}(xz)$  plane. In the summery of the row of characters, E=2, C<sub>2</sub>=0,  $\sigma_{V}(xz)$ =0, and  $\sigma_{V}(yz)$ =2. The number in the sum of row of characters represents the number of bonds

unchanged which was used to determine the vibrational modes involved in the compound.

This resulted two degenerate stretching modes in the Sn-Br bonds of the cis-SnCl<sub>4</sub>Br<sub>2</sub> octahedra, one A<sub>1</sub> symmetry and one B<sub>2</sub> symmetry. The A<sub>1</sub> symmetry mode (E=1, C<sub>2</sub>=1,  $\sigma_V(xz)$ =1 and  $\sigma_V(yz)$ =1) of the Sn-Br bonds happened when vectors were left unchanged by the E operator and was rotated by the C<sub>2</sub> axis. Also, there is no change to the vectors when the bonds were reflected by either the  $\sigma_V(xz)$  plane or the  $\sigma_V(yz)$  plane. For the asymmetric stretching of the Sn-Br bonds of the cis-SnCl<sub>4</sub>Br<sub>2</sub> octahedra, the vectors are unchanged by the E and the  $\sigma_V(yz)$  plane but the directions were reversed by the rotation of the C<sub>2</sub> axis and by the reflection through the  $\sigma_V(xz)$  plane. This is called B<sub>2</sub> asymmetric stretching(E=1, C<sub>2</sub>=-1,  $\sigma_V(xz)$ =-1 and  $\sigma_V(yz)$ =1).

The degree of vibrational freedom is 3n-6=3 for the Sn-Br bonds. Two out of three modes are stretching modes. The last one is a bending mode. The bending mode results in the changes of the bond angle of Br-Sn-Br. Here is also  $A_1$  symmetry(E=1,  $C_2=1$ ,  $\sigma_v(xz)=1$  and  $\sigma_v'(yz)=1$ ), which is related to the effects of each symmetry operation of the  $C_2v$  point group on the bond angle. Here each operation left the bond angle unchanged. According to  $C_2v$  character table,  $A_1$  and  $B_2$  modes both are Raman active.

The bonds left unchanged were found out from each symmetry operation (E, C<sub>2</sub>,  $\sigma_v(xz)$  and  $\sigma_v'(yz)$ ) of the C<sub>2v</sub> character table for Sn-Cl bonds in the cis-SnCl<sub>4</sub>Br<sub>2</sub> octahedra. The E operator leaves four Sn-Cl bonds unchanged. The reflection through the  $\sigma_v'(yz)$  plane leaves two Sn-Cl bonds unchanged so does the reflection through the  $\sigma_v(xz)$  plane. However, rotation by the C<sub>2</sub> axis affects all bonds. In the summery of the row of characters, E=4, C<sub>2</sub>=0,  $\sigma_v(xz)$ =2, and  $\sigma_v'(yz)$ =2. The number in the sum of row of characters represents the number of bonds unchanged which was used to determine the vibrational modes involved in the compound. Here Sn-Cl bonds stretching in cis-SnCl<sub>4</sub>Br<sub>2</sub> octahedra have two A<sub>1</sub>, one B<sub>1</sub> and one B<sub>2</sub> modes.

The degree of vibrational freedom is 3x5-6=9 for the Sn-Cl bonds. There are 4 stretching modes out of total vibrational modes. A<sub>1</sub> symmetry and B<sub>2</sub> symmetry of Sn-Cl bonds are like the ones of Sn-Br bonds. The B<sub>1</sub> symmetry level represents the asymmetric stretching of the Sn-Br bonds of the cis-SnCl<sub>4</sub>Br<sub>2</sub> octahedra where the vectors are unchanged by the E and the  $\sigma_v(xz)$  plane, but the directions were reversed by the rotation of the C<sub>2</sub> axis and by the reflection through the  $\sigma_v'(yz)$  plane. This is B<sub>1</sub> asymmetric stretching (E=1, C<sub>2</sub>=-1,  $\sigma_v(xz)$ =1 and  $\sigma_v'(yz)$ =-1).

## [SnCl₅Br]<sup>2-</sup> octahedra

In this section, the relationship between the numbers of modes the symmetries of vibration that IR / Raman active and the symmetry levels of Sn-Cl<sub>6-n</sub>Br<sub>n</sub> complexes. The octahedral complexes were described as "octahedral" but only

SnX<sub>6</sub> pure halide octahedra Such as SnCl<sub>6</sub> here belongs to the Oh point group. An SnCl<sub>6</sub> complex with the Oh point group exhibits one absorption of Cl stretching region in its IR spectrum, in contrast, the mixed halide complex SnCl<sub>5</sub>Br with the C<sub>4v</sub> point group showed three absorptions, for example, in the IR spectrum of SnCl<sub>5</sub>Br, bands are observed at 2138 cm<sup>-1</sup>, 2052 cm<sup>-1</sup> and 2007 cm<sup>-1</sup>.

The origin of these bands can be understood by using group theory. Consider how many Sn-Cl bonds in SnCl<sub>5</sub>Br complex are left unchanged by each symmetry operation (E, C<sub>4</sub>, C<sub>2</sub>, $\sigma_v$ ,  $\sigma_d$ ) of the C<sub>4v</sub> point group. The E operator leaves all five Sn-Cl bonds unchanged, while rotation around each axis and reflection through a  $\sigma_d$  plane leaves one Sn-Cl bond unchanged. Reflection through a  $\sigma_v$  plane leaves three Sn-Cl bonds unchanged. The vibrational modes of the [SnCl<sub>5</sub>Br]<sup>2-</sup> octahedra therefore have A<sub>1</sub>, B<sub>1</sub> and E symmetry levels. The C<sub>4v</sub> character table shows that the E stretching mode, and the two A<sub>1</sub> stretching modes are IR active modes.

### fac-[SnCl<sub>3</sub>Br<sub>3</sub>]<sup>2-</sup> octahedra

The Sn-Cl bonds/ Sn-Br bonds in fac-[SnCl<sub>3</sub>Br<sub>3</sub>]<sup>2-</sup> formed trigonal pyramidal. The E operator is the identity operator, and it leaves the bonds unchanged. The C<sub>3</sub> axis passes through the Sn atom, which was perpendicular to a plane containing the three Cl atoms/ Br atoms. Each  $\sigma_V$  plane contains Sn-Cl / Sn-Br bond and bisects the opposite Cl-Sn-Cl/ Br-Sn-Br bond angle.

The Sn-Cl bonds/Sn-Br bonds possess  $C_{3v}$  Symmetry. In the Sn-Cl bonds/ Sn-Br bonds in fac-[SnCl<sub>3</sub>Br<sub>3</sub>]<sup>2-</sup>, three  $\sigma_v$  planes in the Sn-Cl bonds/ Sn-Br bonds were present. Sn-Cl bonds/ Sn-Br bonds were rotated 120° by the  $C_3$  axis though the Sn atom twice till the atoms were back to the original state. The Sn-Cl bonds or the Sn-Br bonds in the fac-[SnCl<sub>3</sub>Br<sub>3</sub>]<sup>2-</sup> octahedra contain six degrees of vibration freedom. The normal modes of vibration of Sn-Cl bonds/ Sn-Br bonds in the fac-[SnCl<sub>3</sub>Br<sub>3</sub>]<sup>2-</sup> octahedra have modes which are doubly degenerate. They are asymmetric stretching of Sn-Cl bonds/ Sn-Br bonds and asymmetric deformation of Sn-Cl bonds/ Sn-Br bonds, which both are E symmetry modes from  $C_{3v}$  character table.

Also, they are two symmetric modes which are symmetric stretching A<sub>1</sub> mode and symmetric deformation A<sub>1</sub> mode. They are all Raman active. Hence, there are four absorptions in the Raman Spectrum for Sn-Cl bonds and another four absorptions for Sn-Br bonds which are symmetric stretch A<sub>1</sub>, Symmetric deformation A<sub>1</sub>, asymmetric stretch E, and asymmetric deformation E. There should be eight absorptions at total for fac-[SnCl<sub>3</sub>Br<sub>3</sub>]<sup>2-</sup>.

In the  $C_{3v}$  character table, there are 2 stretching modes out of total vibrational modes.  $A_1$  symmetric stretching and E asymmetric stretching of Sn-Cl bonds are like the ones of Sn-Br bonds. The  $A_1$  symmetry level represents the symmetric stretching of the Sn-Cl bonds or of the Sn-Br bonds of the fac-[SnCl<sub>3</sub>Br<sub>3</sub>]<sup>2</sup>-octahedra where the vectors are unchanged by the E and one bond was unchanged through three  $\sigma_v$  planes. No bonds were unchanged by  $2C_3$  rotations.

The sum of the row of characters is displayed as E=3,  $2C_3$ =0 and  $3\sigma_v$ =1. This results in the two stretching modes mentioned above.

### trans-[SnCl<sub>4</sub>Br<sub>2</sub>]<sup>2-</sup> octahedra

There are nine degrees of vibrational freedom for Sn-Cl bonds in the trans-[SnCl4Br2]<sup>2-</sup> octahedra. The Sn-Cl bonds are in a square planar shape. Three vibrational modes existed according to the character table of D4h point group which are A1g symmetric stretching mode, B1g mode and Eu mode. The Eu mode is doubly degenerate. The A1g and B1g modes are Raman active but Eu mode is not Raman active. The E operator leaves four Sn-Cl bonds unchanged. The horizontal plane through the Sn atom leaves four bonds unchanged. The two vertical mirror planes leave two bonds unchanged. The rotation by the axis through Cl-Sn-Cl bonds leaves two bonds unchanged. For the linear Br-Sn-Br in the trans-[SnCl4Br2]<sup>2-</sup> octahedra, there are four degrees of vibrational freedom. They are one symmetric stretching, one asymmetric stretching and two different deformation bending modes.

### mer-[SnCl<sub>3</sub>Br<sub>3</sub>]<sup>2-</sup> octahedra

Six degrees of vibrational freedom in the Sn-Cl bonds or Sn-Br bonds in the mer-  $[SnCl_4Br_2]^{2-}$  octahedra since the bond structure of the Sn-Cl bonds is the same as the Sn-Br bonds. Take the Sn-Cl bonds as a basic set example, three bonds unchanged were left by the E operator. One bond unchanged was left by the 180° rotation through the axis perpendicular to Cl-Sn-Cl linear bonds. One bond unchanged was left by the vertical plane  $(\sigma_V(xz))$  through the Sn atom but

perpendicular to CI-Sn-CI linear bonds. Three bonds unchanged were left by the reflection by the vertical plane ( $\sigma_V$ '(xy)) through the Sn atom and parallel to the plane formed by three Sn-CI bonds. Two A<sub>1</sub> mode and one B<sub>1</sub> mode formed according to the sum of the row of the characters (E=3, C<sub>2</sub>=1,  $\sigma_V$ (xz)=1 and  $\sigma_V$ '(xy)=3).

#### Optical band gaps

The optical band gaps of samples were used to observe optical properties of compounds. The band gaps were calculated by Tauc plots and Kubelka Munk Function mentioned in section 2.4.2. Tauc plots of samples were plotted as  $[F(R)^*E]^2$  against E(eV) shown in Figure 3.5. Using Tauc method, two tangents are drawn on a Tauc plot of a compound where  $\frac{d[F(R)^*E]^2}{dE}$  is close to zero and where  $\frac{d[F(R)^*E]^2}{dE}$  is close to infinity. By extrapolating a straight line perpendicular to the x axis and crossing the intersection point of the two tangents, a band gap can be determined. For example, the short dash straight line segment indicated that the band gap of  $Cs_2SnCl_6$  is around 4.53 eV on the Tauc plot. This is how to determinate the optical band gaps of all the samples in Figure 3.5.

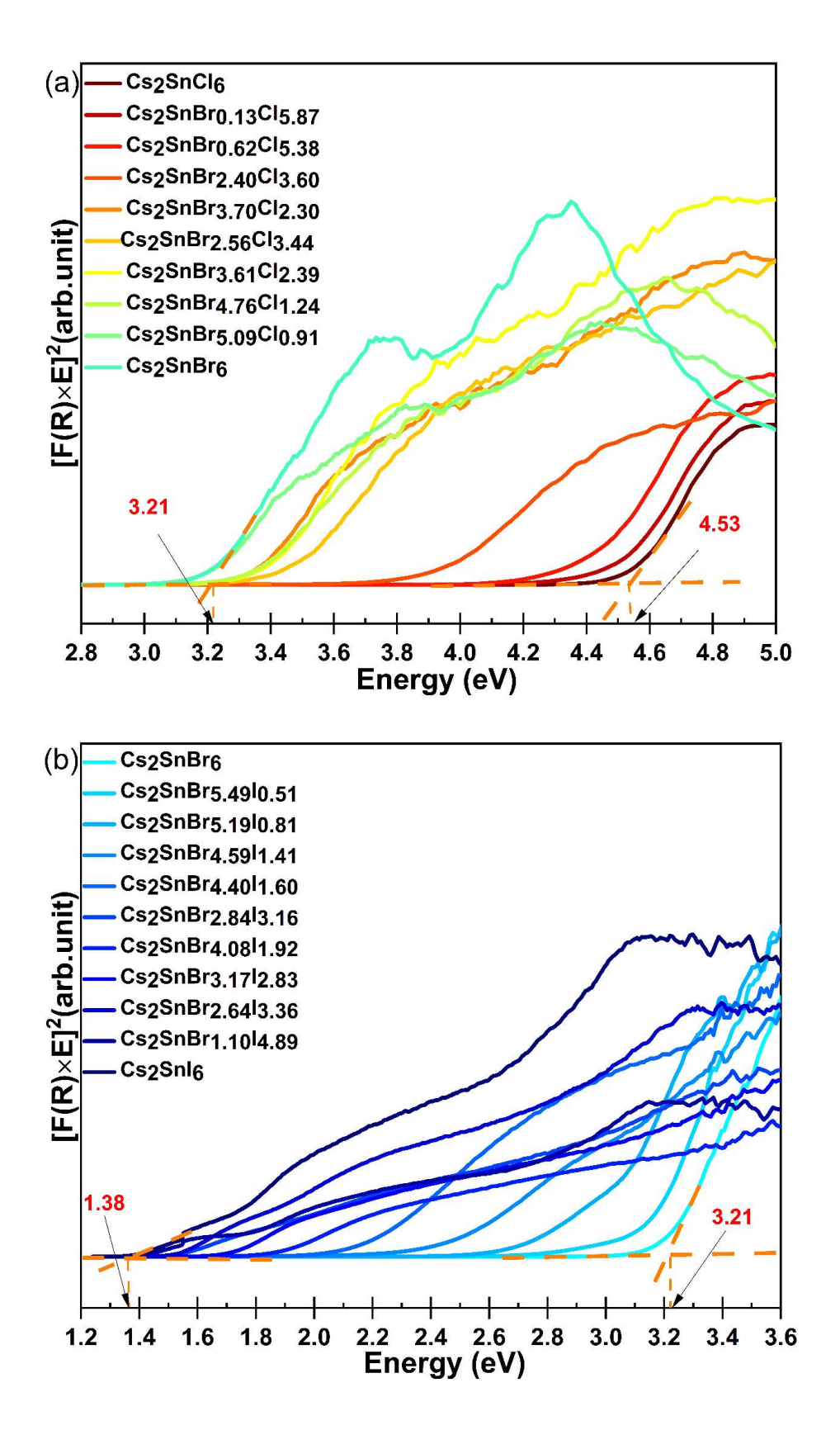


Figure 3.5 Tauc plots of samples in the  $Cs_2SnBr_{6x}Cl_{6-6x}$  series (top) in the graph(a) and in the  $Cs_2SnBr_{6x}l_{6-6x}$  series(bottom) in the graph (b) were shown with their

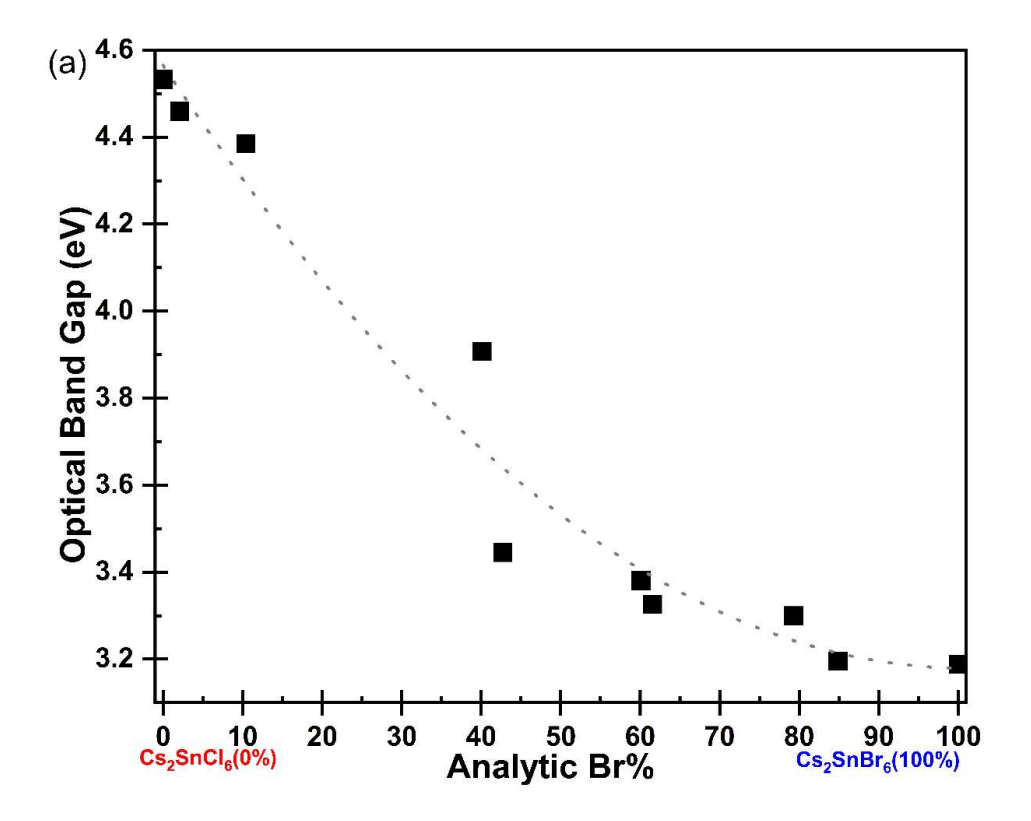
analytical compositions. Band gaps of Cs<sub>2</sub>SnCl<sub>6</sub>, Cs<sub>2</sub>SnBr<sub>6</sub>, and Cs<sub>2</sub>Snl<sub>6</sub> were highlighted in the graph.

The correlation between optical band gaps and analytic bromine percentage of the mixed halide perovskite-like compounds is shown in Figure 3.6. The band gaps of samples decreased as the bromine percentage rises in the Cs<sub>2</sub>SnBr<sub>6x</sub>Cl<sub>6-6x</sub> series. On the contrary, the band gaps of samples in the Cs<sub>2</sub>SnBr<sub>6x</sub>l<sub>6-6x</sub> series increased as the bromine percentage increases.

Therefore, the samples with heavier halide ions produced at room temperature through the solution synthesis have smaller bandgaps. It is related to the electronegativity of halogen elements. The outer shell electrons of the heavier ion such as I<sup>-</sup> in Cs<sub>2</sub>SnI<sub>6</sub> need less energy to excite past the band gap from the valence band to conduction band than that of Cs<sub>2</sub>SnBr<sub>6</sub>. The larger percent of heavier halide ions also cause a drop in the band gaps which is confirmed by the decline trend of the band gaps of samples in the Cs<sub>2</sub>SnBr<sub>6x</sub>Cl<sub>6-6x</sub> series as Br% is increasing shown in Figure 3.6.

Also, bandgaps of Cs<sub>2</sub>SnCl<sub>6</sub>, Cs<sub>2</sub>SnBr<sub>4.25</sub>Cl<sub>1.75</sub>, Cs<sub>2</sub>SnBr<sub>6</sub>, Cs<sub>2</sub>Snl<sub>3.18</sub>Br<sub>2.82</sub> and Cs<sub>2</sub>Snl<sub>6</sub> were highlighted with 4.53 eV, 3.33 eV, 3.21 eV, 1.52 eV and 1.38 eV respectively on the graph. When they were compared with analytic composition of compounds in appendix 6.3 of Compositional analysis, Cs<sub>2</sub>SnBr<sub>4.25</sub>Cl<sub>1.75</sub> (nominal composition: Cs<sub>2</sub>SnCl<sub>3</sub>Br<sub>3</sub>) has a relatively smaller band gap due to the much larger amount of the doped Br in the compound. This also happened to

Cs<sub>2</sub>SnI<sub>3.18</sub>Br<sub>2.82</sub> (nominal composition: Cs<sub>2</sub>SnBr<sub>3</sub>I<sub>3</sub>) due to the slightly larger amount of the doped I in the compounds. Thus, the band gap of Cs<sub>2</sub>Sn Br<sub>4.25</sub>CI<sub>1.75</sub> is closer to that of Cs<sub>2</sub>SnBr<sub>6</sub> instead of Cs<sub>2</sub>SnCl<sub>6</sub> on the graph, and the band gap of Cs<sub>2</sub>SnI<sub>3.18</sub>Br<sub>2.82</sub> is closer to that of Cs<sub>2</sub>SnI<sub>6</sub>. It confirmed the analytic compositions of samples are correct.



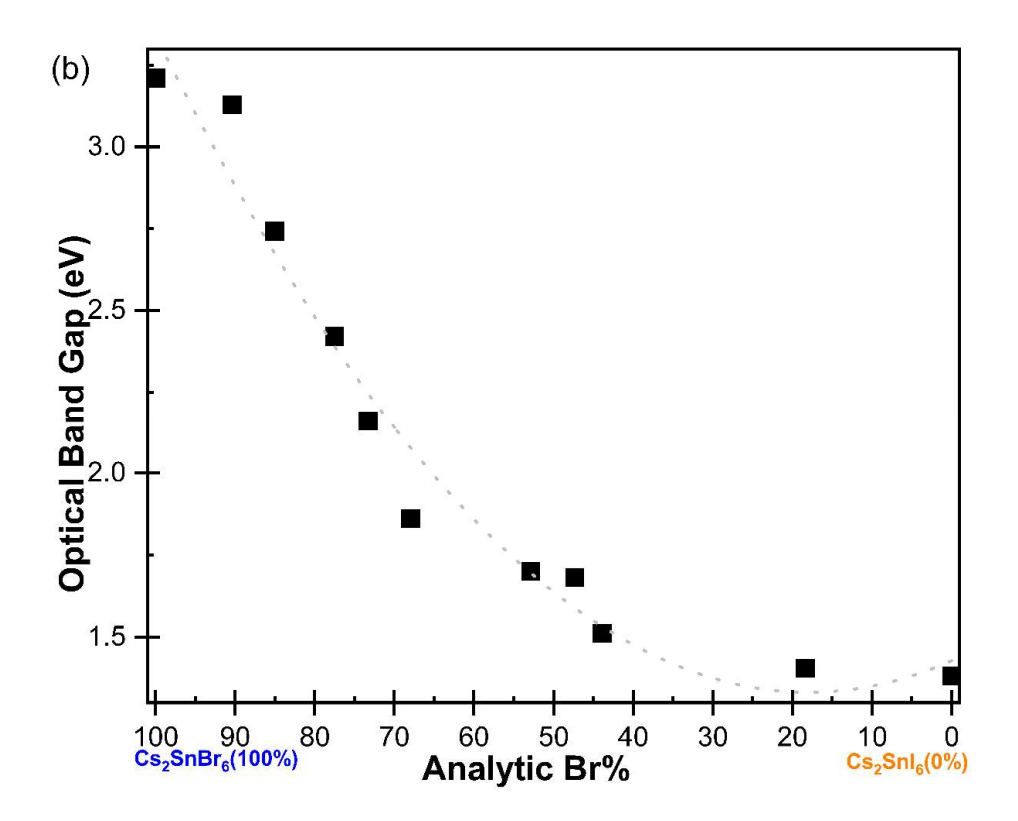


Figure 3.6 (a) The correlation between optical band gaps and analytic Br% of samples in series  $Cs_2SnCl_{6-6x}Br_{6x}$  on the top and (b) the correlation between optical band gaps and analytic Br% of samples in series  $Cs_2Snl_{6-6x}Br_{6x}$  on the bottom were shown above.

### • Thermal stability of pure tin halide perovskites (Cs<sub>2</sub>SnX<sub>6</sub>, X=Cl, Br, or l)

To confirm whether the changes are decomposition or new structure formation, TGA is used to analyse the decomposition points of Cs<sub>2</sub>SnBr<sub>6</sub>, Cs<sub>2</sub>SnCl<sub>6</sub> and the mixed samples of Cs<sub>2</sub>SnBr<sub>6</sub> and Cs<sub>2</sub>SnCl<sub>6</sub>. All the samples are collected and kept in the sample capsules individually at room temperature before TGA testing.

Figure 3.7 below showed the TGA data analysis of pure Cs<sub>2</sub>SnBr<sub>6</sub> perovskite compound. The sample was heated gradually from room temperature to 900°C

in air where the sample was completely decomposed. The results showed that initially the Mass Percentage increased in weight as the sample was heated. However, this is not a result of chemical or physical reaction to the sample but due to the possibility of the Buoyancy Phenomenon or the sensitivity of the balance. When samples were loaded, the balance was still fluctuating. It has no effect on measuring the loss of weight percentage, and the peaks on the first derivative curve of TGA graphs represented the locations of drops in weight percentage on the TGA curve which also indicated the decomposition temperature. The difference in weight percentage was used to identify the suspected decomposition products.

From the TGA data analysis, the data in Figure 3.7 showed that the mass of the sample, Cs<sub>2</sub>SnBr<sub>6</sub>, remained almost constant between 180 °C and 350 °C where the mass percentage of the sample dropped dramatically after 380 °C. Between 180 °C and 350 °C, any fall in mass percentage was the loss of moisture or solvents in the sample. After 350 °C, the dramatic drop in mass percentage showed the decomposition of the sample. After the first drop, the mass percentage of the sample decreased to 49.28 Mass% when the temperature was heated from 350 °C to 500 °C.

Total molecular weight of Cs<sub>2</sub>SnBr<sub>6</sub> is 863.95 g/mol theoretically. There are two Cs atoms account for 30.77 Mass%, one Sn atom account for 13.74 Mass% and six Br atom account for 55.49 Mass%. The melting point of CsBr is 636 °C, and the boiling point of CsBr is 1300 °C. The melting point of SnBr<sub>4</sub> is 31 °C, and the

boiling point of SnBr<sub>4</sub> is 202 °C. Since the melting point and the boiling point of SnBr<sub>4</sub> is low, the chance of SnBr<sub>4</sub> decomposing first is high.

If the loss of Mass% was from SnBr<sub>4</sub>, the loss of Mass% would be 50.73%, and two CsBr molecules remained which account for 49.26 Mass%. This explanation matches the TGA curve of Cs<sub>2</sub>SnBr<sub>6</sub>. Then 6.45% above 100 Mass% at the beginning of the curve was ignored which was caused by sensitive balance of TGA machine. The sample was loaded when the sensitive balance was fluctuating. Also, it matched to XRD data of the mixture of Cs<sub>2</sub>SnBr<sub>6</sub> and Cs<sub>2</sub>SnCl<sub>6</sub> heated to 400°C for 12 hours in Figure 3.13 which was completely decomposed to CsBr. When the temperature was heated to 876°C, the Mass% is zero. Hence, the desired temperature of solid-state synthesis containing Cs<sub>2</sub>SnBr<sub>6</sub> is under 350°C.

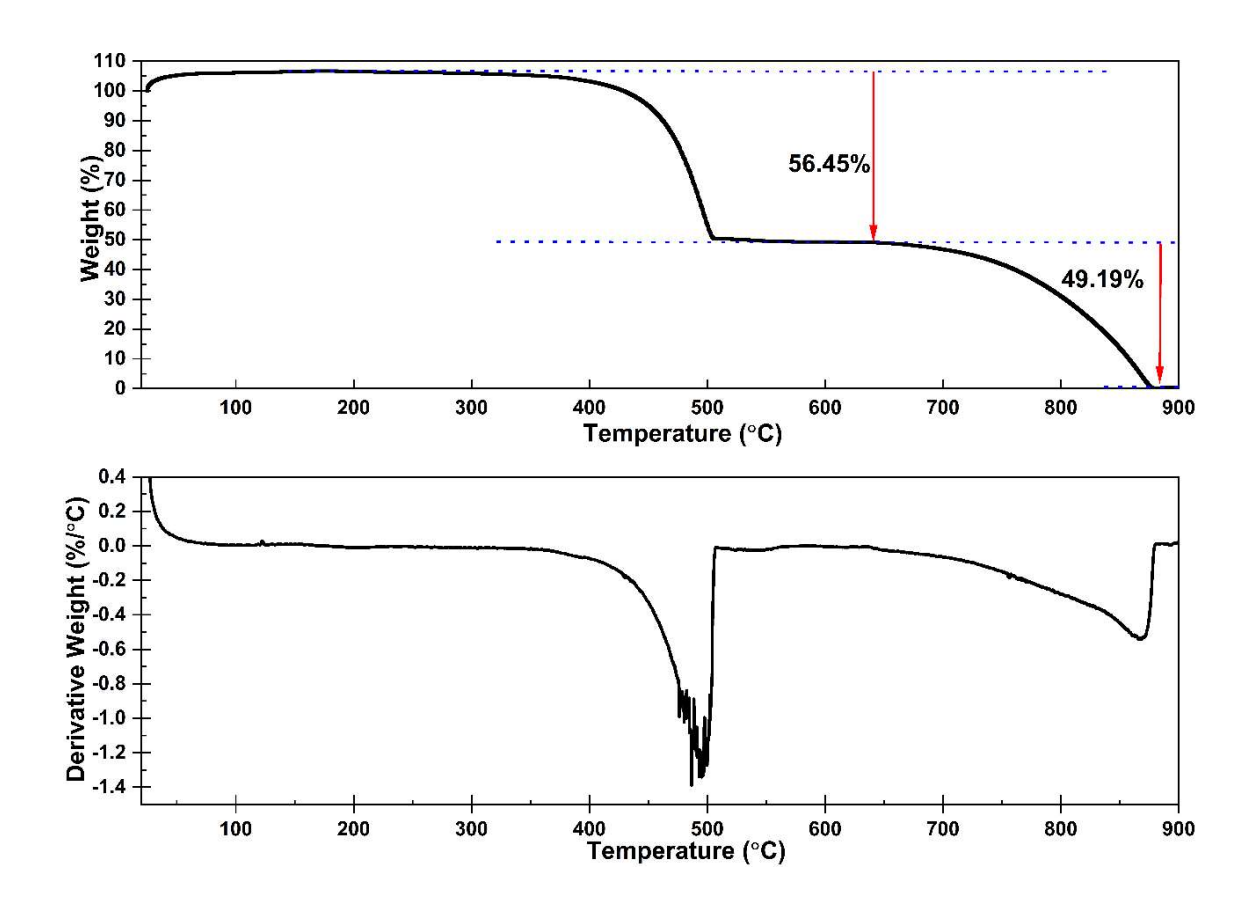


Figure 3.7 TGA data analysis of pure Cs<sub>2</sub>SnBr<sub>6</sub> perovskite compound.

The mass percentage of pure Cs<sub>2</sub>SnCl<sub>6</sub> dropped to about 83.49% when temperature was at 632 °C after the first drop. The first decomposition happened at 620 °C. Here 20.57 Mass% was lost. The second decomposition happened at 771 °C. Here 17.03 Mass% was lost again. The third decomposition happened at 917 °C. Here 39.23 Mass% was lost. At last, 27.52 Mass% remained when temperature was heated to 926°C and above in Figure 3.8.

The total molecular weight of Cs<sub>2</sub>SnCl<sub>6</sub> is 597.24 g/mol. There are two Cs atoms that accounts for 44.51 subtotal Mass%, one Sn atom accounts for 19.88 subtotal Mass% and six Cl atoms accounts for 35.62 subtotal Mass%. The melting point

of CsCl is 645 °C, and the boiling point of CsCl is 1297 °C. The melting point of SnCl<sub>4</sub> is -33 °C, and the boiling point of SnCl<sub>4</sub> is 1300 °C. SnCl<sub>4</sub> is very unstable at high temperature.

The Mass% of CsCl is 28.19% which is close to the remaining Mass% at the end of the experiment. If one CsCl and one Cl<sub>2</sub> were lost during the third decomposition, the total Mass% of one CsCl and one Cl<sub>2</sub> is 39.07% which matches the losses of Mass% from the third decomposition. The loss of the Mass% was around 37.6% when temperature was heated to 783 °C which included the fluctuation of Mass% about 3% at the beginning of the TGA curve caused by the sensitive balance. One Sn with 19.88 Mass% and two Cl with 11.87 Mass% maybe lost from the first decomposition and the second decomposition but this statement cannot be confirmed as the experiment ran in air and oxidations could have happen there. To confirm the calculation with the correct suspected composition products, further XRD analysis about it is required. Hence, the research about the decomposition trend of Cs<sub>2</sub>SnCl<sub>6</sub> to higher temperatures such as 400°C and above would be helpful.

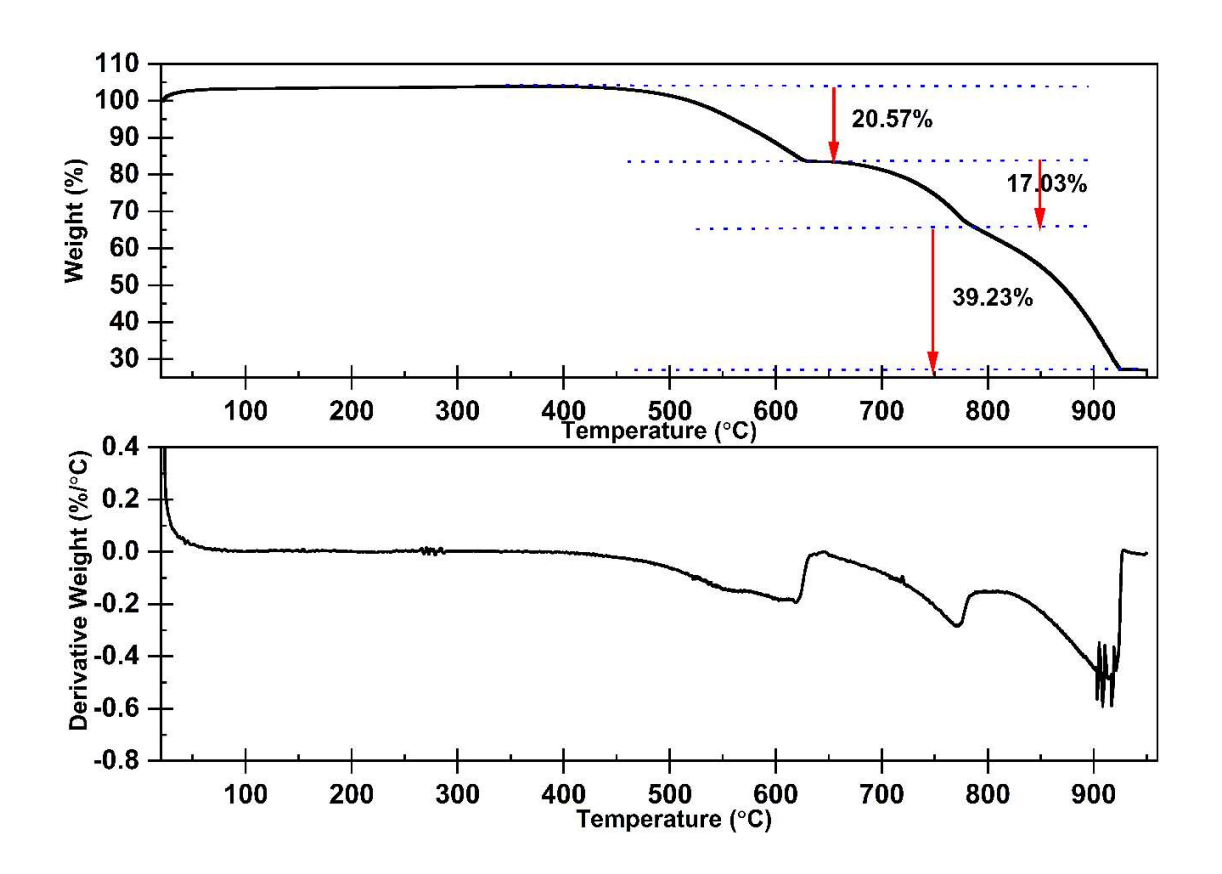


Figure 3.8 TGA data analysis of pure Cs<sub>2</sub>SnCl<sub>6</sub> perovskite compound.

Total molecular weight of Cs<sub>2</sub>Snl<sub>6</sub> is 1145.95 g/mol theoretically. There are two Cs atoms account for 23.20 Mass%, one Sn atom account for 10.36 Mass% and six I atom account for 66.45 Mass%. The melting point of CsI is 620 °C, and the boiling point of CsI is 1277 °C. The melting point of Snl<sub>4</sub> is 143 °C, and the boiling point of Snl<sub>4</sub> is 340 °C. Since the melting point and the boiling point of Snl<sub>4</sub> is low, the chance of Snl<sub>4</sub> decomposing first is high.

The mass percentage of pure Cs<sub>2</sub>SnI<sub>6</sub> started to drop at slightly over 50 °C. There are three tiny peaks in the temperature range between 50 to 200 °C and lost 5.21 Mass%. Then the decomposition happened at around 330-340 °C and lost 41.05

Mass%. If SnI<sub>4</sub> was the product of the decomposition, it accounted for 54.66 Mass% lost which was not in this case. The mass % left behind is around 52 Mass% which may be two CsI with 22.68 Mass% each and one I with 11.07 Mass%. The total deduction is 48 Mass% which is suspected as one SnI<sub>2</sub> and one I. This study requires further experiment of Cs<sub>2</sub>SnI<sub>6</sub> heating up to a higher temperature such as 900 °C to check whether another decomposition happens.

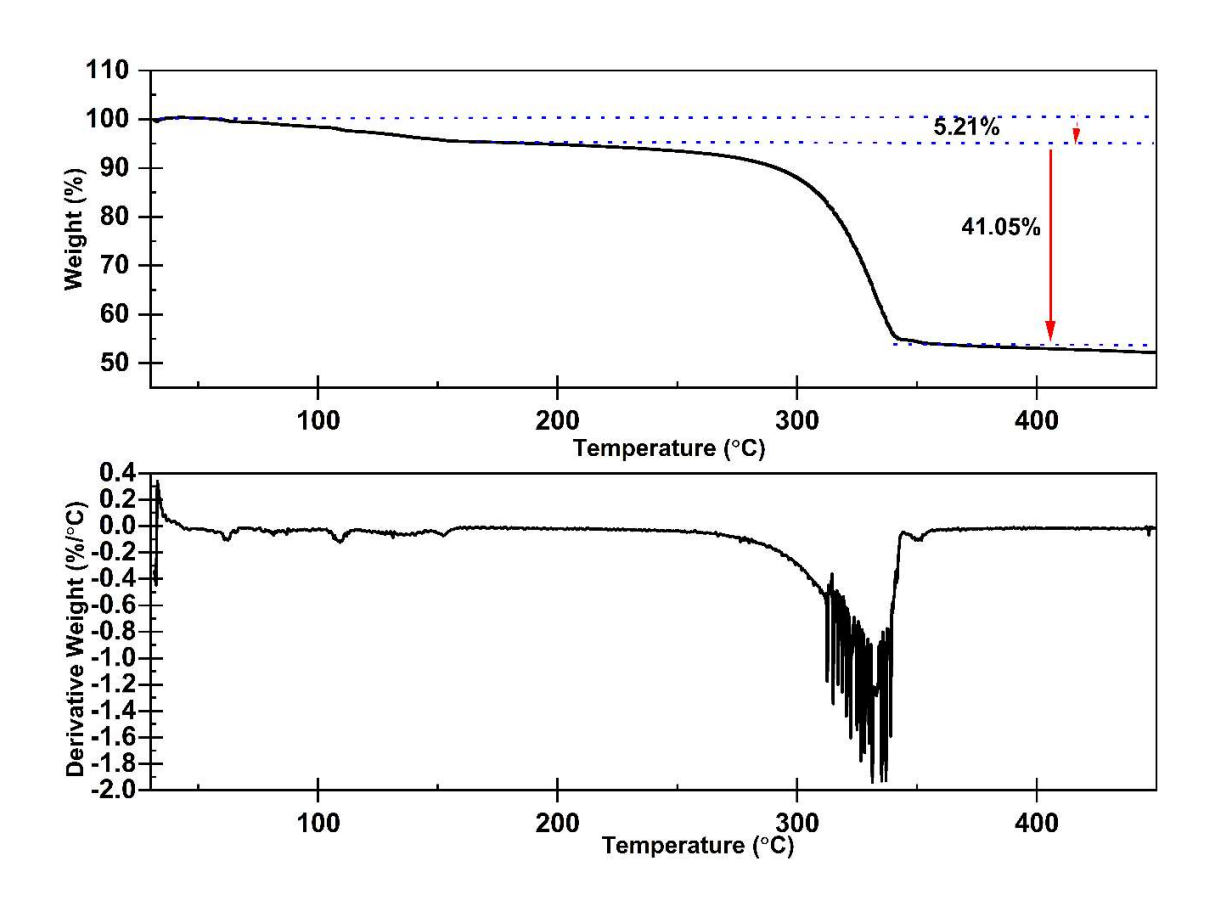


Figure 3.9 TGA data analysis of pure Cs<sub>2</sub>SnI<sub>6</sub> perovskite compound.

# Thermal stability of compounds mixing pure halide perovskites Cs<sub>2</sub>SnBr<sub>6</sub> and Cs<sub>2</sub>SnI<sub>6</sub>

The aim of these experiments is to find out whether Cs<sub>2</sub>SnBr<sub>6</sub> and Cs<sub>2</sub>SnI<sub>6</sub> compounds can react together to form a new structure by high temperatures via solid-state synthesis method. A solid-state synthesis of mixing pure halide Cs<sub>2</sub>SnX<sub>6</sub> compounds was attempted by grinding 0.5g of two different pure halide compounds such as Cs<sub>2</sub>SnCl<sub>6</sub>, Cs<sub>2</sub>SnBr<sub>6</sub> or Cs<sub>2</sub>SnI<sub>6</sub> in a pestle and mortar until the mixtures are evenly mixed fine powders. (Cs<sub>2</sub>SnCl<sub>6</sub>, Cs<sub>2</sub>SnBr<sub>6</sub> and Cs<sub>2</sub>SnI<sub>6</sub> were made via a solution-phase synthesis.) The mixtures were inserted into the bottom of a quartz tube through a glass thistle tube funnel. The tube was held by a clamp stand inside a modular vertical tube furnace in the fume hood. For example, pure halide compounds, Cs<sub>2</sub>SnBr<sub>6</sub> (0.5g, 0.58mmol) and Cs<sub>2</sub>SnI<sub>6</sub> (0.5g, 0.44mmol), were grinded for 15 minutes and heating up to desired high temperatures. This step was repeated so each 1g of the mixtures was heated to 200°C, 250°C, 300°C and 400°C individually.

The heating experiments were tried at different temperatures and times. For example, the mixture sample (collected at room temperature (RT)) had been heated at 200 °C for 12 hours. Then a similar experiment was repeatedly conducted on another collected mixture sample at RT from the same batch at 250 °C for 12 hours. XRD patterns of Cs<sub>2</sub>SnBr<sub>6</sub> (SpS) and Cs<sub>2</sub>SnI<sub>6</sub> (SpS) are used as counterparts to check if the structure of pure halide perovskite compounds can be mixed by the solid-state synthesis method.

The XRD patterns of a 50:50 wt% mixture of Cs<sub>2</sub>SnBr<sub>6</sub> and Cs<sub>2</sub>SnI<sub>6</sub> appear as a sum of that of the pure halide compounds Cs<sub>2</sub>SnBr<sub>6</sub> and Cs<sub>2</sub>SnI<sub>6</sub> at room temperature (T=25 °C) and 200 °C in Figure 3.10. Suddenly the XRD pattern changed dramatically after heating to 250 °C for 12 hours; two most intense peaks with from the XRD patterns of Cs<sub>2</sub>SnI<sub>6</sub> with Miller Indices, (222) and (400), disappeared. The samples of mixing Cs<sub>2</sub>SnBr<sub>6</sub> and Cs<sub>2</sub>SnI<sub>6</sub> which was heated to 300°C or 400°C for 12 hours individually formed a new structure. However, it was not certain the sample was decomposing until it was compared with the ICSD database in Figure 3.11.

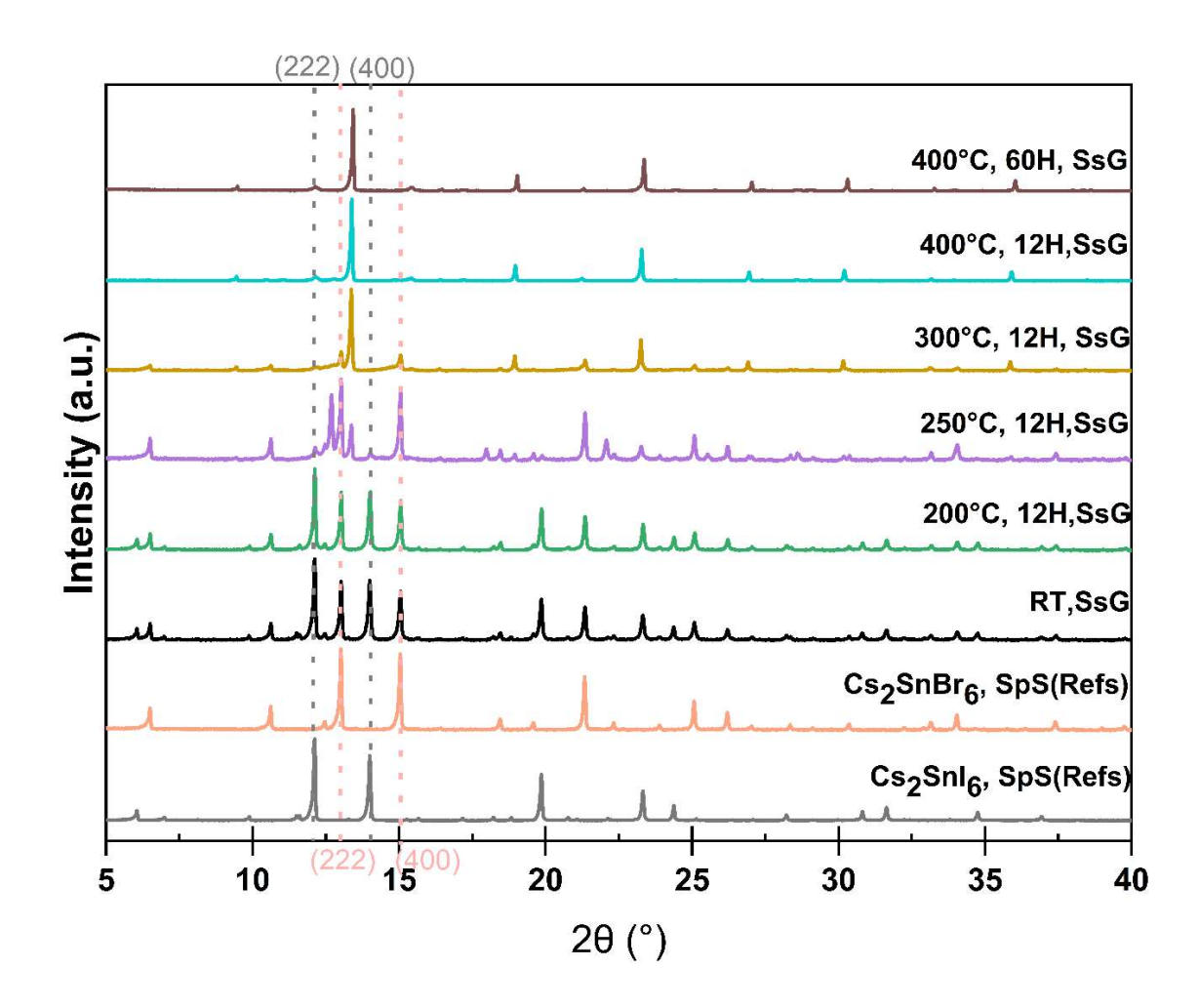


Figure 3.10 The XRD patterns of the mixed samples of pure 0.5g Cs<sub>2</sub>SnBr<sub>6</sub> (SpS) and pure 0.5g Cs<sub>2</sub>SnI<sub>6</sub> (SpS) at room temperature and at high temperatures shown above.

The new formed structure from the XRD patterns in Figure 3.11 are compared with the XRD patterns of Csl<sup>109</sup> and CsBr<sup>110</sup>exported from Inorganic Chemical Service Database (ICSD). The XRD pattern of Csl was matched to the XRD pattern of the mixed sample of Cs<sub>2</sub>SnBr<sub>6</sub> and Cs<sub>2</sub>SnI<sub>6</sub> made by solid-state synthesis heating to 250 °C for 12 hours.

The XRD pattern of CsBr was matched to the XRD pattern of two mixed samples of Cs<sub>2</sub>SnBr<sub>6</sub> and Cs<sub>2</sub>SnI<sub>6</sub> made by solid-state synthesis heating to 300°C and 400 °C for 12 hours individually. Hence, those mixed samples of 0.5g Cs<sub>2</sub>SnBr<sub>6</sub> and 0.5g Cs<sub>2</sub>SnI<sub>6</sub> were decomposing to CsI at 250 °C but iodine was easily evaporated from the quartz tube via the dynamic vacuum system. Without iodine, the remained sample was CsBr in the quartz tube when samples were heated to 300°C with a little amount CsI barely seen at 2θ= 12.6°. At 400°C, the mixed sample was completely decomposed to CsBr which was confirmed by the matching PXRD patterns of Sample (400°C,12H, SsG= the mixture of pure Cs<sub>2</sub>SnBr<sub>6</sub> and pure Cs<sub>2</sub>SnI<sub>6</sub> heated at 400 °C for 12 hours) and CsBr<sup>110</sup> from ICSD database. In Table 3.2, there is a table that summarises the phases existed in the different mixed samples which those samples were heated to 200-400 °C for 12 hours individually.

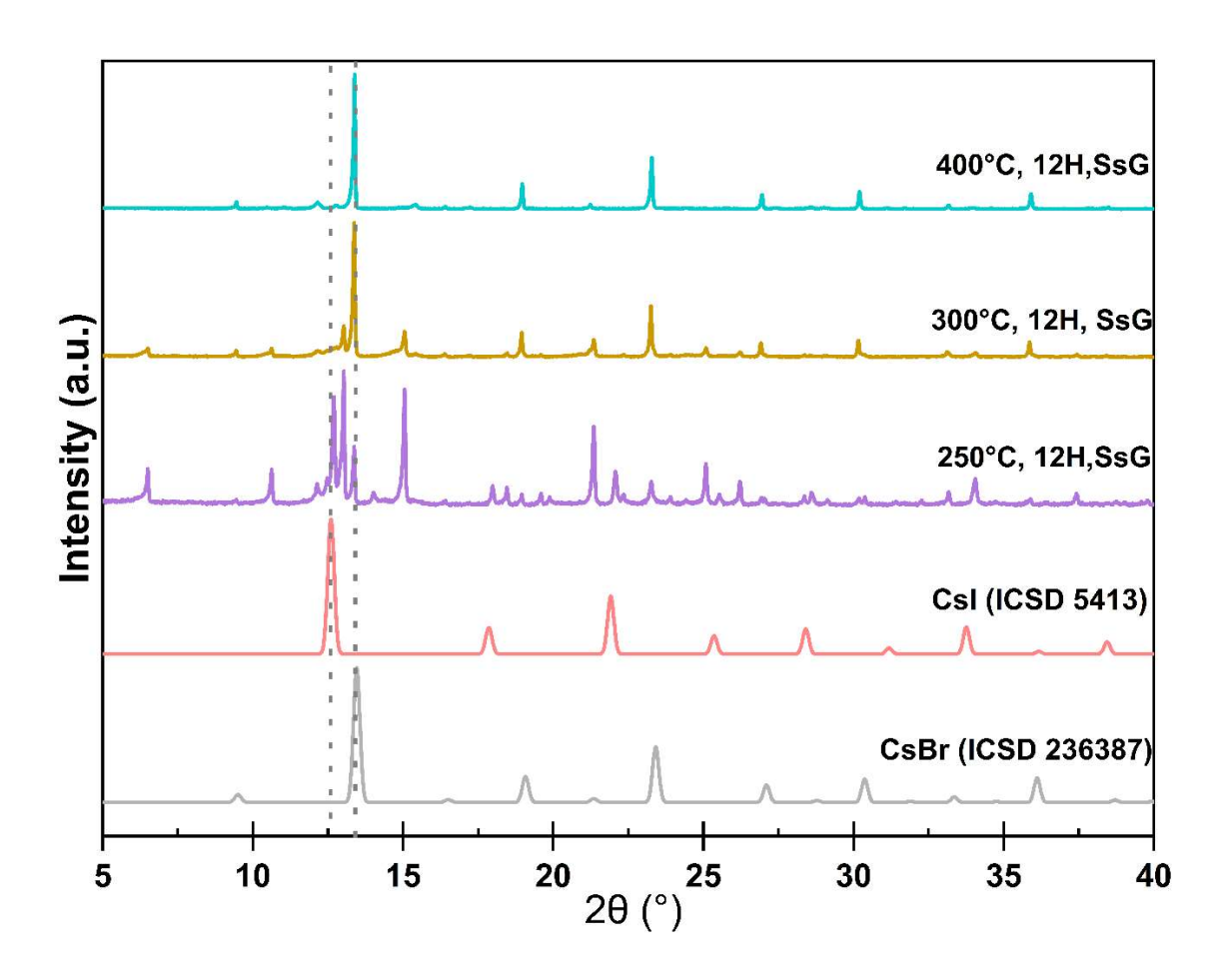


Figure 3.11 The XRD patterns of samples mixing Cs<sub>2</sub>SnBr<sub>6</sub> and Cs<sub>2</sub>SnI<sub>6</sub> at 250°C, 300°C and 400°C individually for 12 hours which were compared with XRD patterns of CsBr<sup>110</sup> and CsCl<sup>111</sup> from ICSD database.

Temperature/°C	Phases present from XRD
25 (RT)	Cs <sub>2</sub> SnI <sub>6</sub> + Cs <sub>2</sub> SnBr <sub>6</sub>
200	Cs <sub>2</sub> SnI <sub>6</sub> + Cs <sub>2</sub> SnBr <sub>6</sub>
250	Cs <sub>2</sub> SnBr <sub>6</sub> + CsI
300	Cs <sub>2</sub> SnBr <sub>6</sub> + CsI + CsBr
400	CsBr

Table 3.2 The list of phases presented in the mixed samples (Cs<sub>2</sub>SnBr<sub>6</sub> + Cs<sub>2</sub>SnI<sub>6</sub>) heated to different temperatures.

Raman spectra of pure halide compounds, Cs<sub>2</sub>SnBr<sub>6</sub> and Cs<sub>2</sub>Snl<sub>6</sub> can help the study of Raman peaks as vibrations of isolated [SnX<sub>6</sub>]<sup>2-</sup> octahedra with either only six Br<sup>-</sup> ions or six l<sup>-</sup>ions.<sup>112</sup> The Raman spectrum of Cs<sub>2</sub>SnBr<sub>6</sub> showed that pure isolated [SnBr<sub>6</sub>]<sup>2-</sup> octahedra vibrated when they encountered laser light incidents and caused scatted light at three different wavelengths with different vibration intensities. The spectrum of Cs<sub>2</sub>Snl<sub>6</sub> showed pure isolated [Snl<sub>6</sub>]<sup>2-</sup> octahedra vibrated at three lower wavenumbers compared to the spectrum of Cs<sub>2</sub>SnBr<sub>6</sub>. Thus, the spectrum of the mixture of Cs<sub>2</sub>SnBr<sub>6</sub> (0.5 g) and Cs<sub>2</sub>Snl<sub>6</sub> (0.5 g) has vibrations of only pure halide octahedra such as [SnBr<sub>6</sub>]<sup>2-</sup> and [Snl<sub>6</sub>]<sup>2-</sup> in Figure 3.12.

When the mixture of  $Cs_2SnBr_6$  (0.5 g) and  $Cs_2SnI_6$  (0.5 g) was heated to 300°C from room temperature, the Raman spectra included a lot of features in the Raman shift range between 100 to 200 cm<sup>-1</sup>. It can be interpreted as the vibrations of different isolated  $[SnX_6]^{2-}$  octahedra types with variable halide compositions.<sup>113</sup> It also means the pure halide octahedra structure changed at 300°C.

When the mixture of Cs<sub>2</sub>SnBr<sub>6</sub> (0.5g) and Cs<sub>2</sub>SnI<sub>6</sub> (0.5g) was heated to 250°C, there is a Raman peak formed when Raman shift is around 125 cm<sup>-1</sup> which also means different isolated octahedra types formed and caused different a vibration intensity at the wavenumber around 125 cm<sup>-1</sup>. It also matched with the XRD data of this mixed sample heated to 250°C which indicated phase changes on the pattern. The newly firmed peak indicated I<sup>-</sup> ions tried to mix in the pure octahedral structure as two Raman peaks around 125 cm<sup>-1</sup> like the smaller versions of the

peaks on Raman spectra of Cs<sub>2</sub>SnBr<sub>3</sub>I<sub>3</sub> (nominal composition). This means the isolated [SnBr<sub>3</sub>I<sub>3</sub>]<sup>2-</sup> octahedra types might appear here. However, the XRD pattern of the mixture of Cs<sub>2</sub>SnBr<sub>6</sub> (0.5 g) and Cs<sub>2</sub>SnI<sub>6</sub> (0.5 g) heated to 200°C was same as the one at room temperature when the Raman peak formed around 125 cm<sup>-1</sup>. It indicated early stages of mixing I<sup>-</sup> ions into the pure octahedral structure, [SnBr<sub>6</sub>]<sup>2-</sup>, would not cause a phase change.

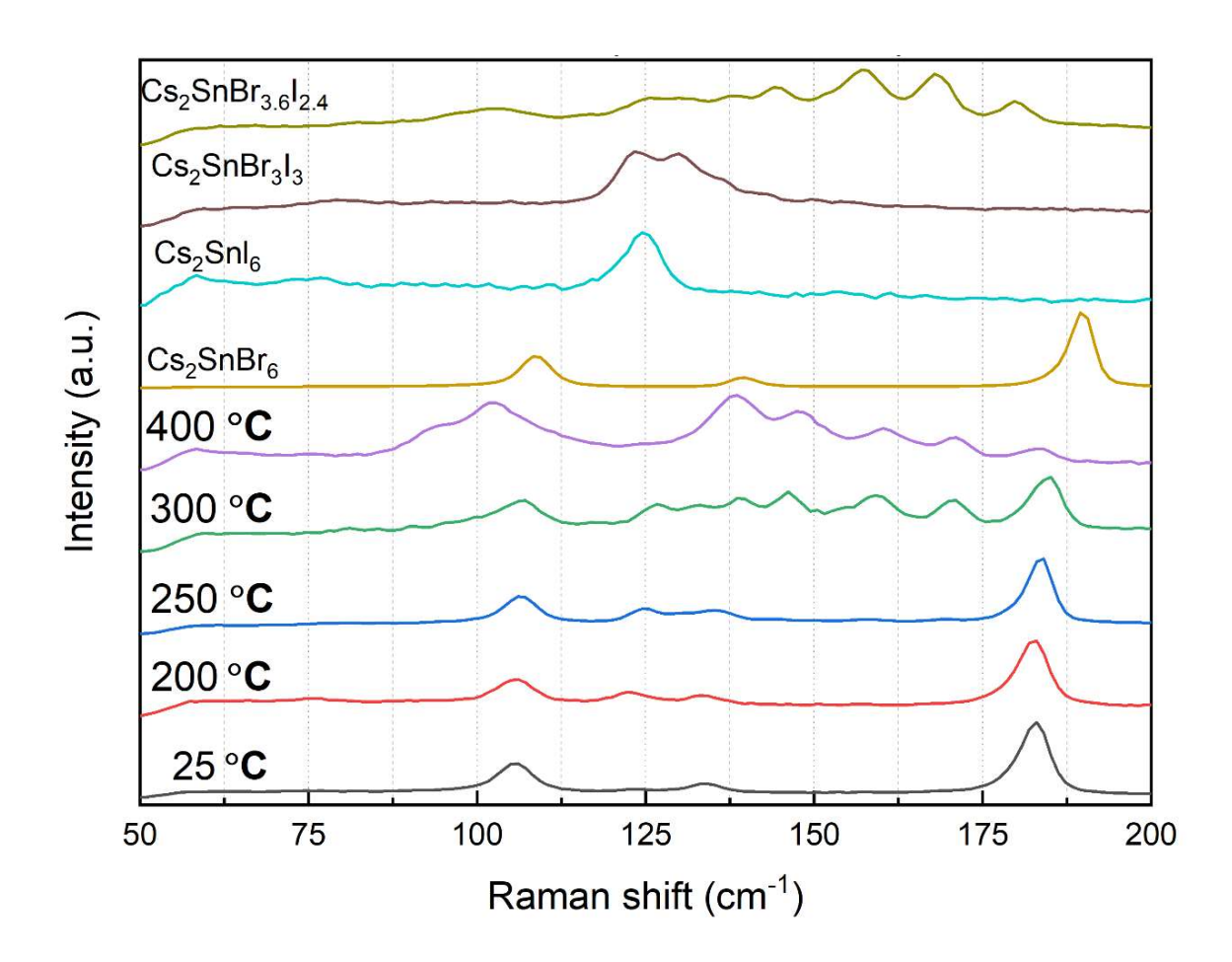


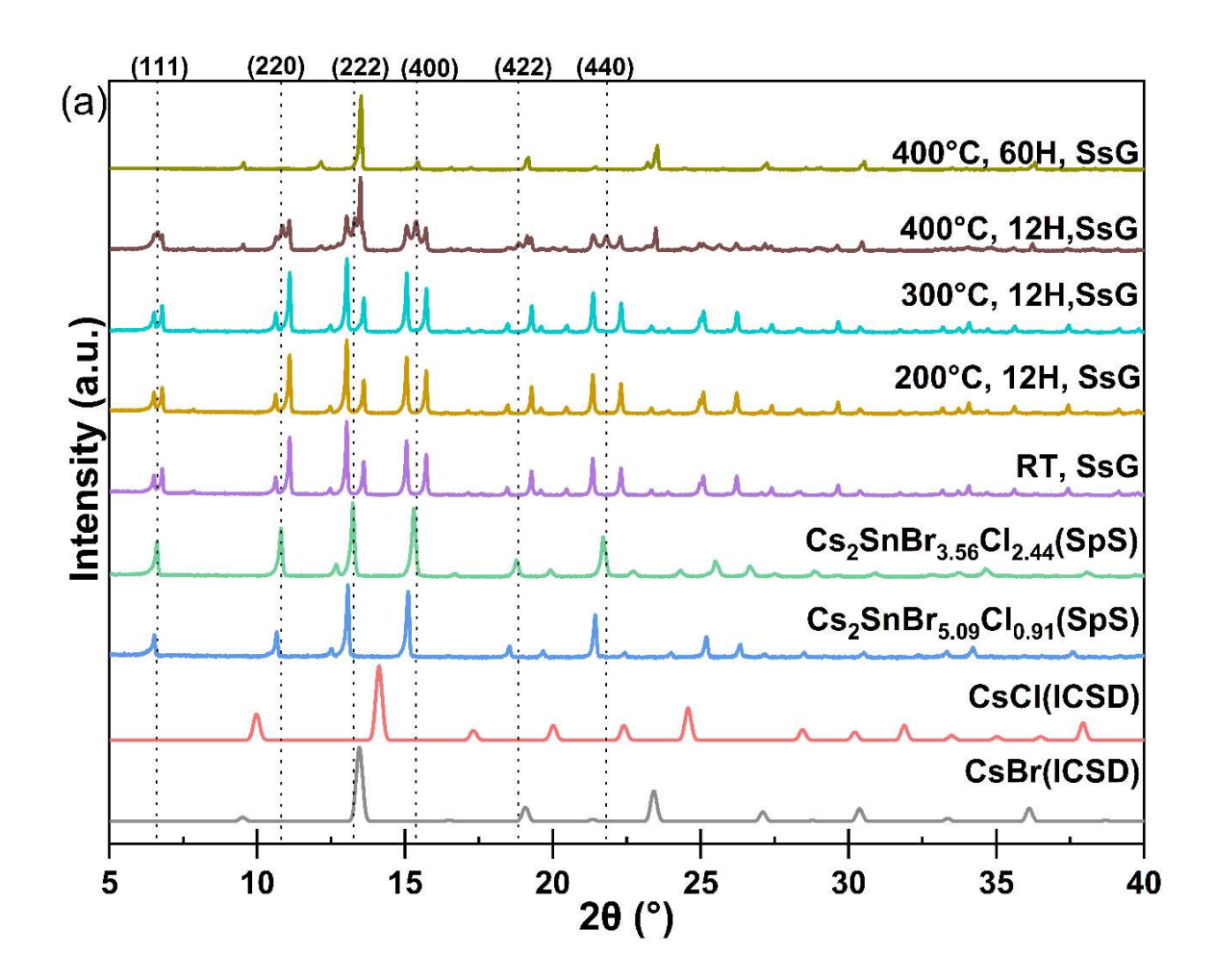
Figure 3.12 The Raman spectra of the mixed sample consisting of  $0.5g \, \text{Cs}_2 \text{SnBr}_6$  and  $0.5g \, \text{Cs}_2 \text{SnI}_6$  at the different temperatures are shown here. (The Raman spectra of  $\text{Cs}_2 \text{SnI}_6$ ,  $\text{Cs}_2 \text{SnBr}_3 \text{I}_3$  and  $\text{Cs}_2 \text{SnBr}_{3.6} \text{I}_{2.4}$  made via SpS were used as counterparts).

# Thermal stability of compounds mixing pure halide perovskites Cs<sub>2</sub>SnBr<sub>6</sub> and Cs<sub>2</sub>SnCl<sub>6</sub>

Cs<sub>2</sub>SnBr<sub>6</sub>(0.5 g) and Cs<sub>2</sub>SnCl<sub>6</sub>(0.5 g) were mixed evenly for 15 minutes. The mixed samples Cs<sub>2</sub>SnBr<sub>6</sub> and Cs<sub>2</sub>SnCl<sub>6</sub> are heated to 200 °C, 300 °C and 400 °C individually. The heating experiments was attempted at different temperatures and times. For example, the mixture sample (collected at RT) had been heated at 200 °C for 12 hours. Then a similar experiment was repeatedly conducted on another collected mixture sample at RT from the same batch at 300 °C for 12 hours.

When the mixed compound was heated to 200 °C and 300 °C for 12 hours respectively from room temperature, the XRD patterns of mixed samples heated to 200 °C and heated to 300 °C individually were unchanged from the initial mixture before heating, which is shown in Figure 3.13 below. However, the XRD pattern of the mixed sample heated to 400 °C for 12 hours showed clear changes which indicated the mixed halide defect-ordered perovskite material was formed and alike to sample Cs<sub>2</sub>SnBr<sub>3.56</sub>Cl<sub>2.44</sub>(SpS). At 20= 5- 15°, three Braggs peaks from XRD pattern of the mixed sample of pure Cs<sub>2</sub>SnBr<sub>6</sub> and pure Cs<sub>2</sub>SnCl<sub>6</sub> by made via HTSsG at 400 °C were roughly matched to that of sample Cs<sub>2</sub>SnBr<sub>3.56</sub>Cl<sub>2.44</sub>(SpS). The PXRD pattern of sample Cs<sub>2</sub>SnBr<sub>3.56</sub>Cl<sub>2.44</sub>(SpS) was also mentioned in Figure 3.13 as the counterpart. Hence, mixed halides sample of pure Cs<sub>2</sub>SnBr<sub>6</sub> and pure Cs<sub>2</sub>SnCl<sub>6</sub> made via HTSsG at 400 °C formed mixed halide double perovskites which was matched to the phase structure of sample

Cs<sub>2</sub>SnBr<sub>3.56</sub>Cl<sub>2.44</sub>(SpS). However, the decomposition also happened slowly, and a small amount of CsBr formed with tiny Braggs peaks. No CsCl was seen in the XRD patterns in Figure 3.13.



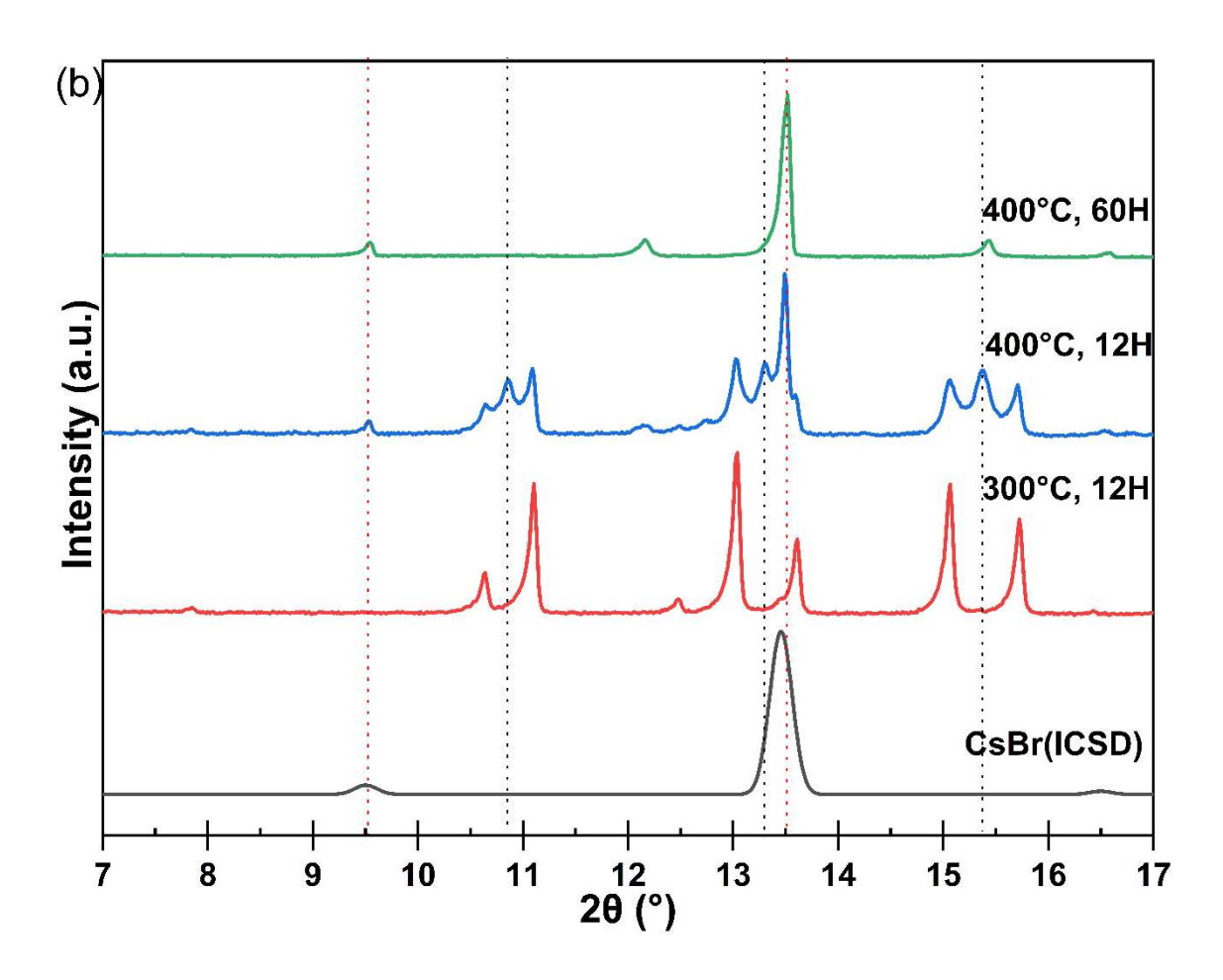


Figure 3.13(a)The XRD patterns of the mixed samples of pure 0.5g Cs<sub>2</sub>SnBr<sub>6</sub> (SpS) and pure 0.5g Cs<sub>2</sub>SnCl<sub>6</sub> (SpS) at room temperature and at high temperatures shown above on the top. XRD patterns of Sample Cs<sub>2</sub>SnBr<sub>3.55</sub>Cl<sub>2.45</sub>(SpS) and XRD patterns of CsBr<sup>110</sup> and CsCl<sup>111</sup> from ICSD database are counterparts. (b)The enlarged area of the XRD patterns of the mixed samples of pure 0.5g Cs<sub>2</sub>SnBr<sub>6</sub> (SpS) and pure 0.5g Cs<sub>2</sub>SnCl<sub>6</sub> (SpS) at 300  $^{\circ}$ C and 400  $^{\circ}$ C at the bottom.

As the decomposition of the mixture, Cs<sub>2</sub>SnBr<sub>6</sub> and Cs<sub>2</sub>SnCl<sub>6</sub>, at high temperatures mentioned above, the mixed sample of Cs<sub>2</sub>SnBr<sub>6</sub> and Cs<sub>2</sub>SnCl<sub>6</sub> might be decomposing to CsBr or CsCl. To confirm it, the XRD pattern of the mixed sample heated to 400°C for 60 hours were compared to the XRD patterns

of CsBr<sup>110</sup> and CsCl<sup>111</sup> exported from ICSD. The mixed sample of Cs<sub>2</sub>SnBr<sub>6</sub>(0.5 g) and Cs<sub>2</sub>SnCl<sub>6</sub>(0.5 g) heated to 400°C for 60 hours was decomposed into CsBr. In the Table 3.2, there is a table that summarises the phases existed in the different mixed samples which those samples were heated to 200-400 °C for 12 hours individually.

Temperature/°C	Phases present from XRD
25(RT)	Cs <sub>2</sub> SnCl <sub>6</sub> + Cs <sub>2</sub> SnBr <sub>6</sub>
300(12h)	Cs <sub>2</sub> SnCl <sub>6</sub> + Cs <sub>2</sub> SnBr <sub>6</sub>
400 (12h)	$Cs_2SnCl_6 + Cs_2SnBr_{3.55}Cl_{2.45} + Cs_2SnBr_6 + CsBr$
400 (60h)	CsBr

Table 3.3 The list of phases presented in the mixed samples (Cs<sub>2</sub>SnBr<sub>6</sub> + Cs<sub>2</sub>SnCl<sub>6</sub>) heated to different temperatures and times.

The mixed samples of 0.5g Cs<sub>2</sub>SnBr<sub>6</sub> and 0.5g Cs<sub>2</sub>SnCl<sub>6</sub> at room temperature have the same spectrum as the ones heated to 200°C and 300°C for 12 hours individually. XRD patterns of those samples also stayed the same as the one made at room temperature. The Raman spectra of the mixture (0.5g Cs<sub>2</sub>SnBr<sub>6</sub> and 0.5g Cs<sub>2</sub>SnCl<sub>6</sub>) at room temperature (assumed 25°C), 200°C and 300°C looked like the coexisted Raman spectra of pure halide compounds, Cs<sub>2</sub>SnCl<sub>6</sub> and Cs<sub>2</sub>SnBr<sub>6</sub>. At the Raman spectrum of the mixed sample heated to 400°C in Figure 3.14, a small peak was formed at around 193.64 cm<sup>-1</sup> which was matched to the same peak from Cs<sub>2</sub>SnBr<sub>5.09</sub>Cl<sub>0.91</sub>. However, XRD pattern of this sample showed new formed Braggs peaks matching to that of Cs<sub>2</sub>Br<sub>3.55</sub>Cl<sub>2.45</sub> with in a

very small intensity. This is an interesting fact. A small amount of CI was doped in Cs<sub>2</sub>SnBr<sub>6</sub> but the types of mixed halide octahedra structure involved in this sample are different to the types of octahedra involved in Cs<sub>2</sub>Br<sub>3.55</sub>Cl<sub>2.45</sub> according to the difference in Raman spectra. The Raman spectrum of the mixed sample heated to 400°C in Figure 3.14 are not matched to the Raman spectrum of Cs<sub>2</sub>Br<sub>3.55</sub>Cl<sub>2.45</sub> in Figure 3.4(c). Hence, the same general phase structure did not exist the same types of octahedra structures if they were made by different synthesises.

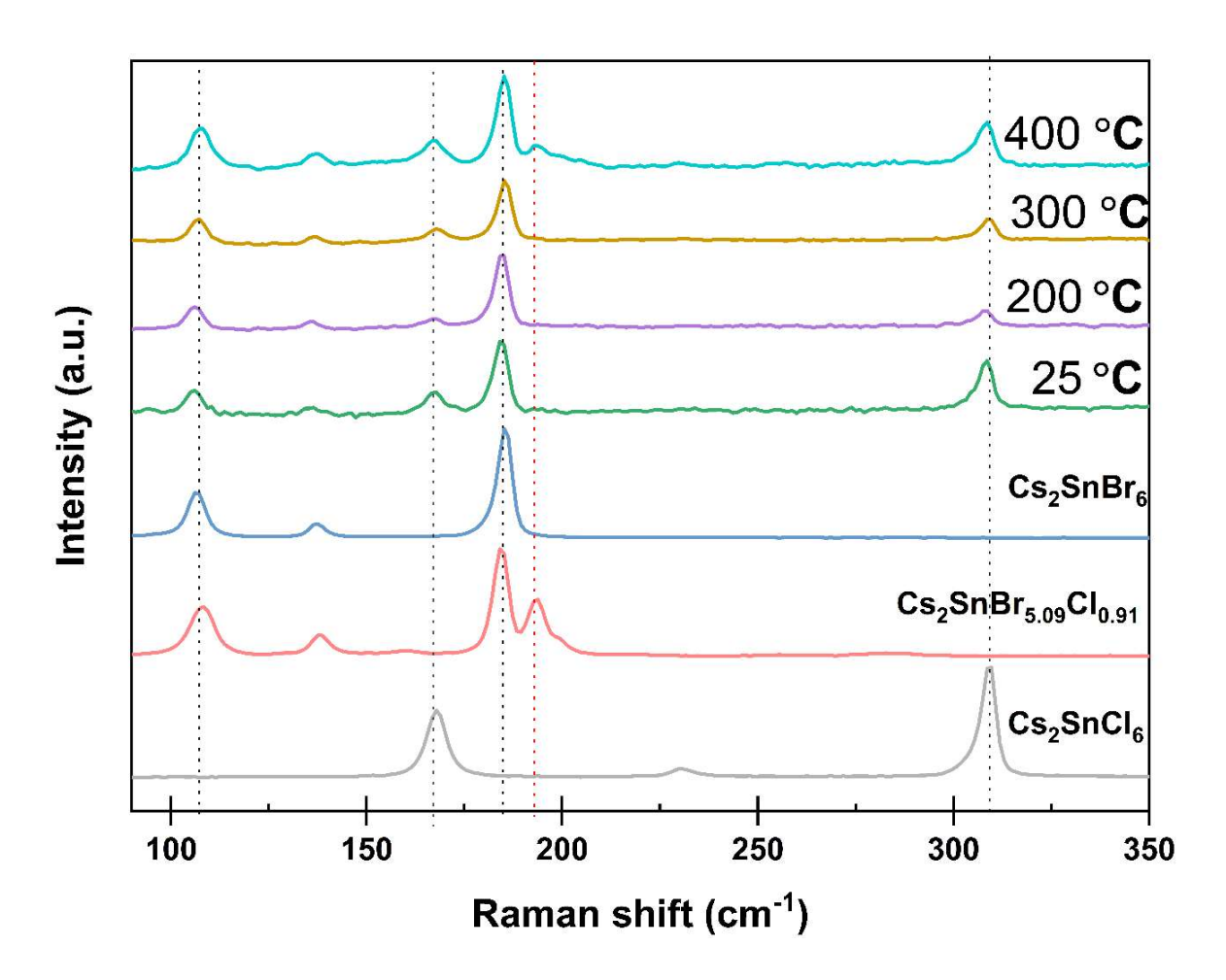


Figure 3.14 The Raman patterns of the mixed sample consisting of 0.5g Cs<sub>2</sub>SnBr<sub>6</sub> and 0.5g Cs<sub>2</sub>SnCl<sub>6</sub> at different temperatures for 12 hours are shown here. Raman spectra of Cs<sub>2</sub>SnCl<sub>6</sub> (SpS), Cs<sub>2</sub>SnCl<sub>5.09</sub>Br<sub>0.91</sub> (SpS) and Cs<sub>2</sub>SnBr<sub>6</sub> (SpS) were used as counterparts.

### 3.1.3 Conclusion

X-site mixing is the focus of the research here. It is useful for tuning optical properties of samples such as band gaps by partially substituting light halide ions with heavier halide ions. The correlation between the band gap and the bromide percentage retrieved from the analysis is in a bowing shape which are shown in figure 3.6 and 3.17, and this is called the band bowing effect.

The bandgap takes on a bowing shape for two reasons. First, it is caused by symmetry forbidden transitions. Electrons are excited from the lower energy state of the valence band instead of the maximum energy state of the valence band. Second, it is caused by hybrid energy states of the valence band of compound such as Cs<sub>2</sub>SnBrCl<sub>5</sub> comparing to the pure Cs<sub>2</sub>SnCl<sub>6</sub>. A little amount of bromine doping into Cs<sub>2</sub>SnCl<sub>6</sub> can cause a huge drop of the band gap as electrons can be excited from the highest energy state offered by Br 4p orbital in the valence band into the same conduction band (consisting of Sn 5p orbital). A little asymmetry of the lattice structure allows the electrons to excite from the maximum of this hybrid energy state of valence band.

The band gaps are decreasing from Cs<sub>2</sub>SnCl<sub>6</sub> to Cs<sub>2</sub>SnBr<sub>6</sub> to Cs<sub>2</sub>Snl<sub>6</sub>. It is affected by the electronegativity of halogen group. The electronegativity of halogens decreases going down Group 17 in the periodic table. The valence band was consisted of electrons in Cl 3p orbital, Br 4p orbital, or I 5p orbital. It caused the band gaps to get narrower from Cs<sub>2</sub>SnCl<sub>6</sub> to Cs<sub>2</sub>SnBr<sub>6</sub> to Cs<sub>2</sub>Snl<sub>6</sub> in the band

structure as the conduction only is consisted of electrons in Sn 5p orbital in this case.

A good band gap can offer an effective light absorber compound for solar cell industry. The molar ratio of different halide ions is the key point to master the accuracy of desired band gaps such as the optimal band gap, 1.34 eV, for single p-n junction solar cell. It can also modulate the lattice structure. However, the options for effective partial substitutions of halide ions are limited to Cl, Br, and I from Group 17 from the periodic table.

Moreover, all double vacancy ordered perovskites produced in Chapter 3.1 are cubic structure only containing lattice parameters a, V (a=b=c, and alpha=beta=gamma=90°). As such refinement is not necessary as any doping into a cubic unit cell will result in expansion or contraction in the one length-based parameter, a. One of the attempts made in the thesis was to confirm if calculations of lattice parameters using 20 values from the different Bragg reflections is accurate, this was additionally discussed by considering the standard deviations of unit cell volume for each sample. Extra precursor phases have been identified using simulated pattern comparison, this has been added into the discussion using patterns for compounds obtained from the ICSD in Figure 3.2.

The thermal ability study of pure halide materials such as Cs<sub>2</sub>SnX<sub>6</sub>(X=Cl, Br, or l) can help understand the decomposition processes in TGA graphs. These graphs

indicated a plot of the change of Mass% versus temperature. This was used to predict the possible suspected decomposition products. This information was helpful for the research of mixing pure halide materials via High temperature solid-state grinding synthesis (HTSsG). This method can also form mixed halide compound such as the mixed sample heating to 400 °C for 12 hours mentioned in Table 3.3. Although HTSsG method can produce mixed halides (CI and Br) perovskites with the same phase structure in Figure 3.13, the local mixed halides octahedra are different to the sample made by SpS shown in Figure 3.14. Hence, it needs further study to determine the cause and how to use this interesting fact to improve the properties of compounds for industrial applications.

The research of the mixed halide materials via two different synthesis methods such as Solution-phased synthesis (SpS) and High temperature solid-state grinding method (HTSsG) expanded the knowledge of different production methods to produce this type of mixed halides materials. The characterisation study in Section 3.1 also provided the knowledge of tuning band gaps by mixing halides at a certain ratio which change the structure size, electronic properties, and light absorption properties. This can help further research in the field to produce light absorbers with better performances.

# 3.2 A<sub>2</sub>SnCl<sub>6-6x</sub>Br<sub>6x</sub> series with different A-site ions (A=Cs<sup>+</sup>, CH<sub>3</sub>NH<sub>3</sub><sup>+</sup>, CH<sub>3</sub>CH<sub>2</sub>NH<sub>3</sub><sup>+</sup>)

Samples of (CH<sub>3</sub>CH<sub>2</sub>NH<sub>3</sub>)<sub>2</sub>SnCl<sub>6-6x</sub>Br<sub>6x</sub> series made via SpS were used to compare with samples of Cs<sub>2</sub>SnCl<sub>6-6x</sub>Br<sub>6x</sub> made via SpS to study the change in structural and electrical properties by substituting different A-site cations. Studying the changes of properties of the variants is not only to understand better the theories/ trends of modulation of perovskites-like compounds by doping but also to improve the current performance of solar cell techniques. This is also a way to show the reason why Cs<sup>+</sup> is preferable for the selection of A-site cations to achieve optimal band gap such as 1.34 eV for Section 3.1 due to the smaller radii of Cs<sup>+</sup>. The small radii of Cs<sup>+</sup> caused samples of series Cs<sub>2</sub>SnCl<sub>6-6x</sub>Br<sub>6x</sub> in the cubic unit cell structure. However, with a bigger A-site organic ion group such as CH<sub>3</sub>CH<sub>2</sub>NH<sub>3</sub><sup>+</sup>, samples of (CH<sub>3</sub>CH<sub>2</sub>NH<sub>3</sub>)<sub>2</sub>SnCl<sub>6-6x</sub>Br<sub>6x</sub> series are in the hexagonal unit cell structure. The trend of crystal growth of A<sub>2</sub>SnCl<sub>6-6x</sub>Br<sub>6x</sub> series affected by different A-site ions. It also caused a huge difference in band gaps of samples in A<sub>2</sub>SnCl<sub>6-6x</sub>Br<sub>6x</sub> series with different A-site ions.

## 3.2.1 Experimental methodology

### • Solution-phased Synthesis (SpS) of (CH<sub>3</sub>CH<sub>2</sub>NH<sub>3</sub>)<sub>2</sub>SnCl<sub>6-6x</sub>Br<sub>6x</sub>

To make (CH<sub>3</sub>CH<sub>2</sub>NH<sub>3</sub>)<sub>2</sub>SnCl<sub>(6-6x)</sub>Br<sub>6x</sub> series, tin halide and ethylamine halide were mixed in defined ratios. The calculation of compositions of precursors was

based on the reactions below. To make 2g of final products, there are five steps to follow from the calculation. First, to make ethylamine halide, 32% diluted hydrogen chloride (HCI) solution, 70% ethylamine solution, CH<sub>3</sub>CH<sub>2</sub>NH<sub>2</sub>, and 47% hydrogen bromide (HBr) solution was prepared in certain molar quantities of the reactants. The amount of the prepared 98% ethanol solution was about 20 grams. When tin halides were dissolved completely in the prepared ethanol solution by stirring, the mixture solution of tin halides was poured into a solution of ethylamine halides. Finally, the final solution was left over to crystallize in air. Heavier halide mixtures took longer time to crystallise, whereas the pure halide crystallized within seconds of mixing. For example, to produce CH<sub>3</sub>CH<sub>2</sub>NH<sub>3</sub>Cl<sub>3</sub>Br<sub>3</sub> (2g, 3.59 mmol, solid) (x=0.5 for (CH<sub>3</sub>CH<sub>2</sub>NH<sub>3</sub>)<sub>2</sub>SnCl<sub>(6-6x)</sub>Br<sub>6x</sub> series), HCl solution(1.99g, 32 wt%), CH<sub>3</sub>CH<sub>2</sub>NH<sub>2</sub> solution (0.53 g, 70 wt%) and HBr solution(3.01 g, 48wt%) were prepared to make 3.59 mmol CH<sub>3</sub>CH<sub>2</sub>NH<sub>2</sub>Cl and 3.59 mmol CH<sub>3</sub>CH<sub>2</sub>NH<sub>3</sub>Br under the reaction shown below. Excessive acid (total of 5g acid) was used to form maximum amount of ethylamine halides.

2 CH<sub>3</sub>CH<sub>2</sub>NH<sub>3</sub> + 2x HBr + (2-2x) HCl 
$$\rightarrow$$
 2x CH<sub>3</sub>CH<sub>2</sub>NH<sub>3</sub>Br + (2-2x) CH<sub>3</sub>CH<sub>2</sub>NH<sub>3</sub>Cl

A certain amount of tin halides was weighed out and added into the ethanol solution that was prepared beforehand. To produce CH<sub>3</sub>CH<sub>2</sub>NH<sub>3</sub>Cl<sub>3</sub>Br<sub>3</sub> crystals (2g, 3.59 mmol), SnCl<sub>4</sub>•5H<sub>2</sub>O powder (0.72g) and SnBr<sub>4</sub> powder (0.90g) were weighed out and dissolved in prepared 20g of ethanol solution completely by stirring. The mixture solution of tin halides was added into the mixture solution CH<sub>3</sub>CH<sub>2</sub>NH<sub>3</sub>Cl and CH<sub>3</sub>CH<sub>2</sub>NH<sub>3</sub>Br under the reaction shown below. It was crystallised overnight.

 $xSnBr_4 + (1-x) SnCl_4 + 2x CH_3CH_2NH_3Br + (2-2x) CH_3CH_2NH_3Cl \rightarrow$   $(CH_3CH_2NH_3)_2SnCl_{(6-6x)}Br_{6x}$ 

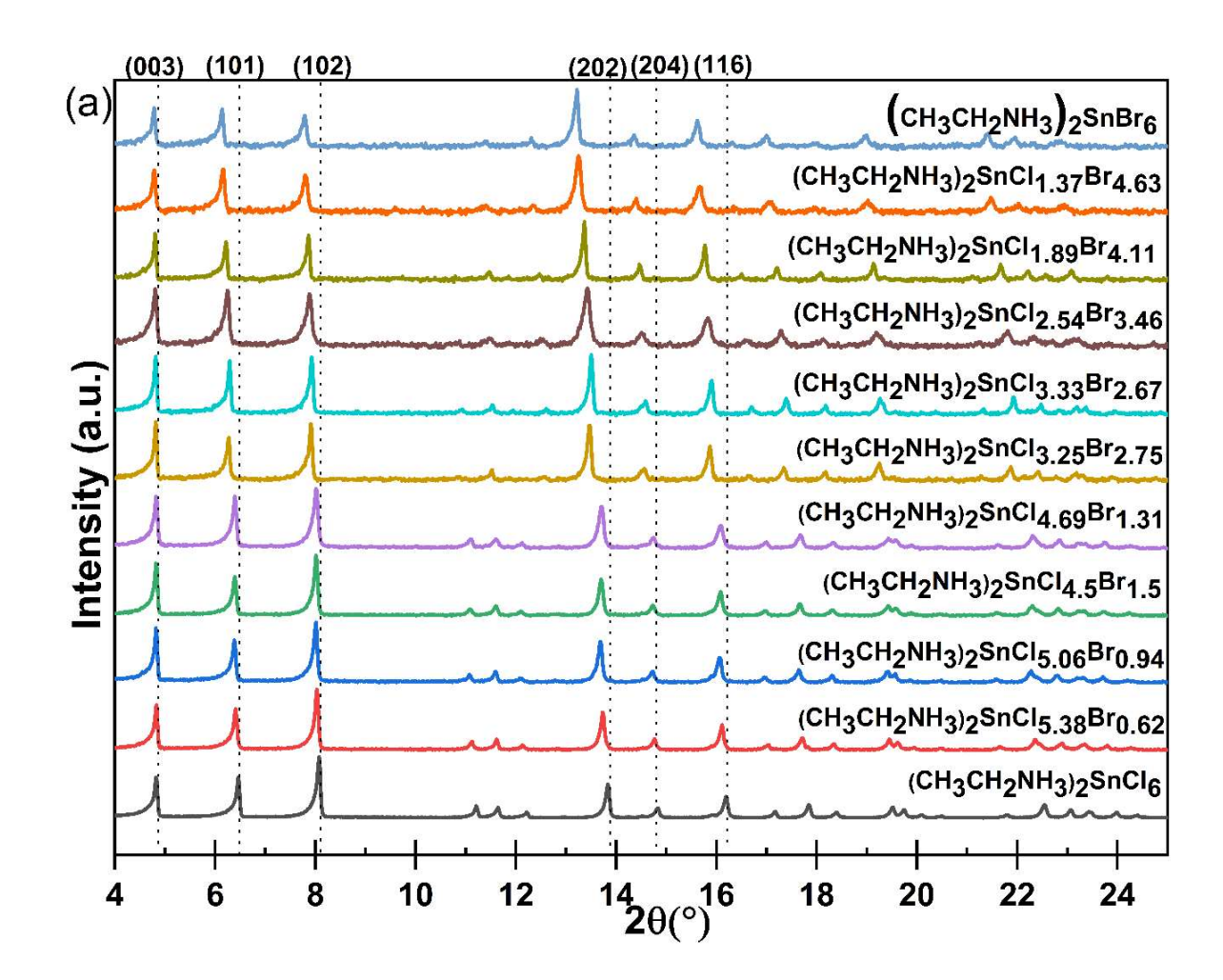
The crystal sample was filtered under vacuum and washed by the ethanol solution until the ethanol solution does not change colour. This is because sometimes tin bromide (SnBr<sub>4</sub>) does not react with ethylamine halides completely and remains in the final solution. SnBr<sub>4</sub> was washed out by the ethanol solution as much as possible.

#### 3.2.2 Results and Discussion

In the comparison of XRD patterns of (CH<sub>3</sub>CH<sub>2</sub>NH<sub>3</sub>)<sub>2</sub>SnCl<sub>6-6x</sub>Br<sub>6x</sub> and Cs<sub>2</sub>SnCl<sub>6-6x</sub>Br<sub>6x</sub> series, samples from the series are hexagonal structures in Figure 3.15. The change of A-site cations from Cs<sup>+</sup> to CH<sub>3</sub>CH<sub>2</sub>NH<sub>3</sub><sup>+</sup> would change the structure of the compounds from cubic structure to hexagonal. According to the position of peaks, there is a similar structure can be found from the Crystal Structure Database in the XRD pattern of K<sub>2</sub>Sn(OH)<sub>6</sub>. Especially when comparing the indexed peaks of (CH<sub>3</sub>CH<sub>2</sub>NH<sub>3</sub>)<sub>2</sub>SnCl<sub>6-6x</sub>Br<sub>6x</sub> series to K<sub>2</sub>Sn(OH)<sub>6</sub>, they all have the peaks at the similar position of 20 (x-axis) with different intensity (y-axis) on Figure 3.15. The Miller Indices (003), (101) and (102) are normally used to identify the hexagonal structure. Later those Miller Indices were used to approximately calculate unit cell parameters according to Bragg's Law.

Wyckoff linked the structure of K<sub>2</sub>Sn(OH)<sub>6</sub> to MA<sub>2</sub>SnCl<sub>6</sub> in 1928.<sup>114</sup> To study the link of different A-site cations, A-site cations of MA<sub>2</sub>SnCl<sub>6</sub> were replaced by

ethylamine ion groups. The samples in the (CH<sub>3</sub>CH<sub>2</sub>NH<sub>3</sub>)<sub>2</sub>SnCl<sub>6-6x</sub>Br<sub>6x</sub> series were produced by substituting different A-site Cations or organic cation groups. The growth mechanism of those samples was studied. The XRD patterns of (CH<sub>3</sub>CH<sub>2</sub>NH<sub>3</sub>)<sub>2</sub>SnCl<sub>6-6x</sub>Br<sub>6x</sub> were used to compare with the XRD patterns of samples from the series of Cs<sub>2</sub>SnX<sub>6</sub> mentioned in Chapter 3.1.



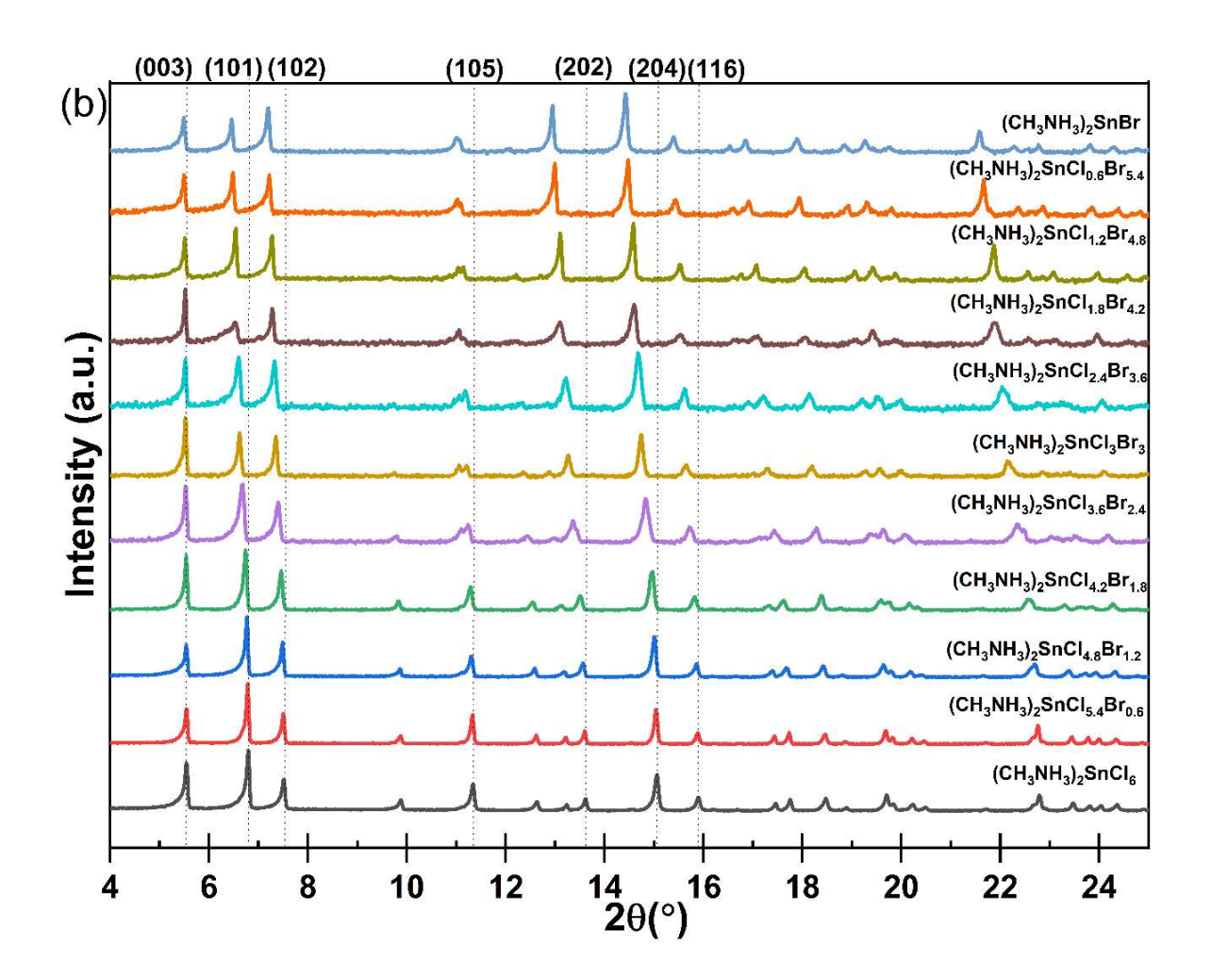
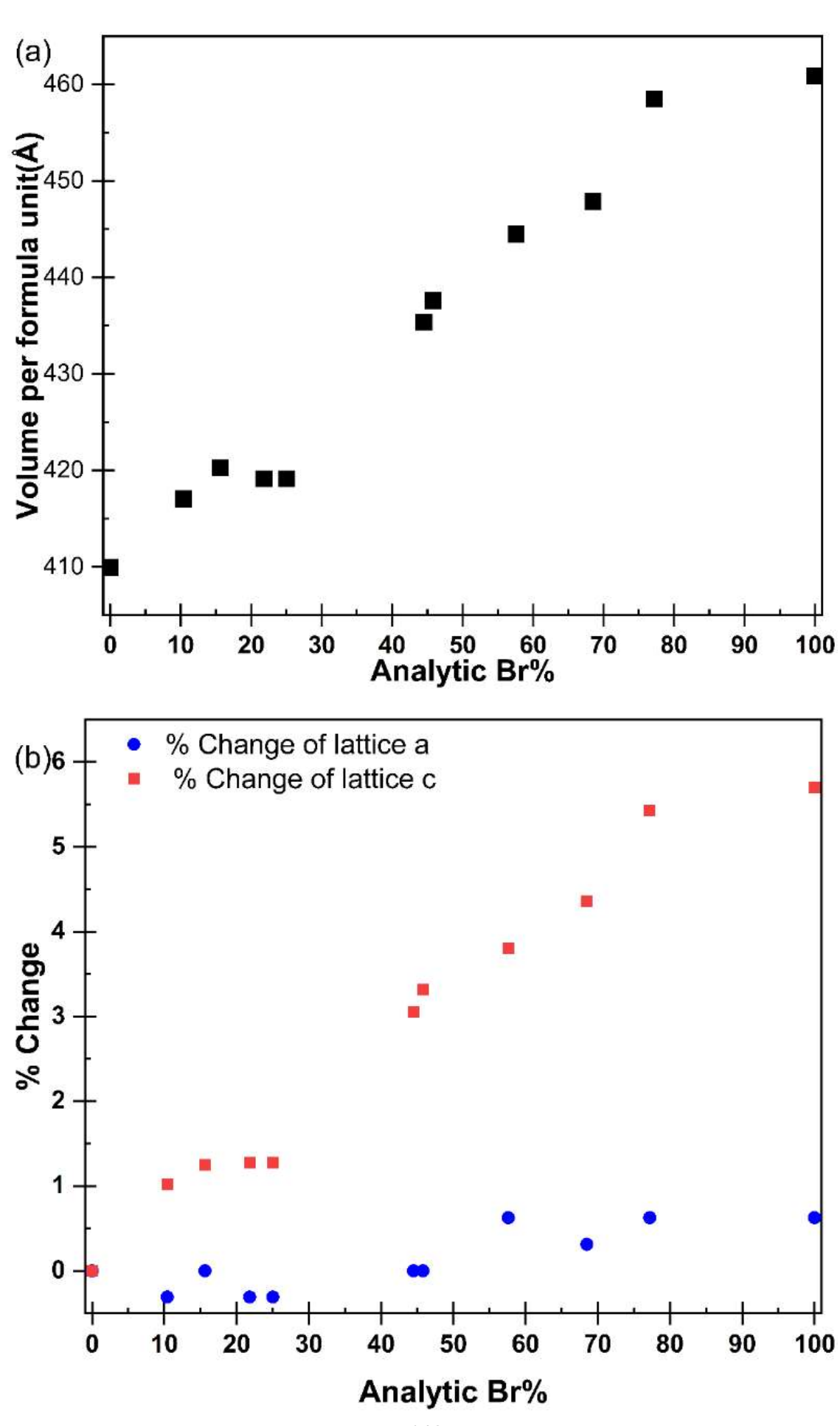


Figure 3.15 (a) The PXRD patterns of samples of  $(CH_3CH_2NH_3)_2SnCl_{6-6x}Br_{6x}$  series on the top (made via SpS method) with analytic atomic composition. (b) The PXRD patterns of samples of  $(CH_3NH_3)_2SnCl_{6-6x}Br_{6x}$  series at the bottom (made via SpS method) with nominal atomic composition used as a reference.

Unit cell parameters of samples recorded are preliminary by the calculation of the peaks of Miller Indices from the XRD data by Bragg's Law. The approximated lattice parameters of the lattice constants, a and c, are a=7.138 Å and c= 22.193 Å for (CH<sub>3</sub>CH<sub>2</sub>NH<sub>3</sub>)<sub>2</sub>SnCl<sub>6</sub>. Unit cell parameters can show the correlation of the size of unit cell volume of samples and the analytic amount of bromine percentage including in the compounds. The cell volume of samples from the

(CH<sub>3</sub>CH<sub>2</sub>NH<sub>3</sub>)<sub>2</sub>SnCl<sub>(6-6x)</sub>Br<sub>6x</sub> series increases when the measured percentage of bromine in the perovskite compounds increases. It is a linear relation between the measured Br% and unit cell volume shown in Figure 3.16(a).

A change in A-site cations of the materials by a bigger A-site cation group such as methylamine or ethylamine resulted in the change of the structure resulting in a hexagonal shape. Also, samples in the (CH<sub>3</sub>CH<sub>2</sub>NH<sub>3</sub>)<sub>2</sub>SnCl<sub>6-6x</sub>Br<sub>6x</sub> series prefer to grow in dimension c by indicating a larger increase in % change of lattice parameter c shown in Figure 3.16(b). The % change of lattice parameter a is little. When it compared to unit cell parameters of Cs<sub>2</sub>SnCl<sub>6-6x</sub>Br<sub>6x</sub> series, unit cell parameters of samples Cs<sub>2</sub>SnCl<sub>6-6x</sub>Br<sub>6x</sub> series increased uniformly and linearly to maintain cubic the shape but unit cell parameters of samples (CH<sub>3</sub>CH<sub>2</sub>NH<sub>3</sub>)<sub>2</sub>SnCl<sub>6-6x</sub>Br<sub>6x</sub> series worked differently. The percentage change of the lattice parameter c was larger than the percentage change of the lattice parameter a, which was almost zero. The same situation also happened to materials in the series (CH<sub>3</sub>NH<sub>3</sub>)<sub>2</sub>SnCl<sub>6-6x</sub>Br<sub>6x</sub> which PXRD patterns and the correlation between analytic Br% and % change of lattice parameters a and c were recorded in Figure 3.16(c) as counterparts.



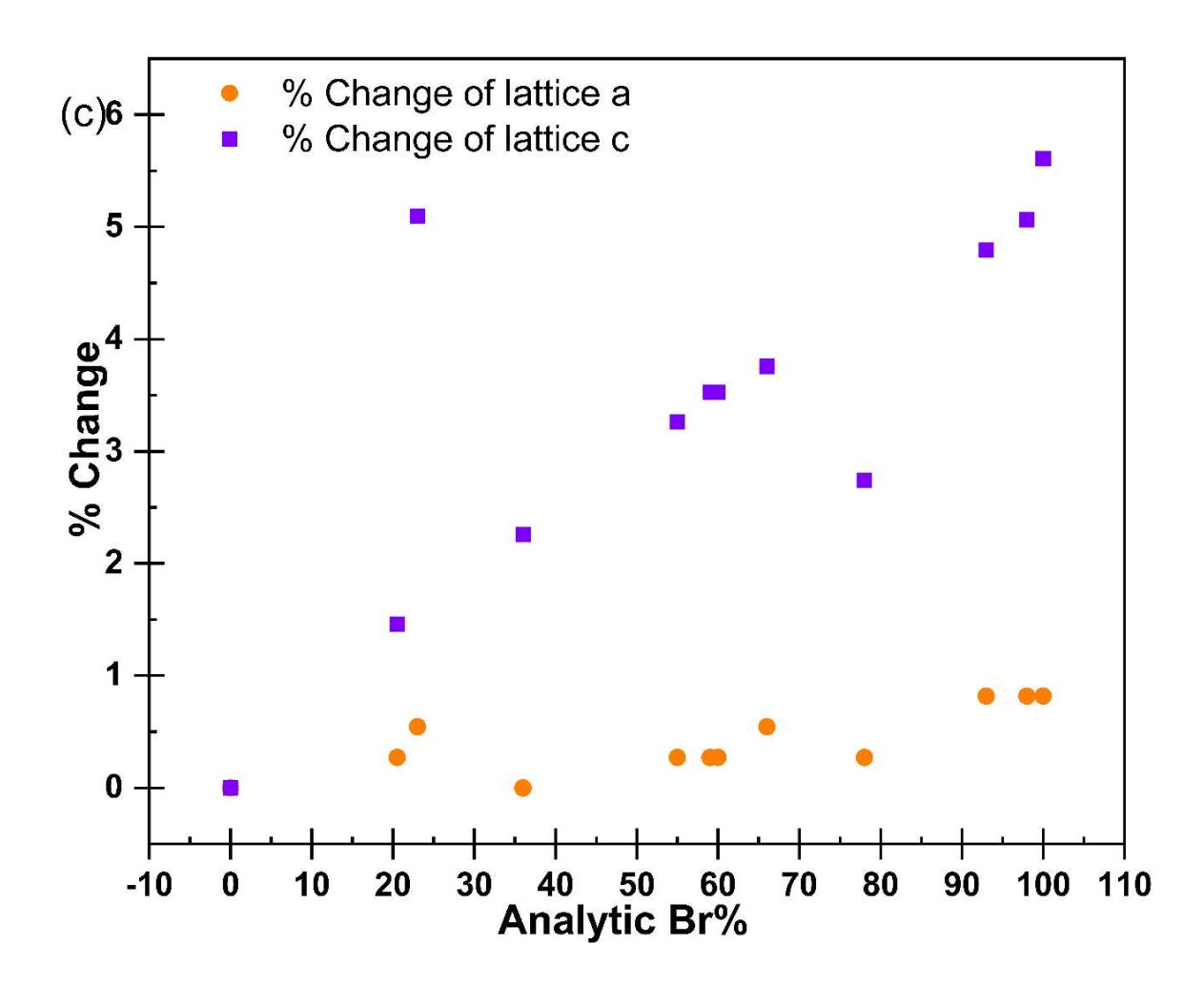


Figure 3.16. (a) The correlation between the analytic Br% and the volume per cell unit of samples in the  $(CH_3CH_2NH_3)_2SnCl_{6-6x}Br_{6x}$  series. (b) The correlation between the analytic Br% and % change of lattice a and lattice c of samples in the  $(CH_3CH_2NH_3)_2SnCl_{6-6x}Br_{6x}$  series. (c) The correlation between % change of lattice parameters (a and c) and analytic Br% of series  $(CH_3NH_3)_2SnBr_{6-6x}Cl_{6x}$ .

The correlations between band gaps and analytic Br% of series Cs<sub>2</sub>SnBr<sub>6-6x</sub>Cl<sub>6x</sub>, series (CH<sub>3</sub>NH<sub>3</sub>)<sub>2</sub>SnBr<sub>6-6x</sub>Cl<sub>6x</sub> and series (CH<sub>3</sub>CH<sub>2</sub>NH<sub>3</sub>)<sub>2</sub>SnBr<sub>6-6x</sub>Cl<sub>6x</sub> were shown in Figure 3.17. This is to compare whether series Cs<sub>2</sub>SnBr<sub>6-6x</sub>Cl<sub>6x</sub>, series (CH<sub>3</sub>NH<sub>3</sub>)<sub>2</sub>SnBr<sub>6-6x</sub>Cl<sub>6x</sub> and series (CH<sub>3</sub>CH<sub>2</sub>NH<sub>3</sub>)<sub>2</sub>SnBr<sub>6-6x</sub>Cl<sub>6x</sub> have anything in common. For example, they all have band bowing effect which represented the non-linear correlations of the band gaps with different compositions of samples

in a certain mixing ratio. The bigger A-site ion group existed in the sample's series with the same mixed halides which have the same Br%, the lower band bowing located on the graph.

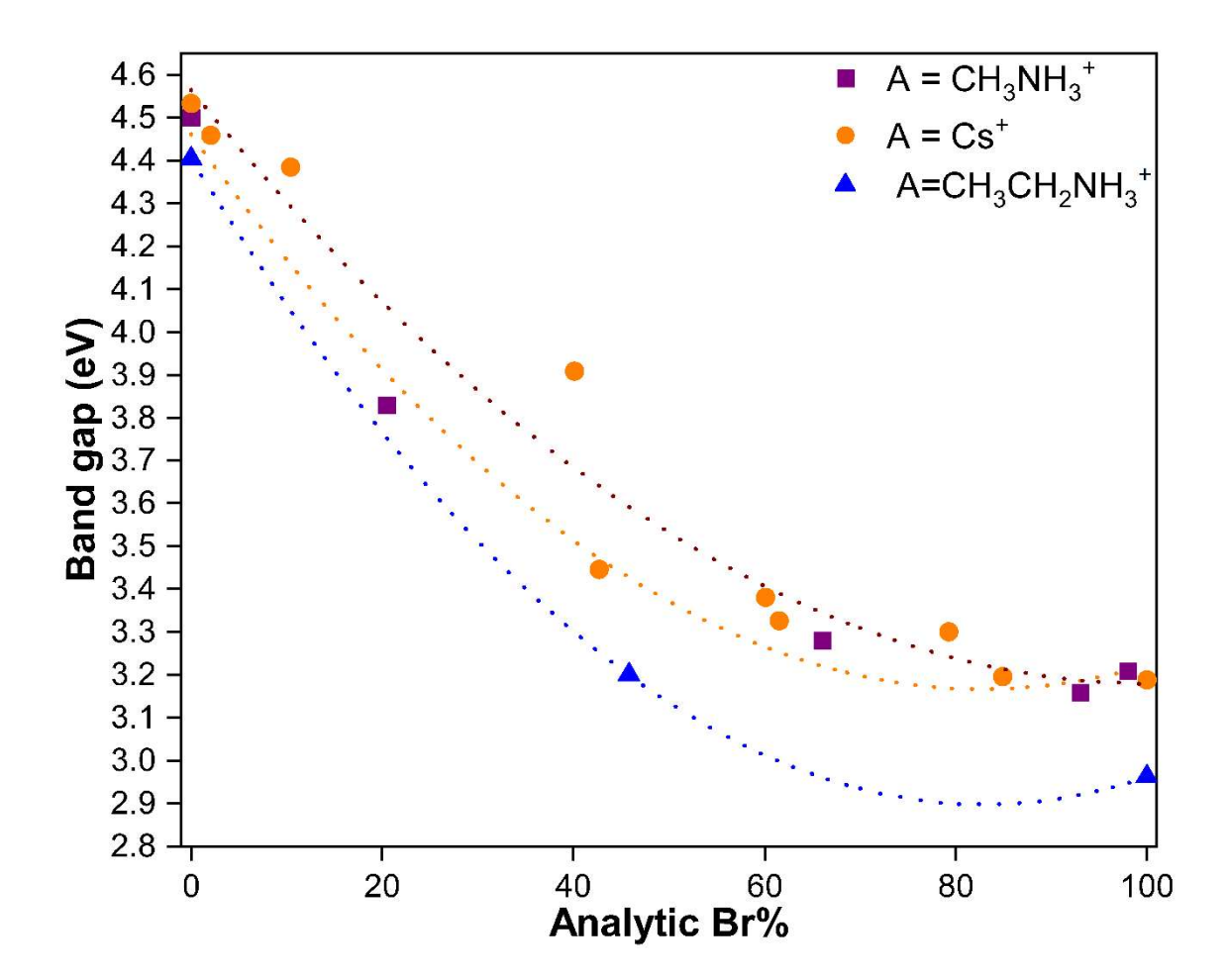


Figure 3.17 The bow-shaped correlation between band gaps and analytic Br% of Samples in series Cs<sub>2</sub>SnBr<sub>6-6x</sub>Cl<sub>6x</sub> and in series (CH<sub>3</sub>NH<sub>3</sub>)<sub>2</sub>SnBr<sub>6-6x</sub>Cl<sub>6x</sub> and in series (CH<sub>3</sub>CH<sub>2</sub>NH<sub>3</sub>)<sub>2</sub>SnBr<sub>6-6x</sub>Cl<sub>6x</sub>.

## 3.2.3 Conclusion

Doping different A-site ions or ion groups in materials in the formula of A<sub>2</sub>SnCl<sub>6</sub> caused a change in size and shape of the unit cell structure. The bigger A-site ions or ion groups in materials in the formula of A<sub>2</sub>SnCl<sub>6</sub> are, the more asymmetry the unit cell structure formed. Also, if the unit cell structure of A<sub>2</sub>SnCl<sub>6-6x</sub>Br<sub>6x</sub> series

with a big A-site ion group such as CH<sub>3</sub>NH<sub>3</sub><sup>+</sup> and CH<sub>2</sub>CH<sub>2</sub>NH<sub>3</sub><sup>+</sup> is hexagonal, the crystal growth of the series would grow in the dimension of the lattice parameter c at a rapid rate when it doped heavier halide elements but the % change of lattice parameter increased very little, comparing to the increasing rate of lattice parameter c. This also means the spacing of the BX<sub>6</sub> octahedra would change to adapt the A-site cation without reduction of overall symmetry which is the distortion of the cubic A<sub>2</sub>BX<sub>6</sub>.

The band gaps of A<sub>2</sub>SnCl<sub>6-6x</sub>Br<sub>6x</sub> series with different A-site ions (A=Cs<sup>+</sup>, CH<sub>3</sub>NH<sub>3</sub><sup>+</sup>, CH<sub>3</sub>CH<sub>2</sub>NH<sub>3</sub><sup>+</sup>) all have band bowing effect. The bigger A-site ion group existed in the sample's series with the same mixed halides shown as the same analytic Br%, the lower location of band bowing located on the graph which was shown by the lower bending band gaps of series (CH<sub>3</sub>CH<sub>2</sub>NH<sub>3</sub>)<sub>2</sub>SnBr<sub>6-6x</sub>Cl<sub>6x</sub> than the bending band gaps of series Cs<sub>2</sub>SnBr<sub>6-6x</sub>Cl<sub>6x</sub> and series (CH<sub>3</sub>NH<sub>3</sub>)<sub>2</sub>SnBr<sub>6-6x</sub>Cl<sub>6x</sub>. Hence, A-site cations can decide the range of band gaps, and a good selection of A-site cation such as Cs<sup>+</sup> can modulate the band gap of the sample to achieve a value close to the optimal band gap such as 1.34 eV mentioned from Shockley-Queisser Limit.

## 3.3 B-site ions Mixing

B-site mixing is to partially substitute Sn<sup>4+</sup> ions with other ions sharing the same oxidation state such as Te<sup>4+</sup> by Solution-phased Synthesis (SpS) and High Temperature Solid-state grinding method (HTSsG) to detect any changes in unit cell structures, compositions and bandgaps of samples made in different circumstances/ processing methods. This is to study whether different synthesises can produce same compounds with similar properties by mixing B-site ions instead of X-site ions mentioned in Section 3.1.

Cs<sub>2</sub>TeCl<sub>6</sub> and Cs<sub>2</sub>SnCl<sub>6</sub> share the same lattice structure in the cubic Fm-3m space group. A small amount of doping Te<sup>4+</sup> into Cs<sub>2</sub>SnCl<sub>6</sub> or vice versa Sn<sup>4+</sup> into Cs<sub>2</sub>TeCl<sub>6</sub> is to detect whether mixing B-site ions of Cs<sub>2</sub>BCl<sub>6</sub> cause band bowing effect as the MASn<sub>1-x</sub>Pb<sub>x</sub>I<sub>3</sub> series did.<sup>115</sup> To study the structural characterisation, optical band gaps and thermal stability of samples mixing B-site ions, the effects of B-site ions mixing can be adjustable and helpful for improving the performance of perovskite-like light absorbers in the form of Cs<sub>2</sub>BX<sub>6</sub>.

## 3.3.1 Experimental Methodology

## • Solution-phased Synthesis (SpS) of pure Cs2TeCl6

 $Cs_2TeCl_6$  was produced using the same solution synthesis method as  $Cs_2SnX_6$  but an additional procedure for making  $TeX_4$  (X = Cl, Br, I) is required (see

Appendix 6.2 for detailed composition calculation of samples). For example, in the synthesis of Cs<sub>2</sub>TeCl<sub>6</sub> (10 g), the first step is to produce CsCl solution as the same as the production of CsBr. Cs<sub>2</sub>CO<sub>3</sub> (3.26 g, 99%) was weighed and poured into the glass beaker containing HCl solution (over 2.27 g, 32 wt.%). If the solution is not colourless, more HCl would be added into the beaker utill the colourless CsCl solution formed.

$$Cs_2CO_3 + 2 HCI \rightarrow 2 CsCI + H_2O + CO_2\uparrow$$

TeCl<sub>4</sub> solution (2.70 g, aqueous) was made of TeO<sub>2</sub> (10 mmol, 1.60 g) and HCl (4.56 g) theoretically following the reaction below. However, it took a long time to dissolve TeO<sub>2</sub> solid completely in HCl solution. Sometime an excessive amount of HCl solution was required to speed up the process.

$$TeO_2 + 4 HCI \rightarrow TeCl_4 + 2 H_2O$$

When the aqueous TeCl<sub>4</sub> solution was mixed with CsCl solution, bright yellow muddy suspension formed immediately. It was filtered by absolute ethanol as well.

After it dried out in air overnight, Cs<sub>2</sub>TeCl<sub>6</sub> solid formed.

## Solution-phased Synthesis of Single halide material Cs<sub>2</sub>Te<sub>1-x</sub>Sn<sub>x</sub>Cl<sub>6</sub> with the mixed B-site variants

The synthesis of single halide  $Cs_2Te_{1-x}Sn_xCl_6$  perovskite was achieved by the same SpS method with the varied nominal molar ratio of tellurium to tin. The nominal molar amount of tin was represented as x. For example, when x= 0.1, the nominal molar ratio of tellurium to tin was 0.9 to 0.1. TeCl<sub>4</sub> (0.9 mmol) was

made by the reaction of TeO<sub>2</sub> (0.9 mmol, 1.44 g) and HCl (3.6mmol, an excess of 4.02 g, 37 wt.%).

$$TeO_2 + 4 HCI \rightarrow TeCl_4 (aq) + 2 H_2O$$

SnCl<sub>4</sub>·5H<sub>2</sub>O (0.1 mmol, 0.26 g) was dissolved completely in HCl (5.00 g, 37 wt.%). CsCl (20 mmol, aqueous) was made by the reaction of Cs<sub>2</sub>CO<sub>3</sub> (10 mmol, 3.25 g) and HCl (20 mmol, an excess of 2.01 g, 37 wt.%)

$$Cs_2CO_3 + 2 HCI \rightarrow 2 CsCl (aq) + H_2O + CO_2\uparrow$$

When CsCl solution was added into the mixture solution of TeCl<sub>4</sub> and SnCl<sub>4</sub>, yellow solids formed immediately in the solution. The excessive HCl was removed by rinsing with a small amount of absolute ethanol solution under a dynamic vacuum system, and the yellow solids was filtered out. The final yellow solid was stored in a sample capsule.

x SnCl<sub>4</sub> + (1-x) TeCl<sub>4</sub> (aq) + 2 CsCl(aq) 
$$\rightarrow$$
 Cs<sub>2</sub>Sn<sub>x</sub>Te<sub>1-x</sub>Cl<sub>6</sub>

#### High Temperature Solid-state Synthesis (HTSsS)

The solid-state approach was making samples by simply grinding two pure defect-ordered halide perovskite compounds such as Cs<sub>2</sub>SnCl<sub>6</sub>(0.5 g, 0.84 mmol) and Cs<sub>2</sub>TeCl<sub>6</sub> (0.5 g, 0.58 mmol) together evenly, and then the mixed samples was heated up under a vacuum system in the fume hood for 12 hours. It was used to figure out whether the temperature changes cause any changes in lattice structures or phase transitions of two pure defect-ordered halide perovskite compounds. It was attempted to produce Cs<sub>2</sub>Sn<sub>x</sub>Te<sub>1-x</sub>Cl<sub>6</sub> by grinding Cs<sub>2</sub>SnCl<sub>6</sub> and Cs<sub>2</sub>TeCl<sub>6</sub> together.

## 3.3.2 Results and Discussion

#### Structural characterizations

By mixing B-site ions of A<sub>2</sub>BX<sub>6</sub>, the change of the composition and the unit cell structure were observed from the XRD patterns and XPS data. The XRD pattern of sample Cs<sub>2</sub>TeCl<sub>6</sub>(SpS) was matched to Cs<sub>2</sub>TeCl<sub>6</sub><sup>116</sup> from ICSD database by comparing the Braggs peaks. So is sample Cs<sub>2</sub>SnCl<sub>6</sub>. Trom the XRD patterns in Figure 3.18 below, the increase of the nominal percentage of Sn in the composition shifts the peaks in the XRD patterns to the left. The shifting cannot be seen clearly at the low range of 2θ, but it was clearer in the high range of 2θ.

For example, the Braggs peak at  $2\theta$ =  $35.25^{\circ}$  shifts to  $35.61^{\circ}$  when the nominal percentage of Sn is increasing from 0% (Cs<sub>2</sub>TeCl<sub>6</sub>) to 100% (Cs<sub>2</sub>SnCl<sub>6</sub>). It means that the unit cell structure of Cs<sub>2</sub>Sn<sub>x</sub>Te<sub>1-x</sub>Cl<sub>6</sub> series gets slightly smaller when the nominal percentage of Sn increases. It can also be proven by checking ionic radii of Tellurium (Te) and Tin (Sn). The ionic radius of Te is 0.66 Å, and the ionic radius of Sn is 0.55 Å.<sup>118</sup> The ionic radius of Te is bigger than that of Sn. Hence, the increase in the nominal percentage of Sn can increase the size of the unit cell structure gradually. However, in addition to the shifting of the XRD patterns, there are peaks at  $2\theta$ =  $9.86^{\circ}$ ,  $13.97^{\circ}$ ,  $19.835^{\circ}$  and  $24.35^{\circ}$  that gradually formed when the nominal percentage of Sn is increasing. They are matched to the XRD patterns of CsCl<sup>111</sup> from ICSD database.

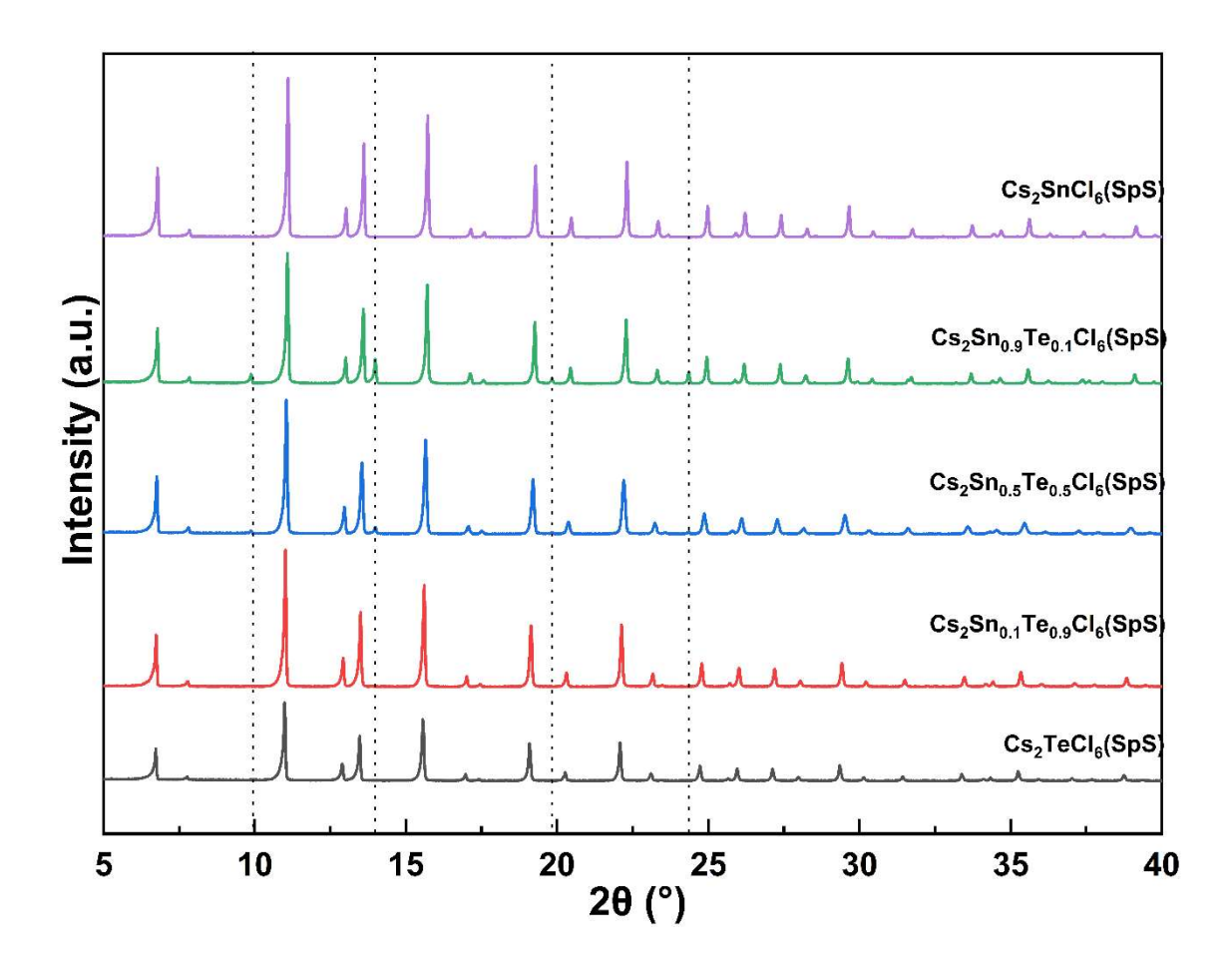


Figure 3.18 The XRD patterns of compounds in series Cs<sub>2</sub>Sn<sub>x</sub>Te<sub>1-x</sub>Cl<sub>6</sub> (SpS).

The Raman spectra of compounds in series Cs<sub>2</sub>Sn<sub>x</sub>Te<sub>1-x</sub>Cl<sub>6</sub> (SpS) were displayed in Figure 3.19(a). The Raman spectrum of Cs<sub>2</sub>TeCl<sub>6</sub> is at relatively lower wavenumbers than that of Cs<sub>2</sub>SnCl<sub>6</sub> except the middle E<sub>g</sub> peak because tellurium is heavier than tin. The T<sub>2g</sub> mode responded to the motion of Cs atoms with respect to the Cl atoms. The symmetric stretching vibration of A<sub>1g</sub> mode caused by the Cl atoms surrounding B-site atoms in the octahedra. For example, the [TeCl<sub>6</sub>]<sup>2-</sup> octahedra have heavier mass than [SnCl<sub>6</sub>]<sup>2-</sup> octahedra. The E<sub>g</sub> modes was related to the asymmetric stretching vibration of Cl ions around B-site ions. The Cl ions around Te ions caused more stretching vibrations than that of Sn. <sup>119</sup>, <sup>120</sup> Mixed B-site Compounds (Cs<sub>2</sub>Te<sub>0.1</sub>Sn<sub>0.9</sub>Cl<sub>6</sub>, Cs<sub>2</sub>Te<sub>0.5</sub>Sn<sub>0.5</sub>Cl<sub>6</sub> and Cs<sub>2</sub>Te<sub>0.9</sub>Sn<sub>0.1</sub>Cl<sub>6</sub>) have peaks at the same locations with different intensities due

to the different amount of isolated  $[SnCl_6]^{2-}$  and  $[TeCl_6]^{2-}$  octahedra apart from the peak at 183 cm<sup>-1</sup>. This indicated no mixed B-site octahedron such as  $[Te_xSn_{1-}xCl_6]^{2-}$  but only  $[SnCl_6]^{2-}$  and  $[TeCl_6]^{2-}$  octahedra in different ratios in mixed B-site double perovskites. The peak at 183 cm<sup>-1</sup> caused by the formation of CsCl shown in Figure 3.19(b), which was also confirmed by PXRD data in Figure 3.18.

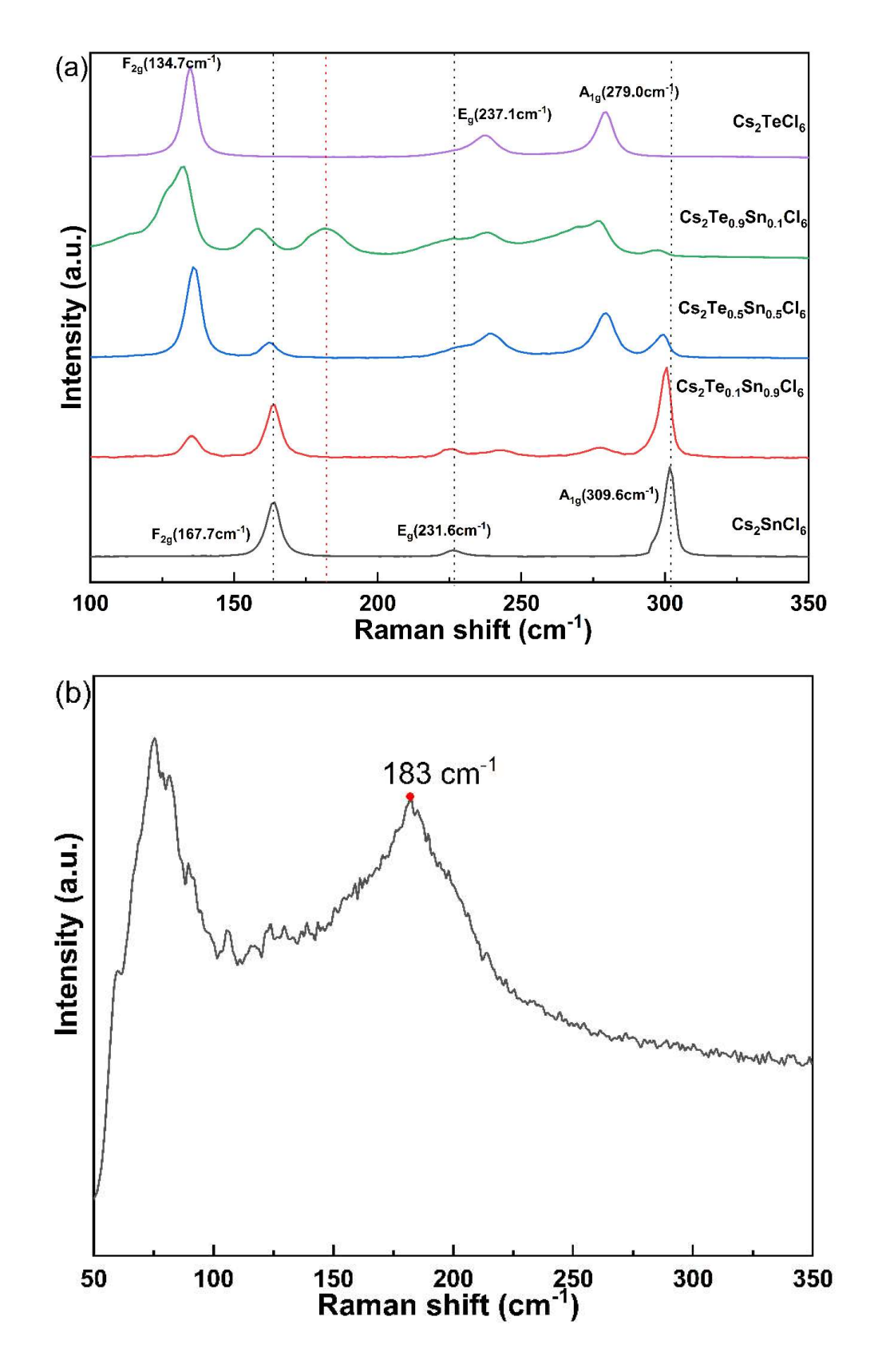


Figure 3.19 (a)The Raman spectra of compounds in series  $Cs_2Sn_xTe_{1-x}Cl_6$ . (b) Raman spectrum of CsCl as a counterpart.

## Optical band gaps

Optical band gaps of compounds in series Cs<sub>2</sub>Sn<sub>x</sub>Te<sub>1-x</sub>Cl<sub>6</sub> (x= 0, 0.1, 0.5, 0.9 and 1, made by SpS) were calculated by Tauc plots and Kubelka Munk Function mentioned in the section 2.4.2. When tin (II) halides were doped into Cs<sub>2</sub>TeCl<sub>6</sub>, the band gap was not changed as much as that of mixed halide compounds. The band bowing effect was not shown in the changes of band gaps vs nominal composition in Table 3.4. It seemed like doping Sn did not affect band gaps of compounds in series Cs<sub>2</sub>Sn<sub>x</sub>Te<sub>1-x</sub>Cl<sub>6</sub> productively. Due to limited data, further research about the effects of B-site mixing on bang gaps is ongoing.

Composition	Band gap/ eV
Cs2TeCl6	2.80
Cs2Te0.9Sn0.1Cl6	2.79
Cs2Te0.5Sn0.5Cl6	2.84
Cs2Te0.1Sn0.9Cl6	2.84
Cs2SnCl6	4.53

Table 3.4 The band gaps of compounds in series  $Cs_2Sn_xTe_{1-x}cl_6$  (x= 0, 0.1, 0.5, 0.9 and 1).

# Thermal stability of compounds mixing pure B-site perovskites Cs<sub>2</sub>TeCl<sub>6</sub> and Cs<sub>2</sub>SnCl<sub>6</sub>

The mixture of Cs<sub>2</sub>SnCl<sub>6</sub> (0.5 g, 0.84 mmol, SpS) and Cs<sub>2</sub>TeCl<sub>6</sub> (0.5 g, 0.83 mmol, SpS) was made in the same way as the production of the mixture of Cs<sub>2</sub>SnBr<sub>6</sub>(SpS) and Cs<sub>2</sub>Snl<sub>6</sub>(SpS) mentioned in Chapter 3.3. The molar ratio of Cs<sub>2</sub>SnCl<sub>6</sub> to Cs<sub>2</sub>TeCl<sub>6</sub> is 50:50. Raman spectra of the mixed samples of Cs<sub>2</sub>SnCl<sub>6</sub> and Cs<sub>2</sub>TeCl<sub>6</sub> at room temperature and heated at 320 °C are shown in Figure

3.20 individually. The spectrum of the mixture at room temperature showed the coexisted Raman spectra of Cs<sub>2</sub>SnCl<sub>6</sub> and Cs<sub>2</sub>TeCl<sub>6</sub>. Six Raman peaks represented as six different vibrational modes of pure halide octahedra, [TeCl<sub>6</sub>]<sup>2</sup>- and [SnCl<sub>6</sub>]<sup>2</sup>-.

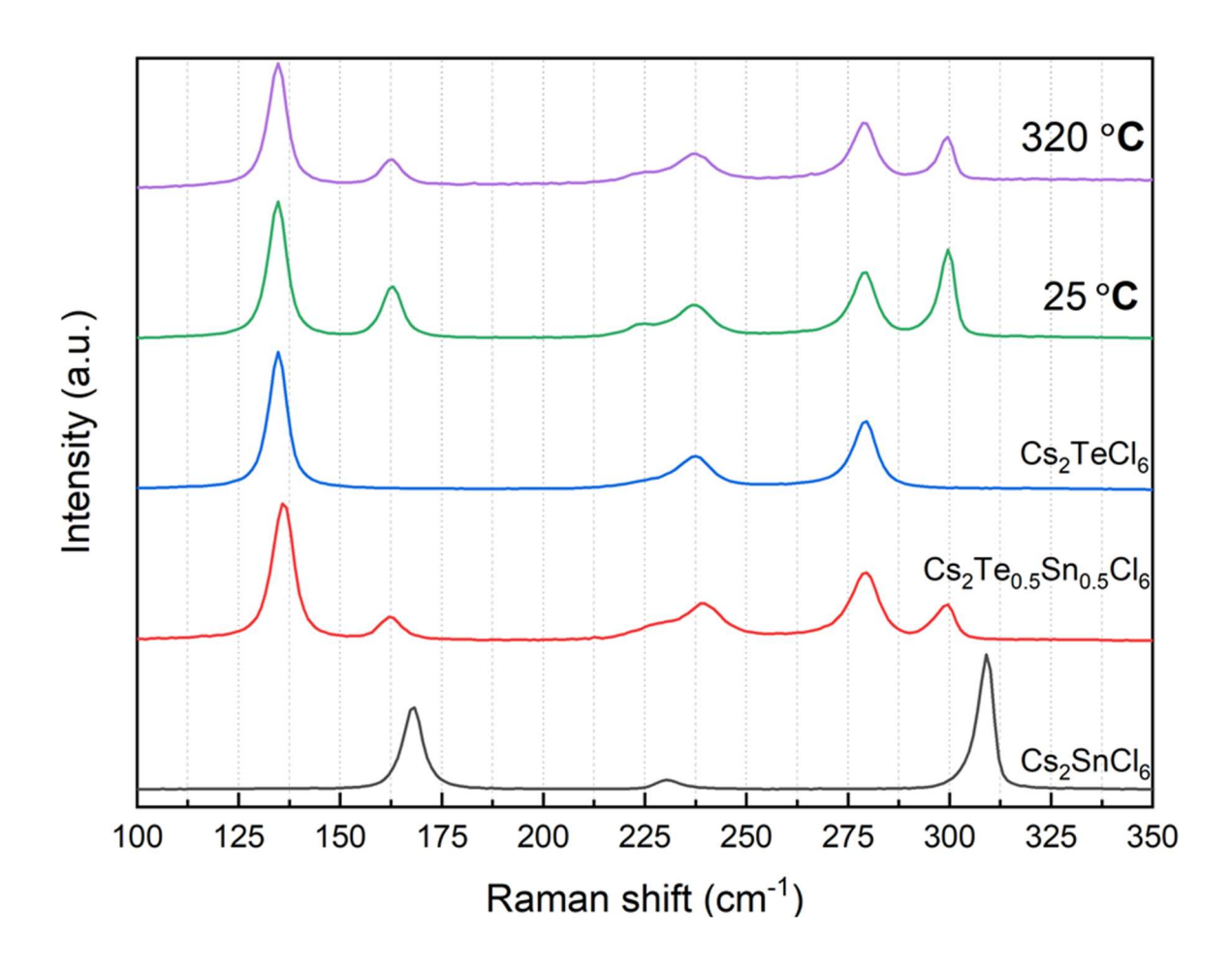


Figure 3.20 The Raman spectrums of mixed Cs<sub>2</sub>SnCl<sub>6</sub> and Cs<sub>2</sub>TeCl<sub>6</sub>.

Tellurium is slightly heavier than tin so the octahedra with tellurium ions, [TeCl<sub>6</sub>]<sup>2-</sup>, is slightly heavier than the one with tin. Hence, the peaks of the spectrum of Cs<sub>2</sub>TeCl<sub>6</sub> are on the left side of the peaks of the spectrum of Cs<sub>2</sub>SnCl<sub>6</sub>. The spectra of the mixture are the same at room temperature and at 320 °C. It was approximately matched to the Raman spectrum of Cs<sub>2</sub>Te<sub>0.5</sub>Sn<sub>0.5</sub>Cl<sub>6</sub>. When the PXRD pattern of the mixture heated to 320°C was compared with the PXRD

pattern of Sample Cs<sub>2</sub>Te<sub>0.5</sub>Sn<sub>0.5</sub>Cl<sub>6</sub> (SpS), not only Braggs peaks of Cs<sub>2</sub>Te<sub>0.5</sub>Sn<sub>0.5</sub>Cl<sub>6</sub> were found in the PXRD pattern of the mixture sample heated to 320 °C but the existence of Cs<sub>2</sub>SnCl<sub>6</sub> was also found in Figure 3.20. It indicates that the mixture of Cs<sub>2</sub>SnCl<sub>6</sub> and Cs<sub>2</sub>TeCl<sub>6</sub> at high temperature has phase changes and possibly started to form mixed B-site compounds.

As it can be seen in Figure 3.21, a tiny peak started to form at  $2\theta = 9.875^{\circ}$  and a sharp peak at  $2\theta = 13.98^{\circ}$  which were also seen in the PXRD pattern of  $Cs_2Te_{0.5}Sn_{0.5}Cl_6$ . The XRD pattern of  $CsCl^{111}$  from ICSD database was compared to the XRD pattern of the mixture to make sure no decomposition happened at  $320^{\circ}C$ . Hence, the samples confirm the hypothesis that high temperature solid-state can possibly cause phase changes and form mixed B-site compound by mixing pure halide perovskite-like compounds such as  $Cs_2SnCl_6$  and  $Cs_2TeCl_6$ .

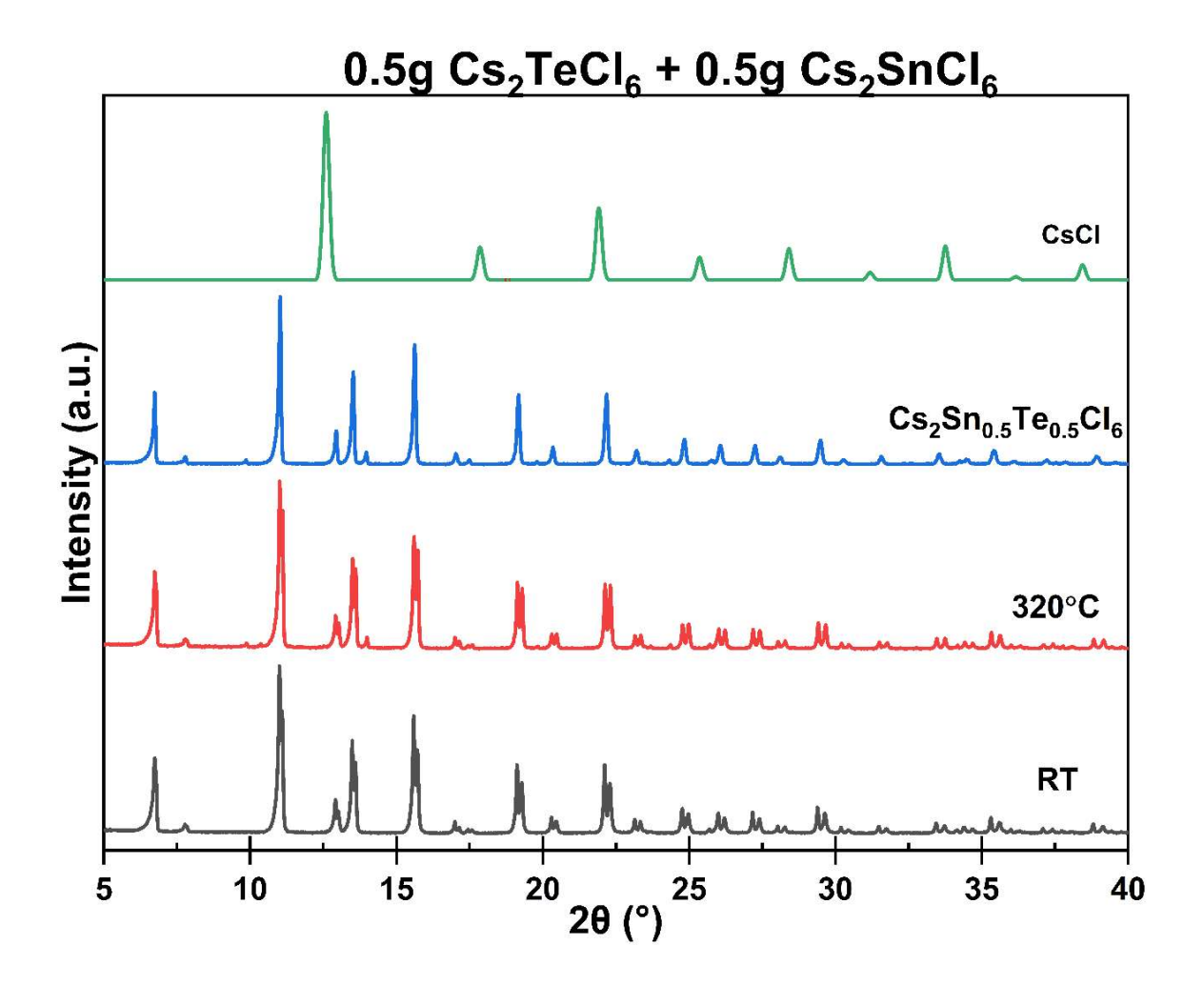


Figure 3.21 XRD Analysis data of samples mixing Cs<sub>2</sub>SnCl<sub>6</sub> and Cs<sub>2</sub>TeCl<sub>6</sub> at 25 °C and 320 °C. XRD patterns of Samples Cs<sub>2</sub>Sn<sub>0.5</sub>Te<sub>0.5</sub>Cl<sub>6</sub>(SpS) and CsCl was counterparts.

## 3.3.3 Conclusion

Tellurium is one of the rarest elements. For a commercially successful light absorber material, tellurium is unsuitable. However, for the proof of the concept, it was used in a laboratory scale. The idea is to try out the possibility of mixing B-site cations to modulate the crystal structure to change optical and electronic properties of the material. Zhou et al. reported Te<sup>4+</sup> shares a similar cationic

radius and oxidation state to Sn<sup>4+</sup>, thus Te<sup>4+</sup> was embedded into the lattice of (C<sub>4</sub>H<sub>7</sub>N<sub>2</sub>)<sub>2</sub>SnCl<sub>6</sub> to enhance crystal quality and to change the band structure.<sup>71</sup> However, the idea to mix B-site ions(Te, Sn) in Cs<sub>2</sub>SnCl<sub>6</sub> may not be successful due to the extra phase of CsCl formed during the production of Sn<sup>4+</sup> doped Cs<sub>2</sub>TeCl<sub>6</sub> compound but this thesis shows feasible traces for further research on mixing B-site ions.

B-site mixing affects less on the size of lattice structures and bandgaps of samples such as Sn<sup>4+</sup> doped Cs<sub>2</sub>TeCl<sub>6</sub> compound in this section due to the similar radii of B-site ions. So far band bowing effect was not seen from compounds in series Cs<sub>2</sub>Sn<sub>x</sub>Te<sub>1-x</sub>Cl<sub>6</sub>. A small amount of Te doped into Cs<sub>2</sub>SnCl<sub>6</sub> caused a huge drop in the band gap. However, a small amount of Sn doped into Cs<sub>2</sub>TeCl<sub>6</sub> caused a small increase in the band gap. There is no trend of band gaps of the mixed B-site perovskites seen yet. Also, C<sub>S</sub>Cl was easily formed in the production of mixing B-site double perovskites in both synthesises which was unwanted.

To confirm any further changes of properties of mixed B-site halide compounds, more research on this specific field is needed. To pursue a stable solar cell performance with an excellent power conversion efficiency, effective light absorbers with high light absorption efficiencies are required. In searching better light absorbers, ideas of trying different doping techniques by different synthesis methods on A-site, B-site and X-site can expand the knowledge of the perovskite-like materials and push forward the development of solar cell industry with every little bit of contributions. Researching and improving functional perovskite-like

materials by studying detailed changes based on composition, structure and band gap is a way to invent better light absorber materials for the solar cell industry.

# 4 Bismuth halide materials(A<sub>3</sub>Bi<sub>2</sub>X<sub>9</sub>) doping Sn<sup>2+</sup>

Bismuth halide materials showed desirable properties as light absorbers. The modulation of structural and electronic properties can improve light absorption and charge transport of these compounds by utilizing different synthesis and the mixed valency doping technique. Here the applications of mixed valency doping of Sn<sup>2+</sup> and Sn<sup>4+</sup> mainly on the Bi site of different A<sub>3</sub>Bi<sub>2</sub>X<sub>9</sub> is to study how mixed valencies affect the structural, electronic, and optical properties.

Two different manufacturing methods (doping mechanisms), Solution-phased Synthesis (SpS) and Solid-state Grinding (SsG), were used to compare how synthesis methods affect the productivity of mixed valency doping Sn. This research was focus on whether mixed valency doping is only suitable for A<sub>3</sub>Bi<sub>2</sub>X<sub>9</sub> materials in the trigonal structure. Are there A<sub>3</sub>Bi<sub>2</sub>X<sub>9</sub> materials in other phase structures that can use this technique to modulate the structural and electronic properties?

## 4.1 Cs<sub>3</sub>Bi<sub>2</sub>Br<sub>9</sub> Materials doping Sn<sup>2+</sup>

Lead-free halide materials, Cs<sub>3</sub>Bi<sub>2</sub>Br<sub>9</sub>, are perovskite-like materials, which are called vacancy-ordered triple perovskites. They exhibit potential in photovoltaic

and optoelectronic applications. Chantelle J. Krajewska et al<sup>88</sup>. reported doping SnBr<sub>2</sub> into Cs<sub>3</sub>Bi<sub>2</sub>Br<sub>9</sub> via Solution-phased Synthesis (SpS) can obtain up to 7% of the substitution of Bi site by equal quantities of Sn<sup>2+</sup> and Sn<sup>4+</sup>. The reproducibility of the same experiment in SpS was used as a counterpart to study the difference in properties caused by another doping mechanism (Solid-state Grinding (SsG)).

## 4.1.1 Experimental Methodology

## A Solution-phased Synthesis method of Cs<sub>3</sub>Bi<sub>2</sub>Br<sub>9</sub> doping Sn<sup>2+</sup>

1 mmol Cs<sub>3</sub>Bi<sub>2</sub>Br<sub>9</sub> can be produce via a solution-phased synthesis. The whole experiment was carried out in air. An acidic solution of CsBr was produced by reacting 1.5 mmol Cs<sub>2</sub>CO<sub>3</sub> with 2 mL aqueous HBr (3M). Separately, 2 mmol BiBr<sub>3</sub> was dissolved in 5 mL aqueous HBr (3 M) and stirred on a heating mantle at 80 °C. After 10 minutes of stirring, the acidic CsBr solution was then added to the BiBr<sub>3</sub> solution. An immediate white precipitate appeared, which was isolated by filtration, washed with ethanol, and stored in air.

The solution-phased synthesis of Sn doped Cs<sub>3</sub>Bi<sub>2</sub>Cl<sub>9</sub> was carried out by mixing the desired ratio of SnBr<sub>2</sub> and BiBr<sub>3</sub> in solution, followed by reaction with acidic aqueous CsBr solution. For example, to obtain 5 g Cs<sub>3</sub>Bi<sub>2</sub>Br<sub>9</sub> doped a nominal Sn dopant concentration of 5%, 0.5 mmol SnBr<sub>2</sub> and 9.5 mmol BiBr<sub>3</sub> were dissolved by stirring in 40 mL HBr (3M) at 80 °C, followed by addition of the CsBr solution.

The acidic aqueous CsBr solution was prepared by dissolving 7.5 mmol Cs<sub>2</sub>CO<sub>3</sub> into 25 mL HBr (3M). The concentrated HBr solution would increase the potential of the formation of Cs<sub>2</sub>SnBr<sub>6</sub> in the process of doping SnBr<sub>2</sub> into Cs<sub>3</sub>Bi<sub>2</sub>Br<sub>9</sub>.

[Sn]/([Sn]+[Bi]) = 0,0.05,0.12,0.25,0.4 and 0.5

Samples with varying nominal amounts of Sn were synthesised in this way such as [Sn]/([Sn]+[Bi]). When Sn was present, yellow precipitate was formed. The product was isolated by filtration, washed with ethanol, and stored in air. Only tin halides were added to the reaction was Sn (II).

## Solid-state grinding of Sn-doped Cs<sub>3</sub>Bi<sub>2</sub>Br<sub>9</sub>

B-site mixed-valent Sn (II) / Sn (IV) doped  $Cs_3Bi_2Cl_9$  microcrystals ( $Cs_3(Sn_xBi_1-x)_2Br_9$ ) were prepared by mechanochemical reaction (solid-state grinding) at room temperature in air from stoichiometric amounts of  $SnBr_2$  and the as-made  $Cs_3Bi_2Br_9$  microcrystals. For example, 5% Sn-doped ( $Cs_3(Sn_xBi_{1-x})_2Br_9$ ) was prepared by grinding  $SnBr_2$  powder (0.053 mmol, 0.011g) together with the assynthesised yellow crystalline  $Cs_3Bi_2Br_9$  (0.500 mmol, 0.567g) in an agate mortar until two solids were homogeneously mixed. No solvent was added to the reaction. The colour of the reactants turned black immediately upon grinding. Samples were made with Sn contents of x = 0, 0.05, 0.12, 0.25. All samples were stored in glass sample vials in air.

## 4.1.2 Results and Discussion

Pure Cesium enneabromodibismuthate (III)(Cs<sub>3</sub>Br<sub>2</sub>Br<sub>9</sub>) and Tin (Sn) doped Cesium enneabromodibismuthate (III)(Cs<sub>3</sub>Br<sub>2</sub>Br<sub>9</sub>) powders were synthesised via the solution-phased synthesis method described in the Section of Experimental Methodology. The additional SnBr<sub>2</sub> was given nominal Sn doping amount of 0, 12, and 25%. The powder XRD analysis was discussed below.

Powder XRD patterns above showed the undoped and Sn-doped Cs<sub>3</sub>Br<sub>2</sub>Br<sub>9</sub> sample powders were consistent with a P3m1 layered vacancy-ordered triple perovskite structure. XRD diffraction pattern showed no sign of secondary phases. At the range of 2θ between 5-40°, a small amount of Sn doping cannot affect the interlayer spacing of the crystal structure of the undoped and Sn-doped Cs<sub>3</sub>Br<sub>2</sub>Br<sub>9</sub> sample powders since there was no sign of Braggs peaks of PXRD data of Cs<sub>2</sub>SnBr<sub>6</sub> located on all sample powders visually in Figure 4.1. This may be covered by the noise signals, or the amount of Cs<sub>2</sub>SnBr<sub>6</sub> is too small to detect. In that case, no existence of Cs<sub>2</sub>SnBr<sub>6</sub> was seen in Figure 4.1. Krajewskaet al. stated the analytic concentration is approximately linear to nominal composition at low nominal Sn%. Then Cs<sub>2</sub>SnBr<sub>6</sub> was seen at a nominal 50 Sn% (which is analytic 23.5 Sn%).<sup>88</sup>

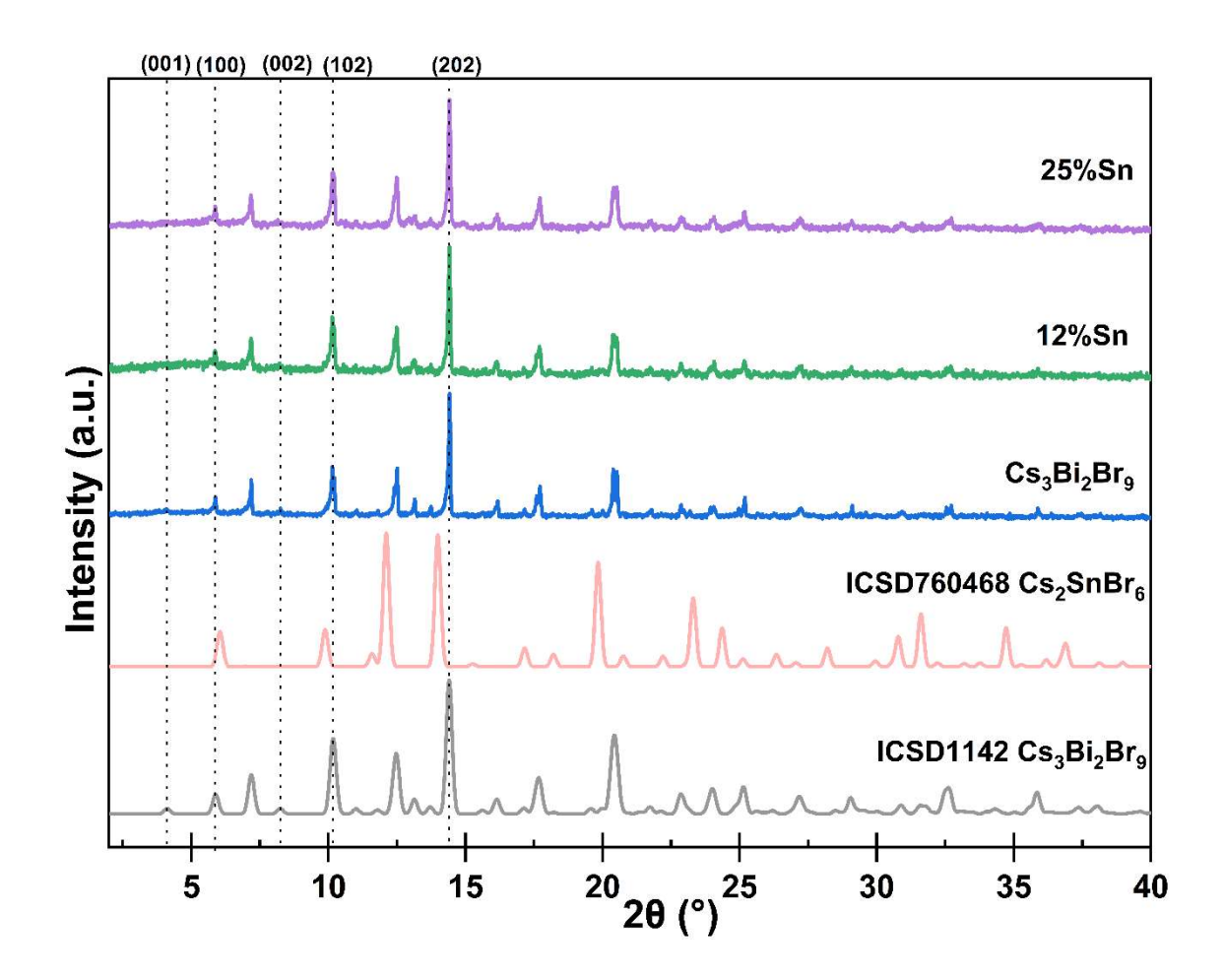


Figure 4.1 The PXRD patterns of pure Cs<sub>3</sub>Br<sub>2</sub>Br<sub>9</sub> and Sn doped Cs<sub>3</sub>Br<sub>2</sub>Br<sub>9</sub> (SpS) powders.

As-produced Cs<sub>3</sub>Bi<sub>2</sub>Br<sub>9</sub> yellow crystal powder displayed a powder diffraction pattern in Figure 4.2, which is alike to the reported structure found in ICSD database reported by Lazarini, F et al.<sup>121</sup>. It is a trigonal structure with the P-3m1 space group. It is also visualised as 2D corrugated layers featuring cornerconnected [BiBr<sub>6</sub>]<sup>3-</sup> octahedra. Rietveld refinement was processed by GSAS II, starting with the model of Lazarini, F et al. A small amount of preferred orientation (100) was inputted by using March-Dollase algorithm to fit in the peak intensities. The locations of the Braggs peaks of the XRD pattern of sample Cs<sub>3</sub>Bi<sub>2</sub>Br<sub>9</sub> was

identical to the reported structure mentioned above. The refined lattice parameters of the undoped sample  $Cs_3Bi_2Br_9$  were a = 7.9504(6) Å, c = 9.8281(6) Å. These data were approximately matched to those provided from ICSD database (code 1142) (a = 7.972(2)Å, c = 9.867(5) Å). No unidentified peaks were seen; a final Rw value of 4.929% was obtained and final reduced chi<sup>2</sup> was 1.84.

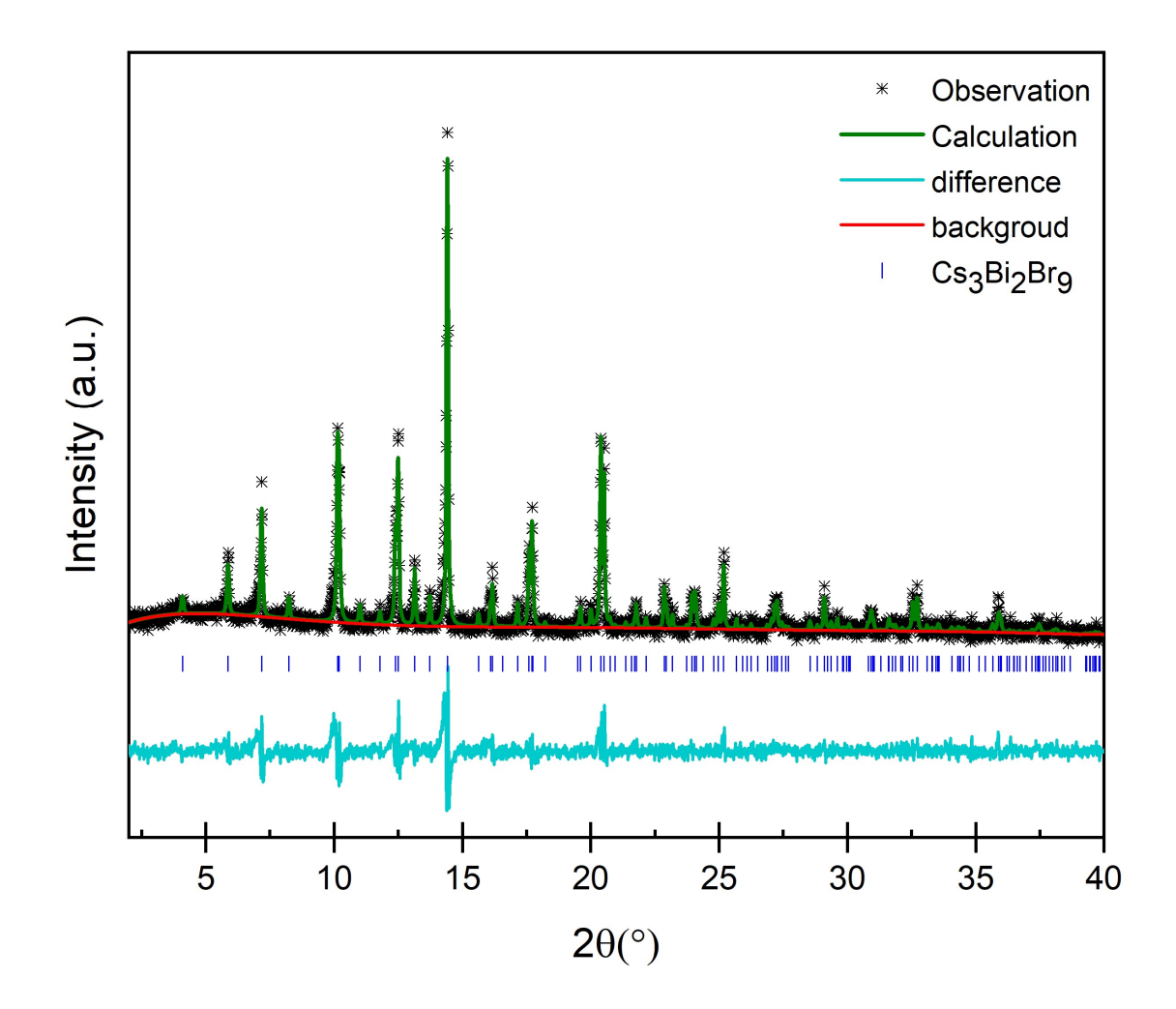


Figure 4.2 The powder XRD pattern of  $Cs_3Bi_2Br_9$  produced by the solution-phased synthesis. The model (green line) was refined from the structure reported by Lazarini, F. et al<sup>121</sup>. The background is shown in red, and it shows how much difference between the sample(observation) and the ICSD data(calculation) in cyan. Navy blue dash marks show positions of reflections.

Comparing to the PXRD patterns of undoped Cs<sub>3</sub>Bi<sub>2</sub>Br<sub>9</sub>(SpS) and Sn-doped Cs<sub>3</sub>Bi<sub>2</sub>Br<sub>9</sub>(SpS) in Figure 4.1, Sn-doped Cs<sub>3</sub>Bi<sub>2</sub>Br<sub>9</sub> produced by Solid-state Grinding (SsG) can obtain good quality of phase structures. However, extra tiny peaks at 20= 28.4° and 33° were seen due to unreacted SnBr<sub>2</sub> left behind which were compared to SnBr<sub>2</sub>(ICSD code 411177)<sup>122</sup>. X-ray diffraction pattern showed no secondary phases, which means no sign of Cs<sub>2</sub>SnBr<sub>6</sub> here. This also means mixed valency doping could be conducted in an easier manufacturing process at lower cost.

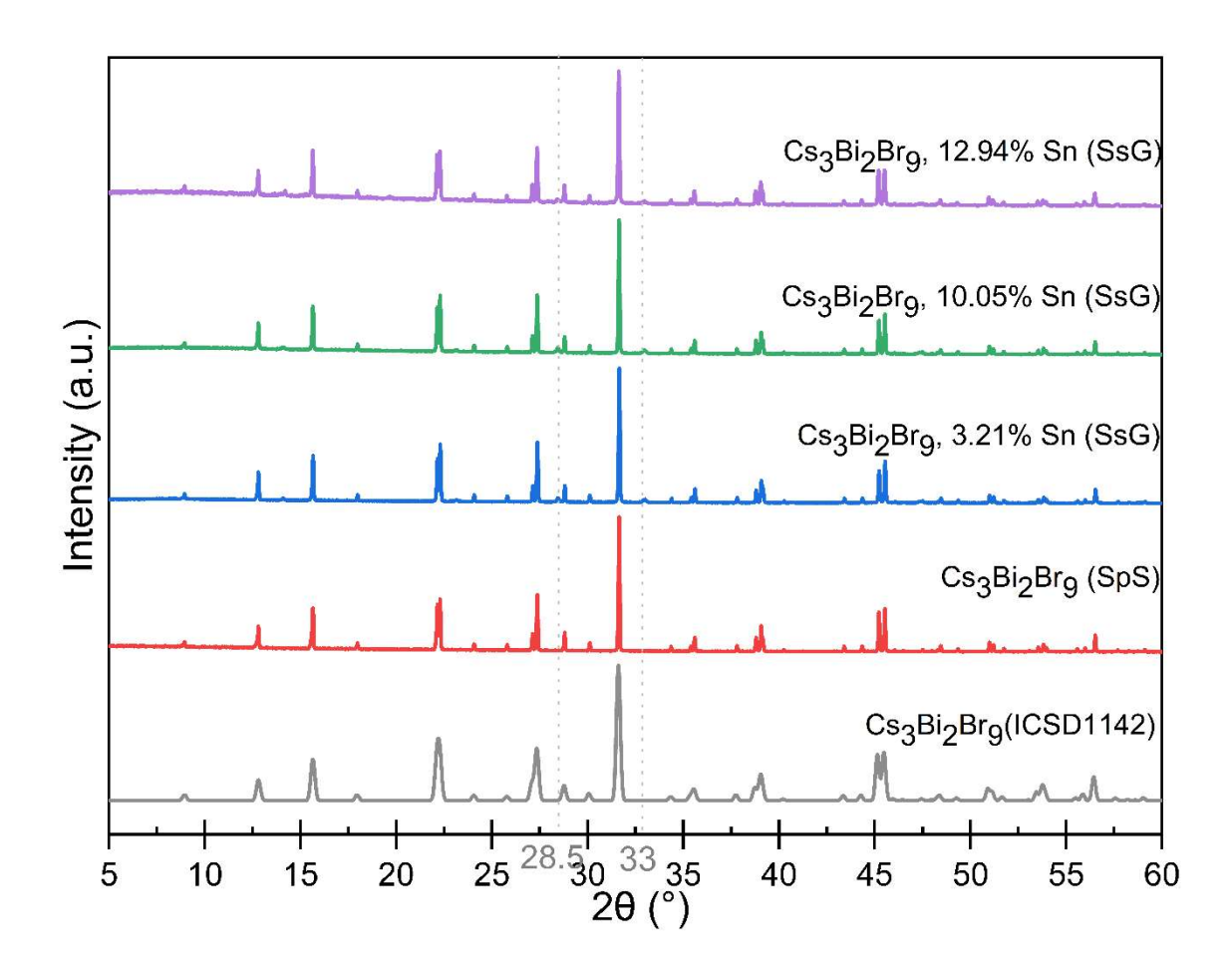


Figure 4.3 The PXRD patterns of Sn-doped Cs<sub>3</sub>Bi<sub>2</sub>Br<sub>9</sub> materials (analytic Sn%=5,12 and 25) produced by Solid-state Grinding (SsG).

XPS was used to study the oxidation sate of Bi, the oxidation states of Sn and binding energy differences between each element. Bi 4f spectra and Sn 3d spectra of samples were shown in Figure 4.4 and 4.5 individually. C 1s was calibrated to 486.8 eV by charge correction to avoid shifting of XPS spectra.

In Figure 4.4. the binding energies of Bi 4f located at 160.3 eV and 165.6 eV for pure Cs<sub>3</sub>Bi<sub>2</sub>Br<sub>9</sub>. The binding energy peaks of Sn-doped Cs<sub>3</sub>Bi<sub>2</sub>Br<sub>9</sub> all shifted to the lower region by ~1eV. To confirm the statement of shifting, the binding energy differences between the Bi 4f<sub>7/2</sub> and Br 3d<sub>5/2</sub> peaks in all undoped and Sn doped Cs<sub>3</sub>Bi<sub>2</sub>Br<sub>9</sub> were calculated. The binding energy differences between the Bi 4f<sub>7/2</sub> and Br 3d<sub>5/2</sub> peaks in undoped and Sn doped Cs<sub>3</sub>Bi<sub>2</sub>Br<sub>9</sub>(Sn=0%, 3.21%,12.94%) are 90.8 eV, and 10.05% Sn doped Cs<sub>3</sub>Bi<sub>2</sub>Br<sub>9</sub> is 90.1 eV which may cause by the excitation of the laser beam. Doping Sn (II) may cause the shifting (~1eV) of the XPS spectra due to addition of valence electrons. However, the undoped sample and Sn doped sample shared the same binding energy difference which also indicated that mixed valency of Sn<sup>2+</sup> and Sn<sup>4+</sup>did not change chemical environment of Bi and Br.

Also, the tiny humps next to Bi 4f binding energy peaks represented as Bi metal. The appearance of Bi metal in XPS is due to the instability of the material under incident X-rays resulting in photo reduction to Bi metal. The intensity of binding energy peaks of Bi metal increased when Sn doped in Cs<sub>3</sub>Bi<sub>2</sub>Br<sub>9</sub>.

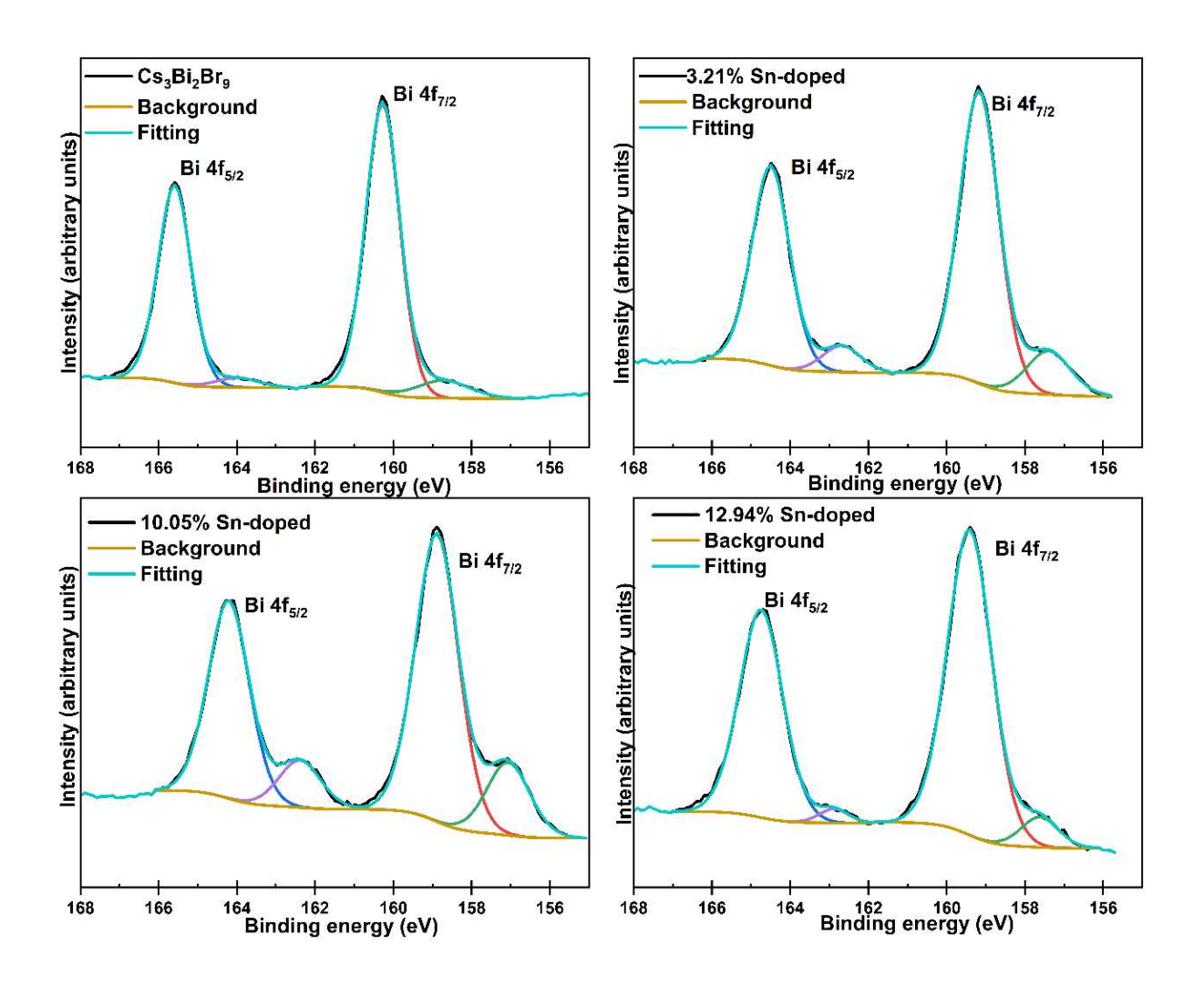


Figure 4.4 Bi 4f spectra of pure Cs<sub>3</sub>Bi<sub>2</sub>Br<sub>9</sub> material and Sn (Sn= 3.21%, 10.05% and 12.94%) doped Cs<sub>3</sub>Bi<sub>2</sub>Br<sub>9</sub> materials.(XPS survey of Cs<sub>3</sub>Bi<sub>2</sub>Br<sub>9</sub> was attached in Appendix 6.4 for additional information.)

With the assumption of no significant change in the chemical environment of Br in pure Cs<sub>3</sub>Bi<sub>2</sub>Br<sub>9</sub> material and Sn doped Cs<sub>3</sub>Bi<sub>2</sub>Br<sub>9</sub> materials, the binding energy difference between Sn 3d<sub>5/2</sub> and Br 3d<sub>5/2</sub> can be interpreted as a change caused by doping Sn<sup>2+</sup>. Sn 3d spectrum of Cs<sub>2</sub>SnBr<sub>6</sub> was used as a reference since it only contains Sn(IV). Here Cs<sub>2</sub>SnBr<sub>6</sub> was synthesised as descried in Section 3.11. The binding energy difference between Sn 3d<sub>5/2</sub> and Br 3d<sub>5/2</sub> of Cs<sub>2</sub>SnBr<sub>6</sub> is 418.8 eV which is used a counterpart for the Sn<sup>4+</sup> solely existed situation. This was used

as a reference to confirm the increase of the peak area of Sn 3d<sub>5/2</sub> and Br 3d<sub>5/2</sub> when tin was doped into Cs<sub>3</sub>Bi<sub>2</sub>Br<sub>9</sub>, which tries to prove the existence of mixed valencies (Sn<sup>2+</sup> and Sn<sup>4+</sup>). This is because the existence of the mixed valences Sn<sup>2+</sup> and Sn<sup>4+</sup>, which can also be explained as the width of the peaks getting wider. Also, the binding energy difference between Sn 3d<sub>5/2</sub> and Br 3d<sub>5/2</sub> is increasing from 418.8 eV to 418.9 eV to 419.1 eV as the doping Sn% enhanced in the Sn-doped samples from Cs<sub>2</sub>SnCl<sub>6</sub> to 3.2% Sn-doped Cs<sub>3</sub>Bi<sub>2</sub>Br<sub>9</sub> to 12.9% Sn-doped Cs<sub>3</sub>Bi<sub>2</sub>Br<sub>9</sub>.

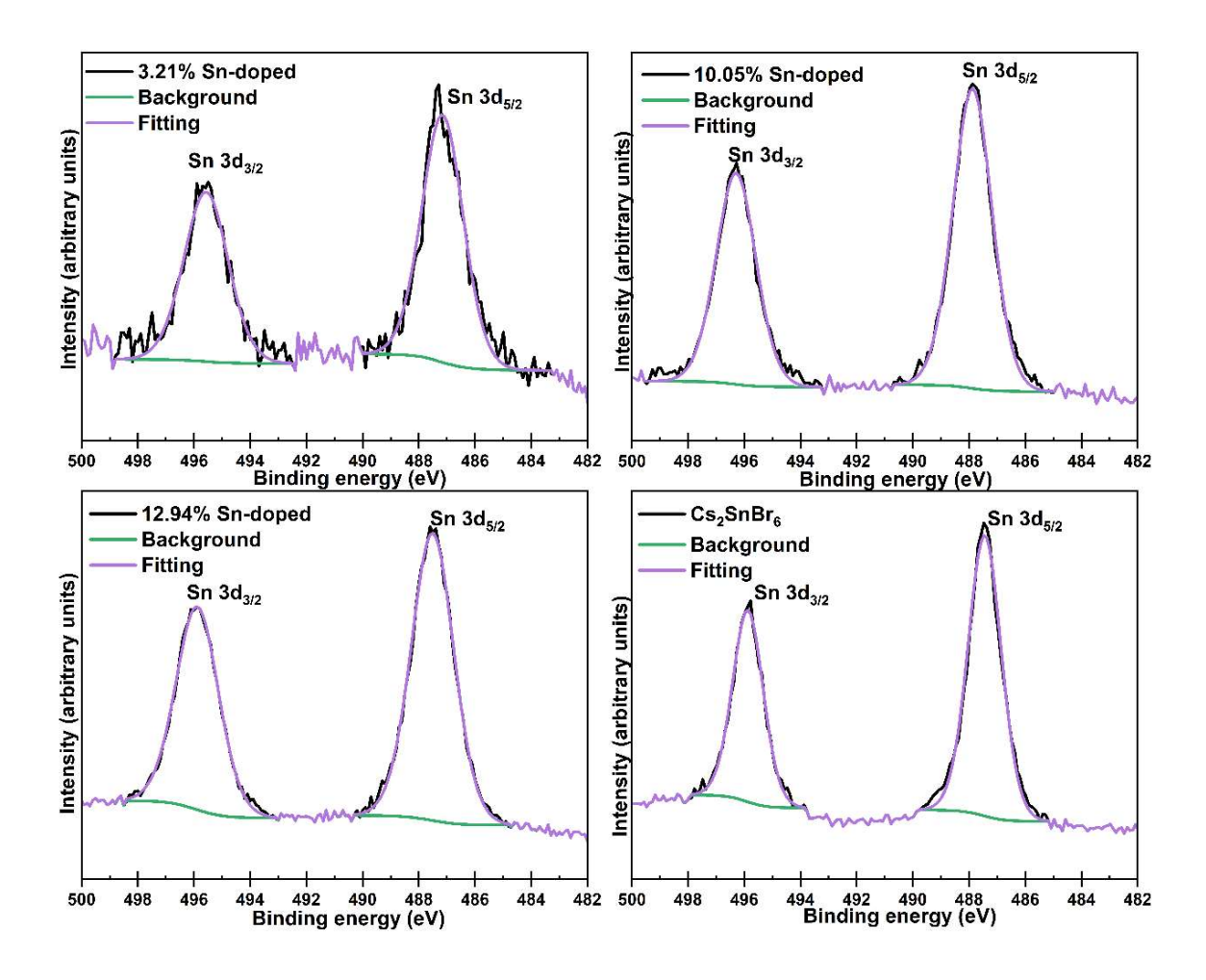


Figure 4.5 Sn 3d spectrum of pure Cs<sub>2</sub>SnBr<sub>6</sub> material and Sn (Sn= 3.21%, 10.05% and 12.94%) doped Cs<sub>3</sub>Bi<sub>2</sub>Br<sub>9</sub> materials

The average amount of the full width at half-maximum (FWHM) of the Cs 3d<sub>5/2</sub> core line in Sn-doped Cs<sub>3</sub>Bi<sub>2</sub>Br<sub>9</sub> materials is 1.43 eV, and that of Cs<sub>2</sub>SnBr<sub>6</sub> is 1.53 eV. The full width at half-maximum (FWHM) of the Sn 3d<sub>5/2</sub> core lines in Sn doped Cs<sub>3</sub>Bi<sub>2</sub>Br<sub>9</sub> materials is larger than that of Cs<sub>2</sub>SnBr<sub>6</sub>. The full width at half-maximum (FWHM) of the Sn 3d<sub>5/2</sub> core line Cs<sub>2</sub>SnBr<sub>6</sub> of is 1.37 eV. The amount of the full width at half-maximum (FWHM) of the Sn 3d<sub>5/2</sub> core line in 3.21%Sn doped Cs<sub>3</sub>Bi<sub>2</sub>Br<sub>9</sub> materials is 1.50 eV. The amount of the full width at half-maximum (FWHM) of the Sn 3d<sub>5/2</sub> core line in 10.05%Sn doped Cs<sub>3</sub>Bi<sub>2</sub>Br<sub>9</sub> materials is 1.56 eV. The amount of the full width at half-maximum (FWHM) of the Sn 3d<sub>5/2</sub> core line in 12.94%Sn doped Cs<sub>3</sub>Bi<sub>2</sub>Br<sub>9</sub> materials is 1.71 eV. The FWHM is increasing by the increase of analytic doping amount of Sn<sup>2+</sup>. The small chemical shift between Sn<sup>2+</sup> and Sn<sup>4+</sup> caused the challenge to determine the peaks with the corresponding Sn valencies but the difference in the full width at half-maximum (FWHM) of the Sn 3d<sub>5/2</sub> core line of these compounds may be interpreted as the existence of the low binding energy peak of Sn<sup>2+</sup>.

The band gap of Cs<sub>3</sub>Bi<sub>2</sub>Br<sub>9</sub> has been recorded by many authors with different values of direct and indirect band gaps using Tauc method to analyse their UV-vis data. Giovilli et al. stated that the direct and indirect band gaps of Cs<sub>3</sub>Bi<sub>2</sub>Br<sub>9</sub> are 2.58 eV and 2.46 eV by Tauc method.<sup>124</sup> The calculated direct bandgap of 2.66 eV was stated by Krajewska et al. using the HSE06+SOC hybrid DFT functional.<sup>88</sup> Also, the Cs<sub>3</sub>Bi<sub>2</sub>Br<sub>9</sub> crystallised in the hexagonal phase with a band gap of 2.83 eV was recorded by Akinbami et al., which was measured by converting the wavelength into absorption energy as estimated from UV-vis peaks using Plank equation.<sup>125</sup> The difficulty of analysing the band gaps of

Cs<sub>3</sub>Bi<sub>2</sub>Br<sub>9</sub> is to define the first slope of the absorption spectrum as the exciton peak or the interband transition.

If the first slope of the Tauc plot was indicated as the band gap in Figure 4.6(a), the direct and indirect band gaps of pure Cs<sub>3</sub>Bi<sub>2</sub>Br<sub>9</sub> are 2.66 eV and 2.59 eV resulted by Tauc method. This is not matched to the statements mentioned by Giovilli et al. and Akinbami et al but was matched to the statements stated by Krajewska et al.<sup>88</sup> There is a chance that the first slope here may not be a band gap.

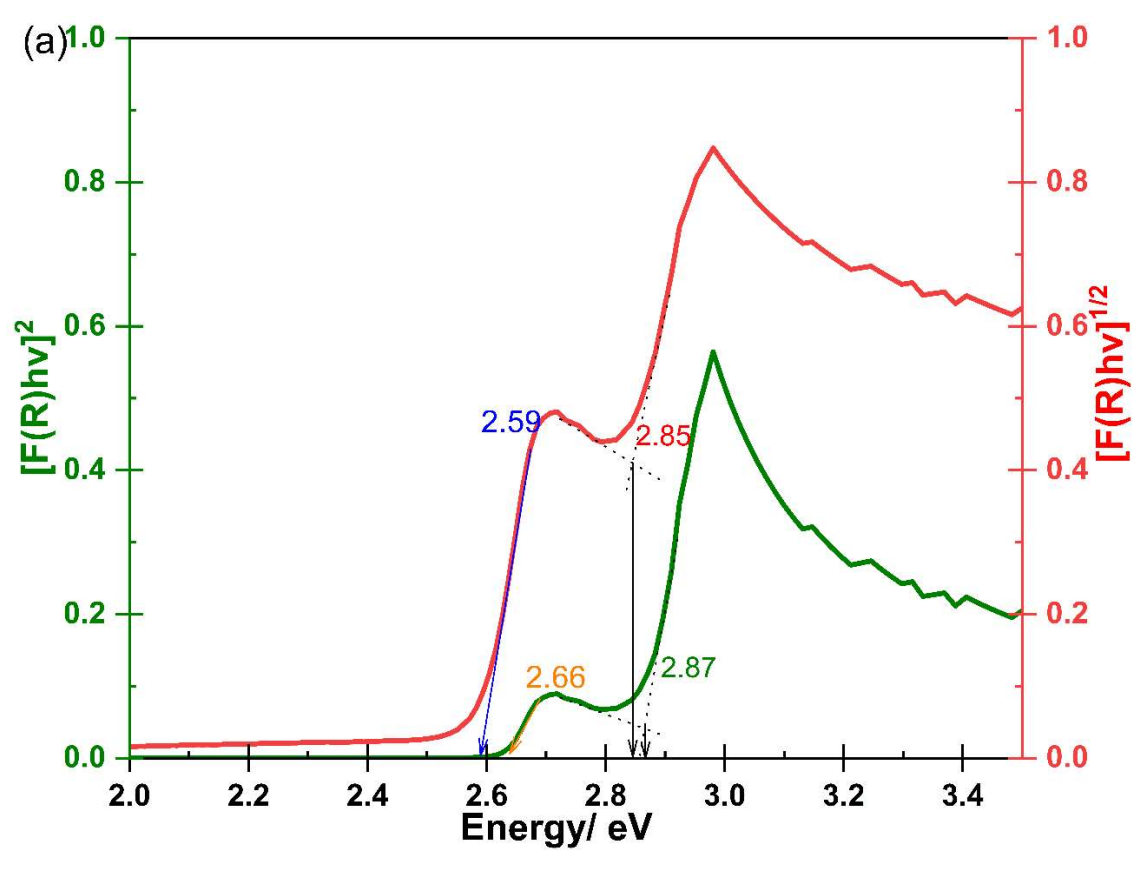
In this case, if the first slope may not be the band gap, it can be an exciton absorption close to the interband absorption edge according to the case of MA<sub>3</sub>Bi<sub>2</sub>Br<sub>9</sub> stated by Jia et al.<sup>126</sup> If the second slope was assumed as the band gap, the values of the direct and indirect band gaps from the Tauc plot are 2.85 eV and 2.87eV. Also, there is another way to measure band gaps by Elliot theory.

The exciton absorption and the inter-band absorption edge were modelled by Elliot theory shown in Figure 4.6(b). Elliot theory was mentioned in Section 2.4.3. The exciton binding energy peak was modelled by a Dirac delta function, and the continued interband absorption was modelled by a Heaviside step function. The sum of these two functions was fitted to the diffuse reflectance spectrum from undoped Cs<sub>3</sub>Bi<sub>2</sub>Br<sub>9</sub>. The exciton peak is located at 2.707 eV, and the band gap is 2.903 eV which was taken as the midpoint of the Heaviside step function. When the band gaps calculated by Tauc method were compared to the band gap of 2.903 eV resulted by Elliot theory, the direct band gap calculated by Tauc method

using the second slope in Figure 4.6(a) is close to the resulted band gap modelled by Elliot theory with the difference of 0.033 eV.

The exciton energy is the difference between the exciton peak and the band gap which is 230 meV. However, this value is much smaller than the approximation estimated by Bass et al., which is 940 eV.<sup>127</sup> Bass et al. stated the polycrystalline powder of Cs<sub>3</sub>Bi<sub>2</sub>Br<sub>9</sub> showed a direct onset of optical absorption at 2.65 eV. The exciton energy was estimated as the difference between the maxima of the exciton peak and the leading edge of the subsequent plateau on the Tauc plot. However, the method of calculating exciton energy here recorded by Bass et al. is not clear.

The further research of this topic is required to improve the accuracy of the data. Elliot model can fit the diffuse reflectance spectrum well to retrieve an accurate exciton energy and a band gap with a fair explanation for the exciton energy than that of Tauc method in this case. For Tauc plot, the indication of the direct and indirect band gap needs to be known first to plot the correct graphs. For Elliot model. It may not for other materials as their fitting curves may go off or as more than one exciton peak existed in their diffuse reflectance spectrums. Extra Dirac functions would need to be added in for later situations to model it by Elliot theory. Plus, Elliot model was also used in section 4.2.2 to measure the exciton energy and the band gap of Cs<sub>3</sub>Bi<sub>2</sub>Cl<sub>9</sub> perfectly.



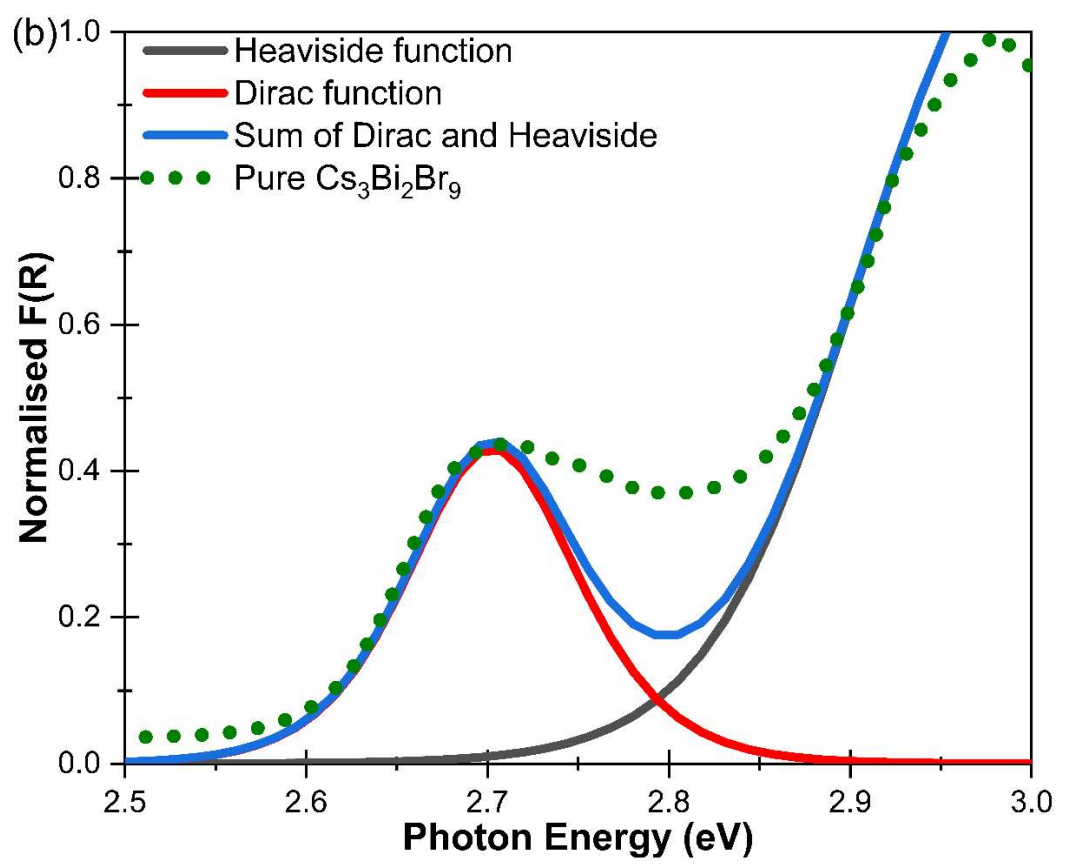


Figure 4.6 (a)Demonstration of direct and indirect bandgap energy calculation from Tauc-analysis for pure Cs<sub>3</sub>Bi<sub>2</sub>Br<sub>9</sub> and (b) A diffuse reflectance spectrum from undoped Cs<sub>3</sub>Bi<sub>2</sub>Br<sub>9</sub> via a solution-phased synthesis which is treated with the Kubelka Munk function (green points). The optical absorption is modelled using the Elliot model in blue line, consisting of an exciton peak modelling by Dirac function in red and a continuum absorption modelling by Heaviside function in black.

On the other hand, the band gaps and exciton energies cannot be determined accurately in the doped samples, due to the strong absorption band that appears upon doping. The existence of mixed valencies (Sn<sup>2+</sup> and Sn<sup>4+</sup>) in samples Sn doped Cs<sub>3</sub>Bi<sub>2</sub>Br<sub>9</sub> caused the intervalence charge transfer (IVCT) absorption. Previous XPS analysis on the samples verified the strong optical absorption is due to IVCT. The optical absorption caused by IVCT can be measured by Marcus-Hush theory for weekly-coupled symmetrical mixed valency system,

Equation 4.1

Where Ea=energy barrier of thermal electron transfer. For one-electron transfer in the system of Sn doped Cs<sub>3</sub>Bi<sub>2</sub>Br<sub>9</sub>, the ground state (on the left side of the arrow) and the excited state (on the right side of the arrow) are shown in the oxidation states below.

$$Sn^{2+} +e \rightarrow Sn^{3+}$$

The optical absorption caused by IVCT of Sn2+ and Sn4+ can be measured by

## V<sub>max</sub>=4Ea-Eo (Eo≠0)

Where Eo is the equilibrium energy between initial and final state due to asymmetry and many electrons transfer. Here Eo represents the difference in energy between the ground state and excited state of Sn. This explains the idea on how IVCT can cause optical absorption.

The first hump of the optical curves was interpreted as exciton energies in Figure 4.7. The optical absorption spectra of pure Cs<sub>3</sub>Bi<sub>2</sub>Br<sub>9</sub> and Sn-doped Cs<sub>3</sub>Bi<sub>2</sub>Br<sub>9</sub> can also observe the trend. The band gap would get smaller when the Sn doping amount was higher. For example, the gradient of the optical curve of pure Cs<sub>3</sub>Bi<sub>2</sub>Br<sub>9</sub> is flatter than that of Sn doped Cs<sub>3</sub>Bi<sub>2</sub>Br<sub>9</sub> samples. It resulted the band gap of Sn doped Cs<sub>3</sub>Bi<sub>2</sub>Br<sub>9</sub> samples would be smaller than that of pure Cs<sub>3</sub>Bi<sub>2</sub>Br<sub>9</sub>. Plus, from visual perspective, undoped Cs<sub>3</sub>Bi<sub>2</sub>Br<sub>9</sub> is pale yellow in appearance. With a very small amount of Sn doping, Sn-doped samples turned darker brown. This also indicated signs of improving light absorption.

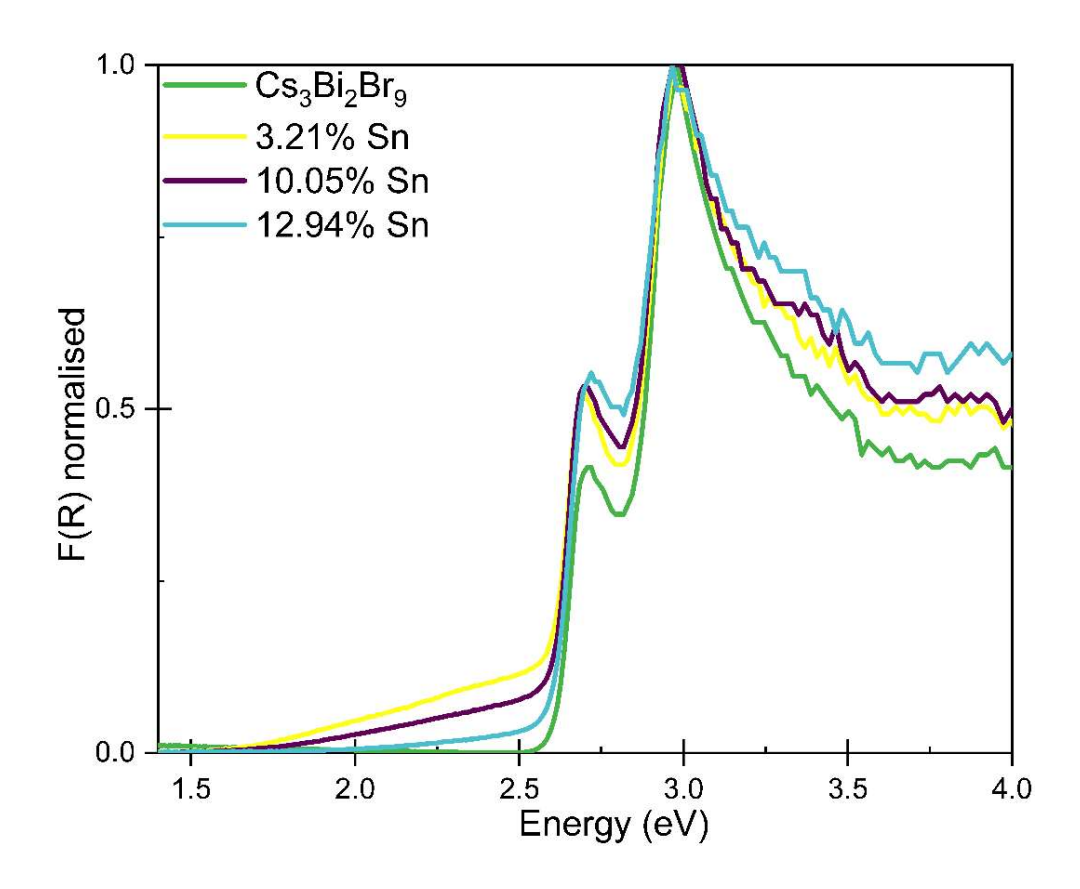


Figure 4.7 Optical absorption spectra of pure Cs<sub>3</sub>Bi<sub>2</sub>Br<sub>9</sub> and Sn-doped Cs<sub>3</sub>Bi<sub>2</sub>Br<sub>9</sub>.

## 4.1.3 Conclusion

In conclusion, the mixed valency doping Sn(II) into the 2D hybrid layered perovskite Cs<sub>3</sub>Bi<sub>2</sub>Br<sub>9</sub> using a room temperature mechanochemical synthesis can achieve same or better results than the solution-phased synthesis with easier manufacturing procedures and less time-consuming. A spontaneous colour change from pale yellow to dark brown was observed during the reaction. Sn doping technique can enhance light absorption, which was attributed to mixed valence doping of Sn(II) and Sn(IV) oxidation state on the Bi site. Different valencies of Sn introduced the intervalence charge transfer (IVCT) into Cs<sub>3</sub>Bi<sub>2</sub>Br<sub>9</sub>. The IVCT process provides an additional energy transition in the visible region,

resulting in a significant enhancement in light absorbance. Powder X-ray diffraction (PXRD) showed that no secondary phases were formed for Sn-doped materials when the concentration of Sn<sup>2+</sup> is low; however, when the concentration of Sn<sup>2+</sup> is high, Cs<sub>2</sub>SnCl<sub>6</sub> was formed. Krajewskaet al. stated the analytic concentration is approximately linear to nominal composition at low nominal Sn%. Cs<sub>2</sub>SnBr<sub>6</sub> was seen at a nominal 50 Sn% (which is analytic 23.5 Sn%).<sup>88</sup> X-ray photoelectron spectroscopy (XPS) suggests the presence of Sn (II) and Sn (IV) oxidation states, while Bi remains Bi (III). This mixed valency ion doped vacancy-ordered triple perovskites showed the existence of the inter-valence charge transfer transition by the presence of Sn (II) and Sn (IV) which provides extra energy transition resulting an improvement of light absorption of the material.

## 4.2 Cs<sub>3</sub>Bi<sub>2</sub>Cl<sub>9</sub> Materials doping Sn<sup>2+</sup>

Cs<sub>3</sub>Bi<sub>2</sub>Cl<sub>9</sub> is a material that can be used for a wide range of applications such as solar cells, photocatalysis, photodetectors, and light-emitting diodes (LEDs). <sup>128129130</sup> The bandgap influences the electronic and optical properties of the perovskite material. The paper explores how surface engineering approaches such as doping impact the bandgap of perovskite materials and subsequently affect their light absorption ability.

## 4.2.1 Experimental Methodology

## A Solution-phased synthesis method of Cs<sub>3</sub>Bi<sub>2</sub>Cl<sub>9</sub> doping Sn<sup>2+</sup>

I mmol Cs<sub>3</sub>Bi<sub>2</sub>Cl<sub>9</sub> can be produce via a solution-phased synthesis. The whole experiment was carried out in air. An acidic solution of CsCl was produced by reacting 1.5 mmol Cs<sub>2</sub>CO<sub>3</sub> with 2 mL aqueous HCl (3M). Separately, 2 mmol BiCl<sub>3</sub> was dissolved in 5 mL aqueous HCl (3M) and stirred on a heating mantle at 80 °C. After 10 minutes of stirring, the acidic CsCl solution was added to the BiCl<sub>3</sub> solution. An immediate white precipitate appeared, which was isolated by filtration, washed with ethanol, and stored in air.

The solution-phased synthesis of Sn doped Cs<sub>3</sub>Bi<sub>2</sub>Cl<sub>9</sub> was carried out by mixing the desired ratio of SnCl<sub>2</sub> and BiCl<sub>3</sub> in solution, followed by reaction with acidic aqueous CsCl solution. For example, to obtain 5g Cs<sub>3</sub>Bi<sub>2</sub>Cl<sub>9</sub> doped a nominal Sn dopant concentration of 5%, 0.5 mmol SnCl<sub>2</sub> and 9.5 mmol BiCl<sub>3</sub> were dissolved by stirring in 40 mL HCl (3 M) at 80 °C, followed by addition of the CsCl solution. The acidic aqueous CsCl solution was prepared by dissolving 7.5 mmol Cs<sub>2</sub>CO<sub>3</sub> into 25 mL HCl (3M). The concentrated HCl solution would increase the potential of the formation of Cs<sub>2</sub>SnCl<sub>6</sub> in the process of doping SnCl<sub>2</sub> into Cs<sub>3</sub>Bi<sub>2</sub>Br<sub>9</sub>.

Samples with varying nominal amounts of Sn were synthesised in this way.

(Nominal Sn% =[Sn]/([Sn]+[Bi])=0,0.05,0.12,0.25,0.4 and 0.5)

When Sn was present, yellow precipitate was formed. The product was isolated by filtration, washed with ethanol, and stored in air. Note that the only species of tin added to the reaction was Sn (II).

## • Solid-state grinding of Sn-doped Cs<sub>3</sub>Bi<sub>2</sub>Cl<sub>9</sub>

B-site mixed-valent Sn (II) / Sn (IV) doped  $Cs_3Bi_2Cl_9$  microcrystals ( $Cs_3(Sn_xBi_1-x)_2Cl_9$ ) were prepared by mechanochemical reaction (solid-state grinding) at room temperature in air from stoichiometric amounts of  $SnCl_2$  and the as-made  $Cs_3Bi_2Cl_9$ . For example, 5% Sn-doped ( $Cs_3(Sn_xBi_{1-x})_2Cl_9$ ) was prepared by grinding  $SnCl_2$  powder (0.053 mmol, 0.011g) together with the as-synthesised white crystal powder  $Cs_3Bi_2Cl_9$  (0.500 mmol, 0.567g) in an agate mortar until two solids were homogeneously mixed. No solvent was added to the reaction. The colour of the reactants turned yellow immediately upon grinding. Samples were made with Sn contents of x = 0, 0.05, 0.12, 0.25. All samples were stored in glass sample vials in air.

To further improve homogeneity of dopant and introduce crystallinity, half of each as-synthesised ( $Cs_3(Sn_xBi_{1-x})_2Cl_9$ ) sample (including x=0,  $Cs_3Bi_2Cl_9$ ) were heated at 200 °C in a furnace in air for two hours.

#### 4.2.2 Results and Discussion

The PXRD data of Cs<sub>3</sub>Bi<sub>2</sub>Cl<sub>9</sub> made via the solution-phased synthesis can dope Sn but in the orthorhombic structure. This means that not only samples in the trigonal structure such as Cs<sub>3</sub>Bi<sub>2</sub>Br<sub>9</sub> and MA<sub>3</sub>Bi<sub>2</sub>Br<sub>9</sub> can dope Sn<sup>2+</sup>, Sn<sup>2+</sup> doping but also worked for Cs<sub>3</sub>Bi<sub>2</sub>Cl<sub>9</sub>. Different characterisation techniques were used to define crystal structure, measure the Sn%, and detect electronic properties and light absorption properties. This would be helpful for the further study of doping mixed valencies into vacancy-ordered triple perovskite materials and for the expansion of the knowledge of different ways to dope mixed valencies.

As-produced Cs<sub>3</sub>Bi<sub>2</sub>Cl<sub>9</sub> white crystal powder displayed a powder diffraction pattern in Figure 4.8 which is alike to the reported structure found in ICSD database reported by Morgan et al.<sup>131</sup>. It is an orthorhombic structure with the Pmna space group. It is also visualised as 1D chains of clusters of [BiCl<sub>6</sub>]<sup>3</sup>-octahedra. Rietveld refinement was processed by GSAS II, starting with the model of Morgan et al. A small amount of preferred orientation (100) was inputted by using March-Dollase algorithm to fit in the peak intensities.

The locations of the Braggs peaks of the XRD pattern of sample  $Cs_3Bi_2Cl_9$  was identical to the reported structure mentioned above. The refined lattice parameters of the undoped sample  $Cs_3Bi_2Cl_9$  were a=18.6397(7) Å, b= 7.6186(5)Å, c=13.19194(9) Å. These data were approximately matched to those provided by Morgan et al from ICSD database (a=7.6182 Å, b=13.186 Å, c=13.186 Å, c=13.186

18.644 Å). No unidentified peaks were seen; a final Rw value of 4.438% was obtained and final reduced chi<sup>2</sup> was 0.85.

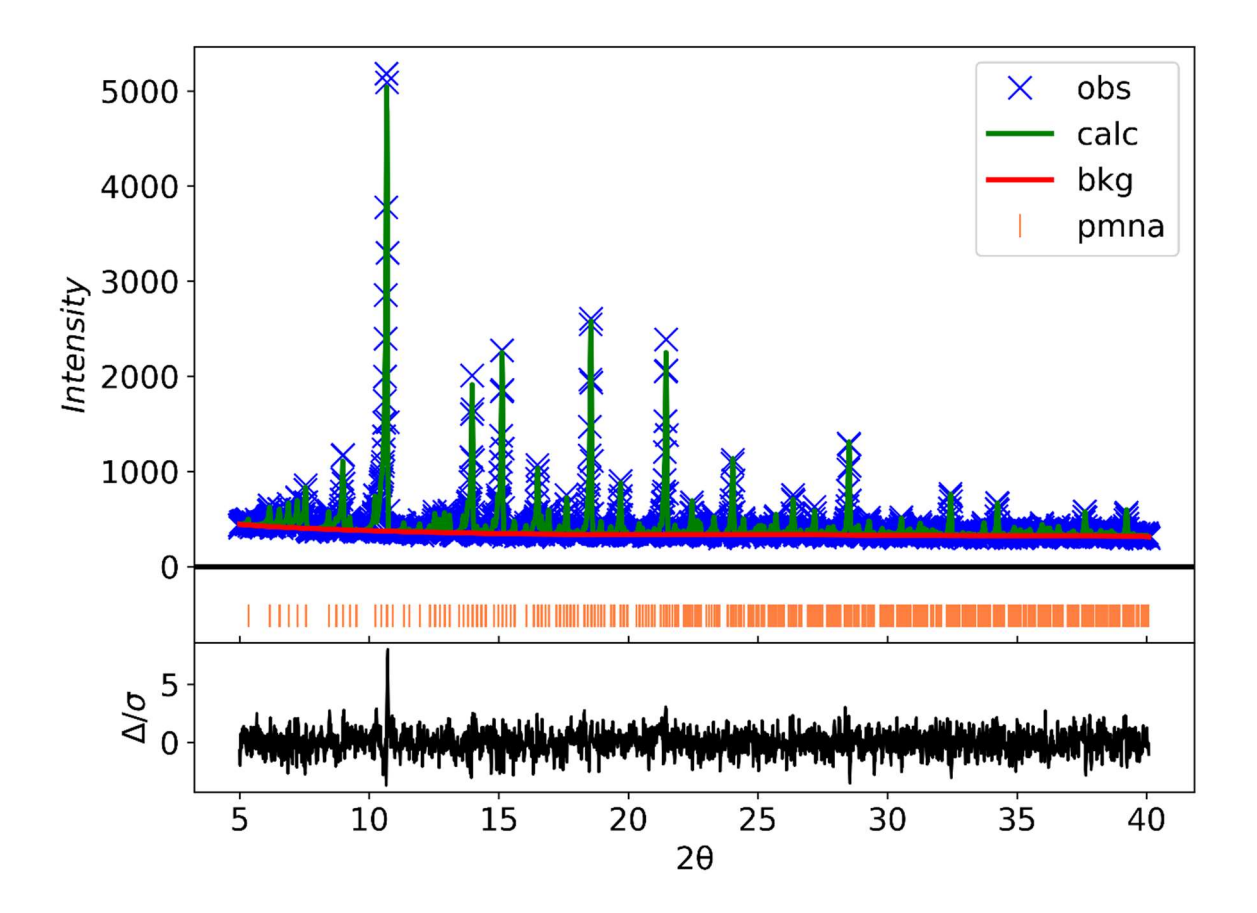


Figure 4.8 The powder XRD pattern of  $Cs_3Bi_2Cl_9$  produced by the solution-phased synthesis. The model (green line) was refined from the structure reported by Morgan et al. The background is shown in red, and the residual is in black, and it shows how much difference between the sample and the ICSD data in Orange. Orange dash marks show positions of reflections.

Powder XRD measurements on the as-synthesised samples were consistent with a Pmna one dimensional vacancy-ordered triple perovskite structure in Figure 4.9. However, a Braggs peak formed when  $2\theta = 11.03^{\circ}$  in the XRD patterns of nominal 40, 50% Sn doped samples. Cs<sub>2</sub>SnCl<sub>6</sub> might form during the solution-phased synthesis which was observed from GSAS II refinement. Around 1 wt%

of Cs<sub>2</sub>SnCl<sub>6</sub> was observed. A slight increase in a parameter and the b parameter was observed with increasing Sn-doped concentration, and the c parameter remained no significant change. Around 10 wt% Cs<sub>2</sub>SnCl<sub>6</sub> was observed in the nominal 40 Sn% doped sample which was also matched to the appeared peak in Figure 4.9. It also suggests that SnCl<sub>2</sub> preferred to react with CsCl to form Cs<sub>2</sub>SnCl<sub>6</sub> instead of BiCl<sub>3</sub> when Sn concentration is increasing to a certain point (~40 nominal Sn%).

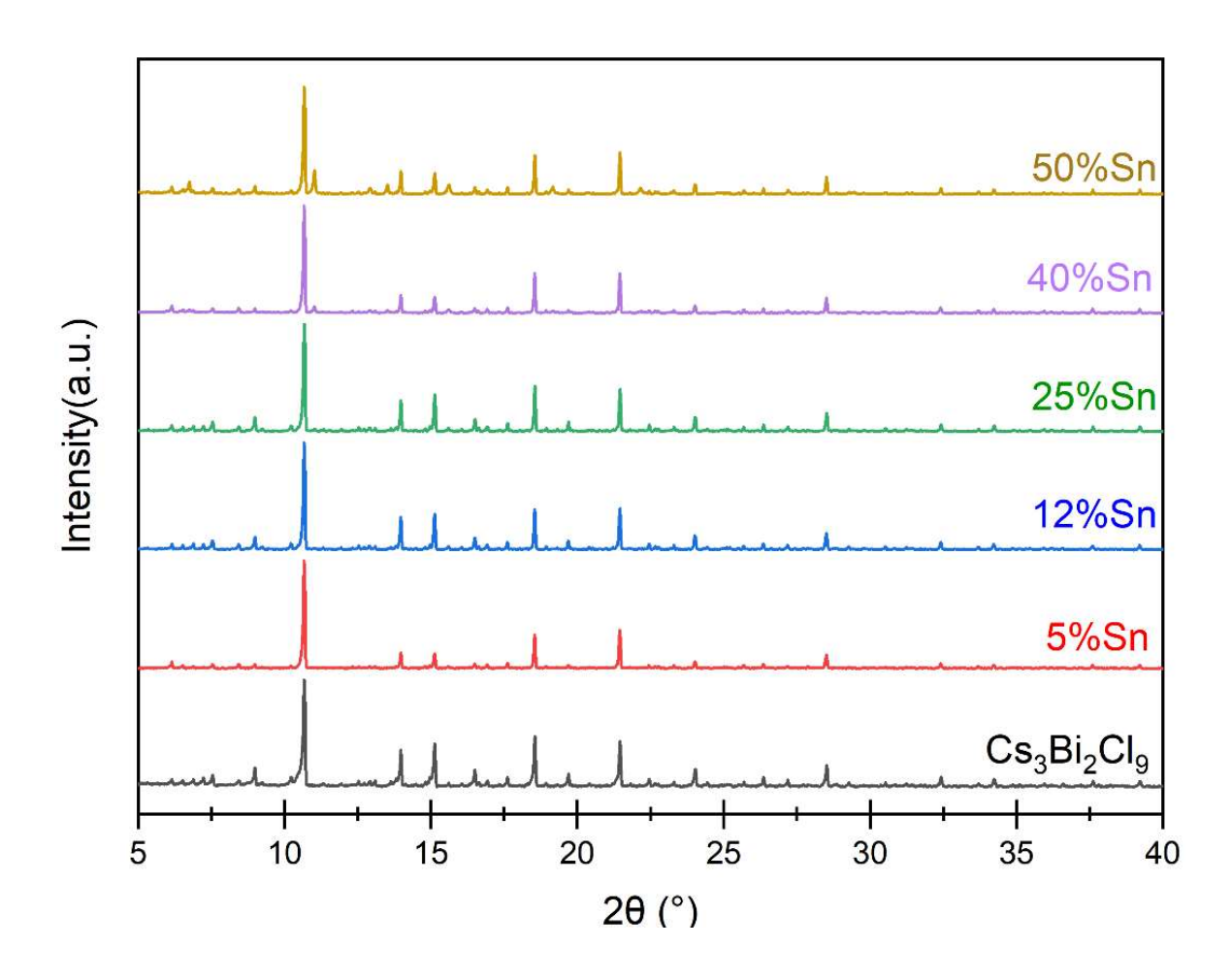


Figure 4.9 Powder XRD patterns from undoped and Sn-doped Cs<sub>3</sub>Bi<sub>2</sub>Cl<sub>9</sub> crystal powders (SpS). Nominal Sn concentration of samples was displayed at the bottom in the legend.

The cell volume parameters with errors were retrieved after refinements by GSAS 2 software. According to Figure 4.9, no secondary phase was detected until 40% Sn doping into Cs<sub>3</sub>Bi<sub>2</sub>Cl<sub>9</sub> which was confirmed by PXRD data. The absence of the extra peak in the PXRD pattern of samples doping Sn in 0%, 5%, 12% and 25% showed that Sn (II) content was doped into the unit cell structure without secondary phases. In Figure 4.10, the correlation between the variation in the unit cell volume and nominal Sn content in 0%, 5%, 12% and 25% is shown above. Final Rwp values were below 8% for samples doping Sn percent in 0%, 5%,12% and 25%. There was a small increase in the lattice parameters with increasing Sn content from 0% Sn with the cell volume,1873.30(4) Å<sup>3</sup> to 12% Sn with the cell volume,1875.65(5) Å<sup>3</sup>, then dropping down at the sample doping nominal amount of 25% Sn with the cell volume, 1873.21(6) Å<sup>3</sup>. There was no change overlapped within the error bars.

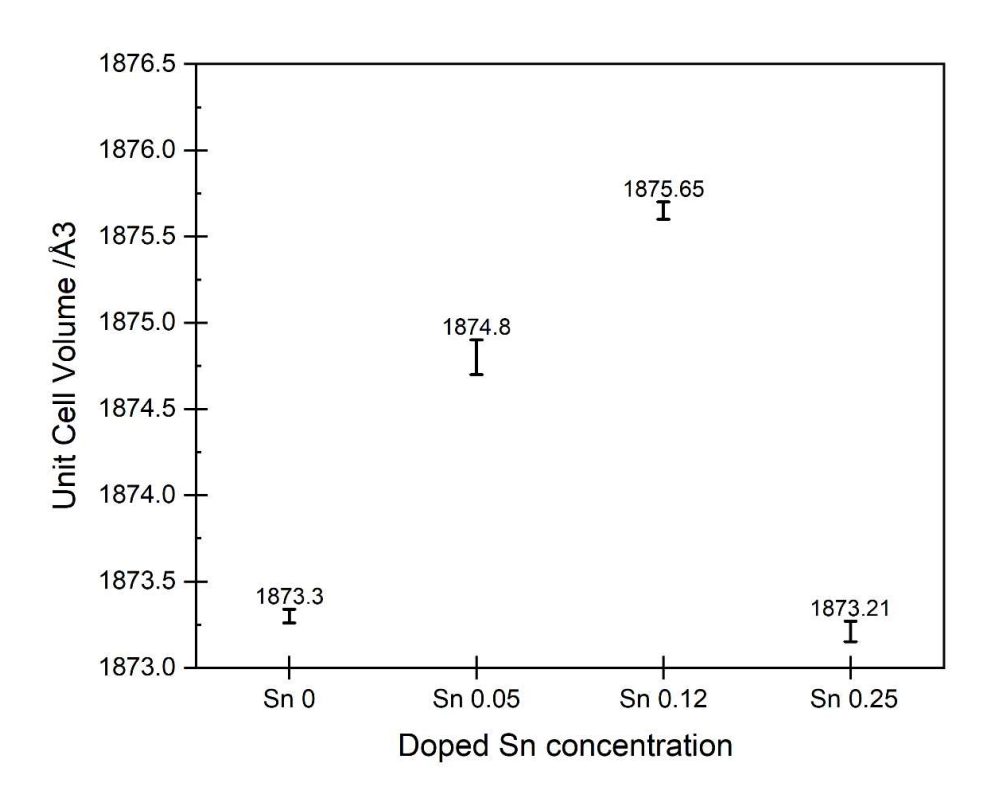


Figure 4.10 The variation in unit cell volume with nominal Sn content in Cs<sub>3</sub>Bi<sub>2</sub>Cl<sub>9</sub>.

Error bars are plus and minus three times the standard deviation.

XRF data of Samples was used to measure the Sn content in bulk and to compare with the weight fractions retrieved by GSAS 2 software to analyse the Sn content doped into Cs<sub>3</sub>Bi<sub>2</sub>Cl<sub>9</sub> via Solution phased Synthesis. Analytic Sn content was calculated by the difference between the Sn content (wt%) in bulk measured by XRF Spectrometer and the weight fraction (wt%) of Cs<sub>2</sub>SnCl<sub>6</sub> retrieved by GSAS 2 software, which was consumed by a certain amount of Sn (IV) but not actually doped into Cs<sub>3</sub>Bi<sub>2</sub>Cl<sub>9</sub> material.

The correlation between Nominal Sn content and Analytic Sn content doped into Cs<sub>3</sub>Bi<sub>2</sub>Cl<sub>9</sub> was shown in Figure 4.11 above. The nominal Sn doped content in 0%, 5%, 12% and 25% was corresponded respectively to the analytic Sn doped content in 0%, 1.25%, 2.39% and 3.90%. The analytic Sn amount doped into Cs<sub>3</sub>Bi<sub>2</sub>Cl<sub>9</sub> was much less than the nominal Sn content. However, there was an increase in Sn respectively around 0-4%, Which could also reflect in the colour of material since Cs<sub>3</sub>Bi<sub>2</sub>Cl<sub>9</sub> is in plain white and Sn doped Cs<sub>3</sub>Bi<sub>2</sub>Cl<sub>9</sub> is in pale yellow.

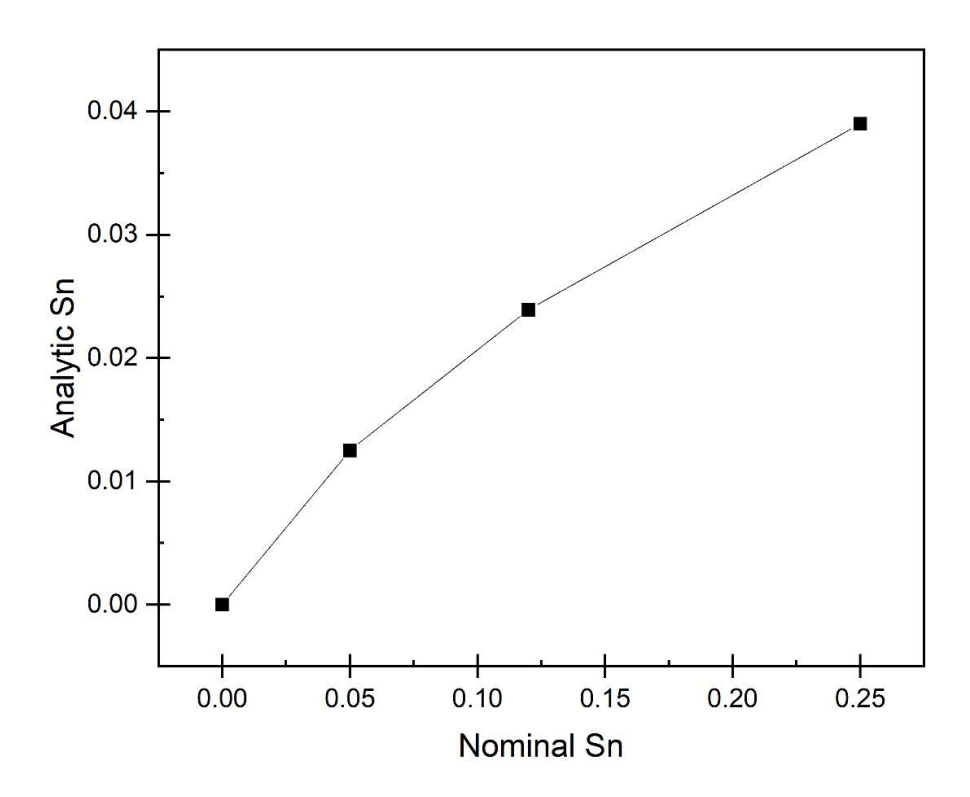


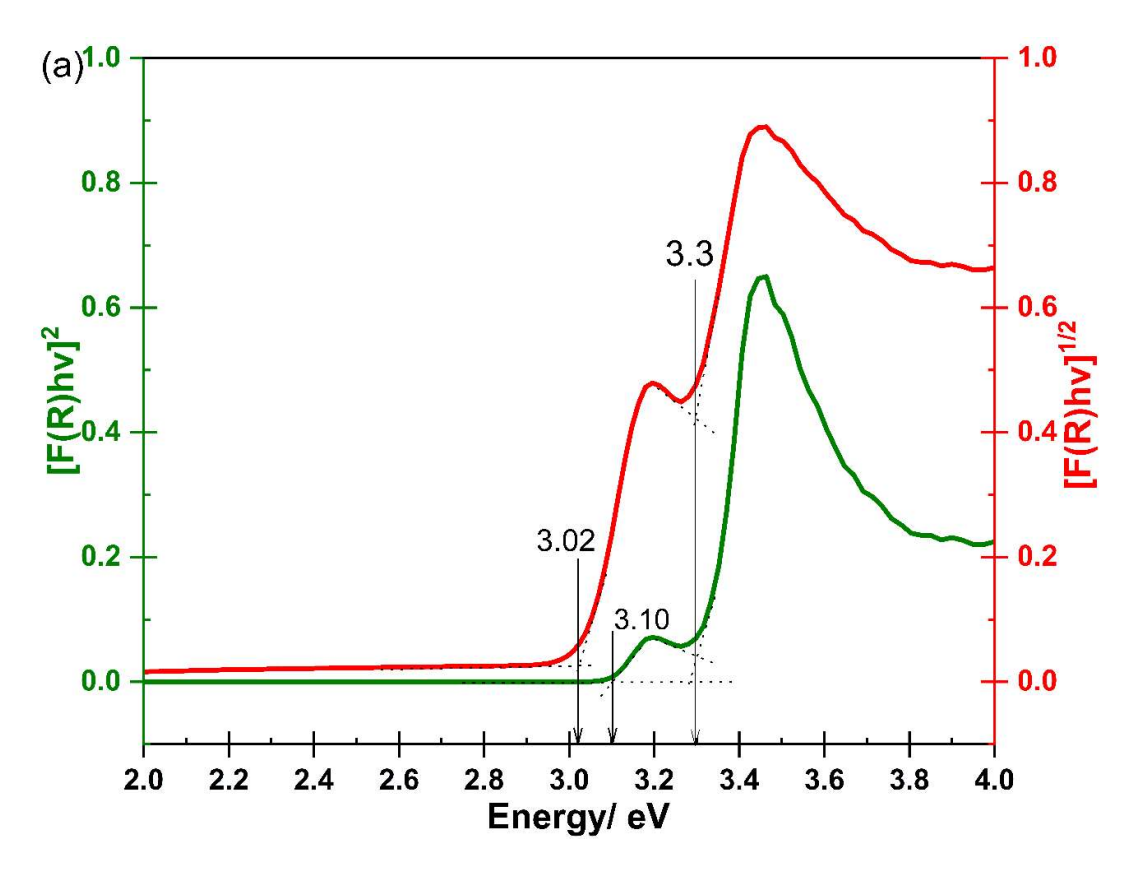
Figure 4.11 The correlation between Nominal Sn content and Analytic Sn content doped into Cs<sub>3</sub>Bi<sub>2</sub>Cl<sub>9</sub>.

The undoped material, Cs<sub>3</sub>Bi<sub>2</sub>Cl<sub>9</sub>, shows an absorption spectrum characteristic of an exciton absorption close to the inter-band absorption edge. This is commonly observed for hybrid perovskites and related materials. The spectrum was modelled close to the absorption edge using Elliot's theory. The continuum absorption is modelled using a Heaviside step function, and the exciton peak modelled using a Dirac delta function. The parameters of these two functions were adjusted to fit the observed spectrum. Pure Cs<sub>3</sub>Bi<sub>2</sub>Cl<sub>9</sub> got a bandgap at 3.37eV in Figure 4.12 taking the mid-point of the Heaviside function with the exciton peak at 3.2 eV, and the exciton building energy is the difference between the bandgap and the exciton peak (170meV). However, the calculated bandgap of the 1D chain (Pmna) of the Cs<sub>3</sub>Bi<sub>2</sub>Cl<sub>9</sub> structure is 2.32 eV, and the experimental

value of the band gap of Cs<sub>3</sub>Bi<sub>2</sub>Cl<sub>9</sub> is about 3 eV stated by Morgan et al. in literature.<sup>132</sup> This is matched band gap of 3 eV measured by Tauc method in Figure 4.12 if the first slop of the Tauc plot of Cs<sub>3</sub>Bi<sub>2</sub>Cl<sub>9</sub> is interpreted as the exciton peak, and the second slope is interpreted as the interband transition.

Exciton energy is another essential parameter that governs the optoelectronic properties of the devices. Excitons having smaller binding energy can be separated easily, which prolongs their lifetime and carrier diffusion length. Due to their lower dimensionality and structure isolation, OD-perovskite structure such as Cs<sub>3</sub>Bi<sub>2</sub>I<sub>9</sub> resulted in a higher exciton binding energy, exceeding a few 100s meV.

However, they have the potential to exhibit optical properties comparable to the Pb-based 3D metal halide perovskites. For example, Machulin et al.<sup>133</sup> reported a higher exciton binding energy of 279 meV for Cs<sub>3</sub>Bi<sub>2</sub>l<sub>9</sub> 0D-perovskite materials. It was suggested that such a higher exciton binding energy could be the reason behind the ambiguity of the bandgap and crystal colour. Similar higher exciton binding energy was reported in the ionic alkali halide compounds, which caused a larger Stoke's shift in absorption and emission spectra. Such high binding energy was responsible for the excitonic absorption peaks even at room temperature. Similarly, even higher exciton binding energy of 300 meV was reported for the MA<sub>3</sub>Bi<sub>2</sub>l<sub>9</sub> 0D-perovskite materials.<sup>134</sup>



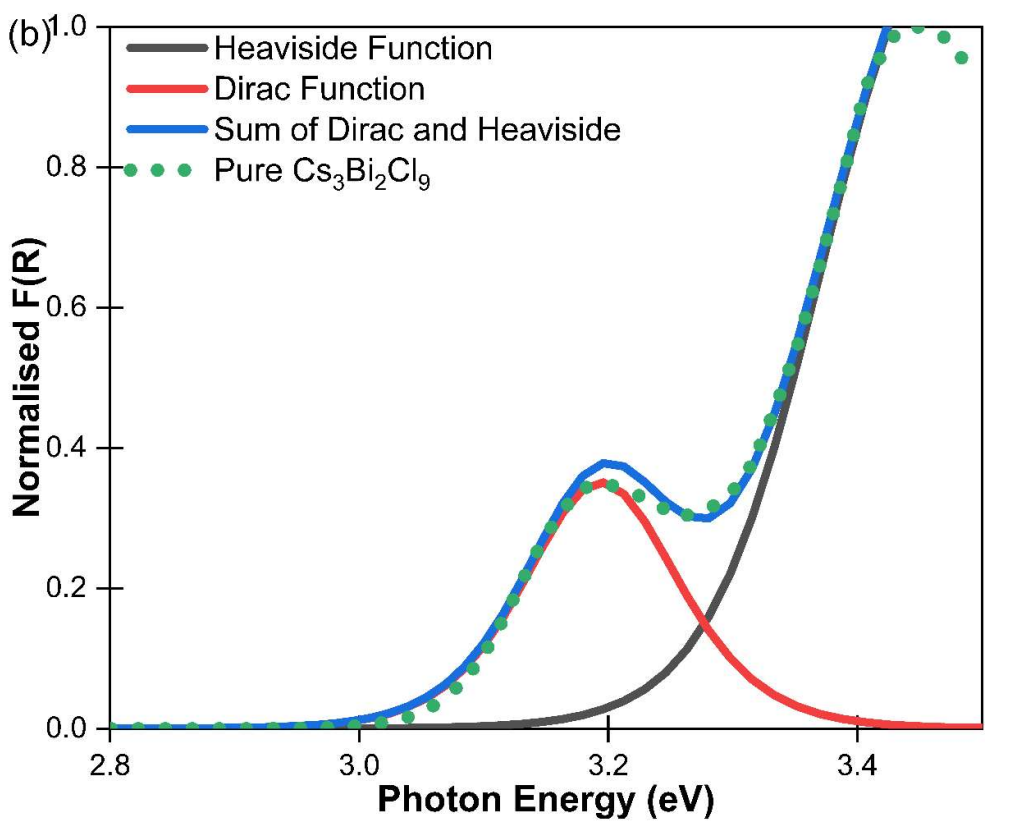


Figure 4.12 (a)Demonstration of direct and indirect bandgap energy calculation from Tauc-analysis for pure Cs<sub>3</sub>Bi<sub>2</sub>Cl<sub>9</sub> (b)A diffuse reflectance spectrum from

undoped Cs<sub>3</sub>Bi<sub>2</sub>Cl<sub>9</sub> via a solution-phased synthesis which is treated with the Kubelka Munk function (green points). The optical absorption is modelled using the Elliot model in blue line, consisting of an exciton peak modelling by Dirac function in red and a continuum absorption modelling by Heaviside function in black.

The UV-vis absorbance spectra of Cs<sub>3</sub>(Sn<sub>x</sub>Bi<sub>(1-x)</sub>)<sub>2</sub>Cl<sub>9</sub> made via solution-phased synthesis was recorded by diffuse reflectance measurements using the Kubelka Munk function shown in Figure 4.13 above. The exciton peak is at ~3.2 eV. The exciton peaks were affected by the amount of Sn doped into the materials which may cause by the content or the ratio of mixed valencies(Sn<sup>2+</sup> and Sn<sup>4+</sup>). 12% Sn doping sample has the smallest exciton energy. However, the band gaps and exciton energies cannot be defined accurately in the Sn doped samples because of the intervalence charge transfer (IVCT) absorption caused by the mixed Sn oxidation states. Due to IVCT absorption at around 3 eV, all Sn doped compounds have higher absorption than the pure Cs<sub>3</sub>Bi<sub>2</sub>Cl<sub>9</sub>.

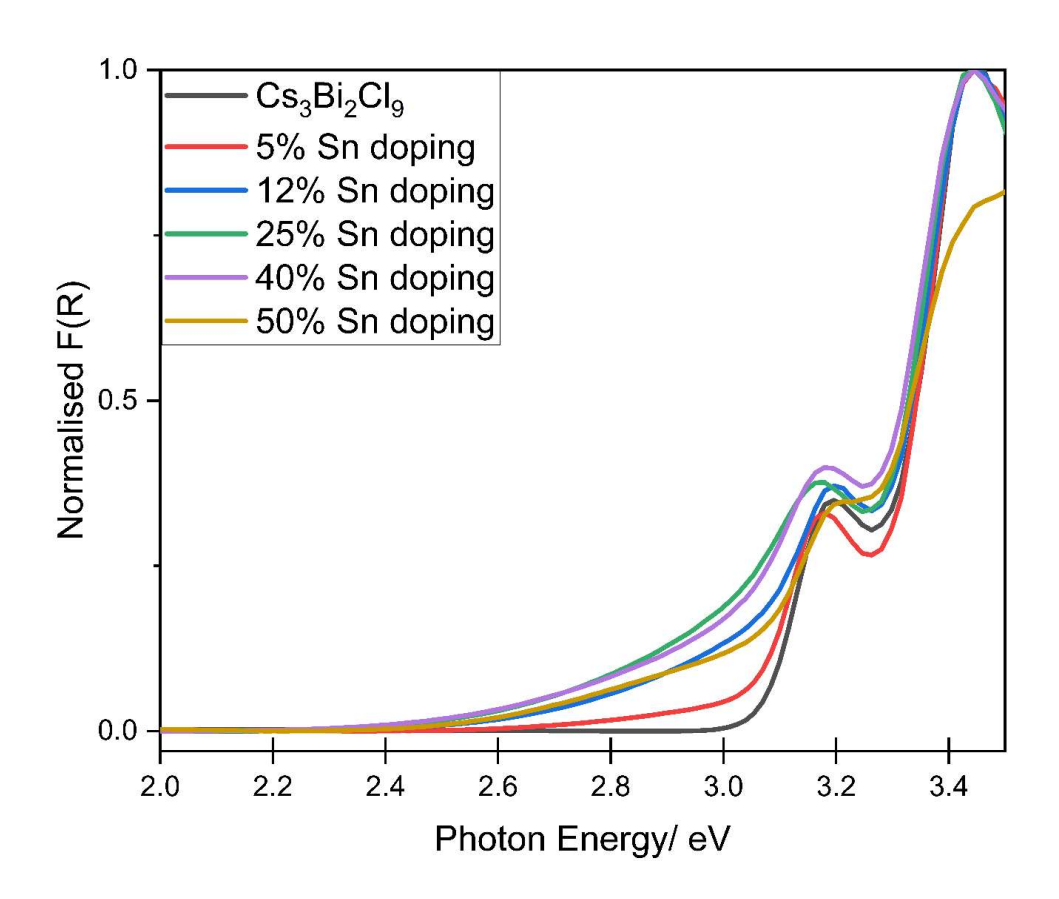


Figure 4.13 Optical absorption spectra of Cs<sub>3</sub>Bi<sub>2</sub>Cl<sub>9</sub> doping Sn in 5%, 12%, 25%, 40% and 50%.

XPS technique was used to observe the composition and chemical environments of Sn in the doped sample environment. The samples were fitted by Casa XPS software. The charge correction was set as C 1s peak energies as 285 eV for samples. There was a movement to right of the Bi 4f spectra of the nominal 12% Sn doped into Cs<sub>3</sub>Bi<sub>2</sub>Cl<sub>9</sub> sample about 0.8 eV after charge correction. There was a movement to left of the Bi 4f spectra of the pure sample Cs<sub>3</sub>Bi<sub>2</sub>Cl<sub>9</sub> about 0.29 eV after charge correction.

The XPS Bi 4f spectra of Cs<sub>3</sub>Bi<sub>2</sub>Cl<sub>9</sub> shown in Figure 4.14 was shifted to the left by 0.67 eV – 0.7 eV comparing to the Bi 4f spectra of the nominal 5% Sn doped 188

into Cs<sub>3</sub>Bi<sub>2</sub>Cl<sub>9</sub> sample. The positions of Bi 4f binding energy peaks in the pure Cs<sub>3</sub>Bi<sub>2</sub>Cl<sub>9</sub> are at 160.29 and 165.59 eV. The positions of Bi 4f binding energy peaks in the nominal 5% Sn doped Cs<sub>3</sub>Bi<sub>2</sub>Cl<sub>9</sub> are at 159.59 and 164.95 eV. The binding energy differences between Bi 4f binding energy peaks are both 5.3 eV. It means that the binding energy of Bi 4f in these two samples are the same. The Bi does not undergo significant chemical change during the doping. However, peak areas of the XPS Bi 4f spectra of Cs<sub>3</sub>Bi<sub>2</sub>Cl<sub>9</sub> were wider than that of the XPS Bi 4f spectra of the nominal 5% Sn doped Cs<sub>3</sub>Bi<sub>2</sub>Cl<sub>9</sub> sample. It may cause by less Bi ions or the formation of Bi metal.

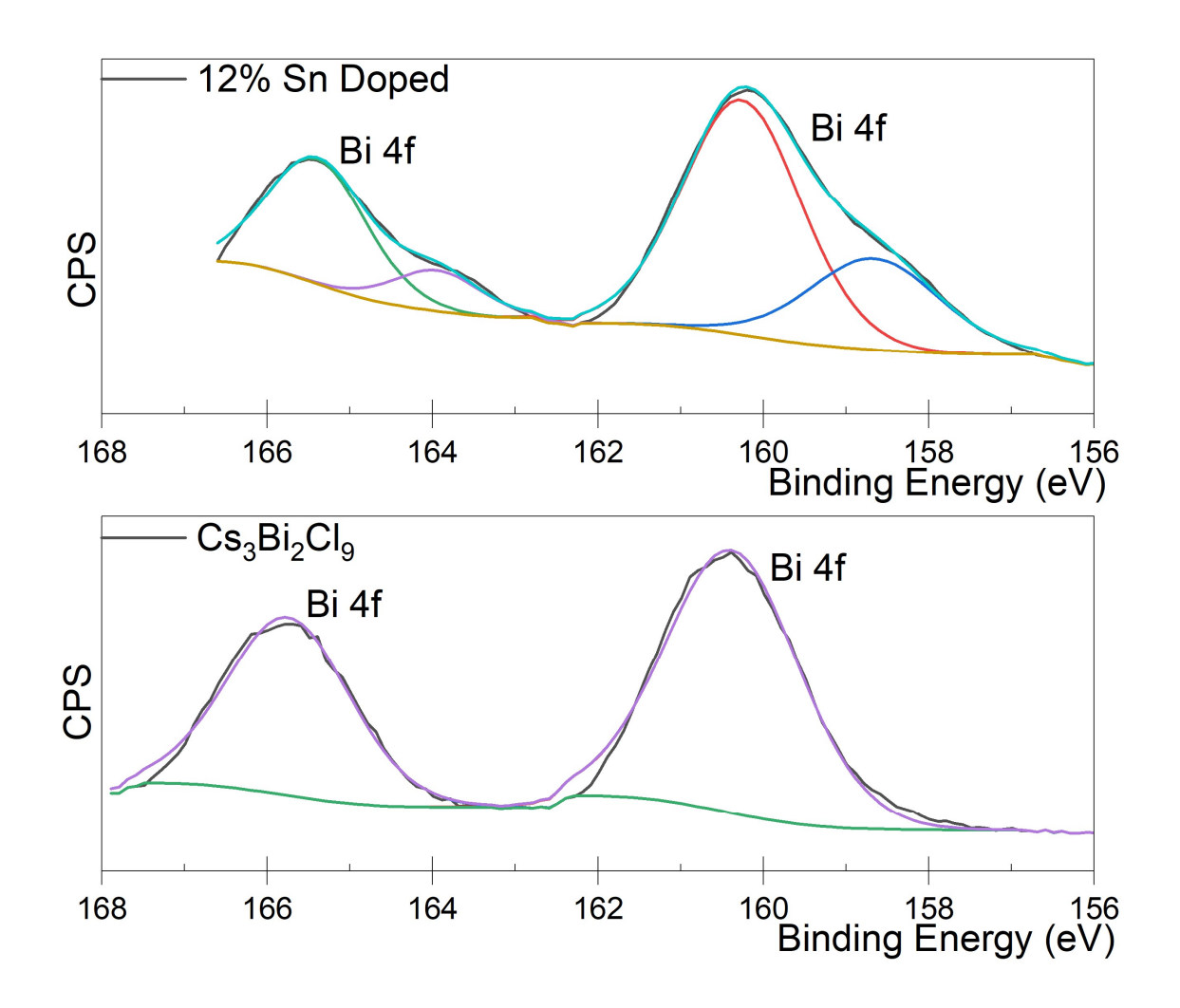


Figure 4.14 Bi 4f spectra from Sn doped (top) and undoped (bottom) Cs<sub>3</sub>Bi<sub>2</sub>Cl<sub>9</sub> with the fitted curves by Casa XPS software.(XPS survey of Cs<sub>3</sub>Bi<sub>2</sub>Cl<sub>9</sub> was attached in Appendix 6.4 for additional information)

Before charge correction of C 1s (peak energies), the positions of Sn 3d binding energy peaks in the pure sample Cs<sub>2</sub>SnCl<sub>6</sub> were at 488.18 and 496.58 eV, and the positions of Sn 3d binding energy peaks in the nominal 5% Sn doped Cs<sub>3</sub>Bi<sub>2</sub>Cl<sub>9</sub> sample were at 486.88 and 495.28 eV in Figure 4.15. After the charge correction, the positions of Sn 3d binding energy peaks in the pure Cs<sub>2</sub>SnCl<sub>6</sub> are at 488.21 and 496.64 eV, and the positions of Sn 3d binding energy peaks in the nominal 5% Sn doped Cs<sub>3</sub>Bi<sub>2</sub>Cl<sub>9</sub> are at 487.76 and 496.17 eV. The XPS Sn 3d

spectrum of Cs<sub>2</sub>SnCl<sub>6</sub> was shifted to the left by 1.3 eV. There was a movement to right of the Sn 3d spectra of the pure sample Cs<sub>2</sub>SnCl<sub>6</sub> about 0.03 -0.06 eV for the charge correction. There was also a movement to right of the Sn 3d spectra of the nominal 5% Sn doped Cs<sub>3</sub>Bi<sub>2</sub>Cl<sub>9</sub> sample about 0.88 eV.

The binding energy differences between Sn 3d binding energy peaks are both 8.4 eV. It means that the binding energy of Sn 3d in the two samples are the same. The Sn does not undergo significant chemical change during the doping. However, peak areas of the XPS Sn 3d spectra of Cs<sub>2</sub>SnCl<sub>6</sub> were wider than that of the XPS Sn 3d spectra of the nominal 5% Sn doped Cs<sub>3</sub>Bi<sub>2</sub>Cl<sub>9</sub>.

In addition to the need to calibrate the binding energy scale using C 1s, the difference in energy between the Sn 3d<sub>5/2</sub> and Cl 2p<sub>3/2</sub> peaks and the difference in energy between the Bi 4f<sub>7/2</sub> and Cl 2p<sub>3/2</sub> peaks were also measured for the binding energy analysis. The binding energy difference between Bi 4f and Cl 2p of the nominal 5% Sn doped Cs<sub>3</sub>Bi<sub>2</sub>Cl<sub>9</sub> was 38.86 eV. The binding energy difference between Sn 3d and Cl 2p of the nominal 5% Sn doped Cs<sub>3</sub>Bi<sub>2</sub>Cl<sub>9</sub> was 289.31 eV. The binding energy difference between Bi 4f and Cl 2p of the pure Cs<sub>3</sub>Bi<sub>2</sub>Cl<sub>9</sub> sample was 38.64 eV. The binding energy difference between Sn 3d and Cl 2p of the pure Cs<sub>2</sub>BiCl<sub>6</sub> was 38.86 eV. There was a difference of 0.22 eV when the binding energy differences between Bi 4f and Cl 2p of pure Cs<sub>3</sub>Bi<sub>2</sub>Cl<sub>9</sub> was compared to that of the sample (nominal 5% Sn doped Cs<sub>3</sub>Bi<sub>2</sub>Cl<sub>9</sub>). This could be cause by doping Sn into Cs<sub>3</sub>Bi<sub>2</sub>Cl<sub>9</sub> which changed the fermi level. There was a difference of 0.25 eV when the binding energy differences between Bi 4f and

Cl 2p of pure Cs<sub>2</sub>SnCl<sub>6</sub> was compared to the sample (the nominal 5% Sn doped Cs<sub>3</sub>Bi<sub>2</sub>Cl<sub>9</sub>). This could cause by the different chemical states.

Moreover, the average amount of the full width at half-maximum (FWHM) of the Cs 3d<sub>5/2</sub> core line in Sn-doped Cs<sub>3</sub>Bi<sub>2</sub>Cl<sub>9</sub> materials is 1.82 eV, and that of Cs<sub>2</sub>SnCl<sub>6</sub> is 1.56eV. The full width at half-maximum (FWHM) of the Sn 3d<sub>5/2</sub> core lines in Sn doped Cs<sub>3</sub>Bi<sub>2</sub>Cl<sub>9</sub> materials is larger than that of Cs<sub>2</sub>SnCl<sub>6</sub>. The full width at half-maximum (FWHM) of the Sn 3d<sub>5/2</sub> core line Cs<sub>2</sub>SnCl<sub>6</sub> of is 1.56 eV. The amount of the full width at half-maximum (FWHM) of the Sn 3d<sub>5/2</sub> core line in nominal 12%Sn doped Cs<sub>3</sub>Bi<sub>2</sub>Cl<sub>9</sub> materials is 2.25 eV. The amount of the full width at half-maximum (FWHM) of the Sn 3d<sub>5/2</sub> core line in nominal 40%Sn doped Cs<sub>3</sub>Bi<sub>2</sub>Br<sub>9</sub> materials is 2.61 eV. The FWHM is increasing by the increase of analytic doping amount of Sn<sup>2+</sup>. The small chemical shift between Sn<sup>2+</sup> and Sn<sup>4+</sup> may cause a challenge to determine the peaks with the corresponding Sn valences but the difference in the full width at half-maximum (FWHM) of the Sn 3d<sub>5/2</sub> core line of these compounds can be interpreted as the existence of the low binding energy peak of Sn<sup>2+</sup>.

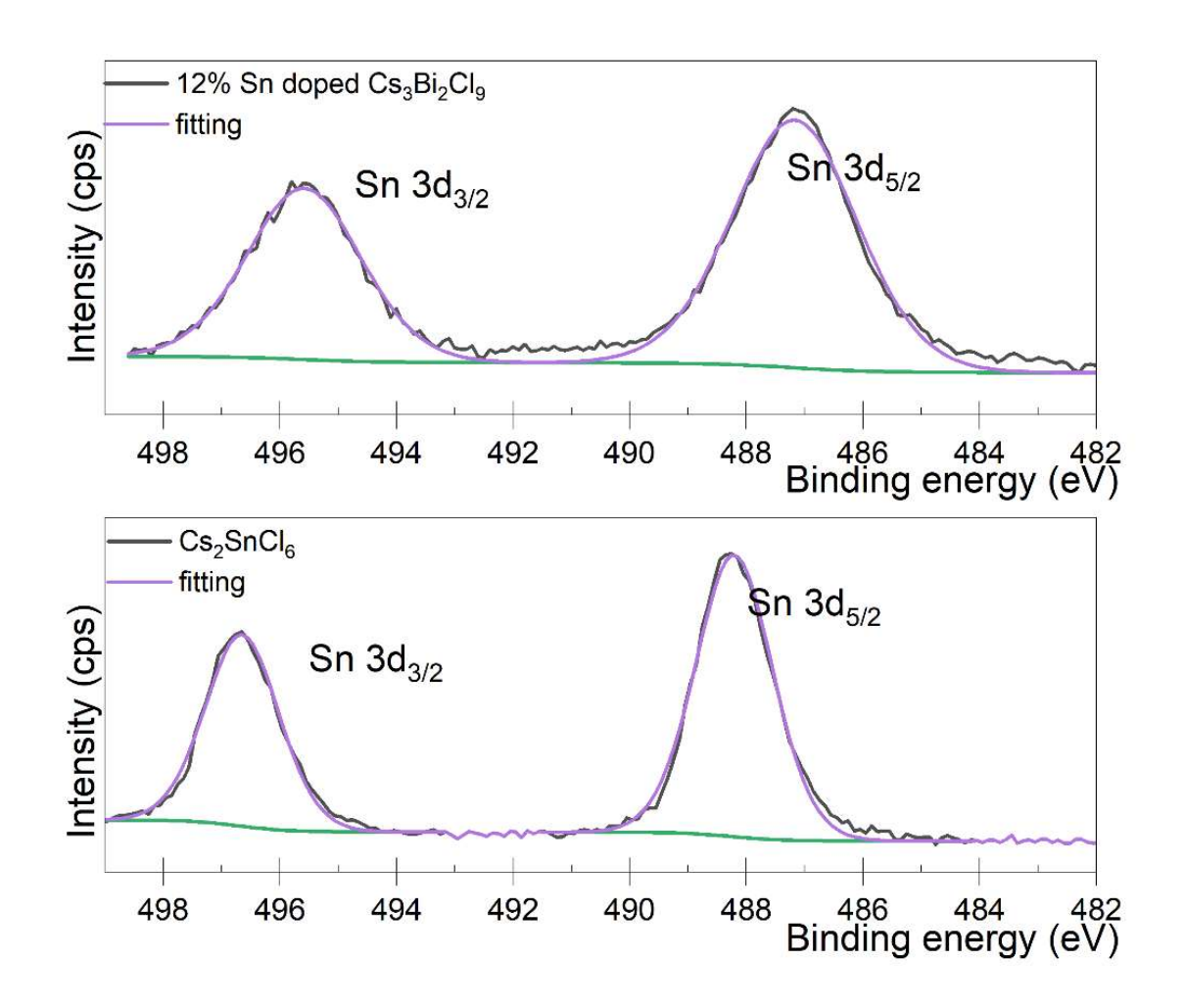


Figure 4.15 Sn 3d spectra from nominal 12% Sn doped Cs<sub>3</sub>Bi<sub>2</sub>Cl<sub>9</sub> (top) and Cs<sub>2</sub>SnCl<sub>6</sub> (bottom), a pure Sn (IV) compound.

The room temperature Raman spectra of orthorhombic pure Cs<sub>3</sub>Bi<sub>2</sub>Cl<sub>9</sub> and Cs<sub>3</sub>Bi<sub>2</sub>Cl<sub>9</sub> doping certain amount of Sn were studied using the 633 nm laser beam shown in the Figure 4.16 above. The Raman spectrum of pure Cs<sub>3</sub>Bi<sub>2</sub>Cl<sub>9</sub> is like the orthorhombic Cs<sub>3</sub>Bi<sub>2</sub>Cl<sub>9</sub> reported by Pradhan et al.<sup>135</sup> All the phases were scanned from 10 to 400 cm<sup>-1</sup> since no bands were observed beyond 350 cm<sup>-1</sup>. There are three Raman band in the range of 200-350 cm<sup>-1</sup> due to the participation of the Bi atom. There are more bands present at the lower frequency region

between 50-150 cm<sup>-1</sup> due to the movement of CI atoms. One of the Raman bands corresponds to the vibration of octahedra along the X-, Y-axes and the other two may be produced by the deformational vibration of the octahedra.<sup>136</sup>

Doping a small amount of Sn did not cause any obvious peak shifts in the spectra but the changes of the peak area at 60 and 263.1cm<sup>-1</sup> were seen. This also could confirm Sn doping did not change the phase structure of the material which was matched to XRD patterns of the same sample respectively. The change of the area of the peaks could indicate the different types of vibrations appeared when Cs<sub>3</sub>Bi<sub>2</sub>Cl<sub>9</sub> material interacted with Sn<sup>2+</sup> ions doped in.

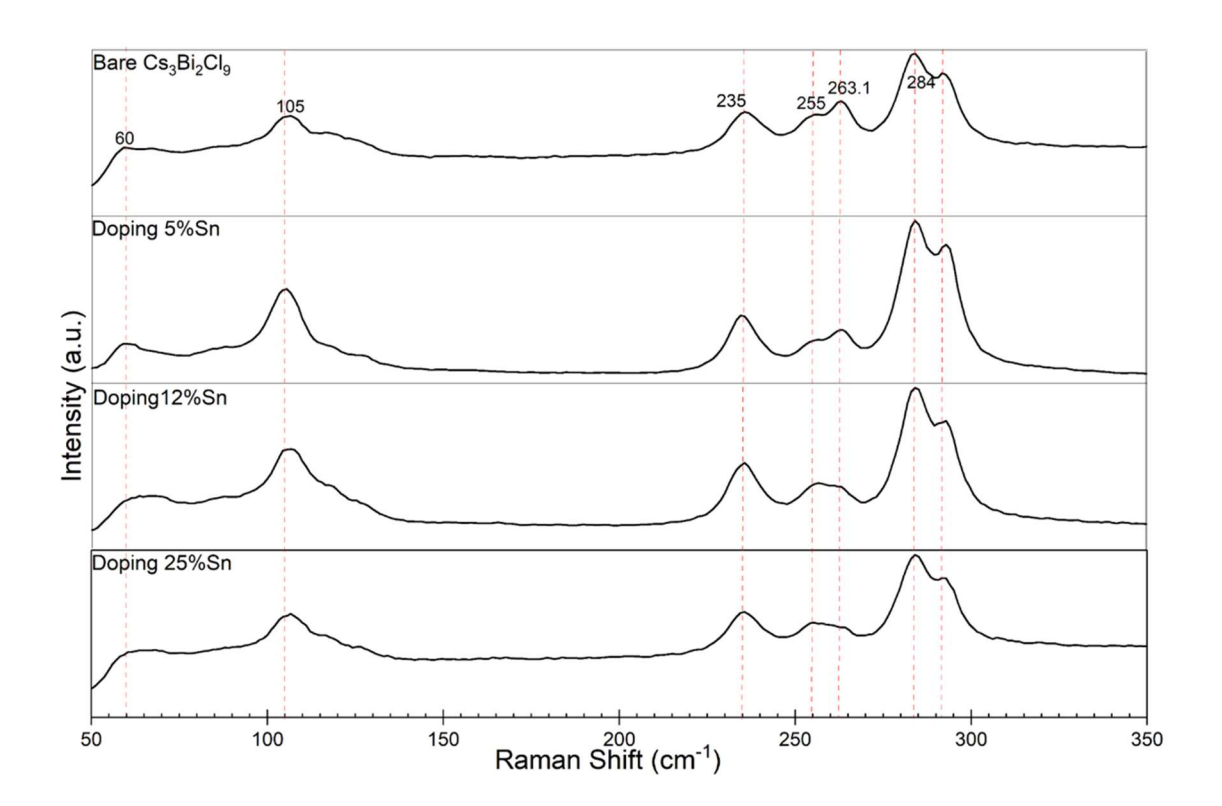


Figure 4.16 Raman Spectra of orthorhombic pure Cs<sub>3</sub>Bi<sub>2</sub>Cl<sub>9</sub> material and Cs<sub>3</sub>Bi<sub>2</sub>Cl<sub>9</sub> doping certain amount of Sn in 5%, 12% and 25%.

Sn doping technique was also tried on Cs<sub>3</sub>Bi<sub>2</sub>Cl<sub>9</sub> by solid-state method, but it could not achieve the similar result as the Sn-doped samples made in Solution-phased Synthesis (as-made via SpS). When SnBr<sub>2</sub> was grinding with Sample Cs<sub>3</sub>Bi<sub>2</sub>Cl<sub>9</sub>(as-made via SpS) by solid-state grinding method to try form Sn-doped Cs<sub>3</sub>Bi<sub>2</sub>Cl<sub>9</sub> with mixed valences Sn<sup>2+</sup> and Sn<sup>4+</sup> with any change of the general phase structure of Cs<sub>3</sub>Bi<sub>2</sub>Cl<sub>9</sub>. The extra phase of Cs<sub>2</sub>SnCl<sub>6</sub> was formed even with the very low nominal percentage of Sn such as nominal 5%Sn. The increased nominal Sn% caused the increase of the intensity of Braggs peaks of Cs<sub>2</sub>SnCl<sub>6</sub> such as the peak at 2θ=24.2° on XRD patterns in Figure 4.17. Hence, solid-state grinding method is not applicable for doping SnCl<sub>2</sub> into Cs<sub>3</sub>Bi<sub>2</sub>Cl<sub>9</sub>.

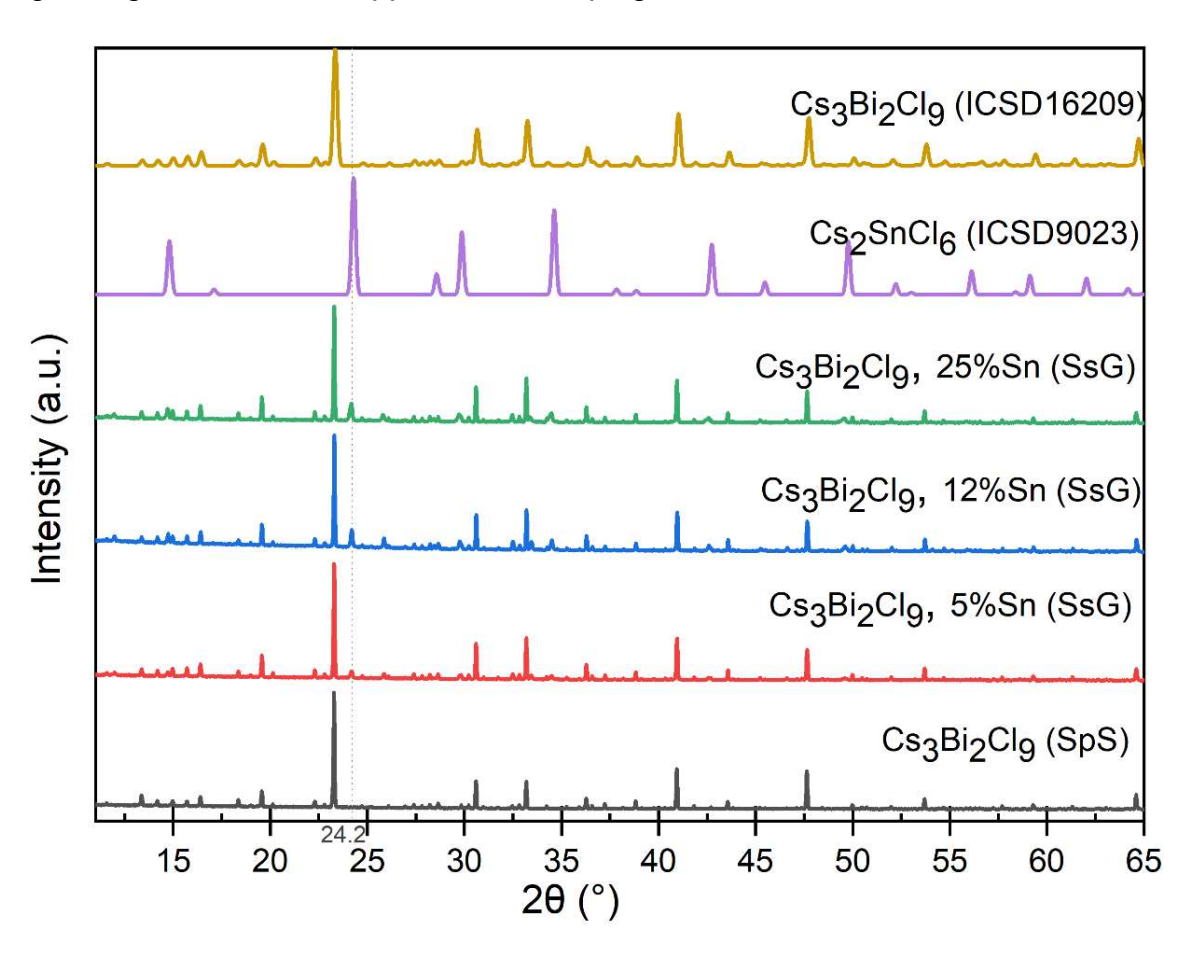


Figure 4.17 XRD patterns of Sn-doped Cs<sub>3</sub>Bi<sub>2</sub>Cl<sub>9</sub> materials produced by Solidstate Grinding (SsG) with nominal Sn% =5%, 12%, and 25%.

#### 4.2.3 Conclusion

Sn doping technique is not only available for Cs<sub>3</sub>Bi<sub>2</sub>Br<sub>9</sub> in the trigonal structure but also applicable for Cs<sub>3</sub>Bi<sub>2</sub>Cl<sub>9</sub> in the orthorhombic structure. Cs<sub>3</sub>Bi<sub>2</sub>Cl<sub>9</sub> is white. An immediately colour change from white to pale yellow happened when Cs<sub>3</sub>Bi<sub>2</sub>Cl<sub>9</sub> doped SnCl<sub>2</sub>. IVCT happened the same way as it occurred to Cs<sub>3</sub>Bi<sub>2</sub>Cl<sub>9</sub> doping SnCl<sub>2</sub>. Mixed valencies of Sn can improve light absorption slightly since the doping amount is low. Also, Sn doped percentage is much lower when it compared to the doping results from Sn doped Cs<sub>3</sub>Bi<sub>2</sub>Br<sub>9</sub>. Solid-state grinding method is not valid for Cs<sub>3</sub>Bi<sub>2</sub>Cl<sub>9</sub> doping tin as secondary phases Cs<sub>2</sub>BiCl<sub>6</sub> formed even at very low Sn% (nominal) such as 5% in Figure 4.17.

### 4.3 Sn doping attempts on Other A<sub>3</sub>B<sub>2</sub>X<sub>9</sub>

Sn doping technique was tried on Cs<sub>3</sub>Sb<sub>2</sub>Cl<sub>9</sub> and Rb<sub>3</sub>Bi<sub>2</sub>Br<sub>9</sub>. This topic is to find out if Sn doping can apply to other structures in form of A<sub>3</sub>B<sub>2</sub>X<sub>9</sub> in either Solution-phased Synthesis or Solid-state Grinding method apart from Cs<sub>3</sub>Bi<sub>2</sub>Br<sub>9</sub>. Can Sn dope in Cs<sub>3</sub>Sb<sub>2</sub>Cl<sub>9</sub> with the trigonal structure or in Rb<sub>3</sub>Bi<sub>2</sub>Br<sub>9</sub> with the monoclinic structure?

Cs<sub>3</sub>Sb<sub>2</sub>Cl<sub>9</sub> and Rb<sub>3</sub>Bi<sub>2</sub>Br<sub>9</sub> used the same methods such as Solution-phased Synthesis (SpS) and Solid-state Grinding (SsG) to try to make Sn<sup>2+</sup> doped Cs<sub>3</sub>Sb<sub>2</sub>Cl<sub>9</sub> materials and Sn<sup>2+</sup> doped Rb<sub>3</sub>Bi<sub>2</sub>Br<sub>9</sub> materials. Hence, the aim of Section 4.3 is the result and the discussion of characterising pure Cs<sub>3</sub>Sb<sub>2</sub>Cl<sub>9</sub> and pure Rb<sub>3</sub>Bi<sub>2</sub>Br<sub>9</sub> via different characterisation techniques and to detect whether Sn<sup>2+</sup> doping can form mixed valences such as Sn<sup>2+</sup> and Sn<sup>4+</sup> in Cs<sub>3</sub>Sb<sub>2</sub>Cl<sub>9</sub> and Rb<sub>3</sub>Bi<sub>2</sub>Br<sub>9</sub> without any change of the general phase structure of pure Cs<sub>3</sub>Sb<sub>2</sub>Cl<sub>9</sub> and pure Rb<sub>3</sub>Bi<sub>2</sub>Br<sub>9</sub>. The experiments and the characterisation analysis of Cs<sub>3</sub>Sb<sub>2</sub>Cl<sub>9</sub> and Rb<sub>3</sub>Bi<sub>2</sub>Br<sub>9</sub> here are alike to that of Cs<sub>3</sub>Bi<sub>2</sub>Cl<sub>9</sub> and Cs<sub>3</sub>Bi<sub>2</sub>Br<sub>9</sub> mentioned in Section 4.1 and Section 4.2. Hence, the information of Experimental Methodology of Cs<sub>3</sub>Sb<sub>2</sub>Cl<sub>9</sub> and Rb<sub>3</sub>Bi<sub>2</sub>Br<sub>9</sub> is skipped as Experimental Methodology of Cs<sub>3</sub>Bi<sub>2</sub>Cl<sub>9</sub> and Cs<sub>3</sub>Bi<sub>2</sub>Br<sub>9</sub> Section 4.1.1 and section 4.2.1 can be used as references.

#### 4.3.1 Results and Discussion (Cs<sub>3</sub>Sb<sub>2</sub>Cl<sub>9</sub>)

The solution synthesis was used to try to produce Cs<sub>3</sub>Bi<sub>2</sub>Cl and Sn doped Cs<sub>3</sub>Bi<sub>2</sub>Cl<sub>9</sub> (SpS). The experimental methodology is the same as that of Cs<sub>3</sub>Bi<sub>2</sub>Cl<sub>9</sub> in Section 4.2.2. Cs<sub>2</sub>CO<sub>3</sub> and HCl were reacted to produce CsCl. Then SbCl<sub>3</sub> and CsCl were reacted to form Cs<sub>3</sub>Sb<sub>2</sub>Cl<sub>9</sub>. Sn doping is followed by samples with varying nominal amounts of Sn were synthesised in the same way also mentioned in Section 4.2.2.

(Nominal Sn% =[Sn]/([Sn]+[Sb]) = 0,0.05,0.12,0.25,0.4 and 0.5)

In Figure 4.19, extra Braggs peak formed at 20=18.5° which was marked by the dot line. Hence, Sn doping does not work for all materials which have similar trigonal structures. For example, Cs<sub>3</sub>Sb<sub>2</sub>Cl<sub>9</sub> doping Sn processed via a solution phased synthesis could not maintain the same phase structure as pure Cs<sub>3</sub>Sb<sub>2</sub>Cl<sub>9</sub>. The pure Cs<sub>3</sub>Sb<sub>2</sub>Cl<sub>9</sub> material made via a solution phased synthesis was in the trigonal structure (with a P3m1 space group) which was matched to ICSD data with collection code (48771).<sup>137</sup>

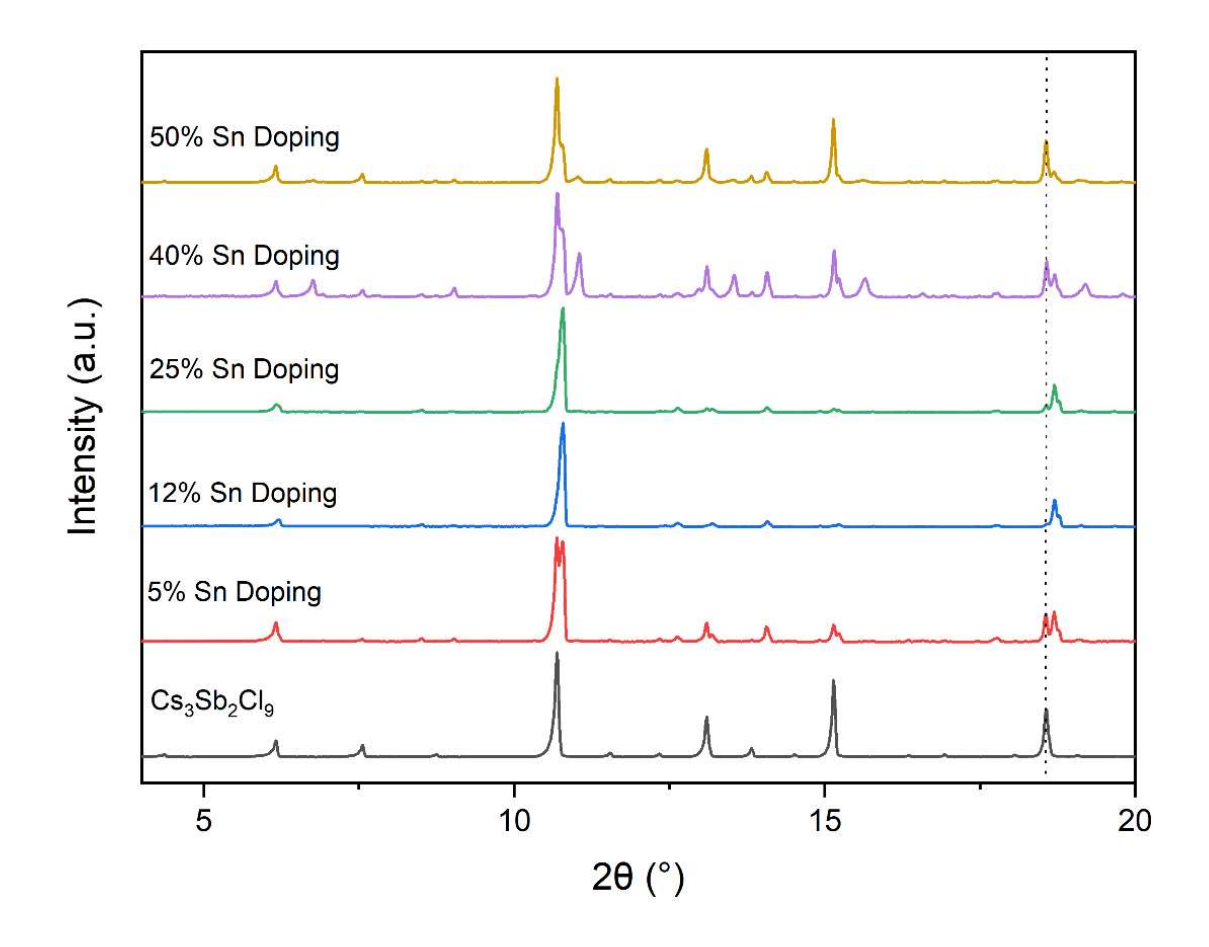


Figure 4.18 XRD patterns of the pure Cs<sub>3</sub>Sb<sub>2</sub>Cl<sub>9</sub> sample and Sn doped Cs<sub>3</sub>Sb<sub>2</sub>Cl<sub>9</sub> samples (SpS) with nominal Sn%=5%, 12%, 25%, 40% and 50%.

Elliot model cannot fit the absorption spectrum of Cs<sub>3</sub>Sb<sub>2</sub>Cl<sub>9</sub> here because it seems like multiple exciton peaks existed between 3 eV and 3.8 eV. Elliot model

was modelled to fit samples that has one exciton peak so far, so a superior Elliot Model is required in this case which analyses multiple exciton peaks. Further study in this field is required to understand the light absorption properties of materials that have multiple exciton peaks.

To determine the optical band gap of Cs<sub>3</sub>Sb<sub>2</sub>Cl<sub>9</sub>, the Kubelka-Munk equation, [k=(1-R)<sup>2</sup>/2R], and the band gap analysis equation, (khv)<sup>1/n</sup>=C(hv-E<sub>g</sub>), were used to calculate the indirect band gap for pure Cs<sub>3</sub>Sb<sub>2</sub>Cl<sub>9</sub> by plotting (khv)<sup>1/n</sup> vs hv. In the band gap analysis equation, k is the absorption coefficient, h is Plank's constant, C is the proportionality constant, v is the frequency of light, E<sub>g</sub> is the band gap, and n is 2, expressing an indirect band gap of the substance. If the first slope of the Tauc plot in Figure 4.19 is the interband transition, the indirect band gap of Cs<sub>3</sub>Sb<sub>2</sub>Cl<sub>9</sub> is 2.96 eV from the calculation of the interception of the trendline. When it was compared to the recorded value (3.4 eV) recorded by Pradhan et al. in literature, it is smaller than that of Cs<sub>3</sub>Sb<sub>2</sub>Cl<sub>9</sub> nanowires due to the quantum confinement effect of Cs<sub>3</sub>Sb<sub>2</sub>Cl<sub>9</sub> nanowires. However, the band gap of bulk Cs<sub>3</sub>Sb<sub>2</sub>Cl<sub>9</sub> is 3.02 eV reported by Vargas et al.<sup>138,139</sup>The measured band gap in Figure 4.19 is very close to the band gap of bulk Cs<sub>3</sub>Sb<sub>2</sub>Cl<sub>9</sub>.

Both the pure Cs<sub>3</sub>Bi<sub>2</sub>Cl<sub>9</sub> compound and the pure Cs<sub>3</sub>Sb<sub>2</sub>Cl<sub>9</sub> compound have valence bands which were contributed by Cl-3p states. Hence, the valence bands stayed the same in both compounds, but conduction bands are totally different. Although both compounds' conduction band were contributed by Sb-p orbitals/

Bi-p orbitals. The energy of Bi-p orbitals is higher than Sb-p states. Hence, the bandgap of Cs<sub>3</sub>Bi<sub>2</sub>Cl<sub>9</sub> was higher than the bandgap of Cs<sub>3</sub>Sb<sub>2</sub>Cl<sub>9</sub>.

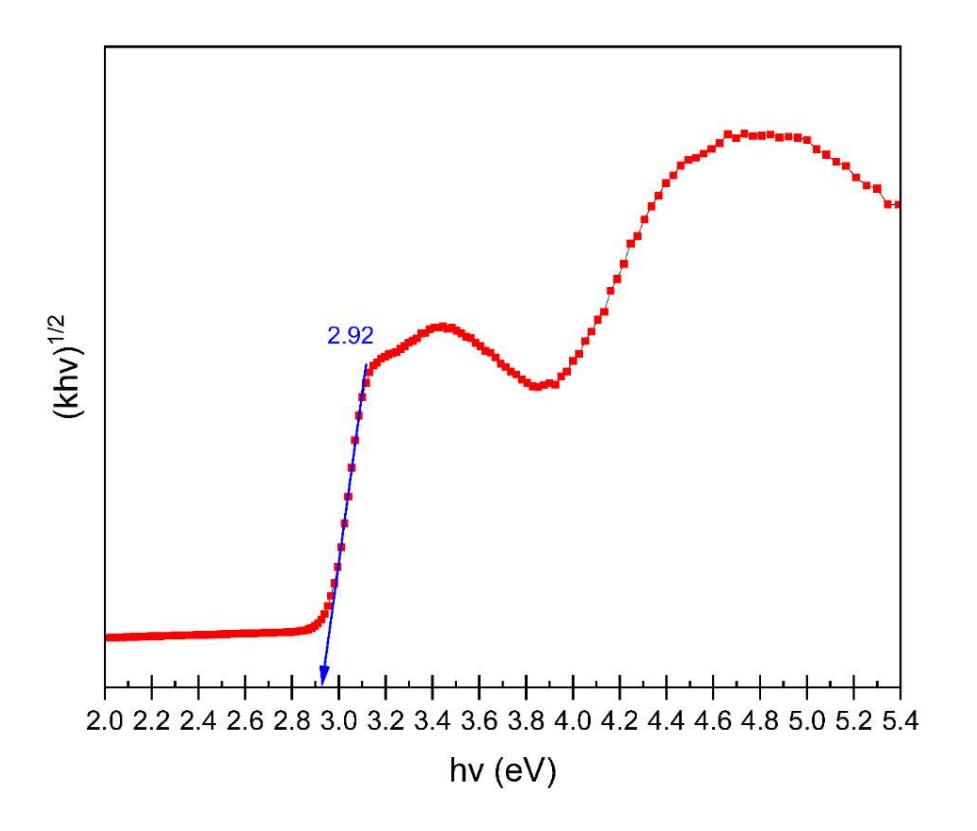


Figure 4.19 UV-vis diffused reflectance study of Cs<sub>3</sub>Sb<sub>2</sub>Cl<sub>9</sub>

#### 4.3.2 Results and Discussion (Rb<sub>3</sub>Bi<sub>2</sub>Br<sub>9</sub>)

Rb<sub>3</sub>Bi<sub>2</sub>Br<sub>9</sub> was synthesised by solid-state grinding method by grinding RbBr and BiBr<sub>3</sub> in the molar ratio of 3 to 1 together. The procedures of the SsG synthesis of trying to make Sn doped Rb<sub>3</sub>Bi<sub>2</sub>Br<sub>9</sub> is the same as that of Cs<sub>3</sub>Bi<sub>2</sub>Br<sub>9</sub> mentioned in Section 4.1.1 by grinding SnBr<sub>2</sub> with pre-made pure Rb<sub>3</sub>Bi<sub>2</sub>Br<sub>9</sub>. According to the XRD patterns of Rb<sub>3</sub>Bi<sub>2</sub>Br<sub>9</sub> made via varying synthesis and different patches in Figure 4.20, the solutions-phased synthesis (SpS) cannot form Rb<sub>3</sub>Bi<sub>2</sub>Br<sub>9</sub> but forms Rb<sub>3</sub>BiBr<sub>6</sub> instead. The PXRD patterns of Sample Rb<sub>3</sub>Bi<sub>2</sub>Br<sub>9</sub> (SpS) and ICSD

data (121650) of Rb<sub>3</sub>BiBr<sub>6</sub><sup>140</sup> were matched. However, the solid-state grinding synthesis (SsG) can be used to produce Rb<sub>3</sub>Bi<sub>2</sub>Br<sub>9</sub>, and it is a repeatable experiment. Sample Rb<sub>3</sub>Bi<sub>2</sub>Br<sub>9</sub> (SsG) is in the monoclinic structure, which was matched to the XRD pattern of ICSD data (431320) of Rb<sub>3</sub>Bi<sub>2</sub>Br<sub>9</sub><sup>141</sup>. The Braggs peaks such as (200), (011), (211) and (411) showing on the PXRD patterns are obtained via ICSD data (431320) of Rb<sub>3</sub>Bi<sub>2</sub>Br<sub>9</sub>. The intensity of Braggs peaks is varied from that of ICSD data (431320) of Rb<sub>3</sub>Bi<sub>2</sub>Br<sub>9</sub>. This may be caused by the ongoing formation of Rb<sub>3</sub>Bi<sub>2</sub>Br<sub>9</sub>. It can be improved by a longer grinding time to improve the formation process of pure Rb<sub>3</sub>Bi<sub>2</sub>Br<sub>9</sub>. Since pure Rb<sub>3</sub>Bi<sub>2</sub>Br<sub>9</sub> is made, is the tin doping technique applicable for materials in a monoclinic structure?

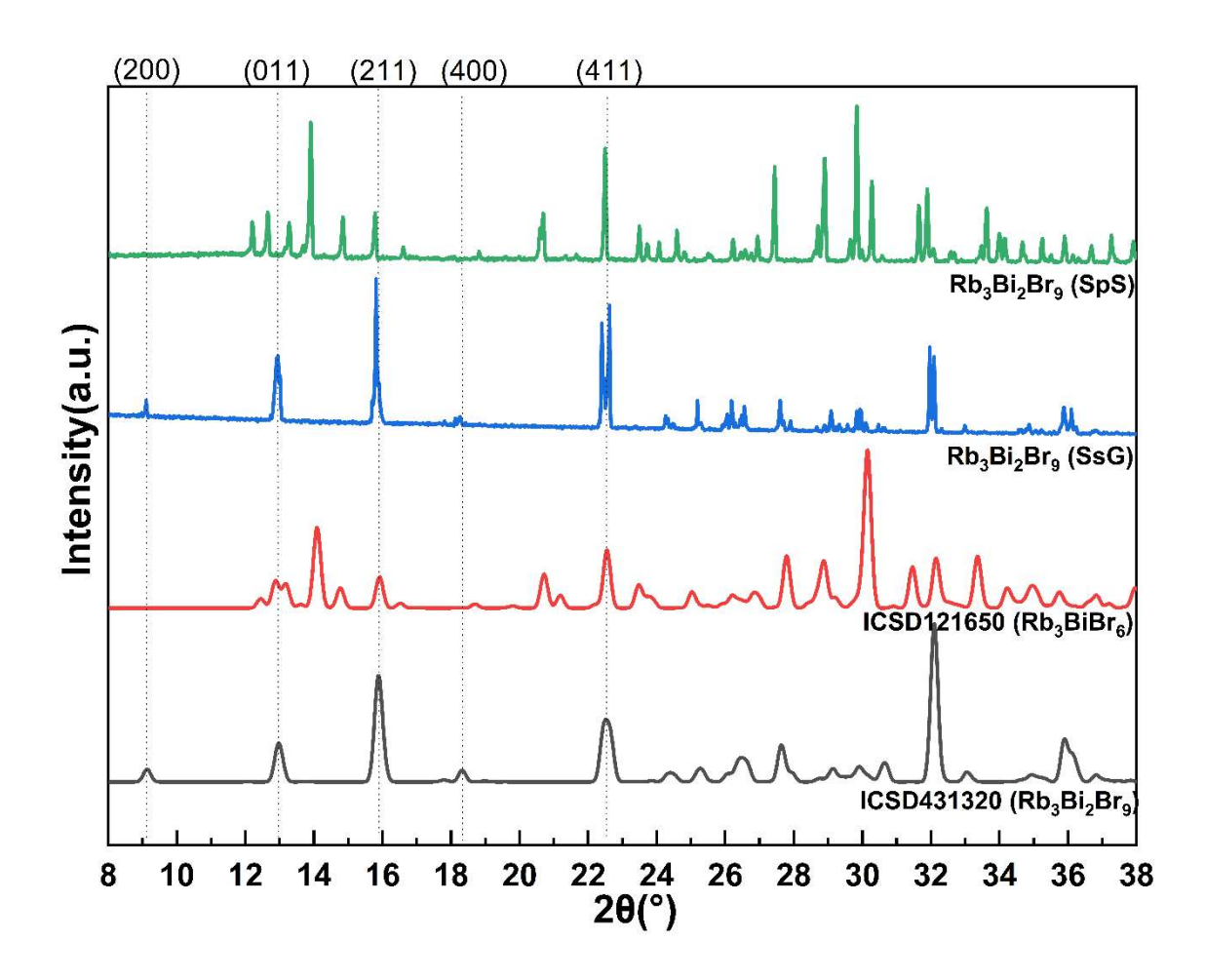


Figure 4.20 XRD patterns of Rb<sub>3</sub>Bi<sub>2</sub>Br<sub>9</sub> samples made via the solution-phased synthesis and the solid-state grinding method at room temperature.

The PXRD pattern of the mixture of 5% SnBr<sub>2</sub> and pure Rb<sub>3</sub>Bi<sub>2</sub>Br<sub>9</sub> is noted as sample 'Doping Sn 5%(SsG)' in Figure 4.21. The PXRD pattern of nominal 5% doped sample (the mixture of 5% SnBr<sub>2</sub> and pure Rb<sub>3</sub>Bi<sub>2</sub>Br<sub>9</sub>) was matched to PXRD pattern of ICSD data (121650) of Cs<sub>3</sub>BiBr<sub>6</sub><sup>140</sup> by matching Braggs peaks at 2θ= 13.1°, 22.5° and 30.1°. This means that the mixture of 5% SnBr<sub>2</sub> and pure Rb<sub>3</sub>Bi<sub>2</sub>Br<sub>9</sub> formed Cs<sub>3</sub>BiBr<sub>6</sub> but not Sn doped Rb<sub>3</sub>Bi<sub>2</sub>Br<sub>9</sub>. The unreacted precursor such as RbBi<sub>3</sub> existed in the mixture of 5% SnBr<sub>2</sub> and pure Rb<sub>3</sub>Bi<sub>2</sub>Br<sub>9</sub> which is shown by the Braggs peak at 2θ= 13.8°. There is also a tiny amount of BiBr<sub>3</sub> in sample Rb<sub>3</sub>Bi<sub>2</sub>Br<sub>9</sub> (SsG) shown by the peak at 2θ= 38.2° due to the ongoing formation of Rb<sub>3</sub>Bi<sub>2</sub>Br<sub>9</sub>.

Solid state grinding method was used to produce pure Rb<sub>3</sub>Bi<sub>2</sub>Br<sub>9</sub> compound which is in the monoclinic unit cell structure. When SnBr<sub>2</sub> was added and mixed with Pure Rb<sub>3</sub>Bi<sub>2</sub>Br<sub>9</sub> material by solid-state grinding method, extra phases formed on the PXRD pattern of the mixture of 5% SnBr<sub>2</sub> and pure Rb<sub>3</sub>Bi<sub>2</sub>Br<sub>9</sub> in Figure 4.21. This indicated the failure of doping Sn<sup>2+</sup> into Rb<sub>3</sub>Bi<sub>2</sub>Br<sub>9</sub> which did not match the intension to form mixed valences of Sn<sup>2+</sup> and Sn<sup>4+</sup> into the monoclinic structure of Rb<sub>3</sub>Bi<sub>2</sub>Br<sub>9</sub> without any change of the general phase structure of the compound. Hence, the interstitial method of doping Sn to modulate the properties of light absorber material might not work for Rb<sub>3</sub>Bi<sub>2</sub>Br<sub>9</sub> by solid-state grinding method.

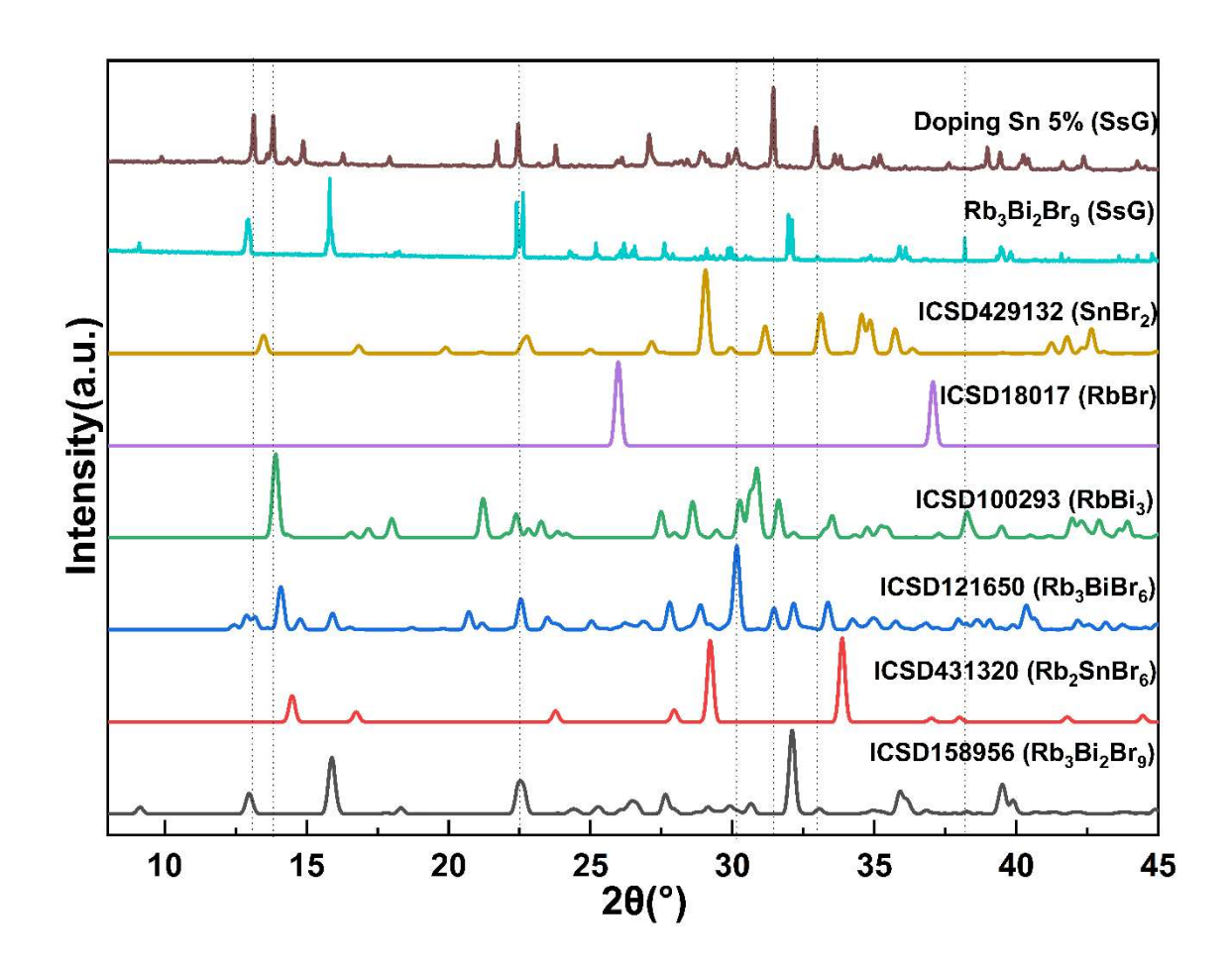


Figure 4.21 PXRD patterns of pure Rb<sub>3</sub>Bi<sub>2</sub>Br<sub>9</sub> (SsG) and 5% Sn doped nominally Rb<sub>3</sub>Bi<sub>2</sub>Br<sub>9</sub> (SsG).

To determine the optical band gap of Rb<sub>3</sub>Bi<sub>2</sub>Br<sub>9</sub>, the Kubelka-Munk equation, [k=(1-R)<sup>2</sup>/2R], and the band gap analysis equation, (khv)<sup>1/n</sup>=C(hv-E<sub>g</sub>), were used to calculate the indirect band gap for pure Cs<sub>3</sub>Sb<sub>2</sub>Cl<sub>9</sub> by plotting (khv)<sup>1/2</sup> vs hv. It was the same method used to calculate the bandgap of Cs<sub>3</sub>Sb<sub>2</sub>Cl<sub>9</sub>. If the first slope of the Tauc plot is interpreted as the interband transition, the direct and indirect band gap of Rb<sub>3</sub>Bi<sub>2</sub>Br<sub>9</sub> are 2.66 eV and 2.62 eV shown in Figure 4.22(a) below. The direct band gap of 2.66 eV in Figure 4.22(a) was closed to the recorded bandgap stated by Weber et al. <sup>142</sup>, which revealed an indirect band gap

of 2.46 eV, and a direct band transition of 2.76 eV. The absorption onset of the Rb<sub>3</sub>Sb<sub>2</sub>Br<sub>9</sub> film is approximately 460 nm.<sup>143,144</sup>

However, the first hump may be the exciton peak of 2.75 eV shown in Figure 4.22(b) which is fitted by Dirac function. If the first hump is seen as the exciton peak, the interband transition is interpreted at the second slope which the band gap is 2.92 eV fitting by Heaviside step function. The exciton energy is the difference between the exciton peak and the interband transition which is 170 meV. The Band gap calculated by Tauc method in this case is about 2.90-2.91 eV which matches the band gap of 2.92 eV measured by Elliot theory. The study of band gap measurement using both Tauc method and Elliot theory for Rb<sub>3</sub>Bi<sub>2</sub>Br<sub>9</sub> is expanding the understanding of the locations of band gaps. Both methods pointed the band gap of Rb<sub>3</sub>Bi<sub>2</sub>Br<sub>9</sub> about 2.9 eV, the first hump of the absorption spectrum may be the exciton peak.

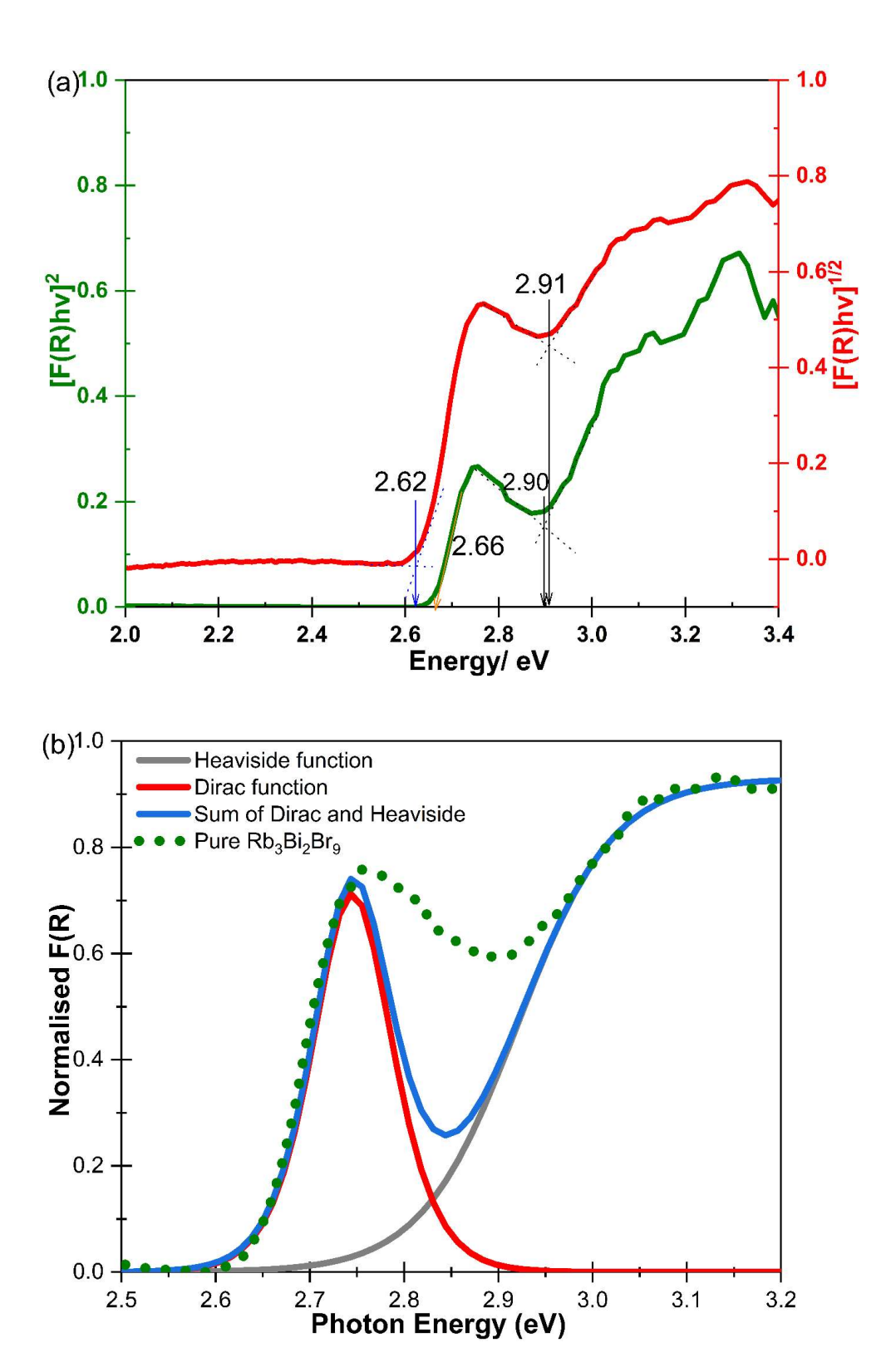


Figure 4.22 (a)UV-vis diffused reflectance study of  $Rb_3Bi_2Br_9$  and (b) A diffuse reflectance spectrum from undoped  $Rb_3Bi_2Br_9$  via a solution-phased synthesis which is treated with the Kubelka Munk function (green points). The optical absorption is modelled using the Elliot model in blue line, consisting of an exciton

peak modelling by Dirac function in red and a continuum absorption modelling by Heaviside function in black.

#### 4.3.3 Conclusion

Cs<sub>3</sub>Sb<sub>2</sub>Cl<sub>9</sub> and Rb<sub>3</sub>Bi<sub>2</sub>Br<sub>9</sub> used the same methods such as Solution-phased Synthesis (SpS) and Solid-state Grinding (SsG) to try to make Sn<sup>2+</sup> doped Cs<sub>3</sub>Sb<sub>2</sub>Cl<sub>9</sub> materials and Sn<sup>2+</sup> doped Rb<sub>3</sub>Bi<sub>2</sub>Br<sub>9</sub> materials but the results in this section disproved the possibility of doping Sn<sup>2+</sup> into Cs<sub>3</sub>Sb<sub>2</sub>Cl<sub>9</sub> or Rb<sub>3</sub>Bi<sub>2</sub>Br<sub>9</sub> by Solution-phased Synthesis (SpS) and Solid-state Grinding (SsG).

The solution-phased synthesis cannot be used to produce Rb<sub>3</sub>Bi<sub>2</sub>Br<sub>9</sub> but produced Rb<sub>3</sub>BiBr<sub>6</sub>. The process of doping SnBr<sub>2</sub> into pure Rb<sub>3</sub>Bi<sub>2</sub>Br<sub>9</sub> by Solid-state Grinding (SsG) formed the extra phase of Rb<sub>3</sub>BiBr<sub>6</sub>. This means that Rb<sub>3</sub>BiBr<sub>6</sub> is favourable in the reaction dynamics. Sn<sup>2+</sup> doping is not applicable for Cs<sub>3</sub>Sb<sub>2</sub>Cl<sub>9</sub> and Rb<sub>3</sub>Bi<sub>2</sub>Br<sub>9</sub> in the synthesis methods mentioned before but it helps the understanding the interband transition of both Cs<sub>3</sub>Sb<sub>2</sub>Cl<sub>9</sub> and Rb<sub>3</sub>Bi<sub>2</sub>Br<sub>9</sub> materials using Tauc method and Elliot theory.

## 5 Conclusion and Future Direction

Mixed halide vacancy-ordered perovskite was applied with substantial doping to mix halogen elements from Group 14 to modulate the structural properties, electronic properties, and optical properties of lead-free halide materials. Pure Cs<sub>2</sub>SnX<sub>6</sub> (X = Cl, Br, and I) compounds and mixed halide materials (Cs<sub>2</sub>SnCl<sub>6-6x</sub>Br<sub>6x</sub> and Cs<sub>2</sub>SnBr<sub>6x</sub>l<sub>6-6x</sub>, x= 0 to 1 in increments of 0.1) were synthesized using a room temperature solution-phased method. The structures of both composition series were single phase without long-range anion ordering observed by diffraction. The cubic A<sub>2</sub>BX<sub>6</sub> structure underwent distortion to accommodate Cs<sup>+</sup> without altering overall symmetry. The optical band gap values varied nonlinearly with anion composition, ranging from 4.89 eV (Cs<sub>2</sub>SnCl<sub>6</sub>) to 1.35 eV (Cs<sub>2</sub>SnI<sub>6</sub>).

Mixed halide compounds exhibited additional lower energy optical transitions not found in pure halide compounds, which resulted from changes in local symmetry within the tin halide octahedra. The electronic structure was analysed using photoemission spectroscopy, and Raman spectroscopy identified specific vibrational modes associated with mixed halide octahedra. This analysis revealed a near-random distribution of halide anions throughout the octahedra structures of mixed anion compounds in Raman spectra. Although deviations from random distribution were observed in mixed iodide-bromide compounds, compounds with larger iodide ions preferred trans configurations.<sup>74</sup>

To conclude, two synthesis methods were attempted to produce compounds. The methods are solution-phase synthesis and a solid-state synthesis. Using a solution-phase synthesis to produce compounds the cost was relatively low; it was easy to manufacture, and it was confirmed to work effectively. On the other hand, using a solid-state synthesis to mix to premade pure halide compounds at high temperature the front cost was high, and it was hard to manufacture due to the decomposition of samples at high temperatures. So far only one sample showed some progress on the production of mixed B-sited pure halide compounds. However, most of decompositions of halide compounds in the form of Cs<sub>2</sub>BX<sub>6</sub> ended with CsBr as the residue. Also, the decomposition temperature of the samples can be a future reference for the heating processes of samples. If heating temperature is well controlled under decomposition temperature, there is still a chance to adjust composition or mix B-site ion or halide ions by desired temperatures.

The results from this thesis showed some implications for double vacancy defect perovskite ( $A_2BX_6$ ) which other people may be able to apply implications to other similar perovskite-like compounds. First, the size of A-site ions maintains the overall symmetry of the lattice structures of the compounds by affecting the spacing of the  $BX_6$  octahedra. Secondly, optical band gaps can be tuned by the ratio of mixed halide in the bowing-shaped correlation. Third, mixing pure halide double perovskites in a ratio to achieve mixed B-site (Sn, Ti) double perovskites was unsuccessful. Solution synthesis is the more efficient method. This also means that different synthesis methods affect quality and purity of products.

In summary, the use of mixed valence doping in the 2D hybrid layered perovskite Cs<sub>3</sub>Bi<sub>2</sub>Br<sub>9</sub> was investigated. The room temperature mechanochemical synthesis method yielded comparable/superior results to the products made via the solution-phased synthesis, offering easier manufacturing procedures and shorter processing time. A spontaneous colour changes from pale yellow to dark brown or very dark brown was observed during the reaction. By doping with Sn, the light absorption of the material was enhanced. This enhancement was attributed to the presence of mixed valence doping, with Sn existing in the both Sn (II) and Sn (IV) oxidation states on the Bi site, without altering the overall crystal structure of the bulk compound. The introduction of different valencies of Sn enabled an intervalence charge transfer (IVCT) process within Cs<sub>3</sub>Bi<sub>2</sub>Br<sub>9</sub>. This IVCT process contributed to additional energy transitions in the visible region, resulting in a significant improvement in light absorbance.

The inert effect of the lone pair of Sn<sup>2+</sup> may contribute to the results of the stability of the mixed valencies of Sn<sup>2+</sup> and Sn<sup>4+</sup>. It refers to the reluctance of the lone-pair electrons in the outermost electron shell, 5s orbital, to participate bonding or chemical reactions. The lone pair of Sn<sup>2+</sup> plays a key role in exciton relaxation and dissociation in low- dimensional halide perovskites. The lone pair leads to stronger excited-state structural distortion and bigger Stokes shift in Sn halides. The bigger Stokes shift slows down excitation energy transport which shows less energy loss caused by defects and enhance the light absorption. The presence of the lone pair of Sn<sup>2+</sup> encourages the dissociation of excitons into free electron and hole carriers. This is because these lone pairs in ns subshell can modify the electron environment, facilitating the separation of electrons and holes. The

strong coupling between metal-halide clusters in the inorganic perovskites can enhance this separation efficiently.<sup>145</sup>

The Sn doping technique is not limited to Cs<sub>3</sub>Bi<sub>2</sub>Br<sub>9</sub> in the trigonal structure; it is also applicable to Cs<sub>3</sub>Bi<sub>2</sub>Cl<sub>9</sub> in the orthorhombic structure. Cs<sub>3</sub>Bi<sub>2</sub>Cl<sub>9</sub> is initially white, but when doped with SnCl<sub>2</sub>, an immediate colour changes from white to pale yellow occurs. Like Cs<sub>3</sub>Bi<sub>2</sub>Br<sub>9</sub> doping with tin, the intervalence charge transfer (IVCT) process occurs in Cs<sub>3</sub>Bi<sub>2</sub>Cl<sub>9</sub> as well. The existence of mixed valences of Sn<sup>2+</sup> and Sn<sup>4+</sup> slightly improves light absorption, considering the low doping amount. However, the percentage of Sn doping is much lower compared to the results obtained with Sn-doped Cs<sub>3</sub>Bi<sub>2</sub>Br<sub>9</sub>. It is worth noting that the solid-state grinding method is not suitable for tin doping in Cs<sub>3</sub>Bi<sub>2</sub>Cl<sub>9</sub>, as it leads to the formation of secondary phases like Cs<sub>2</sub>BiCl<sub>6</sub>, even at low Sn percentages, such as 5%. Other structures such as Cs<sub>3</sub>Sb<sub>2</sub>Cl<sub>9</sub> and Rb<sub>3</sub>Bi<sub>2</sub>Br<sub>9</sub> were not suitable for Sn doping to manifest the light absorption property as secondary phases formed immediately when SnCl<sub>2</sub> or SnBr<sub>2</sub> were added which was observed from XRD diffraction.

This thesis showed the existence of the IVCT caused by the mixed valencies(Sn<sup>2+</sup> and Sn<sup>4+</sup>) in the Sn doped defect-ordered triple perovskite compounds but the further study of the measurements of IVCT of these compounds is required. This opens an alternative doping regime and technique to create additional energy transitions in the visible region, resulting in a significant improvement in light absorbance. It also widens the types of dopants that are available for use in the

B-sites of triple-perovskites, and other such mixed valent pairs can be explored. In the case of the double vacancy ordered perovskites, Sb<sup>3+</sup> and Sb<sup>5+</sup> mixed valency is well known<sup>146</sup>, and In<sup>3+</sup>/ Sb<sup>3+</sup> and Sb<sup>5+</sup> has been previously studied<sup>147</sup>. Other such combinations can be found for the triple-perovskites and compared to the Sn-based doping reported here.

Overall, the thesis looked at researching the synthesis and characterisation of perovskites and perovskite-like materials with the aim of improving them as light absorbers. By exploring various synthesis methods with different doping techniques to adjust and optimize their structural, electronic, and optical properties, hopefully the work from this research can expand the understanding of different kinds of perovskite-like compounds in form of A<sub>2</sub>BX<sub>6</sub> and A<sub>3</sub>B<sub>2</sub>X<sub>9</sub> and help to enhance the performance of future solar cells. May it serve as valuable guidance in the search for new materials that exhibit excellent light absorption properties, further advancing the field of solar energy.

# 6 Appendix

# **6.1** Detailed information about Reagents and Solvents

Reagents and Solvents	Formula	Purity	CAS Number	Manufacturer
Caesium Carbonate	Cs <sub>2</sub> CO <sub>3</sub>	≥ 99.0%	534-17-8	Sigma Aldrich
Hydrobromic Acid	HBr	47.0% – 49.0%	10035-10- 6	Alfa Aesar
Hydrobromic Acid	HBr	48%	10035-10- 6	Acros Organics
Hydrochloric Acid	HCI	≥ 32%	7647-01-0	Honeywell International Inc
Hydrochloric Acid	HCI	37%	7647-01-0	Fisher Chemical
Absolute Ethanol	C <sub>2</sub> H <sub>6</sub> O	99.8%	64-17-5	Sigma Aldrich
Emplura Ethanol Absolute	C <sub>2</sub> H <sub>6</sub> O	99.5+%	64-17-5	Supelco Inc
Tellurium Dioxide	TeO <sub>2</sub>	99%	7446-07-3	Sigma Aldrich
Tributyl Phosphate	C <sub>12</sub> H <sub>27</sub> O <sub>4</sub> P	97%	126-73-8	Sigma Aldrich
Tin (IV) Chloride Pentahydrate	SnCl <sub>4</sub> • 5H <sub>2</sub> O		10026-06- 9	Honeywell International Inc
Chloroform (Trichloromethane Methylidyne Trichloride)	CHCl <sub>3</sub>	99.8%	67-66-3	Fisher Chemical
Water	H <sub>2</sub> O		7732-18-5	Fisher Chemical
Tin (IV) bromide /Stannic bromide	SnBr <sub>4</sub>	99%	7789-67-5	Sigma Aldrich
Tin (IV) iodide /Stannic iodide	Snl₄ mesh	99+%	7790-47-8	Acros Organics
Hydriodic acid	HI	57% stab with 1.5% Hypo- phosphorous acid HI	10034-85- 2	Alfa Aesar
Tin(II) chloride	SnCl <sub>2</sub>	Anhydrous, 99% min Crystalline	7772-99-8	Alfa Aesar
Tin(II) bromide	SnBr <sub>2</sub>	99.2%	10031-24- 0	Sigma Aldrich
Bismuth(III) bromide	BiBr <sub>3</sub>	≥98.0%	7787-58-8	Sigma Aldrich
Bismuth(III) chloride	BiCl <sub>3</sub>	97+%	7787-60-2	Alfa Aesar
Antimony(III) chloride	SbCl <sub>3</sub>	≥99.0%	10025-91- 9	Sigma Aldrich
Rubidium bromide	RbBr	99.8%	7789-39-1	Alfa Aesar

Rubidium carbonate	Rb <sub>2</sub> CO <sub>3</sub>	99.8%	584-09-8	Sigma Aldrich
Ethylamine	CH <sub>3</sub> CH <sub>2</sub> NH <sub>2</sub>	70 wt%	75-04-7	Sigma Aldrich
Methylamine	CH <sub>3</sub> NH <sub>2</sub>	40 wt%	74-89-5	Sigma Aldrich

# **6.2** Compositional Calculation Data

Composition	x	32% HCI	48% HBr	99% Cs <sub>2</sub> (CO <sub>3</sub> )	SnBr <sub>4</sub>	SnCl <sub>4</sub> •5H <sub>2</sub> O
Cs <sub>2</sub> SnCl <sub>6</sub>	0	10	0	1.926731912	0	2.073268088
Cs <sub>2</sub> SnCl <sub>5.4</sub> Br <sub>0.6</sub>	0.1	8.588253768	1.411746232	1.90206263	0.255887028	1.842050342
Cs <sub>2</sub> SnCl <sub>4.8</sub> Br <sub>1.2</sub>	0.2	7.300030034	2.699969966	1.878017078	0.505304294	1.616678626
Cs <sub>2</sub> SnCl <sub>4.2</sub> Br <sub>1.8</sub>	0.3	6.119796662	3.880203338	1.854571896	0.748494106	1.396933996
Cs <sub>2</sub> SnCl <sub>3.6</sub> Br <sub>2.4</sub>	0.4	5.03452085	4.96547915	1.831704876	0.98568682	1.182608304
Cs <sub>2</sub> SnCl <sub>3</sub> Br <sub>3</sub>	0.5	4.03318584	5.96681416	1.809394892	1.217101564	0.973503544
Cs <sub>2</sub> SnCl <sub>2.4</sub> Br <sub>3.6</sub>	0.6	3.106415608	6.893584392	1.787621836	1.442946926	0.769431238
Cs <sub>2</sub> SnCl <sub>1.8</sub> Br <sub>4.2</sub>	0.7	2.246180384	7.753819616	1.766366552	1.66342157	0.570211878
Cs <sub>2</sub> SnCl <sub>1.2</sub> Br <sub>4.8</sub>	0.8	1.445563398	8.554436602	1.745610792	1.87871482	0.375674386
Cs <sub>2</sub> SnCl <sub>0.6</sub> Br <sub>5.4</sub>	0.9	0.698574494	9.301425506	1.72533715	2.08900721	0.18565564
Cs <sub>2</sub> SnBr <sub>6</sub>	1	0	10	1.70552902	2.29447098	0

## • Cs<sub>2</sub>Snl<sub>6-6x</sub>Br<sub>6x</sub> (x=0 to 1 in increments of 0.1)

Composition	X (Br% of	57% washed HI	48% HBr	99% Cs <sub>2</sub> (CO <sub>3</sub> )	SnBr <sub>4</sub>	Snl <sub>4</sub>
	mixed halides)					
Cs <sub>2</sub> SnI <sub>6</sub>	0	10	0	1.382601948	0	2.657802092
Cs <sub>2</sub> SnI <sub>5.4</sub> Br <sub>0.6</sub>	0.1	9.22967299	0.77032701	1.410451004	0.189749858	2.440203178
Cs <sub>2</sub> SnI <sub>4.8</sub> Br <sub>1.2</sub>	0.2	8.419000096	1.580999904	1.439445022	0.387300924	2.213658094
Cs <sub>2</sub> SnI <sub>4.2</sub> Br <sub>1.8</sub>	0.3	7.564726402	2.435273598	1.469656092	0.593144394	1.977603554
Cs <sub>2</sub> SnI <sub>3.6</sub> Br <sub>2.4</sub>	0.4	6.6632372	3.3367628	1.501162488	0.807813582	1.73142797
Cs <sub>2</sub> SnI <sub>3</sub> Br <sub>3</sub>	0.5	5.710506858	4.289493142	1.534049344	1.031888542	1.474466156
Cs <sub>2</sub> SnI <sub>2.4</sub> Br <sub>3.6</sub>	0.6	4.702038716	5.297961284	1.568409418	1.266001288	1.205993334
Cs <sub>2</sub> SnI <sub>1.8</sub> Br <sub>4.2</sub>	0.7	3.632794126	6.367205874	1.60434397	1.510841768	0.925218304
Cs <sub>2</sub> SnI <sub>1.2</sub> Br <sub>4.8</sub>	0.8	2.497108246	7.502891754	1.64196376	1.76716463	0.63127565
Cs <sub>2</sub> SnI <sub>0.6</sub> Br <sub>5.4</sub>	0.9	1.288589658	8.711410342	1.681390184	2.035797014	0.323216842
Cs <sub>2</sub> SnBr <sub>6</sub>	1	0	10	1.722756586	2.317647456	0

## • Cs<sub>2</sub>SnTeCl<sub>6x</sub> (x=0 to 1 in increments of 0.1)

Composition	x	x SnCl <sub>4</sub> =5H <sub>2</sub> O	(1-x) TeO <sub>2</sub>	(1-x)4HCI	Cs <sub>2</sub> CO <sub>3</sub>	2HCI
Cs <sub>2</sub> TeCl <sub>6</sub>	0	0	1.596	4.5575	3.291111	2.27875
Cs <sub>2</sub> Sn <sub>0.1</sub> Te <sub>0.9</sub> Cl <sub>6</sub>	0.1	0.26052	1.4364	4.10175	3.291111	2.27875
Cs <sub>2</sub> Sn <sub>0.2</sub> Te <sub>0.8</sub> Cl <sub>6</sub>	0.2	0.52104	1.2768	3.646	3.291111	2.27875
Cs <sub>2</sub> Sn <sub>0.3</sub> Te <sub>0.7</sub> Cl <sub>6</sub>	0.3	0.78156	1.1172	3.19025	3.291111	2.27875
Cs <sub>2</sub> Sn <sub>0.4</sub> Te <sub>0.6</sub> Cl <sub>6</sub>	0.4	1.04208	0.9576	2.7345	3.291111	2.27875
Cs <sub>2</sub> Sn <sub>0.5</sub> Te <sub>0.5</sub> Cl <sub>6</sub>	0.5	1.3026	0.798	2.27875	3.291111	2.27875
Cs <sub>2</sub> Sn <sub>0.6</sub> Te <sub>0.4</sub> Cl <sub>6</sub>	0.6	1.56312	0.6384	1.823	3.291111	2.27875
Cs <sub>2</sub> Sn <sub>0.7</sub> Te <sub>0.3</sub> Cl <sub>6</sub>	0.7	1.82364	0.4788	1.36725	3.291111	2.27875
Cs <sub>2</sub> Sn <sub>0.8</sub> Te <sub>0.2</sub> Cl <sub>6</sub>	0.8	2.08416	0.3192	0.9115	3.291111	2.27875
Cs <sub>2</sub> Sn <sub>0.9</sub> Te <sub>0.1</sub> Cl <sub>6</sub>	0.9	2.34468	0.1596	0.45575	3.291111	2.27875
Cs <sub>2</sub> SnCl <sub>6</sub>	1	2.6052	0	0	3.291111	2.27875

				Total	5g acid
2g of (CH <sub>3</sub> CH <sub>2</sub> NH <sub>3</sub> ) <sub>2</sub> SnCl <sub>6-6x</sub> Br <sub>6x</sub>	70% CH <sub>3</sub> CH <sub>2</sub> NH <sub>2</sub>	SnBr₄	SnCl₄.5H₂O	g HCI(32 wt%)	g HBr (48 wt%)
0	0.584445049	0	1.59088847	5	0
0.1	0.573039132	0.19501572	1.40385689	4.28126718	0.718732824
0.2	0.562069883	0.38256536	1.22398572	3.62916684	1.370833157
0.3	0.551512699	0.56306963	1.05087148	3.03484342	1.965156583
0.4	0.541344788	0.7369182	0.88414045	2.49094398	2.509056022
0.5	0.531545009	0.90447253	0.72344596	1.99131251	3.008687488
0.6	0.522093726	1.06606837	0.56846603	1.5307559	3.4692441
0.7	0.512972673	1.222018	0.41890113	1.10486273	3.895137268
0.8	0.50416484	1.37261226	0.27447235	0.70986156	4.290138441
0.9	0.495654366	1.51812236	0.13491958	0.3425089	4.657491096
1	0.487426441	1.65880149	0	0	5

## 6.3 Analytic atomic ratio and unit cell parameters of Cs<sub>2</sub>SnX<sub>6</sub>

The atomic number of samples in the series  $Cs_2SnCl_{6-6x}Br_{6x}(x=0 \text{ to 1 in increments of 0.1, } x=0 \text{ represents nominal } Br\%=0)$ :

		2	XPS Ana	alysis			Unit cell pa	rameters
							Lattice a	Volume
nominal %Br	Cs%	Sn%	Br%	CI%	Br%/(Br%+CI%)	Analytic composition	Parameter	
Cs <sub>2</sub> SnCl <sub>6</sub> (0%Br)	24.21	12.99	0	62.8	0.00	Cs <sub>2</sub> SnCl6	10.37864	1117.95
Cs <sub>2</sub> SnBr <sub>0.6</sub> Cl <sub>5.4</sub> (10%Br)	20.15	12.2	1.41	66.15	2.09	Cs <sub>2</sub> SnBr <sub>0.13</sub> Cl <sub>5.87</sub>	10.42647	1122.618
Cs <sub>2</sub> Sn Br <sub>1.2</sub> Cl <sub>4.8</sub> (20%Br)	17.01	7.95	7.8	67.24	10.39	Cs <sub>2</sub> SnBr <sub>0.62</sub> Cl <sub>5.38</sub>	10.422	1131.759
Cs <sub>2</sub> Sn Br <sub>1.8</sub> Cl <sub>4.2</sub> (30%Br)	27.02	17.29	22.33	33.37	40.09	Cs <sub>2</sub> SnBr <sub>2.40</sub> Cl <sub>3.60</sub>	10.447	1140.109
Cs <sub>2</sub> Sn Br <sub>3</sub> Cl <sub>3</sub> (50%Br)	25.11	13.19	37.97	23.73	61.54	Cs <sub>2</sub> SnBr <sub>3.70</sub> Cl <sub>2.30</sub>	10.6685563	1214.278
Cs <sub>2</sub> Sn Br <sub>36</sub> Cl <sub>2.4</sub> (60%Br)	22.07	15.99	25.85	35.43	42.18	Cs <sub>2</sub> SnBr <sub>2.56</sub> Cl <sub>3.44</sub>	10.60669	1193.274
Cs <sub>2</sub> Sn Br <sub>4.2</sub> Cl <sub>1.8</sub> (70%Br)	28.47	19.65	31.18	20.7	60.10	$Cs_2SnBr_{3.61}Cl_{2.39}$	10.661126	1211.74
Cs <sub>2</sub> Sn Br <sub>4.8</sub> Cl <sub>1.2</sub> (80%Br)	27.52	19.62	41.91	10.96	79.27	Cs <sub>2</sub> SnBr <sub>4.76</sub> Cl <sub>1.24</sub>	10.77749	1251.861
Cs <sub>2</sub> Sn Br <sub>5.4</sub> Cl <sub>0.6</sub> (90%Br)	19.51	11.8	58.3	10.39	84.87	Cs <sub>2</sub> SnBr <sub>5.09</sub> Cl <sub>0.91</sub>	10.79136	1256.699
Cs <sub>2</sub> SnBr <sub>6</sub> (100%Br)	25.19	13.87	60.94	0	100.00	Cs <sub>2</sub> SnBr <sub>6</sub>	10.83739	1272.844

Note: The atomic number in red represents outliner of data due to the unmatched atomic ratio to 2:1:6 of samples in the series

 $Cs_2SnCl_{6\text{-}6x}Br_{6x}.$ 

The atomic number of samples in the series  $Cs_2SnI_{6-6x}Br_{6x}(x=0 \text{ to } 1 \text{ in increments of } 0.1, x=0 \text{ represents nominal } Br\%=0)$ :

			XPS A	Analysis				Unit cell pa	arameters
				•			Analytic	Lattice a	Volume
	Br%	Cs%	Sn%	Br%	1%	Br%/(Br%+I%)	composition	parameter	
Cs <sub>2</sub> SnBr <sub>6</sub> (100%Br)	100	25.19	13.87	60.94	0	100	$Cs_2SnBr_6$	10.83739	1272.844
Cs <sub>2</sub> SnBr <sub>5.4</sub> I <sub>0.6</sub> (90%Br)	90.3998	21.55	11.68	60.36	6.41	90.39988019	Cs <sub>2</sub> SnBr <sub>5.49</sub> l <sub>0.51</sub>	10.86087	1281.135
Cs <sub>2</sub> Sn Br <sub>4.8</sub> I <sub>1.2</sub> (80%Br)	85.008	21.04	11.18	57.61	10.16	85.00811569	Cs <sub>2</sub> SnBr <sub>5.19</sub> I <sub>0.81</sub>	10.86732	1283.417
Cs <sub>2</sub> Sn Br <sub>4.2</sub> I <sub>1.8</sub> (70%Br)	77.5	21.50	10.28	52.89	15.33	77.52858399	Cs <sub>2</sub> SnBr <sub>4.59</sub> I <sub>1.41</sub>	10.95381	1314.309
Cs <sub>2</sub> Sn Br <sub>3.6</sub> l <sub>2.4</sub> (60%Br)	73.32	26.74	12.40	44.62	16.23	73.32785538	Cs <sub>2</sub> SnBr <sub>4.40</sub> I <sub>1.60</sub>	11.05538	1351.206
Cs <sub>2</sub> Sn Br <sub>3</sub> I <sub>3</sub> (50%Br)	47.34	24.69	14.96	28.57	31.77	47.3483593	Cs <sub>2</sub> SnBr <sub>2.84</sub> I <sub>3.16</sub>	11.36591	1468.293
Cs <sub>2</sub> Sn Br <sub>2.4</sub> I <sub>3.6</sub> (40%Br)	67.9419	27.97	15.58	38.36	18.10	67.94190577	Cs <sub>2</sub> SnBr <sub>4.08</sub> I <sub>1.92</sub>	11.15454	1387.895
Cs <sub>2</sub> Sn Br <sub>1.8</sub> I <sub>4.2</sub> (30%Br)	52.88	28.25	8.06	33.69	30.02	52.88023858	Cs <sub>2</sub> SnBr <sub>3.17</sub> l <sub>2.83</sub>	11.34501	1460.21
Cs <sub>2</sub> Sn Br <sub>1.2</sub> I <sub>4.8</sub> (20%Br)	43.93385	27.37	15.18	25.24	32.21	43.93385553	Cs <sub>2</sub> SnBr <sub>2.64</sub> I <sub>3.36</sub>	11.47056	1509.224
Cs <sub>2</sub> Sn Br <sub>0.6</sub> I <sub>5.4</sub> (10%Br)	18.37813	23.56	12.08	11.83	52.54	18.37812646	Cs <sub>2</sub> SnBr <sub>1.10</sub> I <sub>4.89</sub>	11.60751	1563.929
Cs <sub>2</sub> SnI <sub>6</sub>	0	21.92	13.63	0	100	0	$Cs_2SnI_6$	11.6	1576.48

Note: The atomic number in red represents outliner of data due to the unmatched atomic ratio to 2:1:6 of samples in the series

 $Cs_2SnI_{6-6x}Br_{6x}$ .

## 6.4 XPS Analysis of Sn doped Cs<sub>3</sub>Bi<sub>2</sub>Br<sub>9</sub>

#### • Analytic atomic % of Sn doped Cs<sub>3</sub>Bi<sub>2</sub>Br<sub>9</sub>

Nominal Sn% doped Cs <sub>3</sub> Bi <sub>2</sub> Br <sub>9</sub>	Analytic Bi%	Analytic Br%	Analytic Cs%	Analytic Sn%
0	13.79	51.27	34.94	0
5	13.97	44.79	38.02	3.21
12	14.5	44.48	30.97	10.05
25	11.01	41.47	34.57	12.94

#### • Binding energy difference Bi-Br

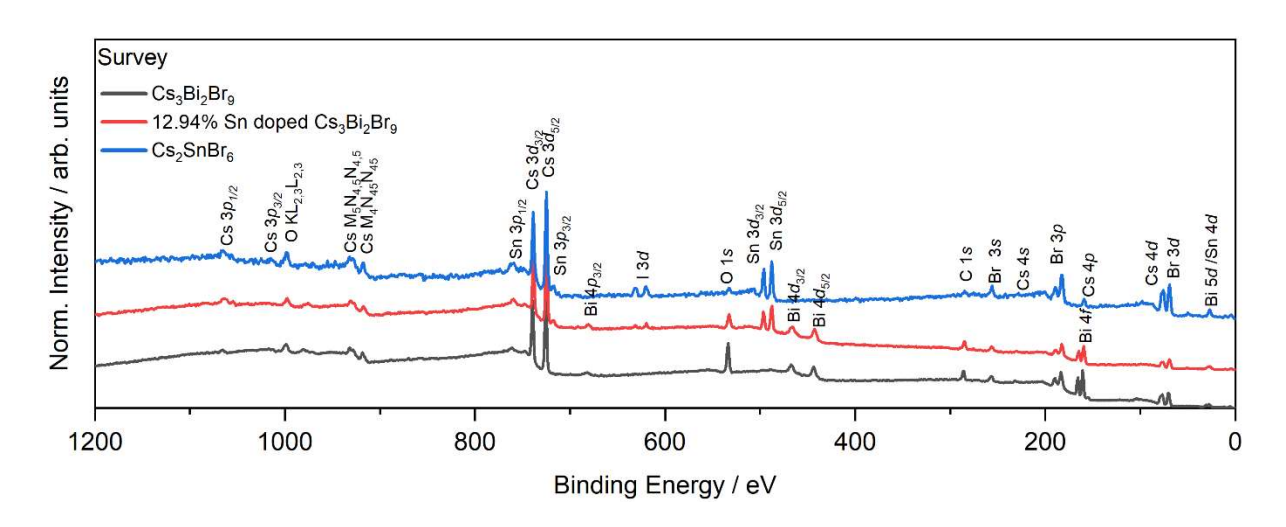
Analytic Sn% of Sn			Binding energy
doped Cs <sub>3</sub> Bi <sub>2</sub> Br <sub>9</sub>	Bi 4f 7/2/ eV	Br 3d <sub>5/2</sub> / eV	difference/ eV
0	160.29	69.48	90.81
3.21	159.19	68.36	90.83
10.05	159.52	69.43	90.09
12.94	159.4	68.51	90.89

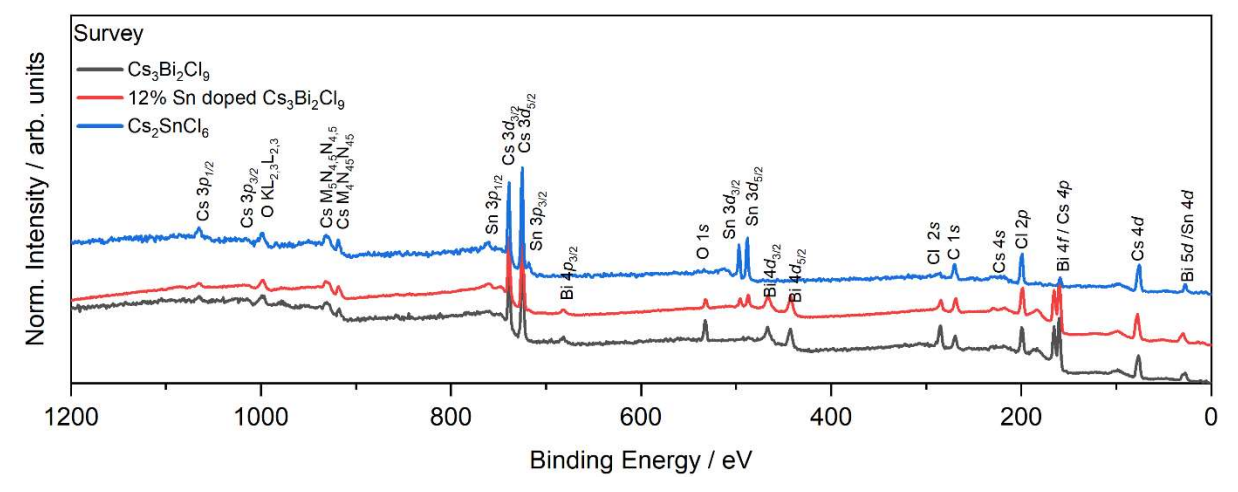
#### • Binding energy difference Sn-Br

		Sn 3d <sub>5/2</sub> / eV	Br 3d <sub>5/2</sub> / eV	Binding energy difference/ eV	FWHM/ eV	Cs 3d <sub>5/2</sub> / eV	FWHM/ eV
Cs2SnBr6		487.5	68.66	418.84	1.37	724.5	1.53
3.21%	Sn-						
doped							
Cs <sub>3</sub> Bi <sub>2</sub> Br <sub>9</sub>		487.29	68.36	418.93	1.74	724.29	1.46
10.05%	Sn-						
doped							
Cs <sub>3</sub> Bi <sub>2</sub> Br <sub>9</sub>		488.51	69.43	419.08	1.67	725.42	1.51

12.94%	Sn-						
doped							
Cs <sub>3</sub> Bi <sub>2</sub> Br <sub>9</sub>		487.6	68.51	419.09	1.77	724.57	1.55

• XPS survey of Cs<sub>2</sub>SnCl<sub>6</sub>, Cs<sub>2</sub>SnBr<sub>6</sub>, pure Cs<sub>3</sub>Bi<sub>2</sub>Br<sub>9</sub>, 12.94%Sn doped Cs<sub>3</sub>Bi<sub>2</sub>Br<sub>9</sub>, pure Cs<sub>3</sub>Bi<sub>2</sub>Cl<sub>9</sub> and nominal 12%Sn doped Cs<sub>2</sub>Bi<sub>2</sub>Cl<sub>9</sub>





## 7 Publications

- 1. Krajewska, C. J.; Kavanagh, S. R.; Zhang, L.; Kubicki, D. J.; Dey, K.; Gałkowski, K.; Grey, C. P.; Stranks, S. D.; Walsh, A.; Scanlon, D. O.; et al. Enhanced visible light absorption in layered Cs<sub>3</sub>Bi<sub>2</sub>Br<sub>9</sub> through mixed valence sn(ii)/sn(iv) doping. *Chemical Science* **2021**, *12* (44), 14686–14699.
- 2. Karim, M. M.; Ganose, A. M.; Pieters, L.; Winnie Leung, W. W.; Wade, J.; Zhang, L.; Scanlon, D. O.; Palgrave, R. G. Anion distribution, structural distortion, and symmetry-driven optical band gap bowing in mixed halide Cs<sub>2</sub>SnX<sub>6</sub> vacancy ordered Double Perovskites. *Chemistry of Materials* **2019**, *31* (22), 9430–9444.

# **8 List of Figures**

Figure 1.1 The schematic diagram representing (a)conduction band, valence band	
and forbidden energy gap. The schematic diagram of the energy band structures of	F
(b) Insulator (such as ceramic), (c)Conductor (such as metal), and (d)	
Semiconductor (such as silicon)	13
Figure 1.2 The schematic band diagram of a p-type semiconductor and a n-type	
semiconductor	16
Figure 1.3 The Schematic diagram of direct bandgap and indirect bandgap	
semiconductors	17
Figure 1.4 The schematic diagram of perovskite structure ABX <sub>3</sub>	25
Figure 1.5 A chart of the highest confirmed conversion efficiencies for various	
research solar cells from 1976 to 2023.	26
Figure 1.6 The diagram of the mechanism of a perovskite solar cell	28
Figure 1.7 A schematic of substitutional and interstitial atomic modification by light	
elements to face-centred-cubic (FCC) a host metal lattice (green). (a) Substitutional	I
atomic displacement by foreign light atoms (blue). (b) Interstitial atomic modification	1
by foreign light atoms (brown).	30
Figure 1.8 The unit cell structure of CsSnI <sub>3</sub>	33
Figure 1.9 (a) Solar cell I-V characteristic curve (b) The diagram of the change of the	,
band gaps, $V_g$ , affecting the ultimate efficiency, $u(x_g)$ , of a single p-n junction solar	
cell.60	38
Figure 1.10 The unit cell structure of Cs <sub>2</sub> SnI <sub>6</sub> . Six iodine anions are normally around	d
one Sn <sup>4+</sup> cation, forming [SnI <sub>6</sub> ] <sup>2-</sup> Octahedral structure	40
Figure 1.11 The crystal structure of Cs <sub>3</sub> Bi <sub>2</sub> Cl <sub>9</sub> in Pmcn space group, Cs <sub>3</sub> Bi <sub>2</sub> Br <sub>9</sub> in P-	
3m1 space group and Cs <sub>3</sub> Bi <sub>2</sub> I <sub>9</sub> in P6 <sub>3</sub> /mmc space group	45
Figure 2.1 The schematic diagram of Bragg's law.	55
Figure 2.2 The schematic mechanism of the XPS spectrometer	60
Figure 2.3 Three different kinds of scattering happened when light irradiates with a	
molecule	65
Figure 3.1 The binding energy shifts of Cs $3d_{5/2}$ and Sn $3d_{5/2}$ core lines with the	
analytic Br% in samples across Cs <sub>2</sub> SnBr <sub>6-6x</sub> Cl <sub>6x</sub> series (left) and Cs <sub>2</sub> SnI <sub>6-6x</sub> Br <sub>6x</sub> series	es:
(right), and two shaded data points are outliners which can be ignored	88

Figure 3.2 The XRD patterns of samples in series Cs <sub>2</sub> SnCl <sub>6-6x</sub> Br <sub>6x</sub> (b) and Cs <sub>2</sub> Sn
$Br_{6x}I_{6-6x}$ (a) ((x= 0 to 1 in increments of 0.1, x=0 represents Br%=0), (c) The
comparation between the PXRD patterns of compound Cs <sub>2</sub> SnBr <sub>5.19</sub> I <sub>0.81</sub> and the
grinded Snl4, (d) The comparation between the PXRD patterns of compound
Cs <sub>2</sub> SnBr <sub>3.61</sub> Cl <sub>2.39</sub> and CsCl from ICSD database(257256)
Figure 3.3 (a) The correlation between the analytic Br% and the volume per cell unit
of samples in Cs <sub>2</sub> SnCl <sub>6-6x</sub> Br <sub>6x</sub> series. (b)The correlation between the analytic Br%
and the volume per cell unit of samples in Cs <sub>2</sub> SnBr <sub>6-6x</sub> I <sub>6x</sub> series96
Figure 3.4 (a)The Raman spectrum of pure Cs₂SnI <sub>6</sub> with point group locations; (b)
The Raman spectra of samples in series Cs <sub>2</sub> SnCl <sub>6-6x</sub> Br <sub>6x</sub> ; (c) The Raman spectra of
samples in series $Cs_2SnBr_{6x}I_{6-6x}$ ((x= 0 to 1 in increments of 0.1, x=0 represents
analytic Br%=0)102
Figure 3.5 Tauc plots of samples in the Cs <sub>2</sub> SnBr <sub>6x</sub> Cl <sub>6-6x</sub> series (top) in the graph(a)
and in the Cs <sub>2</sub> SnBr <sub>6x</sub> I <sub>6-6x</sub> series(bottom) in the graph (b) were shown with their
analytical compositions. Band gaps of Cs <sub>2</sub> SnCl <sub>6</sub> , Cs <sub>2</sub> SnBr <sub>6</sub> , and Cs <sub>2</sub> SnI <sub>6</sub> were
highlighted in the graph111
Figure 3.6 (a) The correlation between optical band gaps and analytic Br% of
samples in series Cs <sub>2</sub> SnCl <sub>6-6x</sub> Br <sub>6x</sub> on the top and (b) the correlation between optical
band gaps and analytic Br% of samples in series Cs <sub>2</sub> SnI <sub>6-6x</sub> Br <sub>6x</sub> on the bottom were
shown above114
Figure 3.7 TGA data analysis of pure Cs₂SnBr <sub>6</sub> perovskite compound117
Figure 3.8 TGA data analysis of pure Cs₂SnCl <sub>6</sub> perovskite compound
Figure 3.9 TGA data analysis of pure Cs <sub>2</sub> SnI <sub>6</sub> perovskite compound
Figure 3.10 The XRD patterns of the mixed samples of pure 0.5g Cs <sub>2</sub> SnBr <sub>6</sub> (SpS)
and pure 0.5g Cs₂SnI <sub>6</sub> (SpS) at room temperature and at high temperatures shown
above123
Figure 3.11 The XRD patterns of samples mixing Cs <sub>2</sub> SnBr <sub>6</sub> and Cs <sub>2</sub> SnI <sub>6</sub> at 250°C,
300°C and 400°C individually for 12 hours which were compared with XRD patterns
of CsBr <sup>104</sup> and CsCl from ICSD database
Figure 3.12 The Raman spectra of the mixed sample consisting of 0.5g Cs₂SnBr <sub>6</sub>
and 0.5g Cs <sub>2</sub> SnI <sub>6</sub> at the different temperatures are shown here( where Cs <sub>2</sub> SnI <sub>6</sub> ,
Cs <sub>2</sub> SnBr <sub>3</sub> I <sub>3</sub> and Cs <sub>2</sub> SnBr <sub>3</sub> sI <sub>2</sub> 4 made via SpS was used as counterparts) 127

Figure 3.13(a)The XRD patterns of the mixed samples of pure 0.5g Cs₂SnBr <sub>6</sub> (SpS)
and pure 0.5g Cs <sub>2</sub> SnCl <sub>6</sub> (SpS) at room temperature and at high temperatures shown
above on the top. XRD patterns of Sample $Cs_2SnBr_{3.55}Cl_{2.45}(SpS)$ and XRD patterns
of CsBr <sup>104</sup> and CsCl <sup>105</sup> from ICSD database are counterparts. (b)The enlarged area
of the XRD patterns of the mixed samples of pure 0.5g Cs₂SnBr <sub>6</sub> (SpS) and pure
0.5g Cs <sub>2</sub> SnCl <sub>6</sub> (SpS) at 300 ℃ and 400 ℃ at the bottom
Figure 3.14 The Raman patterns of the mixed sample consisting of 0.5g Cs₂SnBr <sub>6</sub>
and 0.5g Cs₂SnCl <sub>6</sub> at different temperatures for 12 hours are shown here. Raman
spectra of Cs <sub>2</sub> SnCl <sub>6</sub> (SpS), Cs <sub>2</sub> SnCl <sub>5.09</sub> Br <sub>0.91</sub> (SpS) and Cs <sub>2</sub> SnBr <sub>6</sub> (SpS) were used as
counterparts
Figure 3.15 (a) The PXRD patterns of samples of (CH <sub>3</sub> CH <sub>2</sub> NH <sub>3</sub> ) <sub>2</sub> SnCl <sub>6-6x</sub> Br <sub>6x</sub> series
on the top (made via SpS method) with analytic atomic composition. (b) The PXRD
patterns of samples of (CH <sub>3</sub> NH <sub>3</sub> ) <sub>2</sub> SnCl <sub>6-6x</sub> Br <sub>6x</sub> series at the bottom (made via SpS
method) with nominal atomic composition used as a reference
Figure 3.16 . (a)The correlation between the analytic Br% and the volume per cell
unit of samples in the $(CH_3CH_2NH_3)_2SnCl_{6-6x}Br_{6x}$ series. (b) The correlation between
the analytic Br% and % change of lattice a and lattice c of samples in the
(CH <sub>3</sub> CH <sub>2</sub> NH <sub>3</sub> ) <sub>2</sub> SnCl <sub>6-6x</sub> Br <sub>6x</sub> series. (c) The correlation between % change of lattice
parameters (a and c) and analytic Br% of series (CH <sub>3</sub> NH <sub>3</sub> ) <sub>2</sub> SnBr <sub>6-6x</sub> Cl <sub>6x</sub> 143
Figure 3.17 The bow-shaped correlation between band gaps and analytic Br% of
Samples in series Cs <sub>2</sub> SnBr <sub>6-6x</sub> Cl <sub>6x</sub> and in series (CH <sub>3</sub> NH <sub>3</sub> ) <sub>2</sub> SnBr <sub>6-6x</sub> Cl <sub>6x</sub> and in series
(CH <sub>3</sub> CH <sub>2</sub> NH <sub>3</sub> ) <sub>2</sub> SnBr <sub>6-6x</sub> Cl <sub>6x</sub>
Figure 3.18 The XRD patterns of compounds in series $Cs_2Sn_xTe_{1-x}Cl_6$ (SpS) 150
Figure 3.19 (a)The Raman spectra of compounds in series Cs <sub>2</sub> Sn <sub>x</sub> Te <sub>1-x</sub> Cl <sub>6</sub> . (b)
Raman spectrum of CsCl as a counterpart
Figure 3.20 The Raman spectrums of mixed Cs <sub>2</sub> SnCl <sub>6</sub> and Cs <sub>2</sub> TeCl <sub>6</sub> 154
Figure 3.21 XRD Analysis data of samples mixing Cs <sub>2</sub> SnCl <sub>6</sub> and Cs <sub>2</sub> TeCl <sub>6</sub> at 25 °C
and 320 °C. XRD patterns of Samples Cs <sub>2</sub> Sn <sub>0.5</sub> Te <sub>0.5</sub> Cl <sub>6</sub> (SpS) and CsCl was
counterparts
Figure 4.1 The PXRD patterns of pure Cs <sub>3</sub> Br <sub>2</sub> Br <sub>9</sub> and Sn doped Cs <sub>3</sub> Br <sub>2</sub> Br <sub>9</sub> (SpS)
powders
Figure 4.2 The powder XRD pattern of Cs <sub>3</sub> Bi <sub>2</sub> Br <sub>9</sub> produced by the solution-phased
synthesis. The model (green line) was refined from the structure reported by

Lazarini, F. et al <sup>115</sup> . The background is shown in red, and it shows how much
difference between the sample(observation) and the ICSD data(calculation) in cyan.
Navy blue dash marks show positions of reflections
Figure 4.3 The PXRD patterns of Sn-doped Cs <sub>3</sub> Bi <sub>2</sub> Br <sub>9</sub> materials (analytic Sn%=5,12
and 25) produced by Solid-state Grinding (SsG)
Figure 4.4 Bi 4f spectra of pure Cs <sub>3</sub> Bi <sub>2</sub> Br <sub>9</sub> material and Sn (Sn= 3.21%, 10.05% and
12.94%) doped Cs <sub>3</sub> Bi <sub>2</sub> Br <sub>9</sub> materials.(XPS survey of Cs <sub>3</sub> Bi <sub>2</sub> Br <sub>9</sub> was attached in
Appendix 6.4 for additional information.)
Figure 4.5 Sn 3d spectrum of pure Cs <sub>2</sub> SnBr <sub>6</sub> material and Sn (Sn= 3.21%, 10.05%
and 12.94%) doped Cs <sub>3</sub> Bi <sub>2</sub> Br <sub>9</sub> materials
Figure 4.6 (a)Demonstration of direct and indirect bandgap energy calculation from
Tauc-analysis for pure Cs₃Bi₂Brٶ and (b) A diffuse reflectance spectrum from
undoped Cs <sub>3</sub> Bi <sub>2</sub> Br <sub>9</sub> via a solution-phased synthesis which is treated with the Kubelka
Munk function (green points). The optical absorption is modelled using the Elliot
model in blue line, consisting of an exciton peak modelling by Dirac function in red
and a continuum absorption modelling by Heaviside function in black 173
Figure 4.7 Optical absorption spectra of pure Cs <sub>3</sub> Bi <sub>2</sub> Br <sub>9</sub> and Sn-doped Cs <sub>3</sub> Bi <sub>2</sub> Br <sub>9</sub> . 175
Figure 4.8 The powder XRD pattern of Cs <sub>3</sub> Bi <sub>2</sub> Cl <sub>9</sub> produced by the solution-phased
synthesis. The model (green line) was refined from the structure reported by Morgan
et al. The background is shown in red, and the residual is in black, and it shows how
much difference between the sample and the ICSD data in Orange. Orange dash
marks show positions of reflections
Figure 4.9 Powder XRD patterns from undoped and Sn-doped Cs₃Bi₂Cl <sub>9</sub> crystal
powders (SpS). Nominal Sn concentration of samples was displayed at the bottom in
the legend
Figure 4.10 The variation in unit cell volume with nominal Sn content in Cs <sub>3</sub> Bi <sub>2</sub> Cl <sub>9</sub> .
Error bars are plus and minus three times the standard deviation
Figure 4.11 The correlation between Nominal Sn content and Analytic Sn content
doped into Cs <sub>3</sub> Bi <sub>2</sub> Cl <sub>9</sub>
Figure 4.12 (a)Demonstration of direct and indirect bandgap energy calculation from
Tauc-analysis for pure Cs <sub>3</sub> Bi <sub>2</sub> Cl <sub>9</sub> (b)A diffuse reflectance spectrum from undoped
Cs₃Bi₂Cl <sub>9</sub> via a solution-phased synthesis which is treated with the Kubelka Munk
function (green points). The optical absorption is modelled using the Elliot model in

blue line, consisting of an exciton peak modelling by Dirac function in red and a
continuum absorption modelling by Heaviside function in black
Figure 4.13 Optical absorption spectra of Cs <sub>3</sub> Bi <sub>2</sub> Cl <sub>9</sub> doping Sn in 5%, 12%, 25%,
40% and 50%
Figure 4.14 Bi 4f spectra from Sn doped (top) and undoped (bottom) Cs <sub>3</sub> Bi <sub>2</sub> Cl <sub>9</sub> with
the fitted curves by Casa XPS software.(XPS survey of Cs <sub>3</sub> Bi <sub>2</sub> Cl <sub>9</sub> was attached in
Appendix 6.4 for additional information)
Figure 4.15 Sn 3d spectra from nominal 12% Sn doped Cs <sub>3</sub> Bi <sub>2</sub> Cl <sub>9</sub> (top) and Cs <sub>2</sub> SnCl <sub>6</sub>
(bottom), a pure Sn (IV) compound
Figure 4.16 Raman Spectra of orthorhombic pure Cs <sub>3</sub> Bi <sub>2</sub> Cl <sub>9</sub> material and Cs <sub>3</sub> Bi <sub>2</sub> Cl <sub>9</sub>
doping certain amount of Sn in 5%, 12% and 25%194
Figure 4.17 XRD patterns of Sn-doped Cs <sub>3</sub> Bi <sub>2</sub> Cl <sub>9</sub> materials produced by Solid-state
Grinding(SsG) with nominal Sn% =5%, 12%, and 25%
Figure 4.18 XRD patterns of the pure Cs <sub>3</sub> Sb <sub>2</sub> Cl <sub>9</sub> sample and Sn doped Cs <sub>3</sub> Sb <sub>2</sub> Cl <sub>9</sub>
samples (SpS) with nominal Sn%=5%, 12%, 25%, 40% and 50%
Figure 4.19 UV-vis diffused reflectance study of Cs <sub>3</sub> Sb <sub>2</sub> Cl <sub>9</sub>
Figure 4.20 XRD patterns of Rb <sub>3</sub> Bi <sub>2</sub> Br <sub>9</sub> samples made via the solution-phased
synthesis and the solid-state grinding method at room temperature 201
Figure 4.21 PXRD patterns of pure Rb <sub>3</sub> Bi <sub>2</sub> Br <sub>9</sub> (SsG) and 5% Sn doped nominally
<i>Rb</i> <sub>3</sub> <i>Bi</i> <sub>2</sub> <i>Br</i> <sub>9</sub> (SsG)
Figure 4.22 (a)UV-vis diffused reflectance study of Rb <sub>3</sub> Bi <sub>2</sub> Br <sub>9</sub> and (b) A diffuse
$\textit{reflectance spectrum from undoped } \textit{Rb}_{\textit{3}}\textit{Bi}_{\textit{2}}\textit{Br}_{\textit{9}} \textit{ via a solution-phased synthesis which}$
is treated with the Kubelka Munk function (green points). The optical absorption is
modelled using the Elliot model in blue line, consisting of an exciton peak modelling
by Dirac function in red and a continuum absorption modelling by Heaviside function
in black. 205

## 9 List of Tables

Table 3.1 The theoretical stretching modes of mixed halide octahedra based of	on
Character Tables for commonly encountered point groups	104
Table 3.2 The list of phases presented in the mixed samples (Cs <sub>2</sub> SnBr <sub>6</sub> + Cs <sub>2</sub>	SnI <sub>6</sub> )
heated to different temperatures.	125
Table 3.3 The list of phases presented in the mixed samples (Cs <sub>2</sub> SnBr <sub>6</sub> + Cs <sub>2</sub>	SnCl <sub>6</sub> )
heated to different temperatures and times	131
Table 3.4 The band gaps of compounds in series $Cs_2Sn_xTe_{1-x}cI_6$ (x= 0, 0.1, 0.	5, 0.9
and 1)	153
10 List of Equations	
Equation 1.1 Energy of an electron	18
Equation 1.2 Fill factor equation	35
Equation 1.3 Calculation of maximum power	36
Equation 1.4 The Shockley diode equation	36
Equation 2.1 Bragg's law	54
Equation 2.2 Kinetic energy of an ejected electron	60
Equation 2.3 Rerranged equation of Kinetic energy of an ejected electron	61
Equation 2.4 Calculation of atomic percent of elements(XPS)	63
Equation 2.5 Kubelka-Munk function	69
Equation 2.6 Exciton energy calculation	70
Equation 2.7 Planck- Einstein relation	73
Equation 3.1 D-spacing of a cubic crystal structure	94
Equation 4.1 Marcus-Hush Theory	173
Equation 4.2 Rearranged equation of Marcus-Hush Theory	174

## 11 Bibliography

- <sup>10</sup> Sharma, P.; Goyal, P. Evolution of PV technology from conventional to nanomaterials. Materials Today: Proceedings 2020, 28, 1593–1597.
- <sup>11</sup> Pastuszak, J.; Węgierek, P. Photovoltaic cell generations and current research directions for their development. Materials 2022, 15 (16), 5542.
- <sup>12</sup> Razykov, T. M.; Ferekides, C. S.; Morel, D.; Stefanakos, E.; Ullal, H. S.; Upadhyaya, H. M. Solar Photovoltaic Electricity: Current Status and Future Prospects. Solar Energy 2011, 85 (8), 1580–1608.
- <sup>13</sup> Rachow, T.; Reber, S.; Janz, S.; Knapp, M.; Milenkovic, N. Degradation of silicon wafers at high temperatures for epitaxial deposition. Energy Science & Engineering 2016, 4 (5), 344–351.

<sup>&</sup>lt;sup>1</sup> Singh, B. P.; Goyal, S. K.; Kumar, P. Solar PV cell materials and technologies: Analyzing the recent developments. Materials Today: Proceedings 2021, 43, 2843–2849.

<sup>&</sup>lt;sup>2</sup> Al-Ghussain, L. Global warming: Review on Driving Forces and mitigation. Environmental Progress & Environmental Progr

<sup>&</sup>lt;sup>3</sup> Tang, Y.; Duan, H.; Yu, S. Mitigating Climate Change to Alleviate Economic Inequality under the Paris Agreement. iScience 2023, 26 (1), 105734.

<sup>&</sup>lt;sup>4</sup> Breeze, P. A. Chater 13-Solar Power. In Power Generation Technologies; Newnes, 2019; pp 293–321.

<sup>&</sup>lt;sup>5</sup> J. Andrews and N. Jelley, Energy Science:2nd Revised edition, OXFORD University Press, Oxford, 2013.

<sup>&</sup>lt;sup>6</sup> Belyakov, N. Chapter Seventeen - Solar energy. In Sustainable power generation: Current status, future challenges, and perspectives; Academic Press, 2020; pp 417–438.

<sup>&</sup>lt;sup>7</sup> S. Li, Semiconductor Physical Electronics, 1993, 55-85.

<sup>&</sup>lt;sup>8</sup> TSAKALAKOS, L. In Nanotechnology for photovoltaics; CRC PRESS, 2019; pp 1–48.

<sup>&</sup>lt;sup>9</sup> Richter, A.; Hermle, M.; Glunz, S. W. Reassessment of the limiting efficiency for crystalline silicon solar cells. IEEE Journal of Photovoltaics 2013, 3 (4), 1184–1191.

<sup>14</sup> Rohde, D.; Beck, A.; Wilpert, P.; Dusek, S.; Windfeldt, M. K.; Andersson, L. E. Thermal energy storage for increased waste heat recovery at a silicon production plant in Norway. Applied Thermal Engineering 2022, 215, 118909.

- <sup>15</sup> Bhatia, S. C. 5.6.1 Thin-film technology. In Advanced Renewable Energy Systems; Woodhead, 2014; pp 144–157.
- <sup>16</sup> Kuczyńska-Łażewska, A.; Klugmann-Radziemska, E.; Witkowska, A. Recovery of valuable materials and methods for their management when recycling thin-film CdTe photovoltaic modules. Materials 2021, 14 (24), 7836.
- <sup>17</sup> Chopra, K. L.; Paulson, P. D.; Dutta, V. Thin-Film Solar Cells: An overview. Progress in Photovoltaics: Research and Applications 2004, 12 (23), 69–92.
- <sup>18</sup> Amin, N. Introduction of inorganic solar cells. Comprehensive Guide on Organic and Inorganic Solar Cells 2022, 57–63.
- <sup>19</sup> Asaduzzaman, Md.; Bahar, A. N.; Rahman Bhuiyan, M. M.; Habib, Md. A. Impacts of temperature on the performance of CdTe based thin-film solar cell. IOP Conference Series: Materials Science and Engineering 2017, 225, 012274.
- <sup>20</sup> Chu, S.; Majumdar, A. Opportunities and challenges for a sustainable energy future. Nature 2012, 488 (7411), 294–303.
- <sup>21</sup> Ramos-Ruiz, A.; Wilkening, J. V.; Field, J. A.; Sierra-Alvarez, R. Leaching of cadmium and tellurium from cadmium telluride (CdTe) thin-film solar panels under simulated landfill conditions. *Journal of Hazardous Materials* 2017, 336, 57–64.
- <sup>22</sup> Dunlap-Shohl, W. A.; Zhou, Y.; Padture, N. P.; Mitzi, D. B. Synthetic approaches for halide perovskite thin films. Chemical Reviews 2018, 119 (5), 3193–3295.
- <sup>23</sup> Pastuszak, J.; Węgierek, P. Photovoltaic cell generations and current research directions for their development. Materials 2022, 15 (16), 5542.
- <sup>24</sup> Verduci, R.; Romano, V.; Brunetti, G.; Yaghoobi Nia, N.; Di Carlo, A.; D'Angelo, G.; Ciminelli, C. Solar Energy in Space Applications: Review and Technology Perspectives. Advanced Energy Materials 2022, 12 (29), 2200125.
- <sup>25</sup> Peumans, P.; Yakimov, A.; Forrest, S. R. Small molecular weight organic thin-film photodetectors and solar cells. Journal of Applied Physics 2003, 93 (7), 3693–3723.
- <sup>26</sup> P. Reshmi Varma, Perovskite Photovoltaics, 2018, 197-229...
- <sup>27</sup> C. Stoumpos and M. Kanatzidis, Accounts of Chemical Research, 2015, 48, 2791-2802.
- <sup>28</sup> R. Ali and M. Yashima, Journal of Solid State Chemistry, 2005, 178, 2867-2872.

- <sup>29</sup> Chen, Y.; Zhang, L.; Zhang, Y.; Gao, H.; Yan, H. Large-area perovskite solar cells a review of recent progress and issues. RSC Advances 2018, 8 (19), 10489–10508.
- <sup>30</sup> P. Gao, M. Grätzel and M. Nazeeruddin, Energy Environ. Sci., 2014, 7, 2448-2463.
- <sup>31</sup> C. Eames, J. Frost, P. Barnes, B. O'Regan, A. Walsh and M. Islam, Nature Communications, 2015, 6.
- <sup>32</sup> Green, M., Ho-Baillie, A. and Snaith, H. (2014). The emergence of perovskite solar cells. Nature Photonics, 8(7), pp.506-514.
- <sup>33</sup> A. Kojima, K. Teshima, Y. Shirai and T. Miyasaka, Journal of the American Chemical Society, 2009, 131, 6050-6051.
- <sup>34</sup> H. Jung and N. Park, Small, 2015, 11, 2-2.
- <sup>35</sup> J. Im, C. Lee, J. Lee, S. Park and N. Park, Nanoscale, 2011, 3, 4088.
- <sup>36</sup> H. Kim, C. Lee, J. Im, K. Lee, T. Moehl, A. Marchioro, S. Moon, R. Humphry-Baker, J. Yum, J. Moser, M. Grätzel and N. Park, Scientific Reports, 2012, 2.
- <sup>37</sup> N. Park, The Journal of Physical Chemistry Letters, 2013, 4, 2423-2429.
- <sup>38</sup> D. Son, J. Lee, Y. Choi, I. Jang, S. Lee, P. Yoo, H. Shin, N. Ahn, M. Choi, D. Kim and N. Park, Nature Energy, 2016, 1.
- <sup>39</sup> Best Research-cell Efficiencies https://www.nrel.gov/pv/assets/pdfs/pv-efficiencies-07-17-2018.pdf (accessed Aug 19, 2018).
- <sup>40</sup> B. Zaidi, Solar Panels and Photovoltaic Materials, 2018.
- <sup>41</sup> Y. Hsiao, T. Wu, M. Li, Q. Liu, W. Qin and B. Hu, Journal of Materials Chemistry A, 2015, 3, 15372-15385.
- <sup>42</sup> S. Sun, T. Salim, N. Mathews, M. Duchamp, C. Boothroyd, G. Xing, T. Sum and Y. Lam, Energy Environ. Sci., 2014, 7, 399-407.
- <sup>43</sup> D. Zhou, T. Zhou, Y. Tian, X. Zhu and Y. Tu, Journal of Nanomaterials, 2018, 2018, 1-15.
- <sup>44</sup> Z. Fan, K. Sun and J. Wang, Journal of Materials Chemistry A, 2015, 3, 18809-18828.
- <sup>45</sup> Zhao, Y.; Yavuz, I.; Wang, M.; Weber, M. H.; Xu, M.; Lee, J.-H.; Tan, S.; Huang, T.; Meng, D.; Wang, R.; Xue, J.; Lee, S.-J.; Bae, S.-H.; Zhang, A.; Choi, S.-G.; Yin, Y.; Liu, J.; Han, T.-H.; Shi, Y.; Ma, H.; Yang, W.; Xing, Q.; Zhou, Y.; Shi, P.; Wang, S.; Zhang, E.; Bian, J.; Pan, X.; Park, N.-G.; Lee, J.-W.; Yang, Y. Suppressing Ion Migration in Metal Halide Perovskite via Interstitial Doping with a Trace Amount of Multivalent Cations. Nature Materials 2022, 21 (12), 1396–1402.
- <sup>46</sup> T. Chen, C. Foo and S. Edman Tsang, Chemical Science, 2021, 12, 517-532.

<sup>47</sup> Mizoguchi, H.; Chen, P.; Boolchand, P.; Ksenofontov, V.; Felser, C.; Barnes, P. W.; Woodward, P. M. Electrical and optical properties of SB-doped BaSnO3. Chemistry of Materials 2013, 25 (19), 3858–3866.

- <sup>48</sup> Kuganathan, N.; Ganeshalingam, S.; Chroneos, A. Defects, diffusion, and Dopants in LI2TI6O13: Atomistic simulation study. *Materials* 2019, *12* (18), 2851.
- <sup>49</sup> Chen, T.; Foo, C.; Edman Tsang, S. C. Interstitial, and substitutional light elements in transition metals for heterogeneous catalysis. Chemical Science 2021, 12 (2), 517–532.
- <sup>50</sup> Smith, I. C.; Hoke, E. T.; Solis-Ibarra, D.; McGehee, M. D.; Karunadasa, H. I. A Layered Hybrid Perovskite Solar-cell Absorber with Enhanced Moisture Stability. Angewandte Chemie International Edition 2014, 53 (42), 11232–11235.
- <sup>51</sup> Imran, M.; Caligiuri, V.; Wang, M.; Goldoni, L.; Prato, M.; Krahne, R.; De Trizio, L.; Manna, L. Benzoyl Halides as Alternative Precursors for the Colloidal Synthesis of Lead-Based Halide Perovskite Nanocrystals. Journal of the American Chemical Society 2018, 140 (7), 2656–2664.
- <sup>52</sup> Y. Zhou, Z. Zhou, M. Chen, Y. Zong, J. Huang, S. Pang, and N. Padture, Journal of Materials Chemistry A, 2016, 4, 17623-17635.
- <sup>53</sup> C. Stoumpos and M. Kanatzidis, Accounts of Chemical Research, 2015, 48, 2791-2802.
- <sup>54</sup> P. Gao, M. Grätzel and M. Nazeeruddin, Energy Environ. Sci., 2014, 7, 2448-2463.
- <sup>55</sup> S. Williams, A. Rajagopal, C. Chueh and A. Jen, The Journal of Physical Chemistry Letters, 2016, 7, 811-819.
- <sup>56</sup> B. Lotsch, Angewandte Chemie International Edition, 2013, 53, 635-637.
- <sup>57</sup> S. Singh and P. Nagarjuna, Dalton Transactions, 2014, 43, 5247.
- <sup>58</sup> M. Zhang, M. Lyu, J. Yun, M. Noori, X. Zhou, N. Cooling, Q. Wang, H. Yu, P. Dastoor and L. Wang, Nano Research, 2016, 9, 1570-1577.
- <sup>59</sup> I. Chung, J. Song, J. Im, J. Androulakis, C. Malliakas, H. Li, A. Freeman, J. Kenney, and M. Kanatzidis, Journal of the American Chemical Society, 2012, 134, 8579-8587.
- <sup>60</sup> Hoye, R. L.; Hidalgo, J.; Jagt, R. A.; Correa-Baena, J.; Fix, T.; MacManus-Driscoll, J. L. The role of dimensionality on the optoelectronic properties of oxide and halide perovskites, and their halide derivatives. *Advanced Energy Materials* 2021, *12* (4).
- <sup>61</sup> N. Park, The Journal of Physical Chemistry Letters, 2013, 4, 2423-2429.
- <sup>62</sup> Hayatullah, G. Murtaza, S. Muhammad, S. Naeem, M. Khalid and A. Manzar, Acta Physica Polonica A, 2013, 124, 102-107.

232

<sup>63</sup> W. Shockley and H. Queisser, Journal of Applied Physics, 1961, 32, 510-519.

- <sup>64</sup> S. Lee, R. Levi, W. Qu, S. Lee and C. Randall, Journal of Applied Physics, 2010, 107, 023523.
- <sup>65</sup> G. Xing, N. Mathews, S. Lim, N. Yantara, X. Liu, D. Sabba, M. Grätzel, S. Mhaisalkar and T. Sum, Nature Materials, 2014, 13, 476-480.
- <sup>66</sup> T. Berhe, W. Su, C. Chen, C. Pan, J. Cheng, H. Chen, M. Tsai, L. Chen, A. Dubale and B. Hwang, Energy & Environmental Science, 2016, 9, 323-356.
- <sup>67</sup> M. Grätzel, Nature Materials, 2014, 13, 838-842.
- <sup>68</sup> A. Babayigit, A. Ethirajan, M. Muller and B. Conings, Nature Materials, 2016, 15, 247-251.
- <sup>69</sup> M. Lyu, J. Yun, P. Chen, M. Hao and L. Wang, Advanced Energy Materials, 2017, 7, 1602512.
- <sup>70</sup> A. Maughan, A. Ganose, A. Candia, J. Granger, D. Scanlon and J. Neilson, Chemistry of Materials, 2017, 30, 472-483.
- <sup>71</sup> Zhou, L.; Zhou, S.; Liu, X.; Ma, J.; Zhang, T.; Li, K.; Chang, Y.; Shen, W.; Li, M.; He, R. Embedding Te4+ into Sn4+-Based Metal Halide To Passivate Structure Defects for High-Performance Light-Emitting Application. Inorganic Chemistry 2024, 63 (22), 10335–10345. https://doi.org/10.1021/acs.inorgchem.4c01185.
- <sup>72</sup> A. Rajagopal, R. Stoddard, H. Hillhouse and A. Jen, Journal of Materials Chemistry A, 2019, 7, 16285-16293.
- <sup>73</sup> Lee, B.; Stoumpos, C.; Zhou, N.; Hao, F.; Malliakas, C.; Yeh, C.; Marks, T.; Kanatzidis, M.; Chang, R. Journal of the American Chemical Society 2014, 136, 15379-15385.
- <sup>74</sup> M. Karim, A. Ganose, L. Pieters, W. Winnie Leung, J. Wade, L. Zhang, D. Scanlon and R. Palgrave, Chemistry of Materials, 2019, 31, 9430-9444.
- <sup>75</sup> A. Poglitsch and D. Weber, The Journal of Chemical Physics, 1987, 87, 6373-6378.
- <sup>76</sup> J. Pelzl, V. Waschk, Y. Seo and C. Dimitropoulos, Journal of Molecular Structure, 1983, 111, 363-369.
- <sup>77</sup> S. Kim, H. Jo, S. Sung, K. Kim, Y. Heo and D. Kim, RSC Advances, 2016, 6, 94502-94509.
- <sup>78</sup> R. Wasylishen, O. Knop and J. Macdonald, Solid State Communications, 1985, 56, 581-582.
- <sup>79</sup> W. Geng, L. Zhang, Y. Zhang, W. Lau and L. Liu, The Journal of Physical Chemistry C, 2014, 118, 19565-19571.

<sup>80</sup> A. Togo and I. Tanaka, Scripta Materialia, 2015, 108, 1-5.

- <sup>81</sup> J. Menéndez and M. Cardona, Physical Review B, 1984, 29, 2051-2059.
- <sup>82</sup> Luo, T.M. and J.W. Wei, First principles study of electronic and optical properties of inorganic and lead-free perovskite: Cs3Bi2X9 (X: Cl, Br, I). Materials Chemistry and Physics, 2020. 253.
- <sup>83</sup> Li, Y.J., et al., Lead-free and stable antimony-silver-halide double perovskite (CH3NH3)(2)AgSbl6. Rsc Advances, 2017. 7(56): p. 35175-35180.
- <sup>84</sup> Kim, K., H. Kim, and J. Park, Bandgap Modulation of Cs2AgInX6 (X = Cl and Br) Double Perovskite Nano- and Microcrystals via Cu<sup>2+</sup> Doping. Acs Omega, 2021. 6(41): p. 26952-26958.
- <sup>85</sup> Sebastia-Luna, P., et al., Tuning the Optical Absorption of Sn-, Ge-, and Zn-Substituted Cs2AgBiBr6 Double Perovskites: Structural and Electronic Effects. Chemistry of Materials, 2021. 33(20): p. 8028-8035.
- <sup>86</sup> Yao, M.M., et al., General Synthesis of Lead-Free Metal Halide Perovskite Colloidal Nanocrystals in 1-Dodecanol. Inorganic Chemistry, 2019. 58(17): p. 11807-11818.
- <sup>87</sup> Yan, Y.X., et al., Enhanced Photocatalytic Performance and Mechanism of Au@CaTiO3 Composites with Au Nanoparticles Assembled on CaTiO3 Nanocuboids. Micromachines, 2019. 10(4).
- <sup>88</sup> Krajewska, C.J., et al., Enhanced visible light absorption in layered Cs3Bi2Br9 through mixed-valence Sn(ii)/Sn(iv) doping. Chemical Science, 2021. 12(44): p. 14686-14699.
- <sup>89</sup> Ali, R.F., I. Andreu, and B.D. Gates, Green solvent assisted synthesis of cesium bismuth halide perovskite nanocrystals and the influences of slow and fast anion exchange rates. Nanoscale Advances, 2019. 1(11): p. 4442-4449.
- <sup>90</sup> Xiang, G.B., et al., Dimension-Dependent Bandgap Narrowing and Metallization in Lead-Free Halide Perovskite Cs3Bi2X9 (X = I, Br, and Cl) under High Pressure. Nanomaterials, 2021. 11(10).
- <sup>91</sup> Stan, C.; Beavers, C.; Kunz, M.; Tamura, N. X-ray diffraction under extreme conditions at the Advanced Light Source. Quantum Beam Science 2018, 2 (1), 4.
- <sup>92</sup> Rietveld, H. M. Line profiles of neutron powder-diffraction peaks for structure refinement. Acta Crystallographica 1967, 22 (1), 151–152.
- <sup>93</sup> Moulder, J. F.; Bomben, K. D.; Sobol, P. E.; William F. Handbook of X-ray Photoelectron Spectroscopy: A reference book of standard spectra for identification and interpretation of XPS Data; Chastain, J., Ed.; Physical Electronics, 1995.

<sup>94</sup> D. Harris and M. Bertolucci, Symmetry and spectroscopy, Dover, New York, NY, 2014.

- <sup>95</sup> Klein, J.; Kampermann, L.; Mockenhaupt, B.; Behrens, M.; Strunk, J.; Bacher, G. Limitations of the Tauc plot method. *Advanced Functional Materials* 2023.
- <sup>96</sup> Elliott, R. J. Intensity of optical absorption by excitons. *Physical Review* 1957, *108* (6), 1384–1389.
- <sup>97</sup> Lindquist, K. P.; Mack, S. A.; Slavney, A. H.; Leppert, L.; Gold-Parker, A.; Stebbins, J. F.; Salleo, A.; Toney, M. F.; Neaton, J. B.; Karunadasa, H. I. Tuning the bandgap of cs2agbibr6 through dilute tin alloying. Chemical Science 2019, 10 (45), 10620–10628.
- <sup>98</sup> Morgan, W. E.; Van Wazer, J. R.; Stec, W. J. Inner-orbital photoelectron spectroscopy of the alkali metal halides, perchlorates, phosphates, and pyrophosphates. *Journal of the American Chemical Society* **1973**, *95* (3), 751–755.
- <sup>99</sup> Dalpian, G. M.; Liu, Q.; Stoumpos, C. C.; Douvalis, A. P.; Balasubramanian, M.; Kanatzidis, M. G.; Zunger, A. Changes in charge density vs changes in formal oxidation states: The case of SN Halide Perovskites and their ordered vacancy analogues. *Physical Review Materials* 2017, *1* (2).
- <sup>100</sup> Yuan, G.; Huang, S.; Niu, J.; Qin, S.; Wu, X.; Ding, H.; Lu, A. Compressibility of CS 2 snbr 6 by X-ray diffraction and Raman spectroscopy. Solid State Communications 2018, 275, 68–72.
- <sup>101</sup> Sist, M.; Fischer, K. F. F.; Kasai, H.; Iversen, B. B. Low-Temperature anharmonicity in cesium chloride (CSCL). *Angewandte Chemie International Edition* **2017**, *56* (13), 3625–3629. https://doi.org/10.1002/anie.201700638.
- <sup>102</sup> I. Kanesaka, T. Matsuda and Y. Morioka, Journal of Raman Spectroscopy, 1995, 26, 239-242.
- <sup>103</sup> Torres, D. I.; Freire, J. D.; Katiyar, R. S. Lattice dynamics of crystals having. Physical Review B 1997, 56 (13), 7763–7766.
- <sup>104</sup> Ohe, W. von. Raman spectrum of (NH4)2tif6 and trigonal CS2tif6. The Journal of Chemical Physics 1976, 65 (9), 3575–3585.
- <sup>105</sup> Adams, D. M.; Berg, R. W.; Williams, A. D. Vibrational spectroscopy at very high pressures. part 28. Raman and far-infrared spectra of some complex chlorides A2MCL6 under hydrostatic pressure. The Journal of Chemical Physics 1981, 74 (5), 2800–2807.

- <sup>107</sup> Kaltzoglou, A.; Antoniadou, M.; Kontos, A. G.; Stoumpos, C. C.; Perganti, D.; Siranidi, E.; Raptis, V.; Trohidou, K.; Psycharis, V.; Kanatzidis, M. G.; et al. Optical-vibrational properties of the cs2snx6 (X = cl, br, I) defect perovskites and Hole-transport efficiency in dye-sensitized solar cells. The Journal of Physical Chemistry C 2016, 120 (22), 11777–11785.
- <sup>108</sup> Ullah, S.; Ullah, S.; Wang, J.; Yang, S.-E.; Xia, T.; Guo, H.; Chen, Y. Investigation of air-stable Cs2Sni6 Films prepared by the modified two-step process for lead-free perovskite solar cells. Semiconductor Science and Technology 2020, 35 (12), 125027.
- <sup>109</sup> I. Aleksandrov, A. Goncharov, I. Makarenko, and S. Stishov, Physical Review B, 1991, 43, 6194-6197.
- <sup>110</sup> Demont, A.; Prestipino, C.; Hernandez, O.; Elkaïm, E.; Paofai, S.; Naumov, N.; Fontaine, B.; Gautier, R.; Cordier, S. Unprecedented electron-poor octahedral ta6clusters in a solid-state compound: Synthesis, characterisations and theoretical investigations of Cs2Bata6Br15O3. Chemistry A European Journal 2013, 19 (38), 12711–12719.
- <sup>111</sup> M. Sist, K. Fischer, H. Kasai, and B. Iversen, Angewandte Chemie International Edition, 2017, 56, 3625-3629.
- <sup>112</sup> T. Kuan, Journal of Raman Spectroscopy, 1976, 4, 373-378.
- <sup>113</sup> A. Kaltzoglou, M. Antoniadou, D. Perganti, E. Siranidi, V. Raptis, K. Trohidou, V. Psycharis, A. Kontos and P. Falaras, Electrochimica Acta, 2015, 184, 466-474.
- <sup>114</sup>Wyckoff, R. American Journal of Science 1928, s5-16, 349-359.
- <sup>115</sup> J. Im, C. Stoumpos, H. Jin, A. Freeman, and M. Kanatzidis, The Journal of Physical Chemistry Letters, 2015, 6, 3503-3509.
- <sup>116</sup> G. Engel, Die Naturwissenschaften, 1933, 21, 704-704.
- <sup>117</sup> T. Brill, R. Gearhart and W. Welsh, Journal of Magnetic Resonance (1969), 1974, 13, 27-37.
- <sup>118</sup> R. Shannon, Acta Crystallographica Section A, 1976, 32, 751-767.
- <sup>119</sup> Yoon, S.; Fett, B.; Frebel, A.; Kroisl, S.; Herbig, B.; Widenmeyer, M.; Balke, B.; Sextl, G.; Mandel, K.; Weidenkaff, A. SB-substituted Cs2Agbibr6—as much as it could be?—influence of synthesis methods on sb-substitution level in cs2agbibr6. *Energy Technology* 2022, *10* (8).
- <sup>120</sup> Folgueras, M. C.; Jin, J.; Gao, M.; Quan, L. N.; Steele, J. A.; Srivastava, S.; Ross, M. B.; Zhang, R.; Seeler, F.; Schierl@3&rndt, K.; et al. Lattice Dynamics and

optoelectronic properties of vacancy-ordered double perovskite Cs2Tex6 (X = cl-, BR-, l-) single crystals. *The Journal of Physical Chemistry C* 2021, *125* (45), 25126–25139.

- <sup>121</sup> Lazarini, F. Caesium enneabromodibismuthate(III). *Acta Crystallographica Section B Structural Crystallography and Crystal Chemistry* 1977, 33 (9), 2961–2964.
- <sup>122</sup> Abrahams, I.; Demetriou, D. Z. Inert pair effects in tin and lead dihalides: Crystal Structure of tin(ii) bromide. *Journal of Solid State Chemistry* 2000, *149* (1), 28–32.
- <sup>123</sup> Bhachu, D. S.; Moniz, S. J.; Sathasivam, S.; Scanlon, D. O.; Walsh, A.; Bawaked, S. M.; Mokhtar, M.; Obaid, A. Y.; Parkin, I. P.; Tang, J.; et al. Bismuth oxyhalides: Synthesis, structure and photoelectrochemical activity. Chemical Science 2016, 7 (8), 4832–4841.
- <sup>124</sup> Giovilli, G.; Albini, B.; Grisci, V.; Bonomi, S.; Moroni, M.; Mosconi, E.; Kaiser, W.; De Angelis, F.; Galinetto, P.; Malavasi, L. Band gap tuning through cation and halide alloying in mechanochemically synthesized Cs3(SB1–*x*bi*x*)2br9 and cs3sb2(i1–*x*br*x*)9 solid solutions. *Journal of Materials Chemistry C* 2023, *11* (30), 10282–10291.
- <sup>125</sup> Akinbami, O.; Moepya, R.; Ngubeni, G. N.; Tetyana, P.; Mubiayi, K. P.; Moloto, M. J.; Moloto, N. Lead-free rudorffite-type CS3BI2BR9 nanoparticles for photocatalytic degradation of rhodamine B and Methylene Blue. Journal of Photochemistry and Photobiology A: Chemistry 2021, 419, 113460.
- <sup>126</sup> Jia, X.; Liu, Y.; Bhatt, P.; Perry, R. S.; Parkin, I. P.; Palgrave, R. G. Mixed valence SN doped (CH3Nh3)3bi2br9 produced by Mechanochemical Synthesis. *Physical Chemistry Chemical Physics* 2023, *25* (6), 4563–4569.
- <sup>127</sup> Bass, K. K.; Estergreen, L.; Savory, C. N.; Buckeridge, J.; Scanlon, D. O.; Djurovich, P. I.; Bradforth, S. E.; Thompson, M. E.; Melot, B. C. Vibronic structure in room temperature photoluminescence of the halide perovskite Cs3Bi2Br9. *Inorganic Chemistry* 2016, *56* (1), 42–45.
- <sup>128</sup> Pazoki, M.; Johansson, M. B.; Zhu, H.; Broqvist, P.; Edvinsson, T.; Boschloo, G.; Johansson, E. M. Bismuth iodide perovskite materials for solar cell applications: Electronic structure, optical transitions, and directional charge transport. *The Journal of Physical Chemistry C* 2016, *120* (51), 29039–29046.
- <sup>129</sup> Zhang, G.; Yuan, C.; Li, X.; Yang, L.; Yang, W.; Fang, R.; Sun, Y.; Sheng, J.; Dong, F. The mechanisms of interfacial charge transfer and photocatalysis reaction over CS3BI2CL9 qd/(bio)2co3 heterojunction. *Chemical Engineering Journal* 2022, *430*, 132974.
- <sup>130</sup> Zhao, C.; Gao, Y.; Zhou, D.; Zhu, F.; Chen, J.; Qiu, J. High-efficiency dual-mode luminescence of metal halide perovskite CS3BI2CL9:er3+ and its use in optical temperature measurement with high sensitivity. *Journal of Alloys and Compounds* 2023, *944*, 169134.

<sup>131</sup> Morgan, E.E., et al., Tunable Perovskite-Derived Bismuth Halides: Cs3Bi2(Cl1-xlx)(9) Emily. Inorganic Chemistry, 2020. 59(6): p. 3387-3393.

- <sup>132</sup> Morgan, E. E.; Mao, L.; Teicher, S. M.; Wu, G.; Seshadri, R. Tunable perovskite-derived bismuth halides: Cs3bi2(cl1–xlx)9. *Inorganic Chemistry* 2020, *59* (6), 3387–3393.
- <sup>133</sup> Machulin, V. F.; Motsnyi, F. V.; Smolanka, O. M.; Svechnikov, G. S.; Peresh, E. Yu. Effect of temperature variation on shift and broadening of the exciton band in CS3BI2I9 layered crystals. *Low Temperature Physics* 2004, *30* (12), 964–967.
- <sup>134</sup> McCall, K. M.; Stoumpos, C. C.; Kostina, S. S.; Kanatzidis, M. G.; Wessels, B. W. Strong electron–phonon coupling and self-trapped excitons in the defect halide perovskites a3M2I9 (A = Cs, RB; M = bi, SB). *Chemistry of Materials* 2017, *29* (9), 4129–4145.
- <sup>135</sup> Pradhan, A., et al., Effect of Bi Substitution on Cs3Sb2Cl9: Structural Phase Transition and Band Gap Engineering. Crystal Growth & Design, 2020. 20(5): p. 3386-3395.
- <sup>136</sup> Valakh, M.Y., et al., The Raman spectra of the family crystals Cs3Bi2Br9, Rb3Bi2Br9 and Rb3Sb2Br9. Journal of Molecular Structure, 1997. 437: p. 309-313.
- <sup>137</sup> Pradhan, A., M.K. Jena, and S.L. Samal, Understanding of the Band Gap Transition in Cs3Sb2Cl9-xBrx: Anion Site Preference-Induced Structural Distortion. Acs Applied Energy Materials, 2022. 5(6): p. 6952-6961.
- <sup>138</sup> Pradhan, B., et al., Size Tunable Cesium Antimony Chloride Perovskite Nanowires and Nanorods. Chemistry of Materials, 2018. 30(6): p. 2135-2142.
- <sup>139</sup> Vargas, B., et al., A Direct Bandgap Copper-Antimony Halide Perovskite. Journal of the American Chemical Society, 2017. 139(27): p. 9116-9119.
- <sup>140</sup> Chang, J.; Wang, Y.; Doert, T.; Ruck, M. The polymorphic nature of *m*3bibr6 halides (*m*=cs, RB) and their reversible intercalation with water to isomorphous hydrates at room temperature. *Zeitschrift für anorganische und allgemeine Chemie* 2021, *647* (5), 478–484.
- <sup>141</sup> Chang, J.-H.; Doert, T.; Ruck, M. Structural variety of defect perovskite variants *m*3e2x9(*m*= RB, tl,e= bi, sb,x= br, I). *Zeitschrift für anorganische und allgemeine Chemie* 2016, *642* (13), 736–748.
- <sup>142</sup> Weber, S., et al., Influence of the lodide to Bromide Ratio on Crystallographic and Optoelectronic Properties of Rubidium Antimony Halide Perovskites. Acs Applied Energy Materials, 2019. 2(1): p. 539-547.
- <sup>143</sup> Harikesh, P. C.; Mulmudi, H. K.; Ghosh, B.; Goh, T. W.; Teng, Y. T.; Thirumal, K.; Lockrey, M.; Weber, K.; Koh, T. M.; Li, S.; et al. Rb as an alternative cation for

templating inorganic lead-free perovskites for solution processed photovoltaics. *Chemistry of Materials* 2016, *28* (20), 7496–7504.

- <sup>144</sup> Saparov, B.; Hong, F.; Sun, J.-P.; Duan, H.-S.; Meng, W.; Cameron, S.; Hill, I. G.; Yan, Y.; Mitzi, D. B. Thin-film preparation and characterization of Cs3Sb2l9: A lead-free layered perovskite semiconductor. *Chemistry of Materials* 2015, *27* (16), 5622–5632.
- <sup>145</sup> Shi, H.; Han, D.; Chen, S.; Du, M.-H. Impact of Metal. Physical Review Materials 2019, 3 (3).
- <sup>146</sup> Prassides, K.; Day, P.; Cheetham, A. K. Anion Ordering in Mixed-Valence26and Related Salts. Molecules Into Materials 2007, 125–127.
- <sup>147</sup> Atkinson, L.; Day, P. Charge Transfer in Mixed-Valence Solids.: Part V. Semiconductivity of Hexachloroantimonates(Iii,V). *Molecules Into Materials* **2007**, 137–141.